



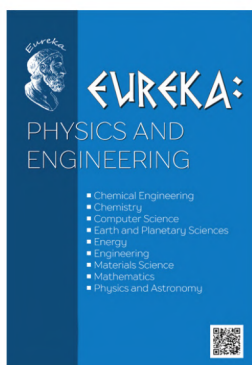
# EUREKA:

## PHYSICS AND ENGINEERING

- Chemical Engineering
- Chemistry
- Computer Science
- Earth and Planetary Sciences
- Energy
- Engineering
- Materials Science
- Mathematics
- Physics and Astronomy

Volume 5(36)  
2021





**EUREKA: Physics and Engineering** – scientific journal whose main aim is to publish materials allowed to see *new discoveries at the intersection of sciences*.

- Chemical Engineering
- Chemistry
- Computer Science
- Earth and Planetary Sciences
- Energy
- Engineering
- Material Science
- Mathematics
- Physics and Astronomy
- Technology Transfer

**EUREKA: Physics and Engineering** publishes 4 types of materials:

- review article,
- progress reports,
- original Research Article,
- reports on research projects

PUBLISHER OÜ «Scientific Route»  
**European Union**

Editorial office  
**EUREKA: Physics and Engineering**  
Narva mnt 7-634, Tallinn, Eesti  
Harju maakond, 10117  
Tel. + 372 602-7570  
e-mail: [info@eu-jr.eu](mailto:info@eu-jr.eu)  
Website: <http://eu-jr.eu>

## EDITORIAL BOARD

### EDITOR-IN-CHIEF

**Masuma Mammadova**, *Institute of Information Technology of the National Academy of Sciences of Azerbaijan, Azerbaijan*

### EDITORS

**Moh'd Al-Nimr**, *Jordan University of Science and Technology, Jordan*

**Marcello Andreetta**, *Federal University of São Carlos (UFSCar), Brazil*

**Hikmet Assadov**, *Research Institute of the Ministry of Defense Industry of Azerbaijan Republic, Azerbaijan*

**Jan Awrejcewicz**, *Lodz University of Technology, Poland*

**Nicolas Berchenko**, *Centre of Microelectronics and Nanotechnology of Rzeszów University, Poland*

**Anna Brzozowska**, *Institute of Logistics and International Management Czestochowa University of Technology, Poland*

**Jean-Marie Buchlin**, *Von Karman Institute Environmental and Applied Fluid Dynamics Department Chaussee de Waterloo, Belgium*

**Levan Chkhartishvili**, *Georgian Technical University, Georgia*

**J. Paulo Davim**, *University of Aveiro, Portugal*

**Jaroslav W. Drelich**, *Michigan Technological University, United States*

**Baher Effat**, *National Research Centre – Egypt, Egypt*

**S. Ali Faghidian**, *Università degli Studi di Napoli Federico II, Italy*

**Luigi Fortuna**, *University of Catania, Italy*

**Ibrahim Abulfaz oglu Gabibov**, *Azerbaijan State Oil and Industry University, Azerbaijan*

**Jahan B Ghasemi**, *University of Tehran, Iran*

**Peyman Givi**, *University of Pittsburgh, United States*

**Prashanth Konda Gokuldoss**, *Tallinn University of Technology, Estonia*

**Tridib Kumar Goswami**, *IIT Kharagpur, India*

**Nenad Gubeljak**, *University of Maribor, Slovenia*

**Manoj Gupta**, *National University of Singapore, Singapore*

**Sergii Guzii**, *Institute of Macromolecular Chemistry of National Academy of Sciences of Ukraine, Ukraine*

**Yuh-Shan Ho**, *Asia University, Taiwan, Province of China*

**Muhammad Mahadi bin Abdul Jamil**, *Universiti Tun Hussein Onn Malaysia (UTHM), Malaysia*

**Dimitris Kanellopoulos**, *University of Patras, Greece*

**Ioannis Kassaras**, *National and Kapodistrian University of Athens, Greece*

**Vladimir Khmelev**, *Biysk Technological Institute (branch) of the federal state budgetary institution of higher education "Altai State Technical University by I. I. Polzunov", Russian Federation*

**Takayoshi Kobayashi**, *Advanced Ultrafast Laser Research Center, The University of Electro-Communications, Japan*

**Jun Ma**, *Lanzhou University of Technology, Gansu, Province of China*

**Ram N. Mohapatra**, *University of Central Florida, United States*

**Syed Taueef Mohyud-Din**, *HITEC University, Pakistan*

**Volodymyr Mosorov**, *Institute of Applied Computer Science Lodz University of Technology, Poland*

**Vahur Oja**, *Tallinn University of Technology, Estonia*

**Franco Pastrone**, *University of Turin, Italy*

**Ján Pitel**, *Technical University of Kosice, Slovakia*

**Mihaela Popescu**, *University of Craiova, Romania*

**Nicola Pugno**, *Università di Trento, via Mesiano, Italy*

**Mohammad Mehdi Rashidi**, *Bu-Ali Sina University, Iran*

**Mat Santamouris**, *UNSW, Australia*

**Ulkar Eldar Sattarova**, *Institute of Control Systems, Azerbaijan National Academy of Sciences, Azerbaijan*

**Miklas Scholz**, *Lund University, Sweden*

**G. S. Seth**, *Indian School of Mines, India*

**Yury Shitov**, *Joint Institute for Nuclear Research, Dubna, Russian Federation*

**Hari Mohan Srivastava**, *University of Victoria, Canada*

**Yana Maolana Syah**, *Institut Teknologi Bandung, Indonesia*

**Francesco Tornabene**, *University of Salento, Italy*

**Kenji Uchino**, *The Pennsylvania State University, United States*

**Ugur Ulusoy**, *Sivas Cumhuriyet University, Turkey*

**Frank Visser**, *Flowserve, Netherlands*

**Sadok Ben Yahia**, *Tallinn University of Technology, Estonia*



## CONTENT

A FUZZY VAULT DEVELOPMENT BASED ON IRIS IMAGES <i>Mohammed A. Taha, Hanaa M. Ahmed</i>	3
THE EFFECT OF MAGNETIC FIELD VARIATIONS IN A MIXTURE OF COCONUT OIL AND JATROPHA ON FLAME STABILITY AND CHARACTERISTICS ON THE PREMIXED COMBUSTION <i>Dony Perdana, Satworo Adiwidodo, Mochamad Choifin, Wigo Ardi Winarko</i>	13
STUDY ON MODEL FOR CUTTING FORCE WHEN MILLING SCM440 STEEL <i>Nguyen Van Thien, Do Duc Trung</i>	23
A DEVELOPMENT METHOD OF CUTTING FORCE COEFFICIENTS IN FACE MILLING PROCESS USING PARALLELOGRAM INSERT <i>Nhu-Tung Nguyen</i>	36
MODELING OF NATURAL CONVECTION OF A CONCENTRATED SOLAR POWER RECEIVER ABSORBER TUBE IN INTERACTION WITH NEIGHBOURING ABSORBERS <i>Olanrewaju Miracle Oyewola, Niyi Ezekiel Olukayode, Olusegun Olufemi Ajide</i>	53
ANALYSIS OF THE NUMBER AND ANGLE OF THE IMPELLER BLADE TO THE PERFORMANCE OF CENTRIFUGAL PUMP <i>Sugeng Hadi Susilo, Agus Setiawan</i>	62
INCREASING THE EFFICIENCY OF MULTY-VARIANT CALCULATIONS OF ELECTROMAGNETIC FIELD DISTRIBUTION IN MATRIX OF A POLYGRADIENT SEPARATOR <i>Jasim Mohmed Jasim Jasim, Iryna Shvedchikova, Igor Panasniuk, Julia Romanchenko, Inna Melkonova</i>	69
ANALYSIS OF RELIABILITY OF THE DRILL PIPE IN THE CLAMPING MECHANISM <i>Emin Musa Afandiyev, Mahammadali Nuraddin Nuriyev</i>	80
ABOUT THE POSSIBILITY OF APPLICATION OF LASER VACUUM WELDING FOR THE INTEGRATION OF ELEMENTS OF HEAT-PROTECTIVE STRUCTURES FROM POWDER MATERIALS <i>Walid Alnusirat, Alexandr Salenko, Olga Chenchewa, Sergii Shlyk, Irina Gusarova, Alexandr Potapov</i>	88
A NUMERICAL STUDY TO IMPROVE THE POSITION AND ANGLE OF THE PRODUCER GAS INJECTOR INSIDE THE INTAKE MANIFOLD TO MINIMIZE EMISSIONS AND EFFICIENCY ENHANCEMENT OF A BI ENGINE <i>Hussein A. Mahmood, Ali O. Al-Sulttani, Osam H. Attia, Nor Mariah. Adam</i>	100
ANALYSIS OF PHYSICAL PROPERTIES AND COMPRESSIBILITY OF AVIAN EGGSHELL NANOPOWDERS IN SOLID STATE REACTION <i>Poppy Puspitasari, Muhammad Asrorul Iftiharsa, Herin Fikri Naufal Zhorifah, Rara Warih Gayatri</i>	110
DEVELOPMENT OF ORGANIZATIONAL AND TECHNICAL METHODS FOR PREDICTING EMERGENCY SITUATIONS AND POSSIBLE LOSSES AS THEIR RESULTS <i>Hryhorii Ivanets, Stanislav Horielyshev, Martin Sagradian, Mykhailo Ivanets, Igor Boikov, Dmitro Baulin, Yuriy Kozlov, Aleksandr Nakonechnyi, Lyudmila Safoshkina</i>	121
USE OF THE PASS-THROUGH METHOD TO SOLVE SOUND RADIATION PROBLEMS OF A SPHERICAL ELECTRO-ELASTIC SOURCE OF ZERO ORDER <i>Oleksii Korzhnyk, Sergey Naida, Sergii Kurdiuk, Valeriia Nizhynska, Maxim Korzhnyk, Anton Naida</i>	133

# A FUZZY VAULT DEVELOPMENT BASED ON IRIS IMAGES

**Mohammed A. Taha**✉

*Department of Computer Sciences<sup>1</sup>  
cs.19.54@grad.uotechnology.edu.iq*

**Hanaa M. Ahmed**

*Department of Computer Sciences<sup>1</sup>*

<sup>1</sup>*University of Technology*

*Alsinaa str., Baghdad, Iraq, 19006*

✉Corresponding author

## Abstract

Biometric systems gather information from the person's biometric attributes, used extensively to authorize the individuals. Due to the obvious convenience of using specific individual traits such as face, fingerprints, palm veins, and irises, biometric authentication is becoming more common. In particular, Iris systems are in high demand for high-assurance applications, because they contain a broad feature set and remain stable. Authentication methods based on iris biometrics are now commonly used in a variety of fields. This is due to the fact that iris biometric authentication is both safer and more comfortable than conventional passwords. Template Security is a major concern in biometric systems. The template security mechanism ensures reusable, permanent, and un-linkable models. The Fuzzy Vault strategy is one of the most popular security schemes for Template protection.

Fuzzy vault has demonstrated to be an effective protection method but lacks revocability and security attacks. This article introduced an improved fuzzy vault system. The improved fuzzy vault system was introduced, which uses more than one key to protect biometric data. Different keys make the search space more detailed. The additional key was used to encrypt vault data, which stopped the intruder from accessing the information on the person's biometry. The system was tested using CASIA.v1 and IITD.v1 datasets, and findings showed that the system ensures the protection and authentication of the iris templates without compromising performance. The proposed modification gave a 0.0 % False Accepted Rate (FAR) for both the dataset and False Rejected Rate (FRR), 0.14 % for CASIA v1 and 0.12 % for IITD v1 False Rejected rate.

**Keywords:** Authentication, Biometrics, Fuzzy vault, Iris, Template protection, GLCM, CASIA v1, IITD v1, FAR, FRR.

DOI: 10.21303/2461-4262.2021.001997

## 1. Introduction

Motivation: Biometrics is a social identity analysis to authenticate or identify substance characters. Identification of biometrics people by their biological attributes, including fingerprint, iris, retina, hand anatomy, face, palm scanning or some forms of actions such as signature, gesture, and voice. Biometric technology requires massive biometric volumes template construction data that causes severe privacy leakage [1, 2]. Biometric authentication offers excellent protection because, instead of smart cards or text passwords, biometric forgery or fraud is very difficult to lose or forget. Biometric security and safety are widely used, primarily due to the precision and uniqueness of biometric features such as Iris. And there are also other attacks that the biological systems experience, such as the brute force attack, position attack, correlation attack, etc. Biological system stability is a significant threat. Thus, the safe security of biological templates caught the attention of people [1].

Contributions. This article's main aim is to propose a new improvement with an iris prototype of the fuzzy vault scheme. Typically, a biometric framework's accuracy is calculated by its False Accepted Rate (FAR) and False Rejected Rate (FRR), also known as matching accuracy [3]. To ensure accuracy, let's strive to reduce the FAR rate. Furthermore, let's aim to minimize FRR as well as time for successful authentication and usability. However, since the traditional fuzzy vault scheme uses a single biological template and the biological function parameters are stored directly in the fuzzy vault, the biological template will not be adequately protected.



To address this problem, let's propose a novel fuzzy vault scheme based on the encryption of the vault, which makes it resist the correlation and brute force attack on the fuzzy vault using the iris template.

Fuzzy vault schema, first implemented in [2], was a well-known biometric system cryptographic architecture. Because of the increasing use of biometric authentication, the fuzzy vault cryptosystem has become a well-studied research field [4]. The author proposes a shift to the fuzzy vault [5]. An additional layer of security is introduced using a password to achieve a high degree of protection. This program offers a high level of security from a secure password. If the password fails, it is similar to the standard fuzzy method. Only the same password would harden the secret key derived from the same prototype. The hardening method requires the following steps. First, the recognition system has a random user password processing feature. Second, the fuzzy vault framework then protects the transformed prototype. Finally, the vault is secured by a password-based key. The author proposes to boost the fuzzy vault scheme in [6]. An iris shuffling algorithm is used in the framework to ensure the revocable iris template based on three key aims: first, no template information should be leaked from the stored data. Second, templates can be withdrawn; once they are infected, they can be released without recovering the iris. Third, the fuzzy vault against the correlation attack should be safe. Source of reference not found. So it is not possible to compare the fuzzy vaults of the same design to determine the key used for building the fuzzy vault. In [7], the author of the article suggests a new way of solving the problems of the new fuzzy vault based on CRC. An updated generator and verifier of chaff points were added. In order to create structural chaff points at the registration stage, continuous hashing and linear projection are used. As a result, the same chaff points are regenerated for the final decision during the authentication stage. The proposed system treats chaff points as a signature for the secure key and biometric template combination. Any changes on the decoded vault are detected during the authentication process to avoid the assault of mixing substitutions. The author proposed a new fuzzy vault schema method. In [8, 9], the authors proposed a modified fuzzy vault framework, A 128-bit Advanced Encryption Standard (AES) key combination of iris data. Experimental results demonstrated that the 128-bit cryptographic keys and iris models with a fuzzy vault system were stable. There are two benefits and improvements to the new method. First, it was implemented as a pattern clustering method to address the variance in extracted iris features. Second, it was used to create fuzzy vault sets as an iris extraction algorithm based on the Independent Component Analysis (ICA). In [10], the author suggested that several models for a user be protected as a single entity. A fuzzy vault system was used to derive one multi-biometric template from individual templates. It shows that a multi-biometric vault offers better identification and more excellent protection than a uni-biometric vault. The proposed method achieves a better value of Genuine Accepted Rate (GAR) and False Accepted Rate (FAR) compared to the uni-biometric fuzzy vault. It also provides higher security than uni-biometric systems.

## 2. Materials and methods

Fuzzy vault is the primary biometric binding cryptographic in different applications; the fuzzy vault method has been widely studied and considered. Fuzzy vault only receives unordered input. A fuzzy vault must be translated into an unordered set of biometrics with features in an ordered set. Assume that  $B$  is a biometric prototype with  $f$ -points. A secret key  $K$  is selected and is encrypted, say as coefficients, into a polynomial  $P$  with a degree  $d$ . Biometric prototype characteristics are now based on the polynomial. Any random points are introduced to cover the genuine elements, which do not cheat on the  $P$  polynomial. As shown in **Fig. 1**, such random points are named chaff points [2, 11].

When the user submits a biometric request  $B$ , authentication is completed if the key  $K$  is regenerated only if  $B$  overlaps with  $A$  and authentication is successful, as shown in **Fig. 2** below.

On the opposite, regeneration of  $K$  is unlikely if there is insufficient overlap between  $A$  and  $B$ , authentication is ineffective. Reed Solomon (RS) procedures are used to correct the polynomial error. The inefficiency of the polynomial reconstruction is based on the non-vulnerability of this approach.

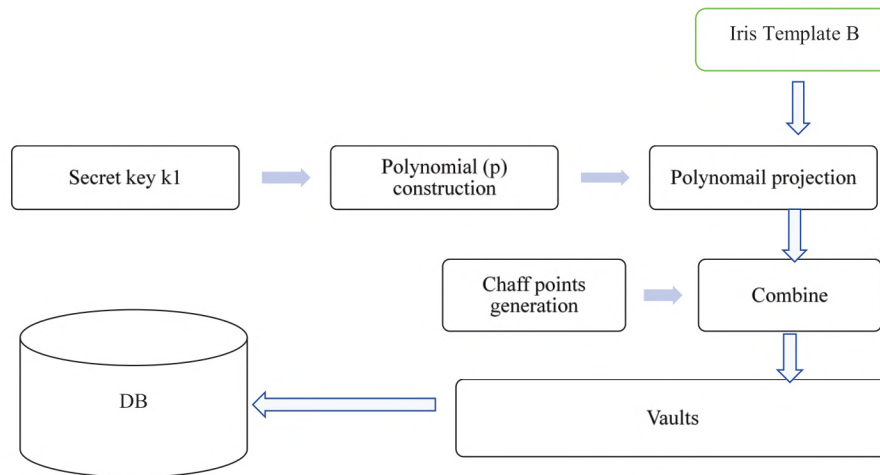


**Fig. 1.** Fuzzy vault encoding process [12]

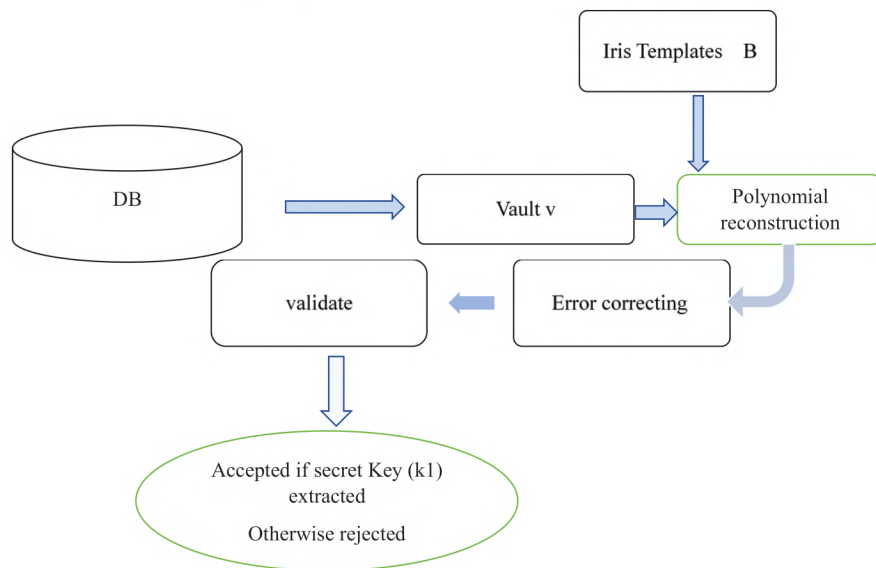


**Fig. 2.** Fuzzy vault decoding process [12]

## 2. 1. Proposed System

This section explains the formal structure of our proposed scheme. The framework contains the following modules.

### 2. 1. 1. Vault Encoding

The method of vault encoding or registration is implemented as follows in our cryptosystem. **Fig. 3** demonstrates the registration process of the device model proposed.

*Iris image template extraction.* The user's iris image is provided as an input in the registration process. The grey level co-occurrence matrix (GLCM) texture extraction methods [13–15] have been used to extract iris textures features.

*Chaff Points Generation.* To hide the real points of a potential attacker, random chaffs points are produced to provide a fair balance between the complexity and the performance of brute force attacks.

*Polynomial Projection.* The fuzzy vault system is a set of  $(X, Y)$  tuples, defining  $(X, Y)$  the system coordinate. The first dimension of a tuple vault,  $X$ , has a fixed value. The second dimension,  $Y$ , is generated randomly under certain conditions. Any genuine point  $X$  is drawn to the secret polynomial  $p$ , and the resulting value is saved as the second tuple variable, i. e.,  $Y = p(X)$ . The polynomial mapping is carried out in a Galois field (GF) so that exact polynomial interpolation is



possible in vault decoding. Then, in the potential results space of polynomial projection, the chaff points are randomly mapped to a number in order not to lie on the polynomial. This mapping gives the second tuple element,  $Y$ , where  $Y$  corresponds to  $p(X)$  [16, 17].

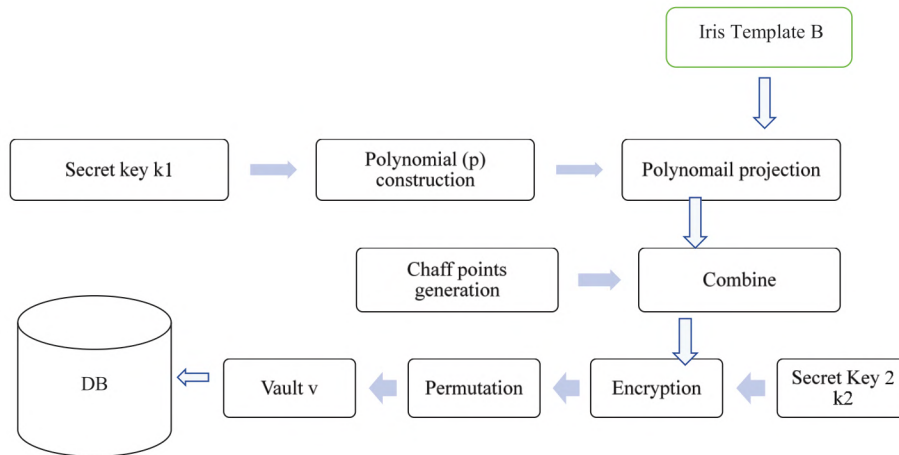


**Fig. 3.** Modified fuzzy vault schema

*Vault encryption.* The proposed change uses vault encryption. There is a suggested improvement that uses more than one key to protect encrypted biometric information. The additional keys ( $K2$ ) used to encrypt vault data expand the search space. An attacker could not use the decoding algorithms to obtain information about user biometrics by inserting the extra key. The keyspace for the cryptographic scheme is the cumulative number of separate keys that need to be used. The safety of the algorithm depends on the key size. The high length key, the more secure the algorithm will be against a brute force attack. The main length is represented uniformly as a number of key bits [17]. A key  $N$ -bit length has the  $2^N$  keyspace choices. The keyspace size should not be less than  $2^{100}$  from the cryptographic perspective to provide a high degree of security [18].

*Vault Scrambling and permutation.* The Vault tuples with genuine points can't be separated from the tuples with chaff points by fusing the encrypted vault.

## 2. 2. Vault Decoding

Vault decoding or authentication is applied, as seen in Fig. 4.

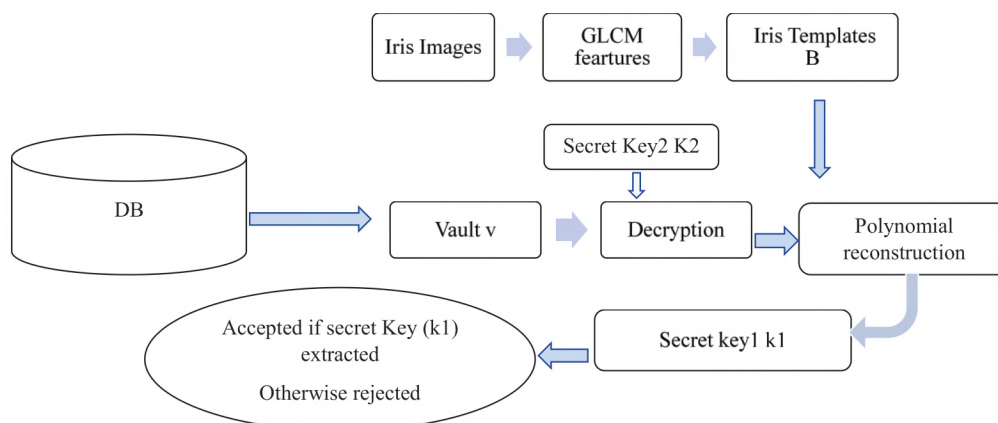


**Fig. 4.** Authentication in the proposed system

*Iris Image and Fuzzy Vault.* The iris image template is extracted from GLCM in the registration process, and the actual (claimed) user's fuzzy vault provided from the database (DB) by using its unique identifier (id) as an input to the verification algorithm.

*Vault Decryption.* A particular key ( $K_2$ ) was used during the validation process to decrypt the locked vault during the enrollment phase.

*Polynomial Interpolation.* Polynomial interpolation shall be performed unless the size of a candidate set at the end of one iteration with two different bases is greater than polynomial degree plus one ( $n+1$ ). The hidden polynomial can't be interpolated if fewer candidates are found. In the case of sufficiently vault tuples, all sub-sets of size  $n+1$  must be evaluated, as not all candidate vertices have genuine points. The interpolation of Lagrange in a Galois field (GF) ( $2^{32}$ ) for each sub-set is achieved by using  $n+1$  vault tuple, interpreted as  $(X, Y)$  sample points with  $X$  and  $Y$  being respectively, the first and second variable for the vault tuple.

*Correct Secret.* When no intrusion is encountered, the proper secret key ( $k_1$ ) is found as well as the user is tested successfully.

### 3. Results and discussions

The simulation parameters used for implementation are presented in this section. It also analyzes the attack by brute force and the attack by correlation to show the consistency of the proposed method.

#### 3. 1. Performance evaluation

##### 3. 1. 2. Database

Both CASIA v1 [19] and the IITD Iris Image database [20] will be tested for the proposed method.

CASIA v1 consists of 756 iris images of 108 persons and seven images each taken during two separate sessions with a difference of at least one month. Both 8-bit grey images are 320 to 280 resolution and preserved in bitmap format [19].

In our experiments, let's use two key images, one for registration and the other for testing. Fig. 5 below shows some database examples.

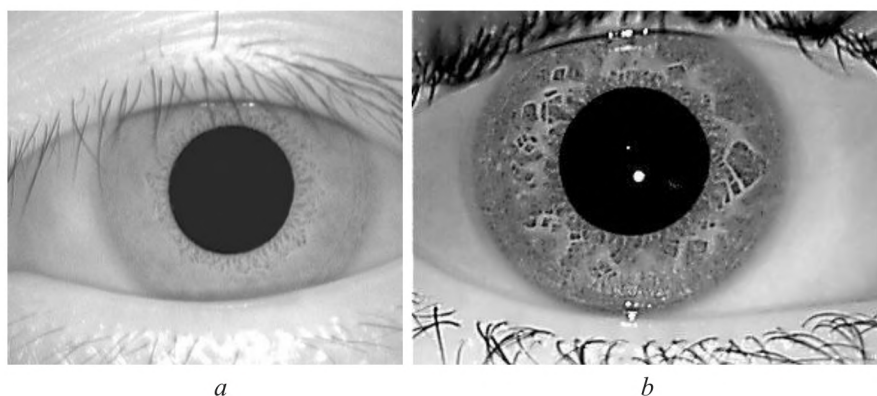


**Fig. 5.** Iris images samples: *a* – CASIA v1 image [19]; *b* – IITD.v1 image [20]

The IITD.v1 image database mainly consists of iris pictures obtained from IIT Delhi students and staff.

This database was compiled by JIRIS, JPC1000, and digital CMOS camera in the Biometrics Research Laboratory from January to July 2007. The collected images have been stored in bitmap format. The database includes 2,240 images from 224 different users that are freely available to researchers. In the sample, all subjects aged 14–55 years consist of 176 men and 48 women. These pictures are 320×240 pixels in size, and all these photographs have been acquired indoors [20].

##### 3. 1. 2. Parameter Values

Different parameters settings can be seen in Table 1.

In Table 1, there are the variables used in the proposed system for evaluation and analysis.



**Table 1**  
Parameters setting

Parameters	
Genuine points number $g$	8
Chaff points number $c$	400
Total vault points $v$	408
Polynomial degree $n$	9

**3. 1. 3. Performance**

With the False Accept (FAR) and False Reject Ratios (FRR), the performance of the proposed iris-based fuzzy vault system was assessed, as seen in **Table 2**.

**Table 2**  
Proposed system performance

Dataset	FAR	FRR	Time
CASIA.v1	0.0	0.16	0.145 ms
ITTD.v1	0.0	0.12	0.133 ms

FAR represents the number of accurate key retrievals by non-authentic device users. FRR represents the number of refusals for actual machine users [21].

**3. 1. 4. Security Analysis**

To extract a hidden polynomial  $P(x)$  with a polynomial degree ( $n$ ), a subset of  $(n+1)$  vault pairs shall be required. In this case, all  $(n+1)$  pairs of vault elements must contain genuine points ( $g$ ), and Chaff points ( $c$ ) are not concealed. In all  $(v = g + c)$ , vault pairs are assumed in the fuzzy vault where ( $v$ ) is the total number of points in the vault, ( $g$ ) is the number of genuine points, and ( $c$ ) is the number of chaff points identified in vault formation. This makes it possible for the attacker  $v_s = (n+1)^V$  vault size pair sub-sets  $(n+1)$  overall.  $g_s = (n+1)^g$  subgroups contain genuine points from these sets, which can be used to interpolate the hidden polynomial properly. This leaves  $(c_s = v_s - g_s)$  pair subsets were containing genuine pairs but include at least one pair of pairs of vaults. If the chaff vault pair is only one member of the candidate sub-set  $(n+1)$ , the secret polynomial fails because the chaff vault pair does not lie on the secret polynomial [10]. The attacker doesn't know which vault pairs have genuine points, so they can only pick one sub-set, again and again, to interpolate at random.

An attacker needs to find an appropriate subset for accurate interpolation of the secret key to determine the estimated number of attempts [21, 22]:

$$totalattempts E(g,c) = \frac{v+1}{g+1} = \frac{\left((n+1)^v + 1\right)}{\left((n+1)^g + 1\right)} = \frac{\frac{v!}{(n+1)(v-n-1)!}}{\frac{g!}{(n+1)(g-n-1)!}}. \quad (1)$$

Let's also note from (1), which shows the number of attempts the attacker needs to break the system and obtain sensitive user information. Therefore, the proposed modification to the fuzzy vault method ensures that the number of attempts increases in a balanced manner consistent with the length of the key ( $K_2$ ) used in the fuzzy vaults encryption, which gives additional strength and protection to sensitive information. Therefore, (2) is as follows:

$$totalattempts E(g,c) = \frac{v+1}{g+1} = \frac{\left(\frac{(n+1)^v + 1}{(n+1)^g + 1}\right)}{\frac{\frac{v!}{(n+1)(v-n-1)!}}{\frac{g!}{(n+1)(g-n-1)!}}} + 2^{encryption\ key\ (K2)\ length}. \quad (2)$$

To determine the expected time for a potential attacker to access a fuzzy vault by subset interpolation randomly, let's multiply the estimated time ( $T$ ) to select a genuine portion with the average time per subset of Lagrange interpolation:

$$Time = \left( \frac{v+1}{g+1} + 2^{encryption\ key\ (K2)\ length} \right) \cdot T. \quad (3)$$

Let's recognize, the average duration of interpolation increases with the polynomial degree ( $n$ ). Let's summarize the effect of the ( $g$ ,  $c$ , and  $n$ ) parameters on the estimated time an attacker has to release the secret and present the expected value  $total\ attempts\ E(g_s, c_s)$  with expanded polynomial coefficients to better display the security impact.

The expected value  $total\ attempts\ E(g_s, c_s)$  decreases as only the denominator increases, so protection decreases. The expected value  $total\ attempts\ E(g_s, c_s)$  increase as encryption key length increased. Expanding the number of chaff points  $c$ ,  $total\ attempts\ E(g_s, c_s)$  also increases, with  $(v = g+c)$  increasing in the nominator. The attacker, therefore, requires further attempts to open the vault on average. Both binomial coefficients of nominators and denominators change by increasing the polynomial degree  $n$ .

### 3. 2. Biometric systems attacks

A variety of attacks are introduced in the biometrics framework. However, attacks on safe models significantly reduce the reliability of the biometric system. The attacks based on the template are either brute force, correlation, known key, replacement, or hill climb attacks. This work focused on both brute force and correlation attacks.

#### 3. 2. 1. Brute force attack

An attacker tries every possible bit mixture in this type of attack before the correct data is calculated or the key is retrieved for the original function. The basic fuzzy vault depends on the degree of the polynomial. The attacker can quickly restore a lower polynomial degree. Higher degree polynomial provides increased stability [23, 24]. Polynomial degree  $n$  in the fuzzy vault, the attacker has to try for brute force ( $g, n+1$ ) of  $g+1$  element combinations, as seen in (1). The proposed modification to the standard fuzzy vault method should increase the number of attempts that the attacker makes to obtain sensitive information, as shown in (2); therefore, getting sensitive information for the user takes a very long time, as shown in (3).

#### 3. 2. 2 Correlation attack

In the case of a correlation attack, at least two vaults belong to one individual. Two different ways can generate the vaults: (1) the fuzzy vault is formed using similar genuine points with different hidden key( $k1$ ). (2) equivalent genuine points with various chaff points. Let the assailant two vaults be intercepted containing two points ( $pts$ ) and ( $pts'$ ). An attacker's goal is to find some transformation on points ( $pts'$ ). i. e ( $Transform\ (pts')$ ). Whether  $distance \leq threshold$  ( $Th$ ), transformed characteristics of  $\{Transform\ (pts'), (pts')\}$  correlate with ( $pts$ ). Let  $V$  consists of fuzzy pairs of vaults  $\{pts\}$  with  $distance(pts, Transform(pts')) \leq Th$ . The error-correcting procedure, Reed Solomon decoder (RS), can be used to open the vault when matching pairs of ( $pts, pts'$ ) is lower than pairs not paired [24, 25]. Assume that genuine and chaff ( $pts$ ) and ( $pts'$ ) are equal in size. There are points of ( $pts$ ) genuine and chaff points of ( $pts'$ ). The proposed modification to the fuzzy vault method should prevent a correlation attack, as encryption for the data prevents interconnection



between the data, as it is possible to encrypt the data of each user with a random key that differs from the other user, which helps prevent penetration and protect the iris template.

**Table 3** compares the proposed Fuzzy Vault with the current polynomial degree 8 methods with the CASIA v1 dataset. Genuine Acceptance Rate (GAR) is defined as a percentage of the system's approved genuine users. It is given by  $GAR = 100 - FRR$  [26–28].

**Table 3**  
Methods comparison

Method	FAR	GAR	Brute force attack solution	Correlation attack solution
Proposed method	0.0	86.0	yes	yes
E. Srinivasa Reddy [3]	0.03	92.0	no	no
E. Srinivasa Reddy [5]	0.0	90.2	yes	no
Youn Joo Lee [26]	0.0004	73.686	no	no

Through **Table 3**, it is clear that the proposed method gives good results compared to other methods and provides solutions for correlation and brute force attacks.

The results of the proposed system displayed in **Table 2** are greatly influenced by the threshold value used. It represents the difference between enrolled template and query template so it must be chosen carefully. Specific use and security considerations must be taken into account when choosing the optimal parameters. For good performance, various thresholds have been made. It always depends on the context of use to decide between security and usability. There is some degradation in the GAR because of in some cases, features could not be reliably extracted from a relatively large region in the iris pattern due to factors like occlusion reflection, motion blur, contrast variation, pupil dilation, blurred image, partially open eye and defocused image. This problem can be compensated by overlooks the occluded regions in the Euclidean distance calculation. However, this problem can't be handled effectively by the proposed system leading to further false rejections. Both CASIA.1 and ITTD.1 has (0.0 %) FAR, making it suitable for a high-security application.

The main advantage of the proposed modification of fuzzy vaults adds a second layer of security against the attacker, even if the attacker succeeds in unlocking the vaults and receiving the key but still can't receive the original template as the encrypted template version has to be solved to get feature points and adds more complexity in our fuzzy vault. The proposed modification ensures that the attacker will increase the number of attempts needed to break the system and obtain sensitive user information, thus providing an effective solution to the brute force attack and correlation attack. This increase in the number of attempts depends the key length ( $K_2$ ) used to encrypt fuzzy vault, giving additional strength and protection to sensitive information.

From a cryptographic standpoint, it's worth noting that the fuzzy vault architecture solves the key management problem, which is a big problem in real-world cryptosystems. The prototype implementation and experimental results indicate that a realistic application of this cryptosystem is possible, as it is more secure than commonly used iris recognition algorithms without compromising quality or runtime efficiency. At the same time, it increases the stability of existing cryptosystems by resisting correlation and brute force attacks. As a consequence, let's assume it is a viable alternative for safe and functional distributed authentication. Despite the apparent benefit of the proposed modification, it adds some complexity and extra time to encrypt and decrypt data, which is one of the disadvantages of the proposed system.

Fuzzy vault is most importantly secure due to the complexity of polynomial reconstruction and the number of randomly generated chaff points. However, the proposed system's security is also largely dependent on the encryption key length. Clearly, the higher the degree polynomial and the more chaff points, the more difficult it is to recover the true polynomial  $P(x)$  for the fusion points. The addition of more chaff points or polynomial degrees will have a direct influence on runtime. The balance between security and the best usage should be determined on each specific application.



As a biometric, the proposed system is based only on the iris. Using multiple biometrics to generate fuzzy vaults that all have to be matched to authenticate is one way to improve security. Using passwords plus biometrics will enhance the system's efficiency.

#### 4. Conclusion

This research has developed and constructed a biometric cryptosystem based on a fuzzy vault that can be utilized for authentication with strong privacy and protection. The implemented scheme uses another hidden based encryption layer to protect the vault data in the original fuzzy vault schema. The proposed system would increase the search space to make the intruder more complicated and challenging to use the template data. When testing the proposed system, it gave 0.0 % acceptable error rate (FAR) for both dataset and false rejection rate (FRR), 0.14 % for CASIA v1 and 0.12 % for ITTD v1 as well as solving the problem of brute force attack and correlation attack on the contrary, to the rest of the previous systems that give a higher FRR, but do not put solutions to these attacks.

#### Acknowledgements

Part of the work described in this paper is based on CASIA-IrisV1 collected by the Institute of Automation of the Chinese Academy of Sciences (CASIA).

---

#### References

- [1] You, L., Wang, T. (2018). A novel fuzzy vault scheme based on fingerprint and finger vein feature fusion. *Soft Computing*, 23 (11), 3843–3851. doi: <https://doi.org/10.1007/s00500-018-3046-8>
- [2] Juels, A., Sudan, M. (2006). A Fuzzy Vault Scheme. *Designs, Codes and Cryptography*, 38 (2), 237–257. doi: <https://doi.org/10.1007/s10623-005-6343-z>
- [3] Reddy, E. S., Babu, I. R. (2008). Authentication Using Fuzzy Vault Based on Iris Textures. 2008 Second Asia International Conference on Modelling & Simulation (AMS). doi: <https://doi.org/10.1109/ams.2008.112>
- [4] Prabhakar, S., Pankanti, S., Jain, A. K. (2003). Biometric recognition: security and privacy concerns. *IEEE Security & Privacy*, 1 (2), 33–42. doi: <https://doi.org/10.1109/msecp.2003.1193209>
- [5] Reddy, E. S., Babu, I. R. (2008). Performance of Iris Based Hard Fuzzy Vault. 2008 IEEE 8th International Conference on Computer and Information Technology Workshops. doi: <https://doi.org/10.1109/cit.2008.workshops.20>
- [6] Fouad, M., El Saddik, A., Zhao, J., Petriu, E. (2011). A fuzzy vault implementation for securing revocable iris templates. 2011 IEEE International Systems Conference. doi: <https://doi.org/10.1109/syscon.2011.5929061>
- [7] Nguyen, M. T., Truong, Q. H., Dang, T. K. (2016). Enhance fuzzy vault security using nonrandom chaff point generator. *Information Processing Letters*, 116 (1), 53–64. doi: <https://doi.org/10.1016/j.ipl.2015.08.012>
- [8] Lee, Y. J., Bae, K., Lee, S. J., Park, K. R., Kim, J. (2007). Biometric Key Binding: Fuzzy Vault Based on Iris Images. *Lecture Notes in Computer Science*, 800–808. doi: [https://doi.org/10.1007/978-3-540-74549-5\\_84](https://doi.org/10.1007/978-3-540-74549-5_84)
- [9] Nandakumar, K., Jain, A. K. (2008). Multibiometric Template Security Using Fuzzy Vault. 2008 IEEE Second International Conference on Biometrics: Theory, Applications and Systems. doi: <https://doi.org/10.1109/btas.2008.4699352>
- [10] Geng, S., Giannopoulou, G., Kabir-Querrec, M. (2019). Privacy Protection in Distributed Fingerprint-based Authentication. *Proceedings of the 18th ACM Workshop on Privacy in the Electronic Society – WPES'19*. doi: <https://doi.org/10.1145/3338498.3358648>
- [11] Koptyra, K., Ogiela, M. R. (2018). Multiply information coding and hiding using fuzzy vault. *Soft Computing*, 23 (12), 4357–4366. doi: <https://doi.org/10.1007/s00500-018-3089-x>
- [12] Panwar, A., Singla, P., Kaur, M. (2017). Techniques for Enhancing the Security of Fuzzy Vault: A Review. *Progress in Intelligent Computing Techniques: Theory, Practice, and Applications*, 205–213. doi: [https://doi.org/10.1007/978-981-10-3376-6\\_23](https://doi.org/10.1007/978-981-10-3376-6_23)
- [13] Rasool, R. A. (2018). Iris Feature Extraction and Recognition based on Gray Level Co-occurrence Matrix (GLCM) Technique. *International Journal of Computer Applications*, 181 (25), 15–17. doi: <https://doi.org/10.5120/ijca2018917826>
- [14] Hajari, K., Gawande, U., Golhar, Y. (2016). Neural Network Approach to Iris Recognition in Noisy Environment. *Procedia Computer Science*, 78, 675–682. doi: <https://doi.org/10.1016/j.procs.2016.02.116>
- [15] Rathgeb, C., Tams, B., Wagner, J., Busch, C. (2016). Unlinkable improved multi-biometric iris fuzzy vault. *EURASIP Journal on Information Security*, 2016 (1). doi: <https://doi.org/10.1186/s13635-016-0049-9>
- [16] Weerasinghe, T. D. B. (2012). Secrecy and Performance Analysis of Symmetric Key Encryption Algorithms. *International Journal of Information and Network Security (IJINS)*, 1 (2). doi: <https://doi.org/10.11591/ijins.v1i2.438>



- [17] Singha, S., Sen, M. (2016). Encoding algorithm using bit level encryption and decryption technique. 2016 International Conference on Computer, Electrical & Communication Engineering (ICCECE). doi: <https://doi.org/10.1109/iccece.2016.8009584>
- [18] Chitra, D., Sujitha, V. (2019). Security analysis of prealigned fingerprint template using fuzzy vault scheme. Cluster Computing, 22 (S5), 12817–12825. doi: <https://doi.org/10.1007/s10586-018-1762-6>
- [19] Woodard, D. L., Ricanek, K. (2009). Iris Databases. Encyclopedia of Biometrics, 770–774. doi: [https://doi.org/10.1007/978-0-387-73003-5\\_168](https://doi.org/10.1007/978-0-387-73003-5_168)
- [20] Kumar, A., Passi, A. (2010). Comparison and combination of iris matchers for reliable personal authentication. Pattern Recognition, 43 (3), 1016–1026. doi: <https://doi.org/10.1016/j.patcog.2009.08.016>
- [21] Uludag, U., Pankanti, S., Jain, A. K. (2005). Fuzzy Vault for Fingerprints. Audio- and Video-Based Biometric Person Authentication, 310–319. doi: [https://doi.org/10.1007/11527923\\_32](https://doi.org/10.1007/11527923_32)
- [22] Weik, M. H. (2000). Brute-Force Attack. Computer Science and Communications Dictionary, 149–149. doi: [https://doi.org/10.1007/1-4020-0613-6\\_1898](https://doi.org/10.1007/1-4020-0613-6_1898)
- [23] Nandakumar, K., Jain, A. K., Pankanti, S. (2007). Fingerprint-Based Fuzzy Vault: Implementation and Performance. IEEE Transactions on Information Forensics and Security, 2 (4), 744–757. doi: <https://doi.org/10.1109/tifs.2007.908165>
- [24] Nagar, A., Nandakumar, K., Jain, A. K. (2010). A hybrid biometric cryptosystem for securing fingerprint minutiae templates. Pattern Recognition Letters, 31 (8), 733–741. doi: <https://doi.org/10.1016/j.patrec.2009.07.003>
- [25] Li, P., Yang, X., Cao, K., Tao, X., Wang, R., Tian, J. (2010). An alignment-free fingerprint cryptosystem based on fuzzy vault scheme. Journal of Network and Computer Applications, 33 (3), 207–220. doi: <https://doi.org/10.1016/j.jnca.2009.12.003>
- [26] Lee, Y. J., Park, K. R., Lee, S. J., Bae, K., Kim, J. (2008). A New Method for Generating an Invariant Iris Private Key Based on the Fuzzy Vault System. IEEE Transactions on Systems, Man, and Cybernetics, Part B (Cybernetics), 38 (5), 1302–1313. doi: <https://doi.org/10.1109/tsmcb.2008.927261>
- [27] Ahmed, H. M., Taha, M. A. (2021). A Brief Survey on Modern Iris Feature Extraction Methods. Engineering and Technology Journal, 39 (1A), 123–129. doi: <https://doi.org/10.30684/etj.v39i1a.1680>
- [28] Taha, M., Ahmed, H. (2021). Second-Order Statistical Methods GLCM for Authentication Systems. Iraqi Journal for Electrical and Electronic Engineering, 17 (1), 1–6. doi: <https://doi.org/10.37917/ijeee.17.1.10>

Received date 09.03.2021

Accepted date 30.07.2021

Published date 13.09.2021

© The Author(s) 2021

This is an open access article  
under the Creative Commons CC BY license

**How to cite:** Taha, M. A., Ahmed, H. M. (2021). A fuzzy vault development based on iris images. EUREKA: Physics and Engineering, 5, 3–12. doi: <https://doi.org/10.21303/2461-4262.2021.001997>

# THE EFFECT OF MAGNETIC FIELD VARIATIONS IN A MIXTURE OF COCONUT OIL AND JATROPHA ON FLAME STABILITY AND CHARACTERISTICS ON THE PREMIXED COMBUSTION

**Dony Perdana**✉

*Department of Mechanical Engineering<sup>1</sup>  
dony\_perdana@yahoo.co.id*

**Satworo Adiwidodo**

*Department of Mechanical Engineering  
State Polytechnic of Malang  
9 Jl. Soekarno-Hatta, Malang, East-Java, Indonesia, 65141*

**Mochamad Choifin**

*Department of Mechanical Engineering<sup>1</sup>*

**Wigo Ardi Winarko**

*Department of Mechanical Engineering  
University of Jember  
37 Jl. Kalimantan, Jember, East-Java, Indonesia, 68121*

<sup>1</sup>*Universitas Maarif Hasyim Latif*

*30 Jl. Ngelom Megare, Taman, Sidoarjo, East-Java, Indonesia, 61257*

✉Corresponding author

## Abstract

This study investigates the effect of attracting and repels magnetic fields with the materials of vegetable oil in the form of a mixture of coconut oil and jatropha (B50) against the behavior of stability and characteristics of flame in the process of premixed burning. The fuel for a mixture of vegetable oil of 600 ml was filled into the boiler heated with a gas stove to be evaporated at a temperature of 300 °C and 3 bar pressure was kept constant was mixed with air from the compressor in the burner room. Then a flame was ignited at the end of the nozzle to form a diffusion flame, the flame formed was then given north (N) and south (S). The results showed that the flame speed of the attractive magnetic field was 52.22 cm/sec, the repulsive magnetic field was 50.49 cm/sec while without a magnetic field was 49.79 cm/sec. The increase in the laminar flame speed in the attractive magnetic field is caused by the electron spin becoming more energetic and due to the change in the spin of the hydrogen proton from para to ortho. The attractive magnetic field has the strongest effect on increasing the flame speed. This makes the flame more stable in the equivalency ratio range of 0.75–1.17 compared to without a magnetic field in the same equivalency ratio range. This was so because O<sub>2</sub> where it is in nature of paramagnetic was pumped more crossing the flame from south to north poles whereas the heat brought by H<sub>2</sub>O in nature of diamagnetic was pumped more crossing north to south poles. Whereas on the repel magnetic field, it was hotter when brought by H<sub>2</sub>O pumped into the flame whereas O<sub>2</sub> tended to be pumped going out of the flame. This caused the combustion in the flame was smaller and the reaction was not maximum. As a consequence, the laminar flame speed was more lacking and the reaction was not to the fullest. As a consequence, the laminar flame speed in the repel was fewer than the attract magnetic field.

**Keywords:** vegetable oil, premix combustion, magnetic field, flame stability, flame characteristics, flame shape, combustion process, laminar flame speed, equivalence ratio, attract magnetic field.

DOI: 10.21303/2461-4262.2021.001996

## 1. Introduction

The increasing environmental threat due to exhaust gas emissions, the problem of global warming, and the threat of instability in fuel supply have had a bad impact on developing countries, especially oil-importing countries. Several researchers have found alternative fuels for internal combustion engines as well as developing various vegetable oils from various plants, such as



jatropha [1], soybean [2], radish [3], algae [4], and canola [5]. Many studies have shown that fuels have the main properties impacting the performance of diesel engines [6, 7]. Studies have shown that the combustion behavior of vegetable oil is similar to that of diesel oil [8]. Using sunflower, cottonseed (CSO), corn, and olive oil on blend diesel fuel in the bus engine, it is shown that the brake thermal efficiency and brake specific fuel consumption is almost the same as diesel fuel. The mixture of 60 % CSO and 40 % diesel which is preheated to 90 °C brake thermal efficiency, ignition delay, and heat release is close to that of diesel fuel [9]. Compression ignition engine fueled with cottonseed oil and its blends with diesel fuel found that brake thermal efficiency, CO<sub>2</sub> and CSO100 peak cylinder pressure were almost the same as diesel at all loads [8–10]. However, each vegetable oil has different characteristics and behavior, this is due to its specific physical and chemical properties. Also, the formation of the precipitate and the piston sticks to long-term use due to the presence of oxygen in the molecule and the reactivity of the unsaturated hydrocarbon chains causing problems in the use of vegetable oils [11]. There are also several problems encountered in its use. Such as clogged filters, injectors, pumps, and deposits on the piston rings in the combustion chamber [12]. However, various solutions were proposed to overcome these problems, among others:

- mixing vegetable oil with diesel oil in different proportions;
- heating vegetable oil;
- exhaust gas recirculation;
- modify the combustion chamber (piston, injector, etc.).

Research using Karanja methyl ester (KME)-diesel oil blends fuel (KME 5, 10, 15, 20, 30, 40, 50, 100) shows that mechanical efficiency achieved with KME30 is higher than diesel at lower loading conditions and emission characteristics are higher than pure diesel but the KME30 has relatively better performance concerning other blends [13]. Another researcher examined the performance of Karanja oil with diesel blends (non-preheated blend and preheated blend) was studied in comparison with diesel fuel by increasing the initial fuel temperature variation from 35–80 °C. The results showed that the emission values of hydrocarbon and nitric oxide were decreased and the carbon-monoxide value was increased for the above-said blend when compared with the diesel fuel operation [14]. Other researchers mixing rapeseed oil with diesel oil showed that at high engine loads, the start of combustion for the blends was slightly earlier than that for diesel fuel, but the peak cylinder pressure and heat release rate were identical and the BSFC of rapeseed oil-diesel blends were higher than that of diesel fuel under all range of engine loads, but the BSEC was improved at high engine loads [13–15]. Alternative fuels such as waste cooking oil (WCO)-based biodiesel were blended with the B10 and B20 found that using B10 and B20 as fuels can decrease these emission factors in the range of 17–52 % and 49–73 % on a mass basis, as well as 21–61 % and 61–83 % on a toxicity basis [16]. Research with variations in fossil fuel diesel (B0), 20 % rapeseed methyl ester in fossil diesel (B20), and pure rapeseed methyl ester (B100) result in the effect was weaker for B0 low SAPS in comparison with high SAPS, while B100 high SAPS leads to increasing the oxidative stress in comparison with B20 high SAPS, thus indicating the role of biofuel composition which may be associated with bio micro markers found for biofuel exhausts as well with higher oxidation and nitrification of the biofuel particle surface, relating with higher reactivity and oxidation behavior [17]. Other researchers used a mixture of conventional diesel oil with biodiesel from microalgae. The fuel blends – B2 (2 % microalgae biodiesel +98 % conventional diesel) showed the HC emissions from B2 decreased by 50.2 % [16–18]. A mixture of 30 % vegetable oil and 70 % diesel fuel can be burned in a CI engine without the need for engine modifications or fuel preheating [19].

Along with continuous improvements in the combustion system, new concepts for the combustion system are required to be investigated. Combustion assisted by magnetic fields can be a viable option in increasing combustion efficiency and flame control. Magnetic fields have been known to influence the flame behavior and flow of gases due to the paramagnetic and diamagnetic properties of the constituent gases. In diffusion flame, HC, H<sub>2</sub>O, N, and CO<sub>2</sub> are diamagnetic while oxygen is the main paramagnetic gas. Because the paramagnetic susceptibility to oxygen is greater, the diamagnetic behavior is considered negligible. Gases that contain more O<sub>2</sub>, such as air, tend to move towards stronger magnetic fields and gases with less O<sub>2</sub> such as fuel or combustion gases tend



to move towards weaker magnetic fields. Based on this, it is possible to use a magnetic field to control the flow field in the combustion area to improve the combustion characteristics. Hydrocarbon fuel molecules treated with a magnetic field tend to break down, creating smaller particles resulting in better combustion [20]. The hydrogen particles in fuels are arranged in two forms of para and ortho isomers. Hydrogen effectively describes efficient combustion. In the state of para spinning from one atom relative to another is in the opposite direction, whereas in the ortho form the rotation of one atom relative to another is in the same direction. When a strong magnet is applied to the fuel, the hydrocarbons change orientation and change from a para form to an ortho form [20]. The ortho forms a sizeable reduction in the inter-molecular force which occurs causing an increase in the space between the hydrogens. Because the magnetic treatment causes the fuel-oxygen relationship to increase, resulting in complete fuel combustion in the combustion chamber [21]. The CO and HC content values decreased by 90 %, and 58 %, respectively, when using a 2000 gauss magnetic field in a four-stroke single-cylinder diesel engine [22]. Two-stroke single-cylinder diesel engines and added a magnetic field with an intensity of 2000–9000 gauss resulted in a 40 % reduction in CO and 30 % HC [20]. The use of a 5000-gauss magnetic field achieves a reduction in HC and CO emissions of 12 %, 22 %, and 7 % in fuel consumption, respectively, but increases in NO<sub>x</sub> and CO<sub>2</sub> 19 % and 7 %, respectively [23]. The magnetic field intensity of 2000–9000 gauss resulted in a reduction of CO and HC by 30 % and 40 %, respectively, the fuel consumption of 9–14 %, proportional to the strength of the magnet, while CO<sub>2</sub> increased by 10 % [20]. From all of these studies, combustion stability which is critical to engine performance has not been discussed. Therefore, further research is needed, especially regarding the effect of magnetic fields in stabilizing the combustion process. This study provides data on the stability of combustion in a magnetic field which greatly supports the combustion process of vegetable oil in the engine to be more efficient. Very few researchers have conducted research on premixed combustion with mixed fuel between vegetable oils which is influenced by magnetic fields. The stability of premixed flames in high velocity flows has been an important topic of investigation in combustion research over the past few decades. The application of flame stability is useful in the combustion of military aircraft, gas turbines. Industrial furnaces and industrial oil burners. Particular attention is paid to the research of alternative fuels that are affected by magnetic fields. In other words, it is necessary to study the effect of these fuels on combustion, especially on industrial oil burner equipment during long-term use. Therefore, this study aims to provide a discussion about the effect of magnetic field strength which is varied by repulsion and attraction and without magnetic fields on the behavior stability and characteristics of the flame in the combustion process. But further research is needed especially for efficient high thermal energy radiation production, combustion characteristics, and flame stability. The present work provides the data for the efficient and stable operation of military aircraft, gas turbines. Industrial furnaces and industrial oil burners using vegetable oil and orientation magnetic field.

## 2. Materials and methods

Vegetable oils tested include coconut oil and jatropha. All vegetable oils were obtained from commercial products. The fatty acid composition, physical properties, chemical properties, glycerol, gum, and water of vegetable oils have been shown in our previous research [24].

### 2. 1. Experimental equipment scheme

The experimental equipment is shown schematically in **Fig. 1**. The fuel for a mixture of coconut oil and jatropha B50 of 600 ml was filled into the boiler, then heated with a gas stove to be evaporated at a temperature of 300 °C, and the 3 bar pressure was kept constant. The fuel inlet valve was opened and the air inlet valve was closed. The next process was the air inlet valve was opened slightly and the height difference is recorded in the flow control. The altitude differences in the fuel flow control are recorded and kept constant.

By increasing the opening of the air inlet valve gradually, every height difference in the airflow control was recorded. Vegetable oil vapor B50 mixture from the boiler was mixed with air from the compressor in the burner room. The reactant mixture then flew into a nozzle with



an inner diameter of 6 mm, then a flame was ignited at the end of the nozzle to form a diffusion flame. By increasing the amount of air in the mixture the flame will gradually change to a premixed flame.

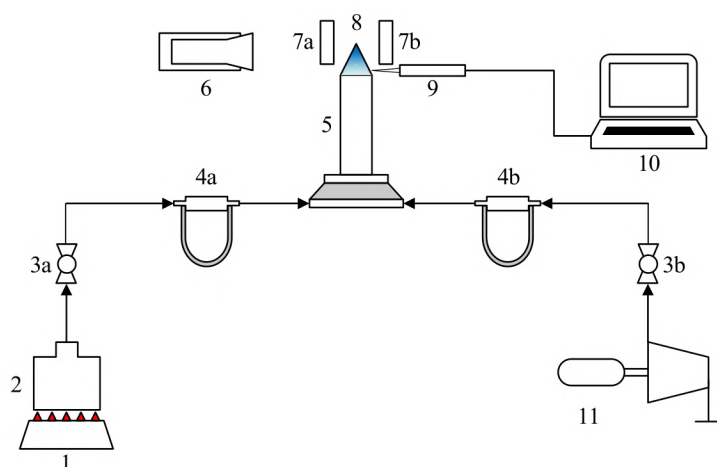


**Fig. 1.** Experimental apparatus:

1 – stove; 2 – boiler; 3 – valve; 4 – flow control; 5 – burner type cylinder; 6 – high speed camera; 7 – magnet permanent; 8 – flame; 9 – thermocouple; 10 – data logger; 11 – compressor

## 2. 2. Thermocouple positions

In the gap between the two magnets which was 12 mm apart was placed a burner with a diameter of 6 mm and a length of 200 mm made of stainless steel pipe. The image of the premixed flame formed at the nozzle's mouth was recorded until the flame went out using a high-speed camera with a speed of 320 fps.

Thermocouple type *K* was connected to the data logger to record the measured temperature by placing the sensor in the reaction zone position 2 mm above the burner tip in **Fig. 2**.

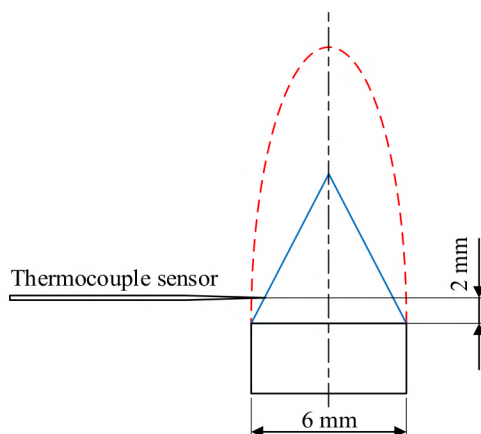


**Fig. 2.** Thermocouple positions

## 2. 3. Magnetic field orientation setting

The flame formed was then given north (N) and south (S) with varying orientations in two conditions, namely the magnetic field of attraction and repulsion as shown in **Fig. 3**.

The magnet was made of a permanent magnet bar with nickel-plated grade N45 neodymium with a magnetic field intensity of 1.1 T (11000 gauss) with dimensions of 40×25×10 mm.

The magnetic bar was placed on a holder made of aluminum plate and tightened by bolts and nuts so that it can be removed and reassembled to change the direction of the magnetic fields attract (S-N) and repel (N-N) (**Fig. 3**).

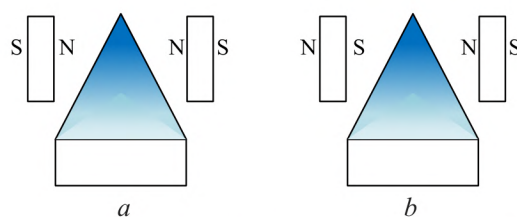


Fig. 3. The orientation of the magnetic field: *a* – repulsive; *b* – attractive

### 3. Results

#### 3.1. The stability and characteristics of the flame at various equivalence ratios and magnetic field directions

Fig. 4, *a–c* shows the premixed flame of the coconut oil and mixture of jatropha B50, respectively. An attractive magnetic field may burn at a poorer equivalence ratio than a magnetic field repels or without a magnetic field. The premixed flames of the attractive magnetic field experience lift-off then blew off at an equivalence ratio below 0.75 while the premixed flames of the magnetic field repel or without magnetic field did not experience lift-off then blow off below 0.83. This shows that the magnetic field repels and without more difficult to evaporate than the attractive magnetic field, giving the attractive magnetic field to the flame as a whole increase the combustion reaction which can be seen from the thinner reaction zone and the shorter flame. Giving an attractive magnetic field to the flame, making the flame brighter, indicating that the magnetic field made the electron spin more energetic, while the proton spin changed from para to ortho then the bonds between *H* atoms in vegetable oil were stretched and combustion occurred, the reaction became more intense.

It can be seen from Fig. 4, *c* that the reaction zone in the flame in the attractive magnetic field was thicker than the reaction zone in the flame, the magnetic field is both repulsive and without.

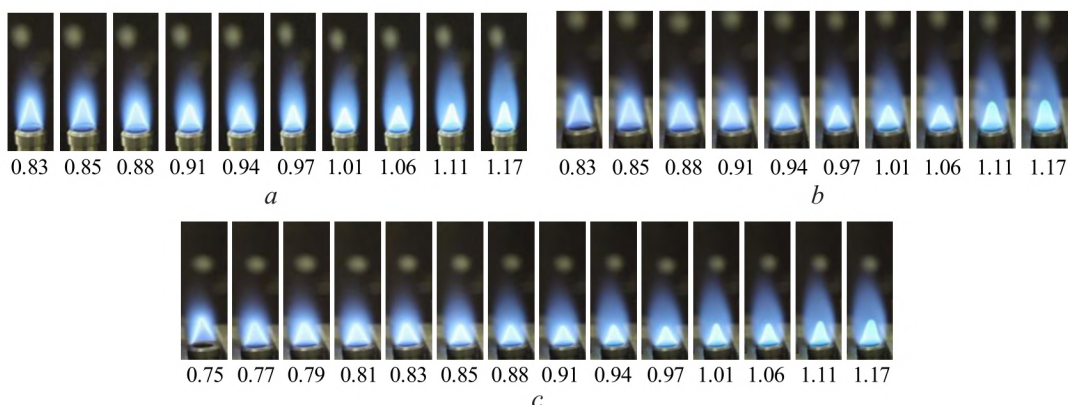


Fig. 4. Stability and flame shape of the vegetable oil B50 mixture to its equivalence ratio: *a* – without a magnetic field; *b* – repulsive magnetic field; *c* – attractive magnetic field

This is because the diffusion rate of the fuel in the flame of the attractive magnetic field is faster than the reaction speed. This happens because the fuel molecules are freer to move. On the other hand, the magnetic field repels, and without a magnetic field doesn't move because it is more difficult to move because the molecular attraction is stronger so that the reaction speed is faster. The magnetic field repels and without a magnetic field does not change the stability of the flame. From the flame image, it can be seen that in the without of a magnetic field (Fig. 4, *a*) the flame became more transparent, while in the magnetic field it repels and attracts attraction (Fig. 4, *b, c*) the flame is thicker. This happens because paramagnetic oxygen will move in the direction of the field while the  $H_2O$  product which carries heat is diamagnetic which tends to move against the direction of the magnetic field line (Fig. 8). In the magnetic field repels or without magnetic field come out of the pole thus it pushes  $O_2$  into the flame, while  $H_2O$  which is the heat source is pulled out of the flame. On the other hand, in the attractive magnetic field (Fig. 4, *c*) the magnetic field lines entered the magnet thus  $O_2$  was pulled out of the flame while  $H_2O$  as a heat source



was pushed into the flame (**Fig. 8**). These two events made chemical reactions not optimal. The direction of the attractive magnetic field gave a stronger effect. The flames became more stable towards the poorer equivalent ratio, from 0.83 to 0.75. Also, the second flame became thinner, which indicates that the combustion reaction in the reaction zone got stronger. This happens because  $O_2$  was pumped across the flame from the pole of the attractive magnetic field while  $H_2O$  as a heat source was pumped across the flame. This cross transport of heat and mass made the maximum reaction.

### 3. 2. The premixed combustion speed at various equivalence ratios and magnetic field directions

**Fig. 5** shows the laminar flame velocity of the coconut oil and jatropha B50 mixed estimated from **Fig. 4**. The maximum laminar flame velocity at the equivalence ratio was about slightly over unity. The maximum flame velocity of the attractive magnetic field occurred in a mixture richer than a magnetic field repels or without a magnetic field. The speed of the laminar flame decreased as the fuel-air mixture gets richer or poorer. The application of a magnetic field causes the speed of a laminar flame to increase as the electrons become more energetic. The magnetic field makes the laminar flame velocity increase more rapidly in the area of the poor mixture and tends to be more stable towards poorer combustion at the repelling magnetic pole.

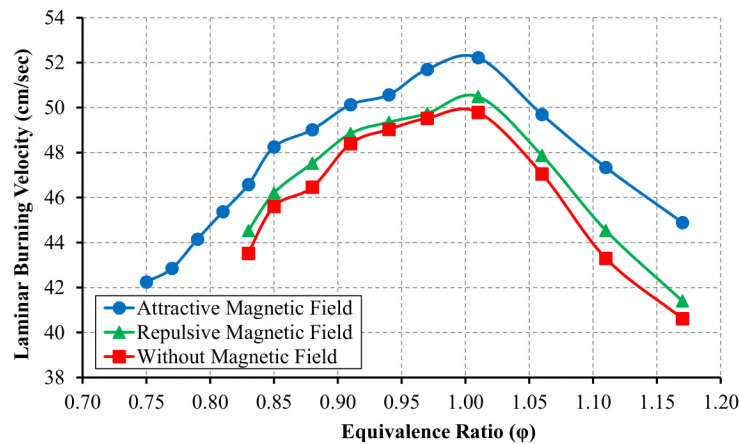


**Fig. 5.** The laminar combustion rate of the vegetable oil B50 mixture toward its equivalence ratio at various magnetic field orientations and without a magnetic field

This shows that the magnetic field helps pump out paramagnetic oxygen and controls the heat carried by more diamagnetic  $H_2O$  to the flame. Different magnetic fields have different effects on the speed of combustion. As previously explained, the repulsive magnetic field gives less effect than the attractive magnetic field. The attractive magnetic field produces a higher flame velocity because it pumps more heat that is carried by  $H_2O$  to the flame (**Fig. 8**). As a result, the combustion reaction becomes faster in the attractive magnetic field.

### 3. 3. The temperature at various equivalence ratios and direction of a magnetic field

**Fig. 6** shows the flame temperature of the premixed combustion of the coconut oil mixture and jatropha B50. It can be seen that the trend of temperature change with the equivalence ratio follows the trend of changes in the speed of the laminar flame. Because the speed of the flame states the speed of the combustion reaction, namely the speed of heat release. Even though the magnetic field increases the temperature of the flame, a higher increase in flame velocity in the absence of magnetic field results in a lower increase in temperature.

This may occur because some of the heat is taken to evaporate the mixed oil B50 which is more difficult to evaporate due to its stronger molecular attractive forces. The temperature drop to the poor mixture region was steeper in the attractive magnetic field which means the flame was less stable in the poor mixture than the magnetic field repels or without magnetic field flame. This

shows that the molecule plays a very important role in helping the magnetic field in stabilizing combustion.

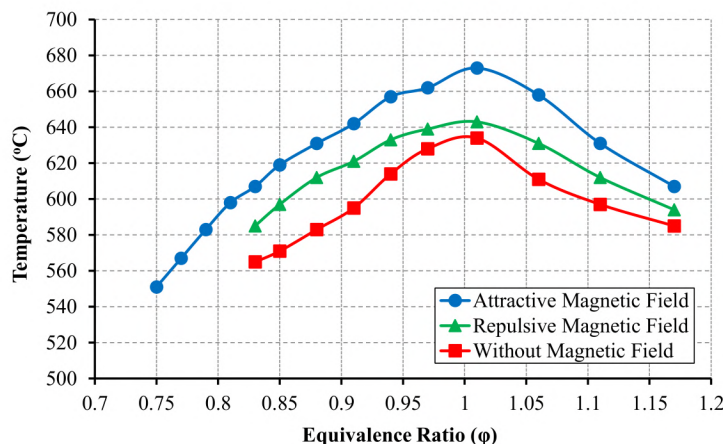


**Fig. 6.** The flame temperature of the vegetable oil B50 mixture toward its equivalent ratio at various magnetic field orientations and without a magnetic field

### 3. 4. Flame height at various equivalence ratios and magnetic field directions

**Fig. 7** shows the flame height of the premixed combustion of the coconut oil mixture and the distance B50 at various polar orientations of the magnetic field. A flame without a magnetic field was higher than a flame with a magnetic field of attraction and repulsion.

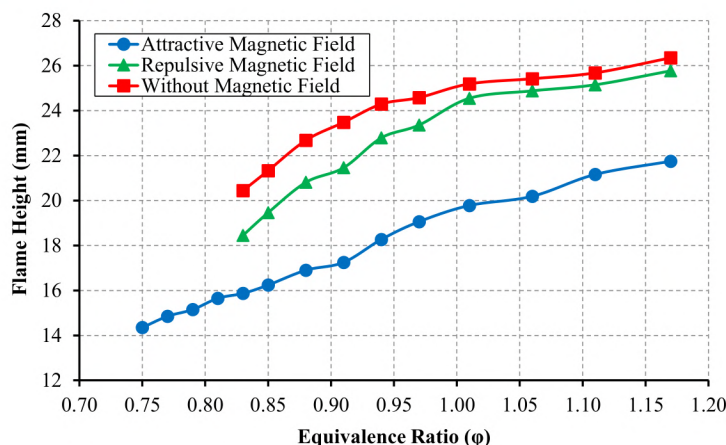


**Fig. 7.** Flame height of vegetable oil mixture B50 toward its equivalence ratio at various magnetic field orientations and without magnetic field

This indicates that a flame without a magnetic field is less stable than a flame with a magnetic field of attraction and repulsion because a higher one indicates that the flame tends to be less stable. After all, it experiences a greater stretch. The magnetic field exerts a greater influence on shortening the flame in the attractive and repulsive magnetic field. This occurs because the magnetic field makes the electrons more energetic thus the increase in reaction speed can compensate for the diffusion rate (**Fig. 5**).

### 4. Discussion of experimental results

From some previous research results, it is known that the magnetic field has a major role in the combustion reaction process [20–23]. The first role is that the magnetic field can change the spin of hydrogen protons in the fuel from para to ortho [20–23]. Higher polarity in coconut attracts stronger electrons so it becomes less mobile in coconut oil thus the spin of hydrogen is para. By giving a magnetic field, the proton spin on coconut can change from para to ortho with weaker



bonds thus the combustion reaction can take place faster. The change from para to ortho is more evident in coconut where laminar burning velocity increases higher because of its stronger electric polarity than jatropha (Fig. 4, 5) [20]. The second role of magnets is to attract paramagnetic molecules which in the case of combustion are oxygen and reject diamagnetic molecules which in this case are products in the form of  $H_2O$  which carry heat. The third magnetic field strength affects the magnetic poles of electrons in molecular bonds, which means that they affect the spin electrons in molecules. With a faster spinning electron due to magnetic field, electrons become more energetic. This is evident from the increase in laminar burning velocity from burning coconut oil and jatropha (Fig. 4, 5). The magnetic field attracts paramagnetic molecules, which in terms of combustion is oxygen, and repels diamagnetic molecules, which in this case is a product in the form of  $H_2O$  which carries heat (Fig. 8).

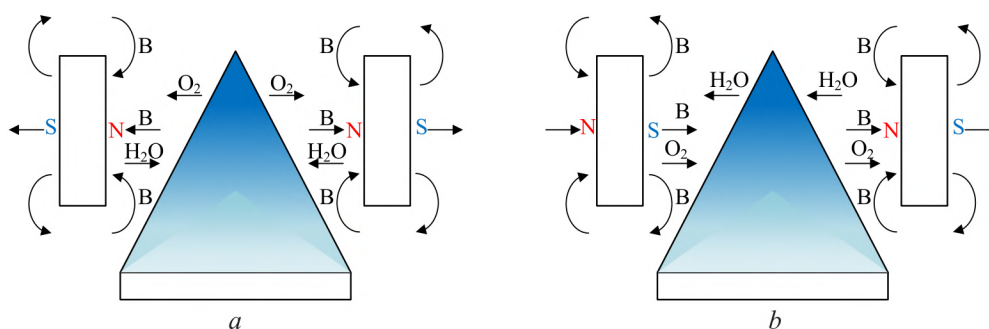


**Fig. 8.** The role of magnetic field orientation on:  
a – paramagnetic  $O_2$ ; b – diamagnetic  $H_2O$  in combustion product

The fuel here is a mixture of vegetable oil B50 while the heat was carried by  $H_2O$ . The control of these three components, namely  $O_2$  withdrawal,  $H_2O$  rejection, and changes in electron and proton spin will determine the combustion process whether it becomes stable, efficient, and low emission or vice versa. The equilibrium between these two events, the proton and electron spin strengthening, and the induction of  $O_2$  and  $H_2O$  determine the stability of the premixed combustion of vegetable oils, determined by the orientation of the magnetic field. The exact combination of these two will determine the combustion quality.

However, this study still has shortcomings related to the number and type of vegetable oil and the intensity of the magnetic field that is not large. This is possible, the reduction in plantation land so affects the amount of vegetable oil production in Indonesia tends to decrease, and the low strength of the magnetic field intensity affects the strength of the small characteristic of combustion. This study also cannot project how the fuel, volumetric and thermal efficiency will be in motorized vehicles. So it is necessary to do research that is more focused on its application to engines for all types of vegetable oil, both pure and its derivatives, and the strength of the magnetic field intensity. So that let's obtain several data for progress in the transportation sector.

## 5. Conclusions

The strength of the magnetic field increases the laminar flame speed of the vegetable oil B50 mixture through its role in increasing electron spin and changing the spin of the hydrogen protons in the fuel.

The magnetic field, in addition to accelerating the rate of combustion reactions through the organizing and strengthening of the spin of electrons and protons, also stirs the flame through the induction of  $O_2$  and  $H_2O$ . The right combination of field strength and magnetic field variation determines the quality of combustion.

## Acknowledgment

I would love to dedicate my special and deep gratitude to the Mechanical Engineering Department and Faculty of Engineering, Universitas Maarif Hasyim Latif Sidoarjo.

---

**References**

- [1] Lin, J.-J., Chen, Y.-W. (2017). Production of biodiesel by transesterification of Jatropha oil with microwave heating. *Journal of the Taiwan Institute of Chemical Engineers*, 75, 43–50. doi: <https://doi.org/10.1016/j.jtice.2017.03.034>
- [2] Buosi, G. M., da Silva, E. T., Spacino, K., Silva, L. R. C., Ferreira, B. A. D., Borsato, D. (2016). Oxidative stability of biodiesel from soybean oil: Comparison between synthetic and natural antioxidants. *Fuel*, 181, 759–764. doi: <https://doi.org/10.1016/j.fuel.2016.05.056>
- [3] Zakaria, R., Harvey, A. P. (2012). Direct production of biodiesel from rapeseed by reactive extraction/in situ transesterification. *Fuel Processing Technology*, 102, 53–60. doi: <https://doi.org/10.1016/j.fuproc.2012.04.026>
- [4] Nautiyal, P., Subramanian, K. A., Dastidar, M. G. (2014). Production and characterization of biodiesel from algae. *Fuel Processing Technology*, 120, 79–88. doi: <https://doi.org/10.1016/j.fuproc.2013.12.003>
- [5] Hong, I. K., Lee, J. R., Lee, S. B. (2015). Fuel properties of canola oil and lard biodiesel blends: Higher heating value, oxidative stability, and kinematic viscosity. *Journal of Industrial and Engineering Chemistry*, 22, 335–340. doi: <https://doi.org/10.1016/j.jiec.2014.07.027>
- [6] Rakopoulos, D. C., Rakopoulos, C. D., Kyritsis, D. C. (2016). Butanol or DEE blends with either straight vegetable oil or biodiesel excluding fossil fuel: Comparative effects on diesel engine combustion attributes, cyclic variability and regulated emissions trade-off. *Energy*, 115, 314–325. doi: <https://doi.org/10.1016/j.energy.2016.09.022>
- [7] Wei, S., He, C., Liu, X., Song, Z., Zhao, X. (2019). Numerical Analysis of the Effects of Swirl Ratio on the Performance of Diesel Engine Fueled with N-Butanol–Diesel Blends. *Journal of Energy Engineering*, 145(3), 04019005. doi: [https://doi.org/10.1061/\(asce\)ey.1943-7897.0000600](https://doi.org/10.1061/(asce)ey.1943-7897.0000600)
- [8] Rakopoulos, D. C., Rakopoulos, C. D., Giakoumis, E. G., Dimaratos, A. M., Founti, M. A. (2011). Comparative environmental behavior of bus engine operating on blends of diesel fuel with four straight vegetable oils of Greek origin: Sunflower, cottonseed, corn and olive. *Fuel*, 90 (11), 3439–3446. doi: <https://doi.org/10.1016/j.fuel.2011.06.009>
- [9] Leenus Jesu Martin, M., Edwin Geo, V., Kingsly Jeba Singh, D., Nagalingam, B. (2012). A comparative analysis of different methods to improve the performance of cotton seed oil fuelled diesel engine. *Fuel*, 102, 372–378. doi: <https://doi.org/10.1016/j.fuel.2012.06.049>
- [10] Daho, T., Vaitilingom, G., Ouiminga, S. K., Piriou, B., Zongo, A. S., Ouoba, S., Koulidiati, J. (2013). Influence of engine load and fuel droplet size on performance of a CI engine fueled with cottonseed oil and its blends with diesel fuel. *Applied Energy*, 111, 1046–1053. doi: <https://doi.org/10.1016/j.apenergy.2013.05.059>
- [11] Savariraj, S., Ganapathy, T., Saravanan, C. G. (2012). Performance and emission characteristics of diesel engine using high-viscous vegetable oil. *International Journal of Ambient Energy*, 33 (4), 193–203. doi: <https://doi.org/10.1080/01430750.2012.709356>
- [12] San José Alonso, J. F., Romero-Ávila, C., San José Hernández, L. M., Awf, A.-K. (2012). Characterising biofuels and selecting the most appropriate burner for their combustion. *Fuel Processing Technology*, 103, 39–44. doi: <https://doi.org/10.1016/j.fuproc.2011.07.023>
- [13] Rath, S., Kumar, S., Singh, R. K. (2011). Performance and emission analysis of blends of karanja methyl ester with diesel in a compression ignition engine. *International Journal of Ambient Energy*, 32 (3), 161–166. doi: <https://doi.org/10.1080/01430750.2011.619885>
- [14] Bharathiraja, M., Manikalithas, P., Venkatachalam, R. (2014). Experimental investigation of performance and emission characteristics of non-preheated and preheated Karanja oil blend as alternate fuel in the compression-ignition engine. *International Journal of Ambient Energy*, 35 (2), 71–79. doi: <https://doi.org/10.1080/01430750.2013.770796>
- [15] Qi, D. H., Lee, C. F., Jia, C. C., Wang, P. P., Wu, S. T. (2014). Experimental investigations of combustion and emission characteristics of rapeseed oil–diesel blends in a two cylinder agricultural diesel engine. *Energy Conversion and Management*, 77, 227–232. doi: <https://doi.org/10.1016/j.enconman.2013.09.023>
- [16] Chang, Y.-C., Lee, W.-J., Wang, L.-C., Yang, H.-H., Cheng, M.-T., Lu, J.-H. et. al. (2014). Effects of waste cooking oil-based biodiesel on the toxic organic pollutant emissions from a diesel engine. *Applied Energy*, 113, 631–638. doi: <https://doi.org/10.1016/j.apenergy.2013.08.005>
- [17] Popovicheva, O. B., Kireeva, E. D., Steiner, S., Rothen-Rutishauser, B., Persiantseva, N. M., Timofeev, M. A. et. al. (2014). Microstructure and Chemical Composition of Diesel and Biodiesel Particle Exhaust. *Aerosol and Air Quality Research*, 14 (5), 1392–1401. doi: <https://doi.org/10.4209/aaqr.2013.11.0336>
- [18] Mwangi, J. K., Lee, W.-J., Whang, L.-M., Wu, T. S., Chen, W.-H., Chang, J.-S. et. al. (2015). Microalgae Oil: Algae Cultivation and Harvest, Algae Residue Torrefaction and Diesel Engine Emissions Tests. *Aerosol and Air Quality Research*, 15 (1), 81–98. doi: <https://doi.org/10.4209/aaqr.2014.10.0268>
- [19] Che Mat, S., Idroas, M. Y., Hamid, M. F., Zainal, Z. A. (2018). Performance and emissions of straight vegetable oils and its blends as a fuel in diesel engine: A review. *Renewable and Sustainable Energy Reviews*, 82, 808–823. doi: <https://doi.org/10.1016/j.rser.2017.09.080>



- [20] Faris, A. S., Al-Naseri, S. K., Jamal, N., Isse, R., Abed, M., Fouad, Z. et. al. (2012). Effects of Magnetic Field on Fuel Consumption and Exhaust Emissions in Two-Stroke Engine. *Energy Procedia*, 18, 327–338. doi: <https://doi.org/10.1016/j.egypro.2012.05.044>
- [21] Patel, P. M., Rathod, G. P., Patel, T. M. (2014). Effect of Magnetic Field on Performance and Emission of Single Cylinder Four Stroke Diesel Engine. *IOSR Journal of Engineering*, 4 (5), 28–34. doi: <https://doi.org/10.9790/3021-04552834>
- [22] Habbo, A. R. A., Khalil, R. A., Hammoodi, H. S. (2011). Effect of Magnetizing the Fuel on the Performance of an S. I. Engine. *AL-Rafdain Engineering Journal (AREJ)*, 19 (6), 84–90. doi: <https://doi.org/10.33899/rengj.2011.26611>
- [23] Ugare, V., Dhoble, A., Lutade, S., Mudafale, K. (2014). Performance of Internal Combustion (CI) Engine Under the Influence of Strong Permanent Magnetic Field. *International Conference on Advances in Engineering & Technology – 2014 (ICAET-2014)*, 11–17. Available at: <http://iosrjournals.org/iosr-jmce/papers/ICAET-2014/me/volume-5/3.pdf>
- [24] Perdana, D., Wardana, I. N. G., Yuliati, L., Hamidi, N. (2018). The role of fatty acid structure in various pure vegetable oils on flame characteristics and stability behavior for industrial furnace. *Eastern-European Journal of Enterprise Technologies*, 5 (8 (95)), 65–75. doi: <https://doi.org/10.15587/1729-4061.2018.144243>

Received date 25.02.2021

Accepted date 14.07.2021

Published date 13.09.2021

© The Author(s) 2021

This is an open access article  
under the Creative Commons CC BY license

**How to cite:** Perdana, D., Adiwidodo, S., Choifin, M., Winarko, W. A. (2021). The effect of magnetic field variations in a mixture of coconut oil and jatropha on flame stability and characteristics on the premixed combustion. *EUREKA: Physics and Engineering*, 5, 13–22. doi: <https://doi.org/10.21303/2461-4262.2021.001996>

# STUDY ON MODEL FOR CUTTING FORCE WHEN MILLING SCM440 STEEL

*Nguyen Van Thien*

*Faculty of Mechanical Engineering<sup>1</sup>*

*Do Duc Trung* ✉

*Faculty of Mechanical Engineering<sup>1</sup>*

*doductrung@haui.edu.vn*

<sup>1</sup>*Hanoi University of Industry*

*298 Cau Dien str., Bac Tu Liem District, Hanoi, Vietnam, 100000*

✉ **Corresponding author**

## Abstract

This article presents empirical study results when milling SCM440 steel. The cutting insert to be used was a TiN coated cutting insert with tool tip radius of 0.5 mm. Experimental process was carried out with 18 experiments according to Box-Behnken matrix, in which cutting speed, feed rate and cutting depth were selected as the input parameters of each experiment. In addition, cutting force was selected as the output parameter. Analysis of experimental results has determined the influence of the input parameters as well as the interaction between them on the output parameters. From the experimental results, a regression model showing the relationship between cutting force and input parameters was built. Box-Cox and Johnson data transformations were applied to construct two other models of cutting force. These three regression models were used to predict cutting force and compare with experimental results. Using parameters including coefficient of determination ( $R-Sq$ ), adjusted coefficient of determination ( $R-Sq(adj)$ ) and percentage mean absolute error (%  $MAE$ ) between the results predicted by the models and the experimental results are the criteria to compare the accuracy of the cutting force models. The results have determined that the two models using two data transformations have higher accuracy than model not using two data transformations. A comparison of the model using the Box-Cox transformation and the model using the Johnson transformation was made with a  $t$ -test. The results confirmed that these two models have equal accuracy. Finally, the development direction for the next study is mentioned in this article.

**Keywords:** SCM440 steel milling, Cutting force, Box-Cox transformation, Johnson transformation,  $t$ -test.

**DOI: 10.21303/2461-4262.2021.001743**

## 1. Introduction

Milling method is widely used in mechanical machining by its high machining productivity. Thanks to the advancement of cutting tool making technology as well as the experimental equipment, the precision of the milling method is also improved. Hence, milling has also been chosen as the final machining method for a variety of machining surfaces in many cases. The cutting force during milling process not only affects the machining accuracy and the durability of the cutting tools, but also works on the energy consumption of the machining process. With the expectation that the cutting force during milling process is of small value, many studies have been done to build the cutting force model. The cutting force model is the basis for predicting cutting force during machining as well as the basis for selecting machining parameters to ensure cutting force has small value. Study on building cutting force model by theoretical method has been done by many authors, such as: when using face milling cutter [1, 2], when using ball end milling [3–5], when using cylindrical end mill [6]. However, when building cutting force models according to these studies, the number of calculations is very large, and there is still a need for more experimental studies to determine some parameters, such as coefficient of friction and shear force coefficient. Therefore, this method is time consuming and costly.

Another simple study direction to build cutting force model which has been done by many authors is based on the results of the experimental process. In those studies, a relationship between cutting force and machining parameters has been established. The cutting force model shows the relationship between the cutting force with the trochoid step and trochoidal milling when milling EN X38CrMoV5-1 material with UNIFR41010xR1 cutting tool [7]. Relationship between cutting force with spindle speed, feed rate, axial depth of cut, radial depth of cut, and percentage of silicon



carbide in the workpiece material when milling LM6/SiCp with a hard alloy cutting tool has been established in document No. [8]. The relationship between cutting force with cutting speed and feed rate has been established when milling UNS A92024-T3 (Al-Cu) material with WC-10Co cutting tool material [9]. In document No. [10], it has built a relationship between cutting force with cutting speed, feed rate and cutting depth when using a titanium cutting tool to mill four different materials including C45 steel, aluminium alloy (7178), grey cast iron, and titanium (purity 99 %). Document No. [11] has established a relationship between cutting force with step over and feed rate when using a hard alloy cutting tool to milling Al 7075-T651 aluminum alloy. The relationship between the cutting force and cutting speed, feed rate, cutting depth and kinematical direction of cut (conventional or climb milling) when using Sumitomo AXMT123504PEERG cutting insert for milling high strength structural steel (S960QL) was performed in document No. [12]. In document No. [13], it presented the relationship between cutting force with cutting speed and feed rate when using TiN coated milling cutter to milling Ti-6Al-4V aluminum alloy. The relationship between cutting force and cutting speed, feed rate and cutting depth when milling medium carbon steel with TiN coated cutting tool has been presented in study No. [14]. Document No. [15] has built the relationship between cutting force and cutting speed, feed rate and cutting depth when using TiN coated milling cutter to milling 1Cr13 martensitic stainless steel.

By some empirical study on building cutting force model mentioned above, they show that cutting speed, feed rate and cutting depth are often selected as input parameters of experimental study. This is also easily explained because the adjustment of these parameters will be more easily done by the worker than by other parameters (vibration and stability of system, etc.).

SCM440 steel is a steel with high deformation resistance and wear resistance. This steel is often used to fabricate components with heavy loads, wear resistance and impact such as gears, drive shafts. This steel is also commonly used to manufacture injection moulding. Study on material type machining technology has been carried out by a number of authors, such as: surveying the flatness of the tool when milling [16], determining the optimal value of cutting parameters when turning to ensure minimum value of surface roughness [17], determining optimal cutting parameters when turning to ensure minimum value of surface roughness and tool wear [18], study on drilling technology this material when using a number of different cooling methods [19]. Study on milling equivalent steels of this steel has also been carried out by a number of studies, such as: building surface roughness models and determining the optimal value of cutting parameters to ensure that surface roughness has the smallest value when milling with TiAlN+TiN coated cutting tool [20], studying the efficiency of using coolant when milling with TiAlN coated cutting tools [21], surveying on surface roughness when milling with cutting tools made of CBN [22], comparing cutting force, tool wear and surface roughness when milling with 5 types of cutting tools coated with different materials (WC-Co-TiC, Al<sub>2</sub>O<sub>3</sub>-TiC, Ti(C, N), Ti(C, N)-WC-Mo<sub>2</sub>C-Ni-Co, and Ti(C, N)-WC-Mo<sub>2</sub>C-Co) [23]. This study has determined that out of five types of cutting tool materials, Ti (C, N) coated cutting tools have the highest efficiency. However, according to the authors of this article, there has been no published study on building cutting force models when milling SCM440 steel as well as steel equivalent to this type of steel up to now.

With the arguments presented above, this study will conduct experiments on steel milling SCM440 process. The aim of this research is to build a cutting force model that shows the relationship between cutting force and parameters of cutting parameters. Study for improving the accuracy of the model has also been performed and that is the main aim of this research.

## 2. Materials and methods

SCM440 steel was selected as the experimental material in this study. The experimental steel sample is a cube with sides equal to 45 mm. In **Table 1**, the chemical composition of steel when spectrally analyzed is shown.

The composition of the elements in **Table 1** is obtained by analyzing the steel sample on a spectrophotometer.

Experiments were performed on a 5-axis CNC milling machine with symbol of DMU 50 ECOLINE. The machine uses SINUMERIK S840DSB operating system. Cutting tool

used during the experiment was a cutting insert coated with Ti(C, N). The insert has the symbol of R390-11T308M. Some geometric parameters of the cutting insert are as follows: tip radius is 0.8 mm, relief angle is 6°, inclination angle is -6°, cutting edge angle is 75°, and rake angle of ceramic tool is -6°. The body of the cutting tool is 14 mm in diameter, on which two symmetrical cut insert are attached. To eliminate the effect of tool wear on the output parameters, each cutting insert is used for only one experiment.

**Table 1**

Chemical composition of SCM440 steel

Element	C	Si	Mn	P	S	Cr	Mo
[%]	0.41	0.33	0.78	<0.03	<0.03	1.12	0.25

The cutting force components of  $F_x$ ,  $F_y$  and  $F_z$  in the  $x$ ,  $y$  and  $z$  directions were measured by Kistler's force sensor with sensor symbol of 9139AA. Use cables to connect the load cell and the data processor, then the measured signal is processed by software in the computer. **Fig. 1** shows the details of the experimental system.

Cutting force at each experiment is determined by the following (1):

$$F_c = \sqrt{F_x^2 + F_y^2 + F_z^2}. \quad (1)$$

$F_x$ ,  $F_y$ ,  $F_z$  are respectively the force components in the three directions of the coordinate system.

Experiments were performed according to Box-Behnken experimental matrix, in which cutting speed, feed rate and cutting depth were selected as the input parameters of the experimental process. In this matrix form, each input parameter will have three values corresponding to coding levels of -1, 0 and 1 [24]. The values of selected input parameters according to the cutting tool manufacturer's recommendation and by study No. [25] are presented in **Table 2**.

**Fig. 1.** Experimental system**Table 2**

Input parameters

Parameter	Unit	Code symbol	Actual symbol	Value at levels		
				-1	0	1
Cutting speed	m/min	$x_1$	$v_c$	140	200	260
Feed rate	mm/tooth	$x_2$	$f_z$	0.1	0.2	0.3
Depth of cut	mm	$x_3$	$a_p$	0.28	0.4	0.52



The experimental matrix was designed in Box-Behnken format with 15 experiments, including 6 experiments at the central level, as shown in **Table 3**.

### 3. Results and discussion

Experiments were carried out in the order shown in **Table 3** and cutting force values at each experiment were also included in this table.

**Table 3**  
Experimental matrices and results

No.	Code value			Actual value			Cutting force
	$x_1$	$x_2$	$x_3$	$v_c$ (m/min)	$f_z$ (mm/tooth)	$a_p$ (mm)	$F_c$ (N)
1	-1	0	1	140	0.2	0.52	130.56
2	0	0	0	200	0.2	0.4	110.08
3	1	1	0	260	0.3	0.4	156.16
4	0	0	0	200	0.2	0.4	112.64
5	1	0	-1	260	0.2	0.28	85.76
6	0	1	-1	200	0.3	0.28	240.64
7	0	1	1	200	0.3	0.52	258.56
8	-1	1	0	140	0.3	0.4	152.32
9	0	0	0	200	0.2	0.4	111.36
10	0	0	0	200	0.2	0.4	104.96
11	1	-1	0	260	0.1	0.4	92.16
12	-1	0	-1	140	0.2	0.28	104.96
13	-1	-1	0	140	0.1	0.4	106.24
14	0	-1	1	200	0.1	0.52	92.16
15	1	0	1	260	0.2	0.52	79.36
16	0	0	0	200	0.2	0.4	104.96
17	0	0	0	200	0.2	0.4	119.04
18	0	-1	-1	200	0.1	0.28	88.32

Three cutting force components ( $F_x$ ,  $F_y$ , and  $F_z$ ) are measured during the time the cutter enters the workpiece, the cutting force value ( $F_c$ ) at each experiment is calculated according to (1).

Minitab 16 statistical software is used to analyze experimental results in **Table 3**. Pareto diagram of the influence of the input parameters on the cutting force is shown in **Fig. 2**.

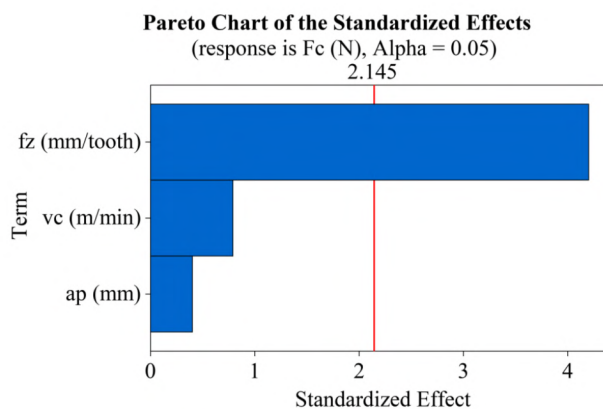


**Fig. 2.** Pareto plot for  $F_c$

With the significance level chosen by 0.05 ( $\alpha = 0.05$ ), **Fig. 2** shows that: feed rate is the only parameter whose Pareto plot surpasses the chart bounding line (red line) among the three input

parameters. Thus, feed rate is only parameter that has a significant influence on the cutting force. This is also easy to explain because changing the feed rate changes the surface response of the part to the insert. Therefore, the cutting force components will change in all directions ( $F_x$ ,  $F_y$ , and  $F_z$ ), leading to a much change in cutting force  $F_c$ . Cutting speed and cutting depth have a negligible effect on cutting force. However, the effect of the cutting speed on the cutting force is greater than the effect of the cutting depth if they are considered in detail.

The Minitab 16 statistical software was again used to determine the influence of the interaction between the input parameters on the cutting force, the results are shown in Fig. 3.

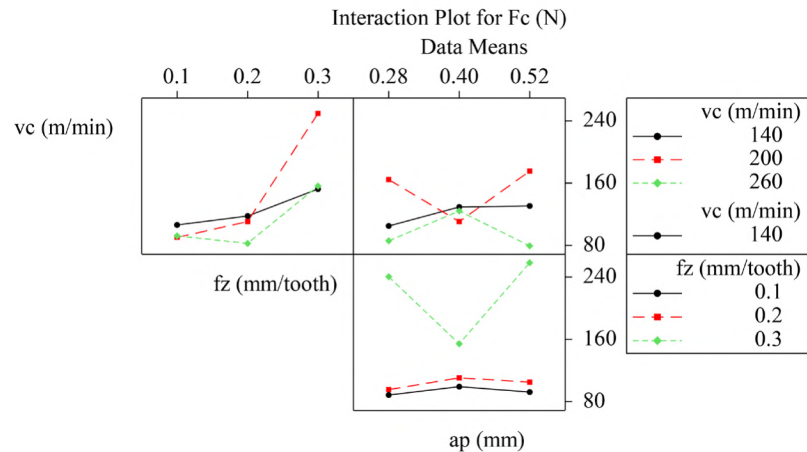


Fig. 3. Interaction effects plot for  $F_c$

Form Fig. 3, it shows that:

- when cutting speed is 140 m/min, increasing the value of the feed rate will cause the cutting force to increase but at a slow speed. When the cutting speed is 200 m/min, if feed rate increases from 0.1 mm/tooth to 0.2 mm/tooth, cutting force will increase slowly, but the cutting force increases rapidly if the feed rate continues to increase. In the case the cutting speed is 260 m/min, cutting force will decrease when the feed rate increases from 0.1 mm/tooth to 0.2 mm/tooth, but cutting force will increase if the feed rate increases from 0.2 mm/tooth to 0.3 mm/tooth;
- when cutting speed is 140 m/min, if cutting depth increases, cutting force will increase slowly. When cutting speed is 200 m/min, cutting force will decrease when cutting depth increases from 0.28 mm to 0.4 mm, but cutting force will increase if cutting depth continues to increase. In the case cutting speed is 260 m/min, cutting force will increase when cutting depth increases from 0.28 mm to 0.4 mm, but cutting force will decrease if cutting depth of continues to increase;
- when feed rate is 0.1 mm/tooth and 0.2 mm/tooth, cutting force is almost unchanged when cutting depth is changed. In the case feed rate is 0.3 mm/tooth, cutting force will decrease rapidly if cutting depth increases from 0.28 mm to 0.4 mm, cutting force will increase rapidly if cutting depth increases from 0.4 mm to 0.52 mm.

The above analysis shows that the influence of the input parameters on the cutting force is very complicated. These are phenomena that occur during the experiment, it is very difficult to explain by the theory of cutting process. Therefore, if only based on the experimental results, it will be difficult to choose the value of the input parameters to ensure that the cutting force is small. In this case, it is necessary to build a cutting force model showing the relationship between cutting force and input parameters. This relationship is the basis for determining the value of the input parameters to ensure the desired value of the output parameter.

From the data in Table 3, a regression model of cutting force has been built as shown in (2).

$$F_c = 110.5067 - 10.0800 \cdot x_1 + 53.6000 \cdot x_2 + 5.1200 \cdot x_3 - 26.7733 \cdot x_1^2 + 42.9867 \cdot x_2^2 + 16.4267 \cdot x_3^2 + 4.4800 \cdot x_1 \cdot x_2 - 8.0000 \cdot x_1 \cdot x_3 + 3.5200 \cdot x_2 \cdot x_3. \quad (2)$$



This model has  $R-Sq = 0.8571$  and adjusted  $R-Sq (adj) = 0.6964$ . The meanings of these values have been discussed in many documents No. [24, 26, 27]. The closer the values of these parameters are to 1, the higher the accuracy of the model. The value of the coefficient determined is 0.8571 and it is possible to increase the value of these parameters by adding to the model higher order quantities of the input parameters ( $x_i^3, x_i^4, \dots, x_i^n$ ) or considering the interaction affect between all three input parameters ( $x_1 \cdot x_2 \cdot x_3$ ). However, this action will make the model much more complex [24, 26, 27]. Value of adjusted coefficient of determination of 0.6964 shows that the change of cutting force is only determined by the change of the input parameters at 69.64 %. Therefore, problem here is how to increase the values of these two parameters ( $R-Sq$  and  $R-Sq(adj)$ ) without adding any additional parameters to the model.

Box-Cox and Johnson data transformations are known as tools to convert non-distributed dataset according to the standard rule into distributed dataset according to the standard rule [27]. Box-Cox transformation has been successfully applied to improve the accuracy of surface roughness model when milling EN 353 steel [28], surface roughness model when milling AISI 1019 steel [29]. The Johnson transformation has also been successfully applied to improve the accuracy of surface roughness model when lathing 3X13 steel [30]. Both of these transformations have also been successfully applied to improve the accuracy of the surface roughness model when turning 9XC steel, which showed that the model using the Box-Cox transformation has higher accuracy than the model using the Johnson transformation [31]; surface roughness model when surface grinding of 65G steel, which also determined the model using Johnson transformation was more accurate than the model using the Box-Cox transformation [32]. In this study, these two transformations will be applied to improve the accuracy of the cutting force model when milling SCM440 steel.

From the data in **Table 3**, using statistical software Minitab 16 has determined the distribution law of cutting force as shown in **Fig. 4** shows that the cutting force values (denoted by red dots) are distributed quite far from the standard line (straight line). On the other hand,  $P\text{-value} < 0.005$  is smaller than the significance level (significance level of  $\alpha = 0.05$  is often chosen). Thus, it can be confirmed that the dataset on cutting force is not distributed according to the standard rule. This is a necessary condition to perform data transformations [27].

Box-Cox transformation is performed by the following formula [27, 33]:

$$\begin{cases} F'_c = F_c^\lambda & \text{when } \lambda \neq 0, \\ F'_c = \ln(F_c) & \text{when } \lambda = 0. \end{cases} \quad (3)$$

In which,  $F'_c$  is the value of cutting force after transformation,  $F_c$  is value of cutting force in the experiment,  $\lambda$  is the exponential transformation factor. Minitab statistical software was used to perform Box-Cox transformation for cutting force data in **Table 3**.

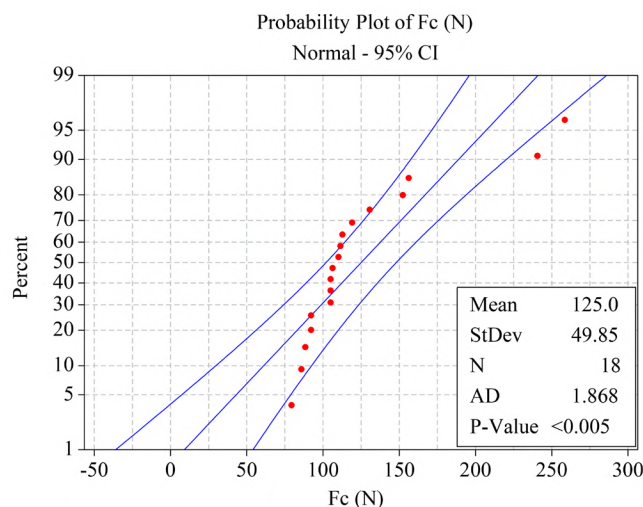


**Fig. 4.** Distribution law of cutting force during experiment

**Fig. 5** shows a graph of the Box-Cox transformation. From this figure, it shows that the coefficient  $\lambda$  is equal to  $-2.00$ . Cutting forces values in **Table 3** after being converted Box-Cox are as shown in **Table 4**.

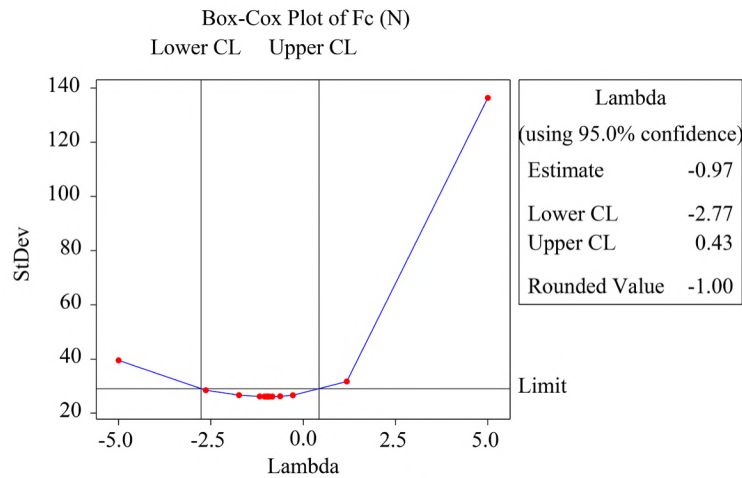


**Fig. 5.** Box-Cox transformation graph

**Table 4**

Value of cutting force before and after transformation

No.	Cutting force		
	Experiment (N)	Box-Cox transformation (dimensionless)	Johnson transformation (dimensionless)
1	130.56	0.0000587	0.6836988
2	110.08	0.0000825	0.1429585
3	156.16	0.0000410	1.1014878
4	112.64	0.0000788	0.2287090
5	85.76	0.0001360	-1.3449952
6	240.64	0.0000173	1.8458145
7	258.56	0.0000150	1.9500000
8	152.32	0.0000431	1.0491470
9	111.36	0.0000806	0.1867316
10	104.96	0.0000908	-0.0533265
11	92.16	0.0001177	-0.7824216
12	104.96	0.0000908	-0.0533265
13	106.24	0.0000886	-0.0007049
14	92.16	0.0001177	-0.7824216
15	79.36	0.0001588	-1.9500000
16	104.96	0.0000908	-0.0533265
17	119.04	0.0000706	0.4158884
18	88.32	0.0001282	-1.1042581

**Fig. 6** shows the distribution rule of cutting force after the Box-Cox transformation. **Fig. 6** shows that the cutting force values distributed around the standard line (straight line); on the other hand,  $P\text{-value} = 0.212$  is much larger than the significance level. Therefore, it is confirmed that the dataset of the cutting force after the Box-Cox transformation was distributed according to the standard rule [27].

From cutting force data after being transformed (**Table 4**) and value of  $\lambda$ , a new model of cutting force is built as shown in (4). This model has the coefficient of determination of 0.8824 and the adjusted coefficient of determination of 0.7500:



$$F_c = \left[ 10^{-4} \cdot \left( \begin{aligned} &0.8235 + 0.2154 \cdot x_1 - 0.4199 \cdot x_2 - 0.0276 \cdot x_3 + 0.1588 \cdot x_1^2 - \\ &- 0.2562 \cdot x_2^2 + 0.1281 \cdot x_3^2 - 0.0781 \cdot x_1 \cdot x_2 + 0.1373 \cdot x_1 \cdot x_3 + \\ &+ 0.0204 \cdot x_2 \cdot x_3 \end{aligned} \right) \right]^{\frac{1}{2}}. \quad (4)$$

Johnson transformation is applied to transform cutting force data in **Table 3**. **Fig. 7** is the graph of transformation. Cutting force values after transformation are also included in **Table 4**.

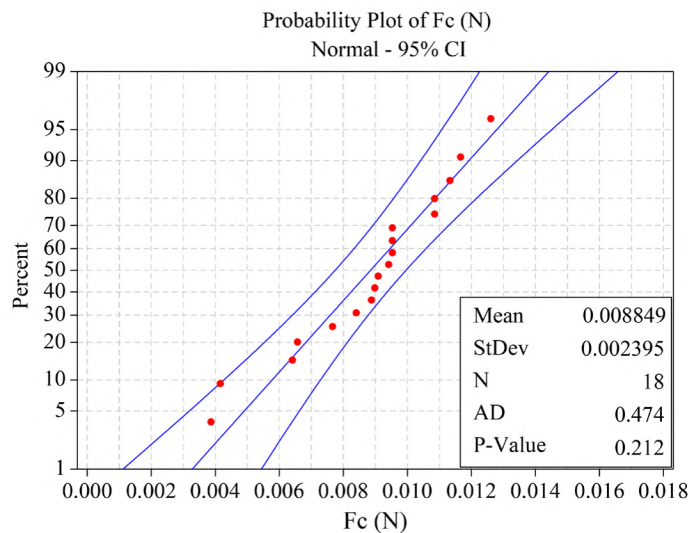


**Fig. 6.** Distribution rule of cutting force after Box-Cox transformation

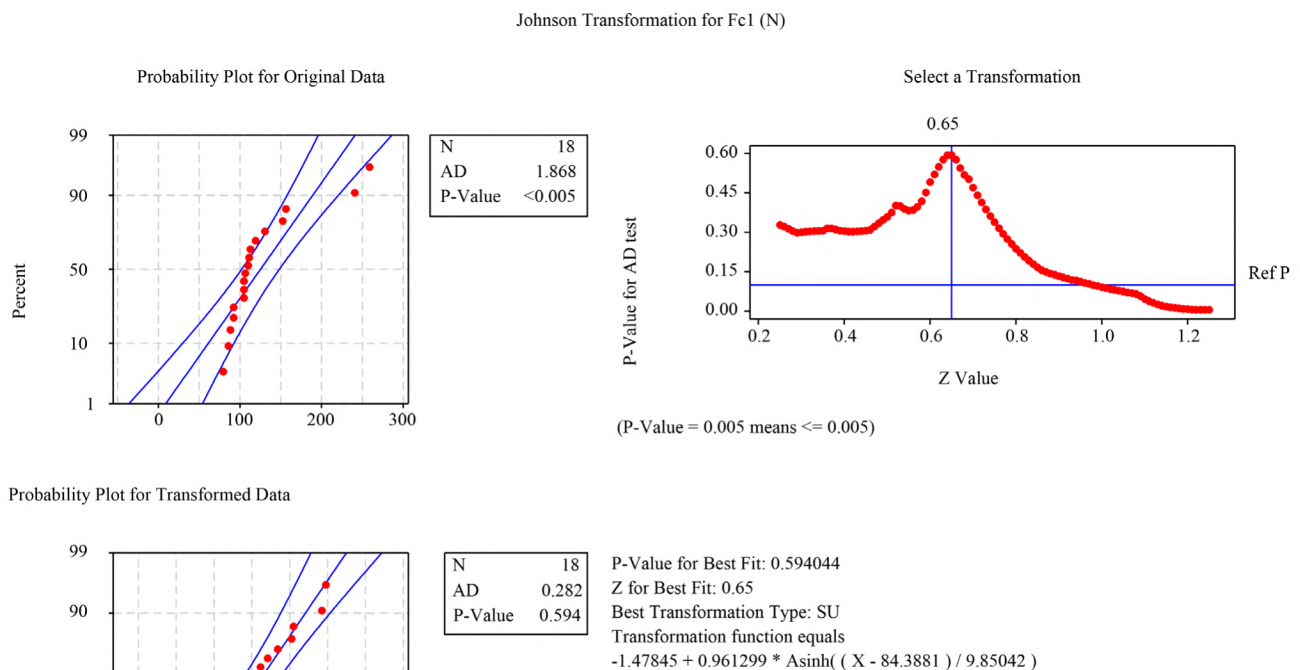


**Fig. 7.** Johnson transformation graph

The upper left part of **Fig. 7** shows the distribution rule of cutting force without transformation (as being analyzed above). The lower left portion of **Fig. 7** shows the distribution rule of the cutting force after being transformed. Observing this figure shows that the cutting force values distributed very close to the standard line. This will also be more obvious when looking at the top right image. On the other hand, the *P-value* of 0.594 is much larger than the significance level. It confirms that the Johnson transformation has been done successfully [27]. In the lower right part of the figure shows the transformation formula, from which a cutting force model is built as shown in (5).

$$\begin{aligned} & -1.47845 + 0.961299 \cdot \text{Asinh}[(F_c - 84.3881)/9.85042] = \\ & = 0.1446 - 0.5818 \cdot x_1 + 1.0770 \cdot x_2 + 0.0698 \cdot x_3 - 0.4731 \cdot x_1^2 + \\ & + 0.6704 \cdot x_2^2 - 0.3377 \cdot x_3^2 + 0.2085 \cdot x_1 \cdot x_2 - 0.3355 \cdot x_1 \cdot x_3 - 0.0544 \cdot x_2 \cdot x_3. \end{aligned} \quad (5)$$

(5) is rewritten in the following form:

$$F_c = 84.3381 + 0.985042 \cdot \text{Sinh} \left( \frac{1.6884 - 0.6052 \cdot x_1 + 1.1204 \cdot x_2 + 0.0726 \cdot x_3 -}{-0.4921 \cdot x_1^2 + 0.6974 \cdot x_2^2 - 0.3513 \cdot x_3^2 +} \right). \quad (6)$$

(6) has the coefficient of determination and adjusted coefficient of determination are 0.8686 and 0.7208, respectively. In order to compare the three models of cutting force that were established above, in addition to coefficient of determination and adjustment coefficient of determination, percentage mean absolute error (% MAE) between the cutting force value during experiment and the cutting force value predicted by these models should also be considered. The value of this parameter is calculated as follows:

$$\%MAE = \left( \frac{1}{N} \sum_i^N \left| \frac{T_i - P_i}{T_i} \right| \right) \cdot 100 \%. \quad (7)$$

In which,  $T_i$  is the cutting force value when experimenting at  $i^{\text{th}}$  experiment;  $P_i$  is the value of cutting force when predicted at  $i^{\text{th}}$  experiment;  $N$  is the number of experiments performed,  $N = 18$ . The values of cutting force when predicted by three models are presented in **Table 5**.

**Table 5**

Values of cutting force when predicting by models

No.	Experimental $F_c$ (N)	Predicted cutting force $F_c$ (N)		
		Without transformation	Box-Cox transformation	Johnson transformation
1	130.56	123.3601	117.0331	115.6442
2	110.08	110.5067	110.1966	110.1273
3	156.16	174.7201	150.1596	152.0765
4	112.64	110.5067	110.1966	110.1273
5	85.76	92.9601	90.6808	89.70174
6	240.64	214.8801	188.0776	197.8411
7	258.56	232.1601	193.0588	201.5439
8	152.32	185.9201	243.3241	232.1583
9	111.36	110.5067	110.1966	110.1273
10	104.96	110.5067	110.1966	110.1273
11	92.16	58.5601	83.3478	83.90721
12	104.96	97.1201	97.1332	96.40385
13	106.24	87.6801	108.3061	107.6719
14	92.16	117.9201	96.7959	96.63355
15	79.36	87.2001	83.4638	84.02749
16	104.96	110.5067	110.1966	110.1273
17	119.04	110.5067	110.1966	110.1273
18	88.32	114.7201	92.7159	92.93838



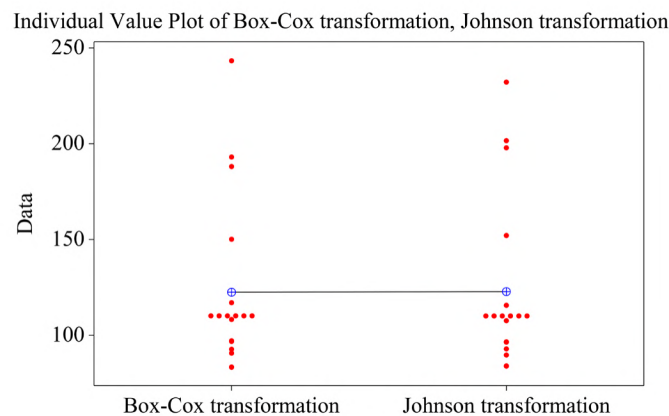
**Table 6** shows the values of  $R-Sq$ ,  $R-Sq(adj)$  and %  $MAE$  of three models.

**Table 6**

Comparison of cutting force models

Models	$R-Sq$	$R-Sq(adj)$	% $MAE$
Without using transformation	0.8571	0.6964	12.15
Using Box-Cox transformation	0.8824	0.7500	10.10
Using Johnson transformation	0.8686	0.7208	9.22

From the data in **Table 6**, it shows that the model without data transformation has  $R-Sq$ ,  $R-Sq(adj)$  smaller than two models using data transformation. On the other hand, the %  $MAE$  value of the model without using data transformation is also larger than this value of the other two models. Since then, it is confirmed that the model that does not use data transformation has the lowest accuracy. When looking at the two models using the data transformation, it can be seen that the model using the Box-Cox transformation has greater  $R-Sq$  and  $R-Sq(adj)$  coefficients than the model using Johnson transformation. However, the model using the Box-Cox transformation also has a larger %  $MAE$  parameter than the model using the Johnson transformation. Therefore, if only 3 parameters including  $R-Sq$ ,  $R-Sq(adj)$  and %  $MAE$  are considered, it is not confirmed that the model using the transformation has higher accuracy. To solve this problem, two sets of data on cutting force predicted by these two models by  $t$ -test should be compared. Minitab 16 statistics software is also applied in this case. With the assumption that the cutting force dataset predicted by the Box-Cox transformation model is «not equal» to the cutting force dataset predicted by the Johnson transformation model, the significance level is chosen to be 0.05. The results of comparing these two datasets are presented in **Fig. 8**. Information about the comparison results is presented in **Table 7**.

**Fig. 8.** Individual value plot of Box-Cox transformation, Johnson transformation**Table 7**

Two-sample T for Box-Cox transformation and Johnson transformation

Models	N	Mean	StDev	SE Mean
Box-Cox transformation	18	122.5	43.4	10
Johnson transformation	18	122.9	43.6	10

Difference =  $\mu$  (Box-Cox transformation) –  $\mu$  (Johnson transformation).

Estimate for difference: –0.3.

95 % CI for difference: (–29.8, 29.2).

T-Test of difference = 0 (vs not =):  $T$ -Value = –0.02;  $P$ -Value = 0.982;  $DF$  = 33

From the data in **Table 7** shows that the mean values of the two models are very close (122.5 and 122.9). When observing the graph in **Fig. 8**, this statement is seen more clearly. The standard deviations of the two models are also very close (43.4 and 43.6). The standard error of two models is equal to 10. In particular, *P-value* of 0.982 is much larger than the significance level, the above hypothesis has been rejected and it can be confirmed that the two data sets are equivalent [27]. In other words, the model using the Box-Cox transformation and the model using the Johnson transformation have equal accuracy.

The  $\lambda$  value in the Box-Cox transformation found in this study is equal to  $-2.00$ . However, this is a rounded result using Minitab software. In fact, the  $\lambda$  value could be a different one, and then the Box-Cox cutting force model will have more accuracy. Thus, the use of Minitab software to determine  $\lambda$  values is a limitation of this study. In order to be able to apply the Box-Cox transformation when building a model with a higher precision, it is necessary to specify the exact value of the  $\lambda$  (instead of the rounding value,  $\lambda = 2.00$ ). This work requires a large number of calculations, and will be carried out by the study's authors in the next time.

In addition, the comparison of the model using the Box-Cox transformation and the model using the Johnson transformation is only done by t-test. In order to get more accurate conclusions, it is necessary to compare these two models when using them in predicting cutting force under certain experimental conditions. This content will also be improved in the coming time.

#### 4. Conclusion

This study has carried out the experiment of milling SCM440 steel with TiN coated cutting tool with a radius tip of 0.5 mm. Influence of cutting speed, feed rate and cutting depth on the cutting force has been conducted; cutting force model and two data transformations of Box-Cox and Johnson have been used to build two new models of shear force. Some conclusions are drawn as follows:

- among three parameters of cutting parameters including cutting speed, feed rate and cutting depth, feed rate is only parameter that significantly affects the cutting force;
- the cutting force model using the Box-Cox transformation and the cutting force model using the Johnson transformation has equal accuracy, and is more accurate than the model that does not use the data transformation. The standard deviations of the two models (using the Box-Cox transformation and Johnson transformation) are also very close (43.4 and 43.6). The standard error of two models is equal to 10;
- Box-Cox and Johnson data transformations have not only succeeded in improving the accuracy of regression models in published documents, but have also succeeded in improving accuracy of the cutting force model in this study. Besides, it also holds promise for success in improving accuracy when used in other studies;
- using three cutting force models built in this study to solve the optimization problem for each case and then comparing with the experimental results are the works that the authors of this article will be conducted in the upcoming time.

#### Acknowledgement

The authors would like to send sincere thanks to Hanoi University of industry for their financial support in the implementation of this study.

---

#### References

- [1] Budak, E. (2006). Analytical models for high performance milling. Part I: Cutting forces, structural deformations and tolerance integrity. *International Journal of Machine Tools and Manufacture*, 46 (12-13), 1478–1488. doi: <https://doi.org/10.1016/j.ijmachtools.2005.09.009>
- [2] Dang, J.-W., Zhang, W.-H., Yang, Y., Wan, M. (2010). Cutting force modeling for flat end milling including bottom edge cutting effect. *International Journal of Machine Tools and Manufacture*, 50 (11), 986–997. doi: <https://doi.org/10.1016/j.ijmachtools.2010.07.004>
- [3] Narita, H. (2013). A determination method of cutting coefficients in ball end milling forces model, *International journal of Automation Technology*, 7 (1), 39–44.



- [4] Gao, G., Wu, B., Zhang, D., Luo, M. (2013). Mechanistic identification of cutting force coefficients in bull-nose milling process. *Chinese Journal of Aeronautics*, 26 (3), 823–830. doi: <https://doi.org/10.1016/j.cja.2013.04.007>
- [5] Guo, M., Wei, Z., Wang, M., Li, S., Liu, S. (2018). An identification model of cutting force coefficients for five-axis ball-end milling. *The International Journal of Advanced Manufacturing Technology*, 99 (1-4), 937–949. doi: <https://doi.org/10.1007/s00170-018-2451-6>
- [6] Wan, M., Zhang, W.-H., Dang, J.-W., Yang, Y. (2010). A novel cutting force modelling method for cylindrical end mill. *Applied Mathematical Modelling*, 34 (3), 823–836. doi: <https://doi.org/10.1016/j.apm.2009.09.012>
- [7] Šajgalík, M., Kušnerová, M., Harničárová, M., Valíček, J., Czán, A., Czánová, T. et. al. (2020). Analysis and Prediction of the Machining Force Depending on the Parameters of Trochoidal Milling of Hardened Steel. *Applied Sciences*, 10 (5), 1788. doi: <https://doi.org/10.3390/app10051788>
- [8] Muthusamy Subramanian, A. V., Nachimuthu, M. D. G., Cinnasamy, V. (2017). Assessment of cutting force and surface roughness in LM6/SiC p using response surface methodology. *Journal of Applied Research and Technology*, 15 (3), 283–296. doi: <https://doi.org/10.1016/j.jart.2017.01.013>
- [9] Salguero, J., Calamaz, M., Batista, M., Girot, F., Marcos Bárcena, M. (2014). Cutting Forces Prediction in the Dry Slotting of Aluminium Stacks. *Materials Science Forum*, 797, 47–52. doi: <https://doi.org/10.4028/www.scientific.net/msf.797.47>
- [10] Constantin, C., Constantin, G. (2013). Empirical model of the cutting forces in milling. *Proceedings in Manufacturing Systems*, 8 (4), 205–212.
- [11] Bağci, E. (2017). Experimental investigation of effect of tool path strategies and cutting parameters using acoustic signal in complex surface machining. *Journal of Vibroengineering*, 19 (7), 5571–5588. doi: <https://doi.org/10.21595/jve.2017.18475>
- [12] Biró, I., Czampa, M., Szalay, T. (2015). Experimental Model for the Main Cutting Force in Face Milling of a High Strength Structural Steel. *Periodica Polytechnica Mechanical Engineering*, 59 (1), 16–22. doi: <https://doi.org/10.3311/ppme.7516>
- [13] Günay, M., Kaçal, A., Turgut, Y. (2011). Optimization of machining parameters in milling of Ti-6Al-4V alloy using Taguchi method. *e-Journal of New World Sciences Academy - Engineering Sciences*, 6 (1), 428–440.
- [14] Patwari, M. A., Amin, A. K. M. N., Faris, W. F. (1970). Prediction of tangential cutting force in end milling of medium carbon steel by coupling design of experiment and response surface methodology. *Journal of Mechanical Engineering*, 40 (2), 95–103. doi: <https://doi.org/10.3329/jme.v40i2.5350>
- [15] Chuangwen, X., Ting, X., Xiangbin, Y., Jilin, Z., Wenli, L., Huaiyuan, L. (2016). Experimental tests and empirical models of the cutting force and surface roughness when cutting 1Cr13 martensitic stainless steel with a coated carbide tool. *Advances in Mechanical Engineering*, 8 (10), 168781401667375. doi: <https://doi.org/10.1177/1687814016673753>
- [16] Chen, J.-Y., Chan, T.-C., Lee, B.-Y., Liang, C.-Y. (2020). Prediction model of cutting edge for end mills based on mechanical material properties. *The International Journal of Advanced Manufacturing Technology*, 107 (7-8), 2939–2951. doi: <https://doi.org/10.1007/s00170-019-04884-8>
- [17] Arunnath, A., Masooth, P. H. S. (2021). Optimization of process parameters in CNC turning process on machining SCM440 steel by uncoated carbide and TiCN/Al<sub>2</sub>O<sub>3</sub>/TiN coated carbide tool under dry conditions. *Materials Today: Proceedings*, 45, 6253–6269. doi: <https://doi.org/10.1016/j.matpr.2020.10.699>
- [18] Thirumalai, R., Srinivas, S., Vinodh, T., Kowshik Kumar, A. L., Kumar, M. K. (2014). Optimization of Surface Roughness and Flank Wear in Turning SCM440 Alloy Steel Using Taguchi Method. *Applied Mechanics and Materials*, 592-594, 641–646. doi: <https://doi.org/10.4028/www.scientific.net/amm.592-594.641>
- [19] Reddy, N. S. K., Yang, M. (2009). Development of an electro static lubrication system for drilling of SCM 440 steel. *Proceedings of the Institution of Mechanical Engineers, Part B: Journal of Engineering Manufacture*, 224 (2), 217–224. doi: <https://doi.org/10.1243/09544054jem1670>
- [20] Basar, G., Kahraman, F. (2018). Modeling and optimization of face milling process parameters for AISI 4140 steel. *Tehnički Glasnik*, 12 (1), 5–10. doi: <https://doi.org/10.31803/tg-20180201124648>
- [21] Sales, W., Becker, M., Barcellos, C. S., Landre, J., Bonney, J., Ezugwu, E. O. (2009). Tribological behaviour when face milling AISI 4140 steel with minimum quantity fluid application. *Industrial Lubrication and Tribology*, 61 (2), 84–90. doi: <https://doi.org/10.1108/00368790910940400>
- [22] Stipkovic, M. A., Bordinassi, É. C., Farias, A. de, Delijaicov, S. (2017). Surface Integrity Analysis in Machining of Hardened AISI 4140 Steel. *Materials Research*, 20 (2), 387–394. doi: <https://doi.org/10.1590/1980-5373-mr-2016-0420>
- [23] Xu, Q., Zhao, J., Ai, X. (2017). Cutting performance of tools made of different materials in the machining of 42CrMo4 high-strength steel: a comparative study. *The International Journal of Advanced Manufacturing Technology*, 93 (5-8), 2061–2069. doi: <https://doi.org/10.1007/s00170-017-0666-6>
- [24] Dean, A., Voss, D., Draguljić, D. (2017). *Design and Analysis of Experiments*. Springer, 840. doi: <https://doi.org/10.1007/978-3-319-52250-0>

- [25] Trung, D. D. (2020). Influence of Cutting Parameters on Surface Roughness during Milling AISI 1045 Steel. *Tribology in Industry*, 42 (4), 658–665. doi: <https://doi.org/10.24874/ti.969.09.20.11>
- [26] Dean, A., Voss, D. (Eds.) (1999). *Design and Analysis of Experiments*. Springer, 742. doi: <https://doi.org/10.1007/b97673>
- [27] Du, N. V., Binh, N. D. (2011). *Design of experiment techniques*. Science and technics publishing House.
- [28] Bhardwaj, B., Kumar, R., Singh, P. K. (2014). An improved surface roughness prediction model using Box-Cox transformation with RSM in end milling of EN 353. *Journal of Mechanical Science and Technology*, 28 (12), 5149–5157. doi: <https://doi.org/10.1007/s12206-014-0837-4>
- [29] Bhardwaj, B., Kumar, R., Singh, P. K. (2013). Effect of machining parameters on surface roughness in end milling of AISI 1019 steel. *Proceedings of the Institution of Mechanical Engineers, Part B: Journal of Engineering Manufacture*, 228 (5), 704–714. doi: <https://doi.org/10.1177/0954405413506417>
- [30] Nguyen, N.-T., Trung, D. D. (2020). Modeling And Improvement of the Surface Roughness Model in Hole Turning Process 3x13 Stainless Steel by Using Johnson Transformation. *International Journal of Mechanical and Production Engineering Research and Development*, 10 (3), 12097–12110. doi: <https://doi.org/10.24247/ijmperdjun20201157>
- [31] Uyen, V. T. N., Son, N. H. (2021). Improving accuracy of surface roughness model while turning 9XC steel using a Titanium Nitride-coated cutting tool with Johnson and Box-Cox transformation. *AIMS Materials Science*, 8 (1), 1–17. doi: <https://doi.org/10.3934/materci.2021001>
- [32] Trung, D. D. (2021). Influence of Cutting Parameters on Surface Roughness in Grinding of 65G Steel. *Tribology in Industry*, 43 (1), 167–176. doi: <https://doi.org/10.24874/ti.1009.11.20.01>
- [33] Sakia, R. M. (1992). The Box-Cox Transformation Technique: A Review. *The Statistician*, 41 (2), 169. doi: <https://doi.org/10.2307/2348250>

Received date 07.04.2021

Accepted date 10.07.2021

Published date 13.09.2021

© The Author(s) 2021

This is an open access article

under the Creative Commons CC BY license

**How to cite:** Thien, N. V., Trung, D. D. (2021). Study on model for cutting force when milling SCM440 steel. *EUREKA: Physics and Engineering*, 5, 23–35. doi: <https://doi.org/10.21303/2461-4262.2021.001743>



# A DEVELOPMENT METHOD OF CUTTING FORCE COEFFICIENTS IN FACE MILLING PROCESS USING PARALLELOGRAM INSERT

*Nhu-Tung Nguyen*

*HaUI Institute of Technology – HIT*

*Hanoi University of Industry*

*298 Cau Dien str., Bac Tu Liem District, Hanoi, 100000*

*tungnn@hau.edu.vn*

## Abstract

This paper presents a modeling method of cutting force and a combination approach of theory and experimental methods in the determination of cutting force coefficients in the face milling process using a parallelogram insert. By the theoretical method, the cutting forces were modeled by a mathematical function of cutting cutter geometry (Cutter diameter, the number of inserts, the insert nose radius, insert cutting edge helix angle, etc.), cutting conditions (depth of cut, feed per flute, spindle speed, etc.), and cutting force coefficients (shear force coefficients, edge force coefficients). By the theoretical method, the average cutting forces in three directions (feed –  $x$ , normal –  $y$ , and axial –  $z$ ) were modeled as the linear functions of feed per flute. By the experimental method, the average cutting forces in these three directions were also regressed as the linear functions of feed per flute with quite large determination coefficients ( $R^2$  were larger than 92 %). Then, the relationship of average cutting forces and feed per flute was used to determine all six cutting force coefficient components. The validation experiments were performed to verify the linear function of average cutting forces, to determine the cutting force coefficients, and to verify the cutting force models in the face milling process using a cutter with one parallelogram insert. The cutting force models were successfully verified by comparison of the shape and the values of predicted cutting forces and measured cutting forces. These proposed methods and models can be applied to determine the cutting force coefficients and predict the cutting force in the face milling process using a parallelogram insert and can be extended with other cutting types or other insert types.

**Keywords:** modeling, force models, cutting forces, force coefficients, average cutting forces, shear cutting coefficients, edge cutting coefficients, face milling, parallelogram insert, C45.

DOI: 10.21303/2461-4262.2021.001890

## 1. Introduction

Nowadays, milling is very popularly employed in computer numerical control (CNC) machines for metal material cutting operations. In the milling process, the cutting forces are the important parameter to predict the machining characteristics such as cutting power, vibrations, chatter, surface roughness, etc., and develop the machining processes with high effectiveness and low cost. The cutting force model plays a decisive role in accuracy when predicting the forces and other machining characteristics in machining processes, especially in milling processes.

Two modeling methods were generally used to model the cutting force in the machining process. In the first method, the cutting force was modeled by the regression model through experimental data. By using this method, the effect of the controllable factors such as cutting conditions, tool geometry, etc., on the cutting force was investigated. This method is easy to perform, and the cutting force model is also easy to model. However, this method was only applied in limited conditions, and the regression model changed with different conditions of experimental. Besides, this method was only applied separately for each pair of tool and workpiece, and the cutting force model changed when applying for different pairs of tool and workpiece. Several researchers applied this method in the investigation of cutting force in the face milling process of SKD61 Hard Steel [1], flat milling process of aerospace aluminum alloys [2], ball milling graded material [3], and so on. In the second method, the cutting force was modeled by the theoretical model through a mathematical function of tool geometry, tool, and workpiece material properties, cutting conditions, and so on. This method is a quite complex method in the modeling process. However, the modeling process was started from the analysis of the metal cutting principle that was the essence of cutting processes; so, this method had been widely applied in cutting processes such as turning, milling, drilling, etc. The reviews of this method are presented in the following.

In milling processes, two model types were often applied to predict the cutting forces. In the first one, the cutting forces are proportional to the chip thickness and cutting force coefficients. In this model, the cutting force coefficients were expressed as the exponential functions of average chip thickness (exponential force coefficient model) [4, 5]. Using this model, the instantaneous cutting force coefficients were predicted from the experimental data of average chip thickness, the instantaneous cutting force, and the average cutting force [6, 7]. This model is convenient for the analysis of dynamic cutting and stability lobes in the machining process. However, the edge forces were often neglected in the cutting force model.

In the second model, the cutting forces are often separated into the shear force and edge force and the average cutting force could be expressed by a linear function of feed rate. This linear function was used to determine three shear force coefficients and three edge force coefficients from the cutting test data of cutting force [8, 9]. This model is easy to apply when the cutting forces can be measured in milling processes. So, it was applied to many types of milling tools such as flat end mill [9], ball-end mill [10], bull-end mill [11], and face milling [12], etc. In the face milling process, the cutting forces were modeled depending on the relationship of average cutting forces and feed per flute when milling using several types of the cutter inserts such as round cutter inserts [12], rectangular and convex triangular cutter inserts [13]. It seems that the cutting force models in face milling processes using the parallelogram cutter inserts have not been mentioned in the previous studies. While, nowadays, these cutter inserts are popularly using in the milling process both for rough milling and finish milling processes. Therefore, modeling of cutting forces in the milling process using the parallelogram cutter inserts are necessary to apply in the prediction of cutting forces and other machining characteristics of these milling processes.

This study was performed to model the cutting forces, to verify the relationship of average cutting forces and feed per flute, to determine the cutting force coefficients, and to verify the cutting force models in the milling process using the parallelogram cutter inserts.

## 2. Materials and methods

In face milling process using the parallelogram insert, the cutting process was the interactive process of cutter inserts and workpiece. During the relative movement of the cutter and the workpiece, the chip is formed from the geometrical intersection process of the cutter inserts and the workpiece. The chip geometry depends on the geometry of the workpiece, the geometry of the cutter inserts, and the relative position of the cutter inserts and workpiece. The geometrical model of face milling process was described in Fig. 1.

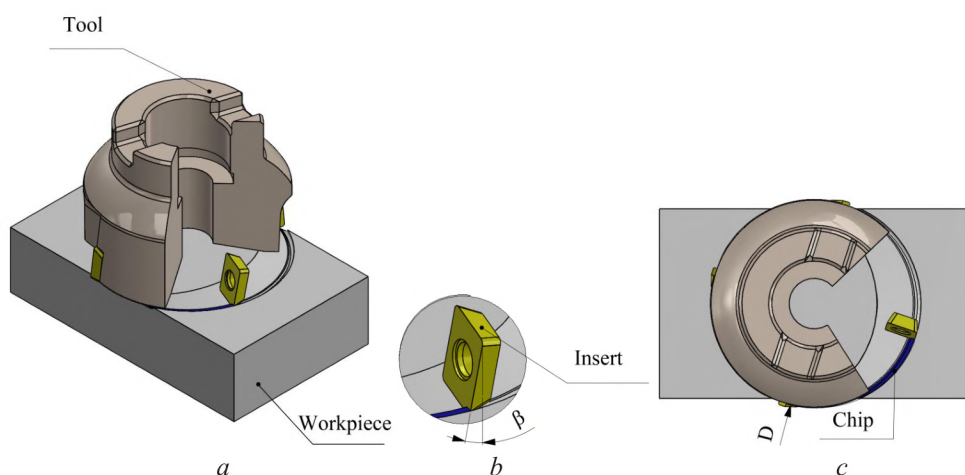


**Fig. 1.** Face milling process: *a* – Tool and workpiece; *b* – Parallelogram Insert; *c* – Chip

In face milling process, the immersion position angle of each cutting edge is measured clockwise from the normal axis. Assuming that the bottom end of flute number one is designated as the reference immersion position angle ( $\phi_1$ ) and the bottom end point of the flute number  $j$  is at



an angle ( $\phi_j$ ), as shown in **Fig. 2**. So, the immersion position angle of the flute number  $j(\phi_j)$  can be calculated by (1):

$$\phi_j = \phi_1 - (j-1)\phi_p, J = 1 \sim N_f, \quad (1)$$

where  $\phi_p$  is the cutter pitch angle that is the lag angle of two cutter inserts side by side as presented by (2):

$$\phi_p = \frac{2\pi}{N_f}. \quad (2)$$

By the influence of the cutter helix angle, the radial lag angle  $\psi$  at each axial depth of cut  $z$  can be expressed in (3):

$$\psi = \frac{2 \tan \beta}{D} z = \frac{\tan \beta}{R} z. \quad (3)$$

At an axial depth of cut  $z$ , the immersion angle is  $\phi_j(z)$  of the flute number  $j$  can be calculated by (4), as shown in **Fig. 2**.

$$\phi_j(z) = \phi_j - \psi = \phi_j - \frac{\tan \beta}{R} z. \quad (4)$$

In case the depth of cut is smaller than the insert nose radius, the cutting process only occurs at part (1) of cutting edge. In case, the depth of cut is larger than the insert nose radius, the cutting process occurs at both part (1) and part (2) of the cutting edge as illustrated in **Fig. 3**.

In general cases, the cutting process occurs at both part (1) and part (2) of the cutting edge, the instantaneous chip thickness will be different in the different parts of the cutting edge. In part (1) of cutting edge, the instantaneous chip thickness is  $h_{j1}(\phi_j(z))$  and in part (2) of cutting edge, the instantaneous chip thickness is  $h_{j2}(\phi_j(z))$ . In part (1) of cutting edge, the instantaneous chip thickness  $h_{j1}(\phi_j(z))$  is determined by (5):

$$h_{j1}(\phi_j(z)) = f_t \cdot \sin(\phi_j(z)) \cdot \sin(\kappa(z)), \quad (5)$$

where  $\kappa(z)$  is the axial immersion angle at  $z$  axial cutting depth. And  $\sin(\kappa(z))$  can be calculated by (6):

$$\sin(\kappa(z)) = \frac{d(\phi_j(z))}{r(\phi_j(z))} = \frac{\sqrt{r^2 - (r-z)^2}}{r}, \quad d = \sqrt{r^2 - (r-z)^2}. \quad (6)$$

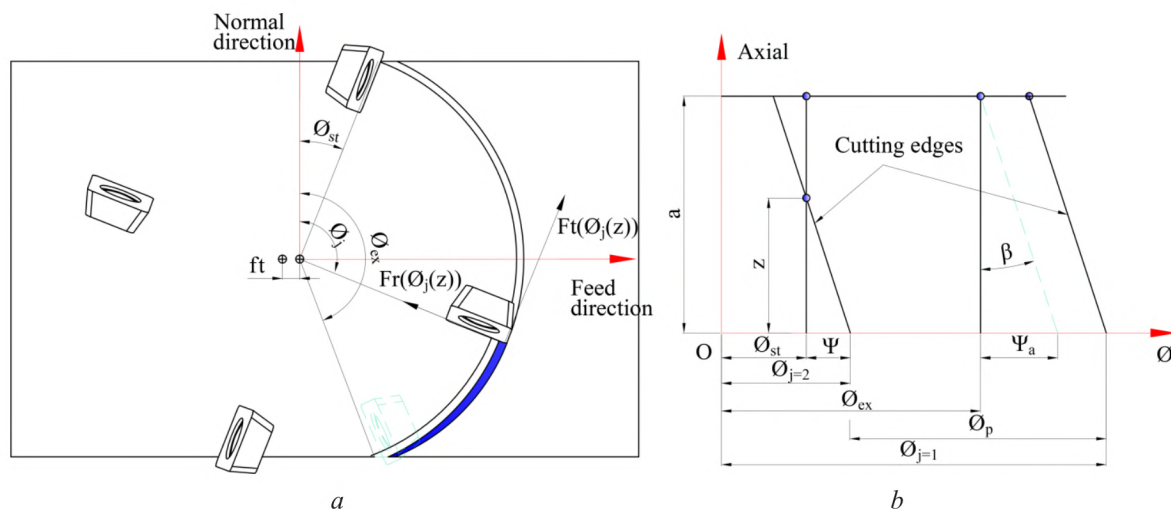


**Fig. 2.** The position angle of cutter inserts: *a* – In feed and normal direction;  
*b* – In axial direction

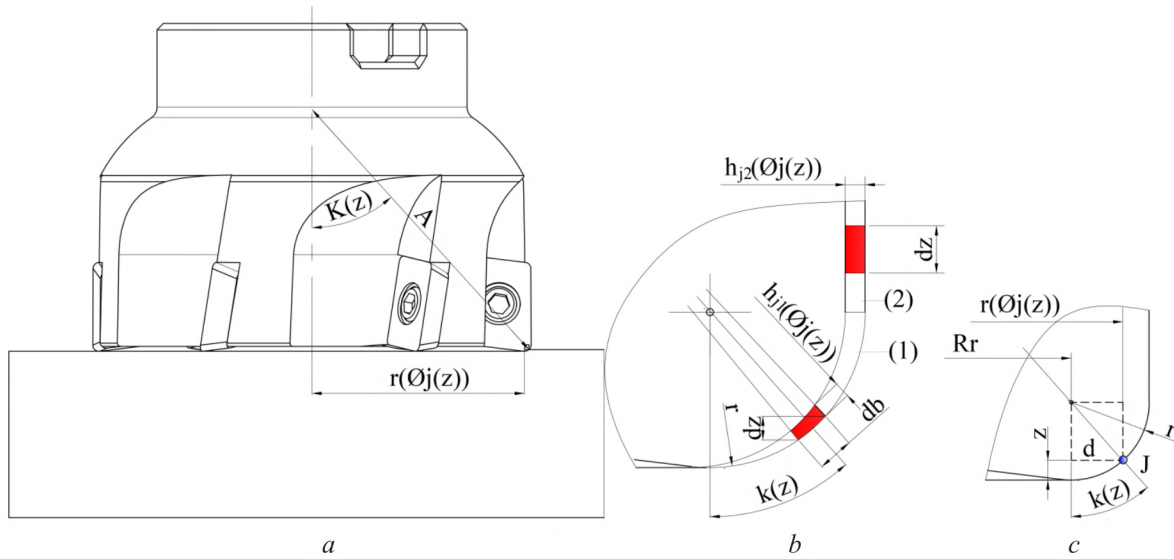


**Fig. 3.** Undeform chip thickness:  
a – Chip position; b – Parts of chip; c – Position of point *J* in the chip

The immersion chip width (*b*) is calculated by (7):

$$db = \frac{dz}{\sin(\kappa(z))}. \quad (7)$$

$r(\phi_j(z))$  is the radius of a circle on *xy* plane at an arbitrary point on the cutting edge. So,  $r(\phi_j(z))$  can be determined by (8):

$$r(\phi_j(z)) = R_r + d = R_r + \sqrt{r^2 - (r - z)^2}. \quad (8)$$

The edge length of the cutting segment *ds* is obtained by the small variation of a vector, which is obtained from the center point to a point *J* on the cutting edge (Fig. 3), with respect to the small variation of rotation angle  $\phi$ . The location of point *J* on the flute number *j* is defined by a vector in cylindrical coordinates as described in Fig. 3 and can be calculated by (9):

$$\vec{r}(\phi_j(z)) = r(\phi_j(z)) \cdot \sin(\phi_j(z)) \cdot \vec{i} + r(\phi_j(z)) \cdot \cos(\phi_j(z)) \cdot \vec{j} + z \cdot \vec{k}. \quad (9)$$

Where *z* is the *z* coordinate of point *J*, and, *ds* can be derived by (10), (11):

$$ds = |\vec{r}(\phi_j(z))| = \sqrt{\left\{ \left[ r(\phi_j(z)) \cdot \sin(\phi_j(z)) \right]' \right\}^2 + \left\{ \left[ r(\phi_j(z)) \cdot \cos(\phi_j(z)) \right]' \right\}^2 + \left\{ [z]' \right\}^2}, \quad (10)$$

$$ds = dz \cdot \sqrt{\frac{(r - z)^2}{r^2 - (r - z)^2} + \left[ \frac{R_r + \sqrt{r^2 - (r - z)^2}}{R} \right]^2 \tan^2 \beta + 1} = M \cdot dz, \quad (11)$$

with

$$M = \sqrt{\frac{(r - z)^2}{r^2 - (r - z)^2} + \left[ \frac{R_r + \sqrt{r^2 - (r - z)^2}}{R} \right]^2 \tan^2 \beta + 1}, \quad (12)$$

So, in the part (1) of cutting edge, the tangential, radial, and axial forces acting on a differential flute element can be expressed as in (13):



$$\begin{cases} dF_{t1,j}(\phi, z) = K_{te} \cdot ds(\phi_j(z)) + K_{tc} \cdot h_j(\phi_j(z)) \cdot db; \\ dF_{r1,j}(\phi, z) = K_{re} \cdot ds(\phi_j(z)) + K_{rc} \cdot h_j(\phi_j(z)) \cdot db; \\ dF_{a1,j}(\phi, z) = K_{ae} \cdot ds(\phi_j(z)) + K_{ac} \cdot h_j(\phi_j(z)) \cdot db, \end{cases} \quad (13)$$

where  $K_{te}$ ,  $K_{rc}$ ,  $K_{ac}$ ,  $K_{te}$ ,  $K_{re}$  are the cutting force coefficients (The values of cutting force coefficients depend on the interaction mechanical of cutter and workpiece). Replacing (5), (7), and (11) into (13), the the tangential, radial, and axial forces can be calculated by (14):

$$\begin{cases} dF_{t1,j}(\phi, z) = [K_{te} \cdot M + K_{tc} \cdot f_t \cdot \sin(\phi_j(z))] dz; \\ dF_{r1,j}(\phi, z) = [K_{re} \cdot M + K_{rc} \cdot f_t \cdot \sin(\phi_j(z))] dz; \\ dF_{a1,j}(\phi, z) = [K_{ae} \cdot M + K_{ac} \cdot f_t \cdot \sin(\phi_j(z))] dz. \end{cases} \quad (14)$$

The cutting forces are often measured in three directions that including feed ( $f$  or  $x$ ), normal ( $n$  or  $y$ ), and axial ( $z$ ) directions. So, using the transformation method, the elemental cutting forces in feed, normal, and axial force are calculated by (15), (16) as shown in **Fig. 4**:

$$\begin{Bmatrix} dF_{f1,j}(\phi, z) \\ dF_{n1,j}(\phi, z) \\ dF_{z1,j}(\phi, z) \end{Bmatrix} = \begin{bmatrix} \cos(\phi_j(z)) & +\sin(\phi_j(z)) \cdot \sin(\kappa(z)) & +\sin(\phi_j(z)) \cdot \cos(\kappa(z)) \\ \sin(\phi_j(z)) & -\cos(\phi_j(z)) \cdot \sin(\kappa(z)) & -\cos(\phi_j(z)) \cdot \cos(\kappa(z)) \\ 0 & \cos(\kappa(z)) & -\sin(\kappa(z)) \end{bmatrix} \begin{Bmatrix} dF_{t1,j}(\phi, z) \\ dF_{r1,j}(\phi, z) \\ dF_{a1,j}(\phi, z) \end{Bmatrix}, \quad (15)$$

so,

$$\begin{aligned} & \begin{cases} dF_{f1,j}(\phi, z) = \cos\left(\phi_j - \frac{\tan\beta}{R}z\right) \cdot dF_{t1,j}(\phi, z) + \sin\left(\phi_j - \frac{\tan\beta}{R}z\right) \cdot \sin(\kappa(z)) \cdot dF_{r1,j}(\phi, z) + \\ + \sin\left(\phi_j - \frac{\tan\beta}{R}z\right) \cdot \cos(\kappa(z)) \cdot dF_{a1,j}(\phi, z); \\ dF_{n1,j}(\phi, z) = \sin\left(\phi_j - \frac{\tan\beta}{R}z\right) \cdot dF_{t1,j}(\phi, z) - \cos\left(\phi_j - \frac{\tan\beta}{R}z\right) \cdot \sin(\kappa(z)) \cdot dF_{r1,j}(\phi, z) - \\ - \cos\left(\phi_j - \frac{\tan\beta}{R}z\right) \cdot \cos(\kappa(z)) \cdot dF_{a1,j}(\phi, z); \\ dF_{z1,j}(\phi, z) = \cos(\kappa(z)) \cdot dF_{r1,j}(\phi, z) - \sin(\kappa(z)) \cdot dF_{a1,j}(\phi, z). \end{cases} \end{aligned} \quad (16)$$

In part (2) of cutting edge, the instantaneous chip thickness  $h_{j2}(\phi_j(z))$  is determined by (17):

$$h_{j2}(\phi_j(z)) = f_t \cdot \sin(\phi_j(z)). \quad (17)$$

So, in this part, the tangential, radial, and axial cutting forces acting on a differential flute element can be expressed as in (18):

$$\begin{cases} \bar{F}_{f2} = \frac{N_f}{2\pi} \int_{\phi_{st} + a_1}^{\phi_{ex} + a_2} \left( \int_{z_{j,2}}^{z_{j,3}} dF_{f2,j}(\phi(z)) \right) d\phi; \\ \bar{F}_{n2} = \frac{N_f}{2\pi} \int_{\phi_{st} + a_1}^{\phi_{ex} + a_2} \left( \int_{z_{j,2}}^{z_{j,3}} dF_{n2,j}(\phi(z)) \right) d\phi; \\ \bar{F}_{a2} = \frac{N_f}{2\pi} \int_{\phi_{st} + a_1}^{\phi_{ex} + a_2} \left( \int_{z_{j,2}}^{z_{j,3}} dF_{a2,j}(\phi(z)) \right) d\phi. \end{cases} \quad (18)$$

Using the transformation method, the feed, normal, and axial cutting forces are calculated by (19), (20):

$$\begin{Bmatrix} DF_{f2,j}(\phi, z) \\ dF_{n2,j}(\phi, z) \\ dF_{z2,j}(\phi, z) \end{Bmatrix} = \begin{bmatrix} -\cos(\phi_j(z)) & -\sin(\phi_j(z)) & 0 \\ \sin(\phi_j(z)) & -\cos(\phi_j(z)) & 0 \\ 0 & 0 & 1 \end{bmatrix} \begin{Bmatrix} dF_{t2,j}(\phi, z) \\ dF_{r2,j}(\phi, z) \\ dF_{a2,j}(\phi, z) \end{Bmatrix}, \quad (19)$$

$$\Rightarrow \begin{cases} dF_{f2,j}(\phi, z) = -\cos(\phi_j(z)) \cdot dF_{t2,j}(\phi, z) - \sin(\phi_j(z)) \cdot dF_{r2,j}(\phi, z); \\ dF_{n2,j}(\phi, z) = \sin(\phi_j(z)) \cdot dF_{t2,j}(\phi, z) - \cos(\phi_j(z)) \cdot dF_{r2,j}(\phi, z); \\ dF_{z2,j}(\phi, z) = dF_{a2,j}(\phi, z). \end{cases} \quad (20)$$

So, in general cases, the cutting forces occur at both part (1) and part (2) of the cutting edge as shown in **Fig. 5**.

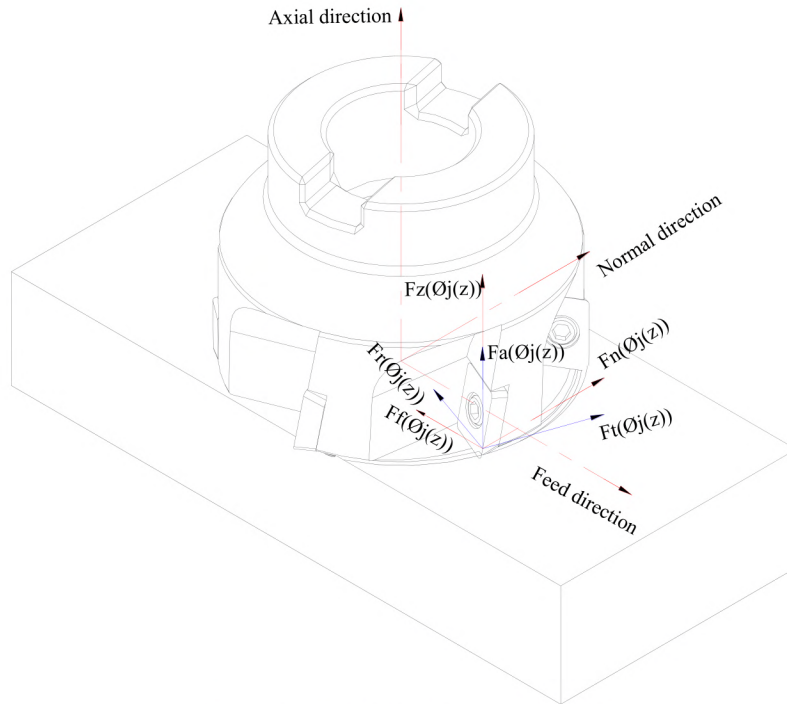


**Fig. 4.** Cutting forces in cutting edge 1

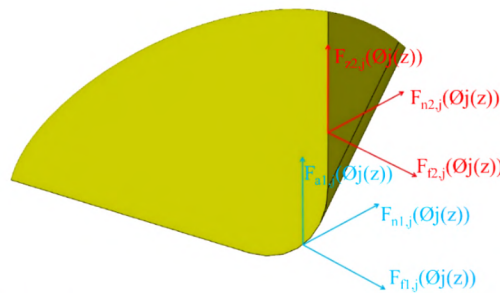


**Fig. 5.** Cutting force in two parts of cutting edge

To determine the total cutting force, the differential cutting forces are integrated analytically along the in-cut portion of the cutting edge of flute  $j$ . So, the total cutting forces in each cutting edge can be calculated by (21):

$$F_q(\phi_j(z)) = F_{q1}(\phi_j, z) + F_{q2}(\phi_j, z) = \int_{z_{1(\phi_j)}}^{z_{2(\phi_j)}} dF_{q1}(\phi_j, z) + \int_{z_{2(\phi_j)}}^{z_{3(\phi_j)}} dF_{q2}(\phi_j, z) \text{ with } q = f, n, a. \quad (21)$$



In cases, there are more than one flute executing the cutting processes simultaneously, the total cutting forces in the feed, normal, and axial directions can be calculated by (22):

$$F_q(\phi_j) = \sum_{j=1}^{N_f} F_{q,j}(\phi_j, z). \quad (22)$$

In the face milling process, the average cutting forces of  $N_f$  flutes in feed, normal, and axial directions per revolution can be calculated by (23):

$$\begin{cases} \bar{F}_f = \bar{F}_{f1} + \bar{F}_{f2}; \\ \bar{F}_n = \bar{F}_{n1} + \bar{F}_{n2}; \\ \bar{F}_z = \bar{F}_{z1} + \bar{F}_{z2}. \end{cases} \quad (23)$$

In the part (1) of the cutting edge, the average cutting forces of  $N_f$  flutes in feed, normal, and axial directions, per revolution can be expressed by (24):

$$\begin{cases} \bar{F}_{f1} = \frac{N_f}{2\pi} \int_{\phi_{st}}^{\phi_{ex} + \psi_{a1}} \left( \int_{z_{j,1}}^{z_{j,2}} dF_{f1,j}(\phi(z)) \right) d\phi; \\ \bar{F}_{n1} = \frac{N_f}{2\pi} \int_{\phi_{st}}^{\phi_{ex} + \psi_{a1}} \left( \int_{z_{j,1}}^{z_{j,2}} dF_{n1,j}(\phi(z)) \right) d\phi; \\ \bar{F}_{a1} = \frac{N_f}{2\pi} \int_{\phi_{st}}^{\phi_{ex} + \psi_{a1}} \left( \int_{z_{j,1}}^{z_{j,2}} dF_{a1,j}(\phi(z)) \right) d\phi. \end{cases} \quad (24)$$

In the part (2) of the cutting edge, the average cutting forces of  $N_f$  flutes in feed, normal, and axial directions, per revolution can be expressed by (25):

$$\begin{cases} \bar{F}_{f2} = \frac{N_f}{2\pi} \int_{\phi_{st} + a1}^{\phi_{ex} + a2} \left( \int_{z_{j,2}}^{z_{j,3}} dF_{f2,j}(\phi(z)) \right) d\phi; \\ \bar{F}_{n2} = \frac{N_f}{2\pi} \int_{\phi_{st} + a1}^{\phi_{ex} + a2} \left( \int_{z_{j,2}}^{z_{j,3}} dF_{n2,j}(\phi(z)) \right) d\phi; \\ \bar{F}_{a2} = \frac{N_f}{2\pi} \int_{\phi_{st} + a1}^{\phi_{ex} + a2} \left( \int_{z_{j,2}}^{z_{j,3}} dF_{a2,j}(\phi(z)) \right) d\phi. \end{cases} \quad (25)$$

Where  $\phi_{st}$ ,  $(\phi_{st} + \psi_{a1})$ ,  $\phi_{ex}$ ,  $(\phi_{ex} + \psi_{a2})$  are cutting boundary conditions.

Set the constants  $C_i$  by from (26) to (46):

$$C_1 = -\frac{N_f}{4\pi} \left[ \int_{\phi_{st}}^{\phi_{st} + \psi_{a1}} \left( \int_0^{\frac{R}{\tan\beta}(\phi_j - \phi_{st})} \left( s \sin 2 \left( \phi_j - \frac{\tan\beta}{R} z \right) \right) dz \right) d\phi + \right. \\ \left. + \int_{\phi_{st} + \psi_{a1}}^{\phi_{ex}} \left( \int_0^r \left( s \sin 2 \left( \phi_j - \frac{\tan\beta}{R} z \right) \right) dz \right) d\phi + \right. \\ \left. + \int_{\phi_{ex}}^{\phi_{ex} + \psi_{a1}} \left( \int_{\frac{R}{\tan\beta}(\phi_j - \phi_{ex})}^r \left( s \sin 2 \left( \phi_j - \frac{\tan\beta}{R} z \right) \right) dz \right) d\phi \right], \quad (26)$$

$$C_2 = -\frac{N_f}{2\pi} \left[ \int_{\phi_{st}}^{\phi_{st} + \psi_{a1}} \left( \int_0^{\frac{R}{\tan\beta}(\phi_j - \phi_{st})} \left( \cos \left( \phi_j - \frac{\tan\beta}{R} z \right) \cdot M \right) dz \right) d\phi + \right. \\ \left. + \int_{\phi_{st} + \psi_{a1}}^{\phi_{ex}} \left( \int_0^r \left( \cos \left( \phi_j - \frac{\tan\beta}{R} z \right) \cdot M \right) dz \right) d\phi + \right. \\ \left. + \int_{\phi_{ex}}^{\phi_{ex} + \psi_{a1}} \left( \int_{\frac{R}{\tan\beta}(\phi_j - \phi_{ex})}^r \left( \cos \left( \phi_j - \frac{\tan\beta}{R} z \right) \cdot M \right) dz \right) d\phi \right], \quad (27)$$

$$C_3 = -\frac{N_f}{4\pi} \left[ \int_{\phi_{st}}^{\phi_{st}+\psi_{a1}} \left( \int_0^{\frac{R}{\tan\beta}(\phi_j-\phi_{st})} \sin(Kz) \cdot \left( 1 - \cos 2 \left( \phi_j - \frac{\tan\beta}{R} z \right) \right) dz \right) d\phi + \right. \\ \left. + \int_{\phi_{ex}}^{\phi_{ex}+\psi_{a1}} \left( \int_0^r \sin(Kz) \cdot \left( 1 - \cos 2 \left( \phi_j - \frac{\tan\beta}{R} z \right) \right) dz \right) d\phi + \right. \\ \left. + \int_{\phi_{ex}}^{\phi_{ex}+\psi_{a1}} \left( \int_{\frac{R}{\tan\beta}(\phi_j-\phi_{ex})}^r \sin(Kz) \cdot \left( 1 - \cos 2 \left( \phi_j - \frac{\tan\beta}{R} z \right) \right) dz \right) d\phi \right], \quad (28)$$

$$C_4 = -\frac{N_f}{2\pi} \left[ \int_{\phi_{st}}^{\phi_{st}+\psi_{a1}} \left( \int_0^{\frac{R}{\tan\beta}(\phi_j-\phi_{st})} \left( \sin(Kz) \cdot \sin \left( \phi_j - \frac{\tan\beta}{R} z \right) \cdot M \right) dz \right) d\phi + \right. \\ \left. + \int_{\phi_{st}+\psi_{a1}}^{\phi_{ex}} \left( \int_0^r \left( \sin(Kz) \cdot \sin \left( \phi_j - \frac{\tan\beta}{R} z \right) \cdot M \right) dz \right) d\phi + \right. \\ \left. + \int_{\phi_{ex}}^{\phi_{ex}+\psi_{a1}} \left( \int_{\frac{R}{\tan\beta}(\phi_j-\phi_{ex})}^r \left( \sin(Kz) \cdot \sin \left( \phi_j - \frac{\tan\beta}{R} z \right) \cdot M \right) dz \right) d\phi \right], \quad (29)$$

$$C_5 = -\frac{N_f}{4\pi} \left[ \int_{\phi_{st}}^{\phi_{st}+\psi_{a1}} \left( \int_0^{\frac{R}{\tan\beta}(\phi_j-\phi_{st})} \left( \cos(Kz) \cdot \left( 1 - \cos 2 \left( \phi_j - \frac{\tan\beta}{R} z \right) \right) \right) dz \right) d\phi + \right. \\ \left. + \int_{\phi_{st}+\psi_{a1}}^{\phi_{ex}} \left( \int_0^r \left( \cos(Kz) \cdot \left( 1 - \cos 2 \left( \phi_j - \frac{\tan\beta}{R} z \right) \right) \right) dz \right) d\phi - \right. \\ \left. + \int_{\phi_{ex}}^{\phi_{ex}+\psi_{a1}} \left( \int_{\frac{R}{\tan\beta}(\phi_j-\phi_{ex})}^r \left( \cos(Kz) \cdot \left( 1 - \cos 2 \left( \phi_j - \frac{\tan\beta}{R} z \right) \right) \right) dz \right) d\phi \right], \quad (30)$$

$$C_6 = -\frac{N_f}{2\pi} \left[ \int_{\phi_{st}}^{\phi_{st}+\psi_{a1}} \left( \int_0^{\frac{R}{\tan\beta}(\phi_j-\phi_{st})} \left( \cos(Kz) \cdot \sin \left( \phi_j - \frac{\tan\beta}{R} z \right) \cdot M \right) dz \right) d\phi + \right. \\ \left. + \int_{\phi_{st}+\psi_{a1}}^{\phi_{ex}} \left( \int_0^r \left( \cos(Kz) \cdot \sin \left( \phi_j - \frac{\tan\beta}{R} z \right) \cdot M \right) dz \right) d\phi + \right. \\ \left. + \int_{\phi_{ex}}^{\phi_{ex}+\psi_{a1}} \left( \int_{\frac{R}{\tan\beta}(\phi_j-\phi_{ex})}^r \left( \cos(Kz) \cdot \sin \left( \phi_j - \frac{\tan\beta}{R} z \right) \cdot M \right) dz \right) d\phi \right], \quad (31)$$

$$C_7 = \frac{N_f}{4\pi} \left[ \int_{\phi_{st}}^{\phi_{st}+\psi_{a1}} \left( \int_0^{\frac{R}{\tan\beta}(\phi_j-\phi_{st})} \left( 1 - \cos 2 \left( \phi_j - \frac{\tan\beta}{R} z \right) \right) dz \right) d\phi + \right. \\ \left. + \int_{\phi_{st}+\psi_{a1}}^{\phi_{ex}} \left( \int_0^r \left( 1 - \cos 2 \left( \phi_j - \frac{\tan\beta}{R} z \right) \right) dz \right) d\phi + \right. \\ \left. + \int_{\phi_{ex}}^{\phi_{ex}+\psi_{a1}} \left( \int_{\frac{R}{\tan\beta}(\phi_j-\phi_{ex})}^r \left( 1 - \cos 2 \left( \phi_j - \frac{\tan\beta}{R} z \right) \right) dz \right) d\phi \right], \quad (32)$$

$$C_8 = \frac{N_f}{2\pi} \left[ \int_{\phi_{st}}^{\phi_{st}+\psi_{a1}} \left( \int_0^{\frac{R}{\tan\beta}(\phi_j-\phi_{st})} \left( \sin \left( \phi_j - \frac{\tan\beta}{R} z \right) \right) \cdot M dz \right) d\phi + \right. \\ \left. + \int_{\phi_{st}+\psi_{a1}}^{\phi_{ex}} \left( \int_0^r \left( \sin \left( \phi_j - \frac{\tan\beta}{R} z \right) \right) \cdot M dz \right) d\phi + \right. \\ \left. + \int_{\phi_{ex}}^{\phi_{ex}+\psi_{a1}} \left( \int_{\frac{R}{\tan\beta}(\phi_j-\phi_{ex})}^r \left( \sin \left( \phi_j - \frac{\tan\beta}{R} z \right) \right) \cdot M dz \right) d\phi \right], \quad (33)$$



$$C_9 = -\frac{N_f}{4\pi} \left[ \int_{\phi_{st}}^{\phi_{st}+\psi_{a1}} \left( \int_0^{\frac{R}{\tan\beta}(\phi_j-\phi_{st})} \left( \sin(Kz) \cdot \sin 2 \left( \phi_j - \frac{\tan\beta}{R} z \right) \right) dz \right) d\phi + \right. \\ \left. + \int_{\phi_{st}+\psi_{a1}}^{\phi_{ex}} \left( \int_0^r \left( \sin(Kz) \cdot \sin 2 \left( \phi_j - \frac{\tan\beta}{R} z \right) \right) dz \right) d\phi + \right. \\ \left. + \int_{\phi_{ex}}^{\phi_{ex}+\psi_{a1}} \left( \int_{\frac{R}{\tan\beta}(\phi_j-\phi_{ex})}^r \left( \sin(Kz) \cdot \sin 2 \left( \phi_j - \frac{\tan\beta}{R} z \right) \right) dz \right) d\phi \right], \quad (34)$$

$$C_{10} = -\frac{N_f}{2\pi} \left[ \int_{\phi_{st}}^{\phi_{st}+\psi_{a1}} \left( \int_0^{\frac{R}{\tan\beta}(\phi_j-\phi_{st})} \left( \sin(Kz) \cdot \cos \left( \phi_j - \frac{\tan\beta}{R} z \right) \cdot M \right) dz \right) d\phi + \right. \\ \left. + \int_{\phi_{st}+\psi_{a1}}^{\phi_{ex}} \left( \int_0^r \left( \sin(Kz) \cdot \cos \left( \phi_j - \frac{\tan\beta}{R} z \right) \cdot M \right) dz \right) d\phi + \right. \\ \left. + \int_{\phi_{ex}}^{\phi_{ex}+\psi_{a1}} \left( \int_{\frac{R}{\tan\beta}(\phi_j-\phi_{ex})}^r \left( \sin(Kz) \cdot \cos \left( \phi_j - \frac{\tan\beta}{R} z \right) \cdot M \right) dz \right) d\phi \right], \quad (35)$$

$$C_{11} = -\frac{N_f}{4\pi} \left[ \int_{\phi_{st}}^{\phi_{st}+\psi_{a1}} \left( \int_0^{\frac{R}{\tan\beta}(\phi_j-\phi_{st})} \left( \cos(Kz) \cdot \sin 2 \left( \phi_j - \frac{\tan\beta}{R} z \right) \right) dz \right) d\phi + \right. \\ \left. + \int_{\phi_{st}+\psi_{a1}}^{\phi_{ex}} \left( \int_0^r \left( \cos(Kz) \cdot \sin 2 \left( \phi_j - \frac{\tan\beta}{R} z \right) \right) dz \right) d\phi + \right. \\ \left. + \int_{\phi_{ex}}^{\phi_{ex}+\psi_{a1}} \left( \int_{\frac{R}{\tan\beta}(\phi_j-\phi_{ex})}^r \left( \cos(Kz) \cdot \sin 2 \left( \phi_j - \frac{\tan\beta}{R} z \right) \right) dz \right) d\phi \right], \quad (36)$$

$$C_{12} = -\frac{N_f}{2\pi} \left[ \int_{\phi_{st}}^{\phi_{st}+\psi_{a1}} \left( \int_0^{\frac{R}{\tan\beta}(\phi_j-\phi_{st})} \left( \cos(Kz) \cdot \cos \left( \phi_j - \frac{\tan\beta}{R} z \right) \cdot M \right) dz \right) d\phi + \right. \\ \left. + \int_{\phi_{st}+\psi_{a1}}^{\phi_{ex}} \left( \int_0^r \left( \cos(Kz) \cdot \cos \left( \phi_j - \frac{\tan\beta}{R} z \right) \cdot M \right) dz \right) d\phi + \right. \\ \left. + \int_{\phi_{ex}}^{\phi_{ex}+\psi_{a1}} \left( \int_{\frac{R}{\tan\beta}(\phi_j-\phi_{ex})}^r \left( \cos(Kz) \cdot \cos \left( \phi_j - \frac{\tan\beta}{R} z \right) \cdot M \right) dz \right) d\phi \right], \quad (37)$$

$$C_{13} = \frac{N_f}{2\pi} \left[ \int_{\phi_{st}}^{\phi_{st}+\psi_{a1}} \left( \int_0^{\frac{R}{\tan\beta}(\phi_j-\phi_{st})} \left( \cos(Kz) \cdot \sin \left( \phi_j - \frac{\tan\beta}{R} z \right) \right) dz \right) d\phi + \right. \\ \left. + \int_{\phi_{st}+\psi_{a1}}^{\phi_{ex}} \left( \int_0^r \left( \cos(Kz) \cdot \sin \left( \phi_j - \frac{\tan\beta}{R} z \right) \right) dz \right) d\phi + \right. \\ \left. + \int_{\phi_{ex}}^{\phi_{ex}+\psi_{a1}} \left( \int_{\frac{R}{\tan\beta}(\phi_j-\phi_{ex})}^r \left( \cos(Kz) \cdot \sin \left( \phi_j - \frac{\tan\beta}{R} z \right) \right) dz \right) d\phi \right], \quad (38)$$

$$C_{14} = \frac{N_f}{2\pi} \left[ \int_{\phi_{st}}^{\phi_{st}+\psi_{a1}} \left( \int_0^{\frac{R}{\tan\beta}(\phi_j-\phi_{st})} \left( \cos(Kz) \cdot M \right) dz \right) d\phi + \right. \\ \left. + \int_{\phi_{st}+\psi_{a1}}^{\phi_{ex}} \left( \int_0^r \left( \cos(Kz) \cdot M \right) dz \right) d\phi + \right. \\ \left. + \int_{\phi_{ex}}^{\phi_{ex}+\psi_{a1}} \left( \int_0^r \left( \cos(Kz) \cdot M \right) dz \right) d\phi \right], \quad (39)$$

$$C_{15} = -\frac{N_f}{2\pi} \left[ \int_{\phi_{st}}^{\phi_{st}+\psi_{a1}} \left( \int_0^R \frac{R}{\tan\beta} (\phi_j - \phi_{st}) \left( \sin(Kz) \cdot \sin\left(\phi_j - \frac{\tan\beta}{R} z\right) \right) dz \right) d\phi + \right. \\ \left. + \int_{\phi_{ex}}^{\phi_{ex}+\psi_{a1}} \left( \int_0^r \sin(Kz) \cdot \sin\left(\phi_j - \frac{\tan\beta}{R} z\right) \right) dz \right) d\phi + \\ \left. + \int_{\phi_{ex}}^{\phi_{ex}+\psi_{a1}} \left( \int_{\frac{R}{\tan\beta}(\phi_j - \phi_{ex})}^r \left( \sin(Kz) \cdot \sin\left(\phi_j - \frac{\tan\beta}{R} z\right) \right) dz \right) d\phi \right], \quad (40)$$

$$C_{16} = -\frac{N_f}{2\pi} \left[ \int_{\phi_{st}}^{\phi_{st}+\psi_{a1}} \left( \int_0^R \frac{R}{\tan\beta} (\phi_j - \phi_{st}) \left( \int_0^{\frac{R}{\tan\beta}(\phi_j - \phi_{st})} \sin(Kz) \cdot M dz \right) \right) d\phi + \right. \\ \left. + \int_{\phi_{ex}}^{\phi_{ex}+\psi_{a1}} \left( \int_0^r \sin(Kz) \cdot M dz \right) d\phi + \right. \\ \left. + \int_{\phi_{ex}}^{\phi_{ex}+\psi_{a1}} \left( \int_{\frac{R}{\tan\beta}(\phi_j - \phi_{ex})}^r \sin(Kz) \cdot M dz \right) d\phi \right], \quad (41)$$

$$C_{17} = -\frac{N_f}{4\pi} \left[ \int_{\phi_{st}}^{\phi_{st}+\psi_{a2}} \left( \int_r^{\frac{R}{\tan(\beta)}(\phi_j - \phi_{ex})} \sin 2\left(\phi_j - \frac{2\tan\beta}{D} z\right) dz \right) d\phi + \right. \\ \left. + \int_{\phi_{st}}^{\phi_{st}+\psi_{a1}} \left( \int_r^a \sin 2\left(\phi_j - \frac{2\tan\beta}{D} z\right) dz \right) d\phi + \right. \\ \left. + \int_{\phi_{ex}}^{\phi_{ex}+\psi_{a2}} \left( \int_{\frac{R}{\tan(\beta)}(\phi_j - \phi_{ex})}^a \sin 2\left(\phi_j - \frac{2\tan\beta}{D} z\right) dz \right) d\phi \right], \quad (42)$$

$$C_{18} = -\frac{N_f}{4\pi} \left[ \int_{\phi_{st}}^{\phi_{st}+\psi_{a2}} \left( \int_r^{\frac{R}{\tan(\beta)}(\phi_j - \phi_{ex})} \left( 1 - \cos 2\left(\phi_j - \frac{2\tan\beta}{D} z\right) \right) dz \right) d\phi + \right. \\ \left. + \int_{\phi_{st}}^{\phi_{st}+\psi_{a1}} \left( \int_r^a \left( 1 - \cos 2\left(\phi_j - \frac{2\tan\beta}{D} z\right) \right) dz \right) d\phi + \right. \\ \left. + \int_{\phi_{ex}}^{\phi_{ex}+\psi_{a2}} \left( \int_{\frac{R}{\tan(\beta)}(\phi_j - \phi_{ex})}^a \left( 1 - \cos 2\left(\phi_j - \frac{2\tan\beta}{D} z\right) \right) dz \right) d\phi \right], \quad (43)$$

$$C_{19} = -\frac{N_f}{2\pi} \left[ \int_{\phi_{st}}^{\phi_{st}+\psi_{a2}} \left( \int_r^{\frac{R}{\tan(\beta)}(\phi_j - \phi_{ex})} \cos\left(\phi_j - \frac{2\tan\beta}{D} z\right) dz \right) d\phi + \right. \\ \left. + \int_{\phi_{st}}^{\phi_{st}+\psi_{a1}} \left( \int_r^a \cos\left(\phi_j - \frac{2\tan\beta}{D} z\right) dz \right) d\phi + \right. \\ \left. + \int_{\phi_{ex}}^{\phi_{ex}+\psi_{a2}} \left( \int_{\frac{R}{\tan(\beta)}(\phi_j - \phi_{ex})}^a \cos\left(\phi_j - \frac{2\tan\beta}{D} z\right) dz \right) d\phi \right], \quad (44)$$

$$C_{20} = -\frac{N_f}{2\pi} \left[ \int_{\phi_{st}}^{\phi_{st}+\psi_{a2}} \left( \int_r^{\frac{R}{\tan(\beta)}(\phi_j - \phi_{ex})} \sin\left(\phi_j - \frac{2\tan\beta}{D} z\right) dz \right) d\phi + \right. \\ \left. + \int_{\phi_{st}}^{\phi_{st}+\psi_{a1}} \left( \int_r^a \sin\left(\phi_j - \frac{2\tan\beta}{D} z\right) dz \right) d\phi + \right. \\ \left. + \int_{\phi_{ex}}^{\phi_{ex}+\psi_{a2}} \left( \int_{\frac{R}{\tan(\beta)}(\phi_j - \phi_{ex})}^a \sin\left(\phi_j - \frac{2\tan\beta}{D} z\right) dz \right) d\phi \right], \quad (45)$$



and

$$C_{21} = -\frac{N_f}{2\pi} \left[ \int_{\phi_{st}+\psi_{a1}}^{\phi_{st}+\psi_{a2}} \left( \int_r^D \frac{D}{\tan(\beta)} (\phi_j - \phi_{st}) (dz) \right) d\phi + \right. \\ \left. + \int_{\phi_{ex}+\psi_{a2}}^{\phi_{ex}+\psi_{a1}} \left( \int_r^a dz \right) d\phi + \int_{\phi_{ex}+a1}^{\phi_{ex}+a2} \left( \int_r^D \frac{D}{\tan(\beta)} (\phi_j - \phi_{st}) dz \right) d\phi \right]. \quad (46)$$

Then, the average cutting forces in part (1) and part (2) of the cutting edge were calculated by (47) and (48):

$$\begin{cases} \bar{F}_{f1} = (C_1 K_{tc} + C_3 K_{rc} + C_5 K_{ac}) f_t + C_2 K_{te} + C_4 K_{re} + C_6 K_{ae}; \\ \bar{F}_{n1} = (C_7 K_{tc} + C_9 K_{rc} + C_{11} K_{ac}) f_t + C_8 K_{te} + C_{10} K_{re} + C_{12} K_{ae}; \\ \bar{F}_{a1} = (C_{13} K_{rc} + C_{15} K_{ac}) f_t + C_{14} K_{re} + C_{16} K_{ae}, \end{cases} \quad (47)$$

$$\begin{cases} \bar{F}_{f2} = (C_{17} K_{tc} + C_{18} K_{rc}) f_t + C_{19} K_{te} + C_{20} K_{re}; \\ \bar{F}_{n2} = (-C_{18} K_{tc} + C_{17} K_{rc}) f_t - C_{20} K_{te} + C_{19} K_{re}; \\ \bar{F}_{a2} = -C_{20} K_{ac} f_t + C_{21} K_{ae}. \end{cases} \quad (48)$$

So, the average cutting forces in the entire of one cutting edge were calculated by (49):

$$\begin{cases} \bar{F}_f = ((C_1 + C_{17}) K_{tc} + (C_3 + C_{18}) K_{rc} + C_5 K_{ac}) f_t + (C_2 + C_{19}) K_{te} + (C_4 + C_{20}) K_{re} + C_6 K_{ae}; \\ \bar{F}_n = ((C_7 - C_{18}) K_{tc} + (C_9 + C_{17}) K_{rc} + C_{11} K_{ac}) f_t + (C_8 - C_{20}) K_{te} + (C_{10} + C_{19}) K_{re} + C_{12} K_{ae}; \\ \bar{F}_a = (C_{13} K_{rc} + (C_{15} - C_{20}) K_{ac}) f_t + C_{14} K_{re} + (C_{16} + C_{21}) K_{ae}. \end{cases} \quad (49)$$

Besides, the average cutting forces can be regressed by the linear functions of feed per flute as by (50):

$$\begin{cases} \bar{F}_f = \bar{F}_{fc} \cdot f_t + \bar{F}_{fe}; \\ \bar{F}_n = \bar{F}_{nc} \cdot f_t + \bar{F}_{ne}; \\ \bar{F}_a = \bar{F}_{ac} \cdot f_t + \bar{F}_{ae}, \end{cases} \quad (50)$$

where  $\bar{F}_{fc}$ ,  $\bar{F}_{fe}$ ,  $\bar{F}_{nc}$ ,  $\bar{F}_{ne}$ ,  $\bar{F}_{ac}$ ,  $\bar{F}_{ae}$  are the linear regression constants that were determined by analyzing relationship of the experimental data of average cutting forces and feed per flute. From the (49) and (50), the relationship of the linear regression constants ( $\bar{F}_{fc}$ ,  $\bar{F}_{fe}$ ,  $\bar{F}_{nc}$ ,  $\bar{F}_{ne}$ ,  $\bar{F}_{ac}$ ,  $\bar{F}_{ae}$ ), the setting constants ( $C_i$ ), and the cutting force coefficients were presented by (51):

$$\begin{cases} \bar{F}_{fc} = ((C_1 + C_{17}) K_{tc} + (C_3 + C_{18}) K_{rc} + C_5 K_{ac}); \\ \bar{F}_{fe} = (C_2 + C_{19}) K_{te} + (C_4 + C_{20}) K_{re} + C_6 K_{ae}; \\ \bar{F}_{nc} = ((C_7 - C_{18}) K_{tc} + (C_9 + C_{17}) K_{rc} + C_{11} K_{ac}); \\ \bar{F}_{ne} = (C_8 + C_{20}) K_{te} + (C_{10} + C_{19}) K_{re} + C_{12} K_{ae}; \\ \bar{F}_{ac} = (C_{13} K_{rc} + (C_{15} - C_{20}) K_{ac}); \\ \bar{F}_{ae} = C_{14} K_{re} + (C_{16} + C_{21}) K_{ae}. \end{cases} \quad (51)$$

Finally, the cutting force coefficients were calculated by (52):

$$\left\{ \begin{aligned} k_{ac} &= \frac{\bar{F}_{ac} \left( \frac{(C_3 + C_{18})(C_7 - C_{18})(C_{15} - C_{20})}{-(C_1 + C_{17})(C_9 + C_{17})(C_{15} - C_{20})} \right) - (C_7 - C_{18})C_{13}(C_{15} - C_{20})\bar{F}_{fc} + (C_1 + C_{17})C_{13}(C_{15} - C_{20})\bar{F}_{nc}}{(C_3 + C_{18})(C_7 - C_{18})(C_{15} - C_{20})^2 - C_5(C_7 - C_{18})C_{13}(C_{15} - C_{20}) - (C_1 + C_{17})(C_9 + C_{17})(C_{15} - C_{20})^2 + (C_1 + C_{17})C_{11}C_{13}(C_{15} - C_{20})}; \\ k_{ae} &= \frac{\bar{F}_{ae} \left( \frac{(C_4 + C_{20})(C_8 + C_{20})(C_{16} + C_{21})}{-(C_2 + C_{19})(C_{10} + C_{19})(C_{16} + C_{21})} \right) - (C_8 + C_{20})C_{14}(C_{16} + C_{21})\bar{F}_{fe} + (C_2 + C_{19})C_{14}(C_{16} + C_{21})\bar{F}_{ne}}{(C_4 + C_{20})(C_8 + C_{20})(C_{16} + C_{21})^2 - C_6(C_8 + C_{20})C_{14}(C_{16} + C_{21}) - (C_2 + C_{19})(C_{10} + C_{19})(C_{16} + C_{21})^2 + (C_2 + C_{19})C_{12}C_{14}(C_{16} + C_{21})}; \\ k_{rc} &= \frac{\bar{F}_{ac} \left( \frac{(C_1 + C_{17})C_{11}}{-C_5(C_7 - C_{18})} \right) + (C_7 - C_{18})C_{15}\bar{F}_{fc} - (C_1 + C_{17})(C_{15} - C_{20})\bar{F}_{nc}}{(C_3 + C_{18})C_7(C_{15} - C_{20}) - C_5(C_7 - C_{18})C_{13} - (C_1 + C_{17})(C_9 + C_{17})(C_{15} - C_{20}) + (C_1 + C_{17})C_{11}C_{13}}; \\ k_{re} &= \frac{\bar{F}_{ae} \left( \frac{(C_2 + C_{19})C_{12}}{-C_6(C_8 + C_{20})} \right) + (C_8 + C_{20})(C_{16} + C_{21})\bar{F}_{fe} - (C_2 + C_{19})(C_{16} + C_{21})\bar{F}_{ne}}{(C_4 + C_{20})(C_8 + C_{20})(C_{16} + C_{21}) - C_6(C_8 + C_{20})C_{14} - (C_2 + C_{19})(C_{10} + C_{19})(C_{16} + C_{21}) + (C_2 + C_{19})C_{12}C_{14}}; \\ k_{fc} &= \frac{\bar{F}_{fc} - (C_3 + C_{18})\bar{F}_{rc} - C_5\bar{F}_{ac}}{(C_1 + C_{17})}; \\ k_{fe} &= \frac{\bar{F}_{fe} - (C_3 + C_{18})\bar{F}_{re} - C_6\bar{F}_{ae}}{(C_2 + C_{19})}. \end{aligned} \right. \quad (52)$$

The experimental process was performed to verify the relationship of average cutting force and feed per flute as presented by (50), to determine the cutting force coefficients as presented by (52), and to verify the cutting force models in face milling process as presented by (21) and (22). The cutting tests were performed in face milling processes of C45 steel using the cutter with parallelogram insert. The compositions of C45 steel are listed in **Table 1**.

**Table 1**

Chemical compositions of C45 Steel

Elements	C	Si	Mn	Cr	Ni	Mo	V	Ti	B	Cu
Composite (%)	0.44	0.23	0.65	0.15	0.15	0.04	0.01	0.001	0.0004	0.21

The main mechanical and physical properties of C45 steel are presented in **Table 2**. The workpiece dimensions (length × width × height) were 45 × 45 × 45 mm as shown in **Fig. 6**.

**Table 2**

Mechanical and Physical properties of C45 Steel

Properties	Elastic modulus	Poisson's ratio	Shear modulus	Density	Hardness
Unit	GPa	—	Gpa	kg/m <sup>3</sup>	HRC
Value	200	0.3	80	7800	23

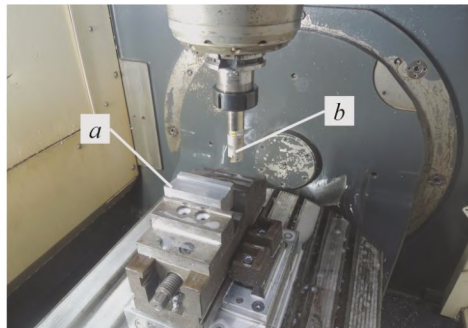


**Fig. 6.** Experimental workpiece and cutter insert: *a* – Workpiece; *b* – Cutter insert

A series of face milling experiments were performed. The cutter was chosen as follows: Face milling cutter with diameter  $D = 20$  mm. The parallelogram cutter insert (R390-11 T3 08M-PM 1025)



was using with helix angle  $\beta = 30^\circ$ , rake angle  $\alpha_r = 5^\circ$ , and insert nose radius  $r = 0.4$  mm as shown in **Fig. 6**. The number of insert  $N_f$  was 1 insert.

Milling machine was used for experimental method was five-axis CNC machine center (Model: DMU 50 ECOLINE) with SINUMERIK S840DSB control system as shown in **Fig. 7**. This CNC machine has the specifications as follow:  $X/Y/Z$  axis stroke: 500/450/400 mm,  $X/Y/Z$  axis rapid: 30/30/30 m/min, and the maximum spindle speed: 14000 rpm.

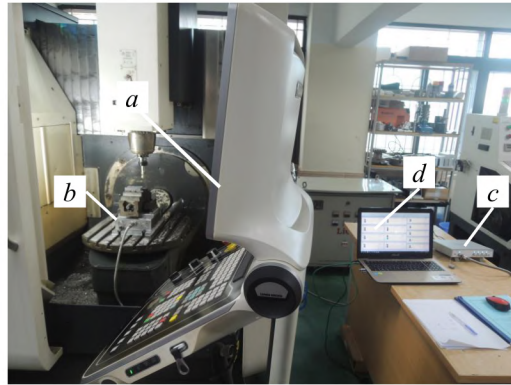


**Fig. 7.** CNC machine and cutting force measurement system:  
 $a$  – CNC machine;  $b$  – Dynamometer;  $c$  – Processing System;  $d$  – Software and PC

A dynamometer system was used to measure the cutting forces in experimental work. The KISTLER dynamometer system with dynamometer: Type 9139AA and the auxiliary equipments. The detail of this system is illustrated in **Fig. 7**. In the setting process, the dynamometer was fixed on the table of CNC machine. The dynamometer was connected to the computer through the processing system that including the data processing box (3160-B-042) and the multi-channel charge amplifier by using connecting cable. The DynoWare software was used to store and analyze the experimental data of cutting forces.

The cutting tests include two sets as listed in **Table 3**. Set 1 was performed to verify the relationship of the average cutting force and feed per flute and determine the cutting force coefficients. In these cases, the cutting tests were carried out in slot milling (facing). The cutting conditions were selected at the stable cutting conditions with small of cutting depth and small of spindle speed to decrease the influence of chatter and vibrations [9, 14].

**Table 3**  
Experimental plan

Run. No	$a$ (mm)	$b$ (mm)	$f_t$ (mm/flute)	$n$ (rpm)
<b>Set 1: Verification of average force model and determination of cutting force coefficients</b>				
1	0.5	20	0.1	750
2	0.5	20	0.15	750
3	0.5	20	0.2	750
4	0.5	20	0.25	750
5	0.5	20	0.3	750
<b>Set 2: Verification of dynamic cutting force model</b>				
6	0.2	20	0.4	1000
7	0.6	20	0.5	850

At the constant depth of cut and constant spindle speed, the cutting tests were repeated with variations of feed per flute. Set 2 was performed to verify the cutting force models. In these cases, the cutting tests were selected with different cutting conditions. The cutting parameters of all cutting tests were listed in **Table 3**.

### 3. Results and Discussions

#### 3. 1. Verification of Average Cutting Force Model and Determination of Cutting Force Coefficients in Face Milling Process

The cutting tests were performed at stable cutting conditions with small of cutting depth and small of spindle speed (set 1) as listed in **Table 3**. For each experiment, the average cutting force in feed, normal, and axial directions were calculated from the measured data of cutting forces. The relationship of the average cutting force and the feed per flute was estimated and illustrated in **Fig. 8**. In this figure, all the absolute values of average cutting forces increase with the increasing of feed per flute. This obtained result was quite the same with the results when using the flat-end mill as presented in reference [9] and when milling using ball-end mill tool as presented in reference [10].

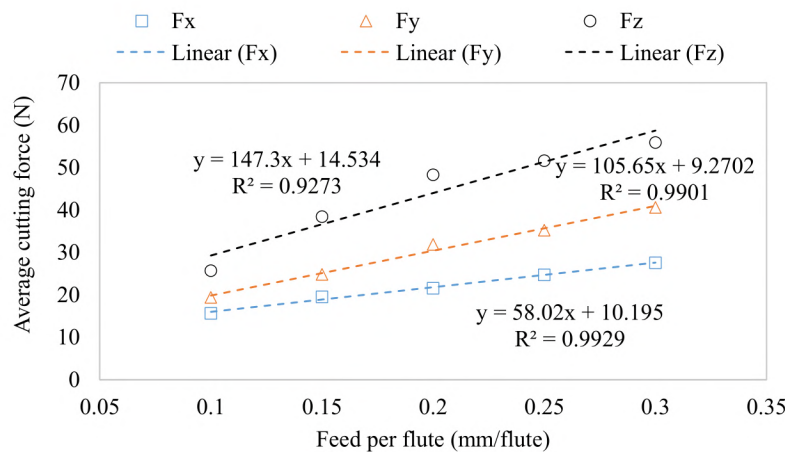


**Fig. 8.** Relationship of average cutting forces and feed per flute

The verified results show that the theoretical and experimental results have a good agreement. So, in face milling process using parallelogram cutter insert, the relationship of average cutting forces and feed per flute can be expressed as a linear function. In this study, the measured average cutting force can be expressed by the linear function of feed per flute with the large determination coefficients  $R^2$  (from 92.73 % to 99.29 %) as shown in **Fig. 8**. So, the average cutting force models were successfully verified by the analyzed of the relationship of average cutting forces and feed per flute. The analyzed result again proves that in face milling processes, the average cutting force can be modeled as a linear function of feed per flute not only with a specific pair of cutting tool and workpiece as mentioned in some previous studies [10, 14] but also different pairs of cutting tool and workpiece. Applying (52), the measured average cutting forces were used to determine all six cutting force coefficients as listed in **Table 4**.

**Table 4**

Calculated values of the cutting force coefficients

Shearing force coefficient (N/mm <sup>2</sup> )	Edge force coefficient (N/mm)
$K_{tc} = 1592.8$	$K_{te} = 1.2028$
$K_{rc} = 859.9$	$K_{re} = 12.8051$
$K_{ac} = -1855.2$	$K_{ae} = -37.4348$

The obtained results from **Table 4** showed that the absolute values of shear force coefficients ( $K_{tc}$ ,  $K_{rc}$ ,  $K_{ac}$ ) are often much larger than those ones of edge force coefficients ( $K_{te}$ ,  $K_{re}$ ,  $K_{ae}$ ). So, by analyzing the average cutting force data and the relationship of average cutting forces and feed per flute, all six cutting force coefficient components can be determined in face milling processes.



### 3.2. Verification of the proposed cutting force models in face milling process using parallelogram cutter insert

Using the obtained cutting force coefficient as stored in **Table 4**, the cutting forces were predicted and compared with the measured cutting forces. The predicted cutting forces and measured cutting forces were compared and shown from **Fig. 9** to **Fig. 11** for different cutting parameters (set 1 and set 2). The results from these figures showed that, for different cutting parameters, the predicted cutting forces were quite close to the measured cutting forces both the shape and the amplitude values. In the verifying cutting tests, exiting some different points between predicted cutting forces and measured forces (highlighted by circle and error in **Fig. 9** to **Fig. 11**).

**Fig. 9** showed the compared results of predicted and measured cutting force for normal cutting condition (medium depth of cut: 0.5 mm, medium feed per flute: 0.1 mm/flute, medium small spindle speed: 750 rpm), therefore, the predicted cutting forces were very close to the measured cutting forces. This issue can be explained that with the normal cutting condition and with small spindle speed, the vibrations were quite mall, then the influence of vibrations on the cutting forces are also small, so the predicted cutting forces were very close to the measured cutting forces.

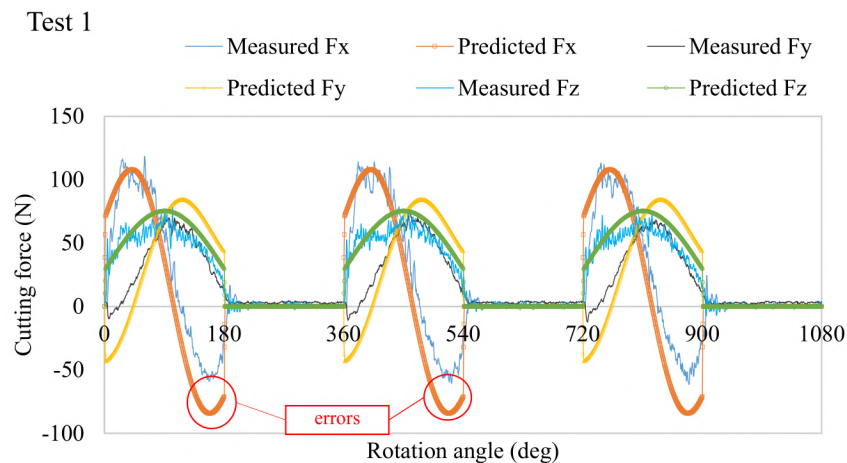


**Fig. 9.** Comparison of predicted and measured cutting forces of Test 1

These evaluated results of cutting forces were the same the results in **Fig. 11** (test 7). Despite the large feed per flute, the depth of cut is a medium value, and the spindle speed is a small value, so this cutting condition is the normal cutting conditions. Therefore, the influence of vibrations on cutting forces was quite small, and so the difference of predicted and measured cutting forces was quite small.

**Fig. 10** showed the compared results of predicted and measured cutting force for small depth of cut (0.5 mm), large feed per flute (0.5 mm/flute), and larger spindle speed (750 rpm), the predicted cutting forces were more different to the measured cutting forces. This issue can be explained that with the larger spindle speed, the vibrations were bigger, then the influence of vibrations on the cutting forces was also larger, so the predicted cutting forces were different to the measured cutting forces.

Although there are still differences between the predicted and measured cutting forces, in general, these differences are quite small. Therefore, the predicted results from research model agree satisfactorily with experimental results. So, from all above analyzed results, the cutting force models and cutting force coefficient models in this study can be used to determine the cutting force coefficients and predict the cutting force in face milling process using parallelogram cutter insert.

The reasons for the above differences can be from the vibrations, the chatter, the cutter run-out, the deflection, the inconstancy of cutting depth, the unstable of workpiece hardness, the temperature, the friction, and so on. Although, the effect of factors (vibration, noise, temperature, etc.) is limited in the experiments, but in fact, this effect still exists in the experiment processes. Integration of other parameters such as vibrations, cutter run-out, deflection, temperature, etc into cutting force models will be the research direction in the future to overcome the limitations of this study.

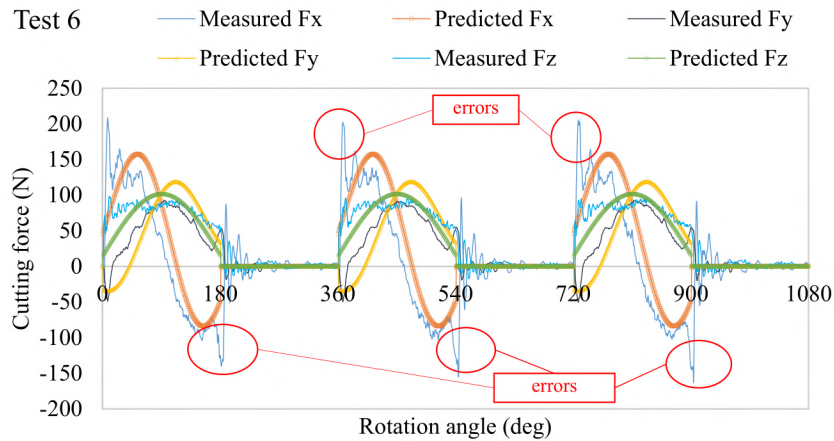


**Fig. 10.** Comparison of predicted and measured cutting forces of Test 6

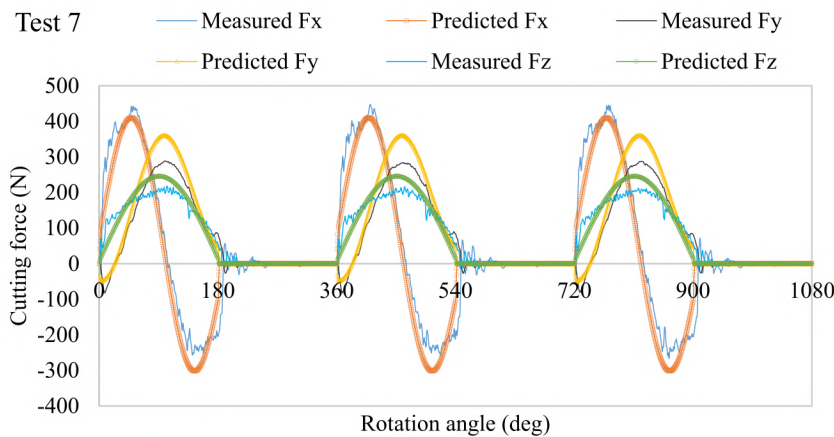


**Fig. 11.** Comparison of predicted and measured cutting forces of Test 7

#### 4. Conclusions

By analyzing the theoretical face milling process using a parallelogram cutter insert, the average cutting forces can be modeled as the linear function of feed per flute.

By the experimental method, the average cutting forces in three directions ( $x$ ,  $y$ ,  $z$ ) can also be modeled as the linear function of feed per flute with the large determination coefficients  $R^2$  (from 92.73 % to 99.29 %). The average cutting force models were successfully verified by the analysis of the relationship of average cutting forces and feed per flute.

By analyzing the average cutting force data and the relationship of average cutting forces and feed for flute. Which, the absolute values of shear force coefficients ( $K_{tc}$ ,  $K_{rc}$ ,  $K_{ac}$ ) are often much larger than those ones of edge force coefficients ( $K_{te}$ ,  $K_{re}$ ,  $K_{ae}$ ).

The predicted results from the research model agree satisfactorily with experimental results. So, from all the above-analyzed results, the cutting force models and cutting force coefficient models in this study can be used to determine the cutting force coefficients and predict the cutting force in the face milling process using a parallelogram cutter insert.

The reasons for the differences between predicted and measured cutting forces can be from the vibrations, the chatter, the cutter run-out, the deflection, the inconstancy of cutting depth, the unstable workpiece hardness, the temperature, the friction, and so on. Investigation of these parameters on the cutting forces and values of cutting force coefficients will be the next research directions of this study.

#### Acknowledgements

The authors appreciate the support from the research project 02-2020-RD/HĐ-ĐHCN. Thanks also extend to the support from the Faculty of Mechanical Engineering, Hanoi University of Industry, Vietnam.



---

**References**

- [1] Hoang, D. T., Nguyen, N.-T., Tran, Q. D., Nguyen, T. V. (2019). Cutting Forces and Surface Roughness in Face-Milling of SKD61 Hard Steel. *Strojniški Vestnik – Journal of Mechanical Engineering*, 65 (6), 375–385. doi: <https://doi.org/10.5545/sv-jme.2019.6057>
- [2] Salguero, J., Batista, M., Calamaz, M., Girot, F., Marcos, M. (2013). Cutting Forces Parametric Model for the Dry High Speed Contour Milling of Aerospace Aluminium Alloys. *Procedia Engineering*, 63, 735–742. doi: <https://doi.org/10.1016/j.proeng.2013.08.215>
- [3] Irgolic, T., Cus, F., Paulic, M., Balic, J. (2014). Prediction of Cutting Forces with Neural Network by Milling Functionally Graded Material. *Procedia Engineering*, 69, 804–813. doi: <https://doi.org/10.1016/j.proeng.2014.03.057>
- [4] Budak, E. (2006). Analytical models for high performance milling. Part I: Cutting forces, structural deformations and tolerance integrity. *International Journal of Machine Tools and Manufacture*, 46 (12-13), 1478–1488. doi: <https://doi.org/10.1016/j.ijmachtools.2005.09.009>
- [5] Wan, M., Lu, M.-S., Zhang, W.-H., Yang, Y. (2012). A new ternary-mechanism model for the prediction of cutting forces in flat end milling. *International Journal of Machine Tools and Manufacture*, 57, 34–45. doi: <https://doi.org/10.1016/j.ijmachtools.2012.02.003>
- [6] Perez, H., Diez, E., Marquez, J. J., Vizan, A. (2013). An enhanced method for cutting force estimation in peripheral milling. *The International Journal of Advanced Manufacturing Technology*, 69 (5-8), 1731–1741. doi: <https://doi.org/10.1007/s00170-013-5153-0>
- [7] Wang, B., Hao, H., Wang, M., Hou, J., Feng, Y. (2013). Identification of instantaneous cutting force coefficients using surface error. *The International Journal of Advanced Manufacturing Technology*, 68 (1-4), 701–709. doi: <https://doi.org/10.1007/s00170-013-4792-5>
- [8] Wang, M., Gao, L., Zheng, Y. (2014). An examination of the fundamental mechanics of cutting force coefficients. *International Journal of Machine Tools and Manufacture*, 78, 1–7. doi: <https://doi.org/10.1016/j.ijmachtools.2013.10.008>
- [9] Kao, Y.-C., Nguyen, N.-T., Chen, M.-S., Su, S.-T. (2014). A prediction method of cutting force coefficients with helix angle of flat-end cutter and its application in a virtual three-axis milling simulation system. *The International Journal of Advanced Manufacturing Technology*, 77 (9-12), 1793–1809. doi: <https://doi.org/10.1007/s00170-014-6550-8>
- [10] Kao, Y.-C., Nguyen, N.-T., Chen, M.-S., Huang, S.-C. (2015). A combination method of the theory and experiment in determination of cutting force coefficients in ball-end mill processes. *Journal of Computational Design and Engineering*, 2 (4), 233–247. doi: <https://doi.org/10.1016/j.jcde.2015.06.005>
- [11] Gao, G., Wu, B., Zhang, D., Luo, M. (2013). Mechanistic identification of cutting force coefficients in bull-nose milling process. *Chinese Journal of Aeronautics*, 26 (3), 823–830. doi: <https://doi.org/10.1016/j.cja.2013.04.007>
- [12] Euan, I. G., Ozturk, E., Sims, N. D. (2013). Modeling Static and Dynamic Cutting Forces and Vibrations for Inserted Ceramic Milling Tools. *Procedia CIRP*, 8, 564–569. doi: <https://doi.org/10.1016/j.procir.2013.06.151>
- [13] Engin, S., Altintas, Y. (2001). Mechanics and dynamics of general milling cutters.: Part II: inserted cutters. *International Journal of Machine Tools and Manufacture*, 41 (15), 2213–2231, doi: [https://doi.org/10.1016/s0890-6955\(01\)00046-3](https://doi.org/10.1016/s0890-6955(01)00046-3)
- [14] Agarwal, A., Desai, K. A. (2020). Importance of bottom and flank edges in force models for flat-end milling operation. *The International Journal of Advanced Manufacturing Technology*, 107 (3-4), 1437–1449. doi: <https://doi.org/10.1007/s00170-020-05111-5>

Received date 16.06.2021

Accepted date 08.08.2021

Published date 13.09.2021

© The Author(s) 2021

This is an open access article  
under the Creative Commons CC BY license

**How to cite:** Nguyen, N.-T. (2021). A development method of cutting force coefficients in face milling process using parallelogram insert. *EUREKA: Physics and Engineering*, 5, 36–52. doi: <https://doi.org/10.21303/2461-4262.2021.001890>

# MODELING OF NATURAL CONVECTION OF A CONCENTRATED SOLAR POWER RECEIVER ABSORBER TUBE IN INTERACTION WITH NEIGHBOURING ABSORBERS

**Olanrewaju Miracle Oyewola** ✉

*School of Mechanical Engineering*

*Fiji National University*

*Suva, Fiji*

*Department of Mechanical Engineering<sup>1</sup>*

*oooyewola001@gmail.com, olanrewaju.oyewola@fnu.ac.fj*

**Niyi Ezekiel Olukayode**

*Department of Mechanical Engineering*

*Ekiti State University*

*Ado-Ekiti, Nigeria, 362103*

**Olusegun Olufemi Ajide**

*Department of Mechanical Engineering*

*University of Ibadan*

*Oduduwa Road, Ibadan, Nigeria, 200132*

<sup>1</sup>*University of Ibadan*

*Oduduwa Road, Ibadan, Nigeria, 200132*

✉ Corresponding author

## Abstract

Concentrated Solar Power (CSP) technology stands out among other renewable energy sources not only because of its ability to address current energy security and environmental challenges but because its energy can be stored for future use. To ensure optimum performance in this system, the heat losses need to be evaluated for better design.

This work studies the natural convection in the receiver absorber tube of a CSP plant taking into consideration the influence of neighboring absorbers. A 2-Dimensional model was adopted in this study. Initially, a single absorber tube was considered, it was subjected to heat flux at the top wall, the bottom wall was insulated and a temperature differential was set up at the lateral walls. The dimensionless forms of Navier-Stokes and energy equations were solved using the finite element formulation of COMSOL Multiphysics software. The result obtained for a single absorber tube showed good agreement with existing research works. This validated model was then extended to multiple absorber tubes (two to six absorber tubes). On the basis of the study, there is an observed increase in the intensity and dominance of convective heat transfer with an increase in the number of absorber tubes. This is occasioned by an increase in the average surface temperature as well as average Nusselt number. For the Rayleigh number of  $10^4$ ,  $10^5$  and  $10^6$ , the average Nusselt number increases with the number of absorber tubes by 13.87 %, 6.26 %, and 1.55 %, respectively. This increment suggests effect of thermal interactions among the neighboring absorber tubes.

**Keywords:** Concentrated Solar Power, Receiver Absorber Tubes, Natural convection, Dimensionless Parameters.

DOI: 10.21303/2461-4262.2021.001871

## 1. Introduction

The current global energy security and environmental challenges have shifted the world's focus into replacing fossil fuels with renewable energy sources. The use of Concentrated Solar Power (CSP) stands out among other renewable energy sources not only because it is environmentally benign or cost-effective but also because its energy can be harnessed and saved for future use.

**Nomenclature Symbols:**  $g$  – acceleration due to gravity,  $m/s^2$ ;  $\theta$  – Dimensionless Temperature;  $Nu(X)$  – Local Nusselt number;  $\mu$  – Dynamic viscosity;  $Nu_{avg}$  – Average Nusselt number;  $\beta$  – Coefficient of volumetric expansion;  $P$  – pressure, Pa;  $\rho$  – Density of the heat transfer fluid,  $kg/m^3$ ;



Pr – Prandtl number;  $\alpha$  – Thermal diffusivity;  $q''$  – heat flux, W/m<sup>2</sup>;  $\nu$  – Kinematic viscosity; Ra – Rayleigh Number; T – Dimensional temperature, K.

**Subscripts:**  $T_h$  – Temperature of hot wall;  $K_{avg}$  – average;  $T_c$  – Temperature of cold wall;  $h$  – hot;  $U$  – velocity in the  $x$ -direction, m/s;  $c$  – cold;  $v$  – velocity in the  $y$ -direction, m/s in input;  $L$  – Length;  $u^*$  – Dimensionless form of velocity in  $x$  direction;  $v^*$  – Dimensionless form of velocity in  $y$  direction;  $x^*$  – Dimensionless form of horizontal coordinate;  $y^*$  – Dimensionless form of vertical coordinate;  $p^*$  – Dimensionless form of pressure.

Even though this technology is attractive due to its ability to harness unlimited solar energy, the prevention of heat losses remains a big challenge. Avoiding or minimising heat losses will make CSP plant efficient and cost-effective. Natural convective heat loss in a CSP plant contributes a significant percentage to the overall heat loss in the system [1]. Therefore, research works on convective heat losses in CSP plants are very crucial to improving their performance efficiency. Considerable experimental and numerical studies have been conducted to evaluate heat losses in cavities, tubes, and receivers of concentrated solar power systems. One of such works was carried out by [2]. The authors developed a 3-D numerical model to simulate natural convection heat losses in a cavity receiver with plate fins. The influence of the orientation of the cavity and the number of plate fins were investigated. They found that convective heat loss from the cavity receiver was greatly affected by the inclination of the cavity, and by the number of plate fins. In addition, the total heat loss was also found to be reduced by using plate fins. Further, [3] numerically investigated natural convection heat transfer by subjecting the cavity to differential heating at the inclined walls. The source of heat was placed at the bottom wall and the governing equations were solved with ANSYS Fluent, finite volume-based software. The fluid flow and heat transfer activities within the cavity were found to depend on Rayleigh number, the heater's size and position as well as the aspect ratio of the cavity. A similar research work was carried out [4] involving a closed air-filled cavity using finite volume approach to evaluate the velocity vector, stream function, and temperature gradient. The influence of Rayleigh number was analyzed at different angles of inclination and the local and average Nusselt numbers were used to describe the activities of convective heat transfer at the flow regimes. In another dimension, a tilted open cavity was investigated by [5]. Natural convection heat transfer was studied numerically using both the laminar and Boussinesq approximation model. The governing equations were solved with a combination of finite volume method, SIMPLEC algorithm, SMART scheme, and Central Differencing scheme. Results were obtained for Rayleigh number ranging from  $10^4$  to  $10^7$  at different inclination angles of the cavity. They found that an increased in the inclination angles lead to a change in the average Nusselt number change. In addition, instabilities in airflow and Nusselt number oscillation were also observed at low inclination angle and high Rayleigh number. Remarkably, another notable 3-Dimensional-numerical study was done to investigate heat losses in a Linear Fresnel Reflector (LFR) by [6]. They compared both convective and radiative heat losses at different values of heat transfer coefficient and emissivity, respectively. Convective heat losses were found to be higher at lower absorber tube temperature (350 K) and higher value of heat transfer coefficient (25 W/mK) compared to heat loss by radiation. It worth noting that [7] investigated the trapezoidal cavity of a LFR consisting of eight absorber tubes where natural convective and radioactive heat losses were analyzed using both experimental and CFD methods. Eight heating elements were provided for the absorber tubes. Although radiation heat loss was found to be dominant, losses by natural convection were described as significant. The CFD results were found to be consistent with the experimental values.

Moreover, significant research works have also been done on parabolic trough collectors. For instance, [8] employed both numerical modeling and experimental measurements to study a 250 kW solar thermal power plant in order to compare heat losses in vacuum, lost vacuum (air) and broken glass (bare) tube. It was reported that there was a significant reduction in the heat losses in the absorber tube with vacuum relative to others. Further, by considering three different heat transfer fluids in a parabolic trough collector, [9] used COMSOL Multiphysics software with the assumption of constant flow rate of fluid to study three-dimensional temperature distributions of an absorber tube. The heat flux was evaluated with Microsoft Excel and compared to values from Soltrace software. In their research work, three different fluids were used as the heat transfer fluids and the

simulation was carried out using  $k$ - $\epsilon$  model. It was reported that a higher temperature was observed at the outlet of the absorber tube when the flow rate was 0.5 m/s and solar flux was 938 W/m<sup>2</sup>.

Despite numerous works on the subject matter, it worth noting that most of the works discussed in the literature (which encompasses parabolic trough collector and linear Fresnel reflector) did not take into consideration the effect of neighbouring absorber tubes in their models which might influence the heat transfer phenomena in the system. Hence, the contribution of neighboring absorber tubes to convective heat transfer activities has not been ascertained. The presence of multiple absorber tubes in a receiver whether evacuated or non-evacuated is expected to have a significant impact on the overall fluid flow and heat transfer in the assembly. This research work therefore numerically investigates the effect of neighboring absorber tubes in its study of natural convective heat transfer.

## 2. Materials and Method

**Fig. 1** depicts the geometry of the problem. The absorber tube is represented in 2-D by a rectangular cavity filled with an incompressible fluid, water, which serves as the Heat Transfer Fluid (HTF). The absorber tube is enclosed in an air-filled cavity. The dimension of the absorber tube and the aspect ratio of the enclosure is maintained constant throughout the simulation. To generate a buoyancy-driven flow and to initiate convection, the left vertical wall is kept at a relatively low temperature ( $T_c$ ) and the right vertical wall is maintained at a relatively high temperature ( $T_h$ ). The top wall of the tube is subjected to uniform heat flux while the bottom wall is insulated. The properties of the HTF are assumed to be constant except for the density variation, which is approximated by the Boussinesq model.

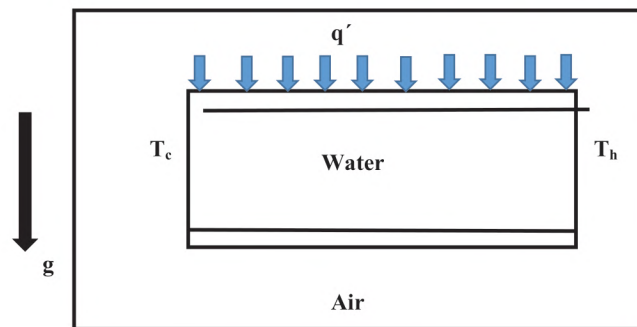


**Fig. 1.** Geometry of the 2D-Problem

The governing equations for the problem are described in two dimensions by the Navier-Stokes equation and the energy equation. The momentum equation in the y-direction has a buoyancy term, which is simplified using Boussinesq approximation.

The Dimensional Governing Equations were as follows:

Continuity Equation:

$$\frac{\partial u}{\partial x} + \frac{\partial v}{\partial y} = 0. \quad (1)$$

Momentum equation:

$$\rho \left( u \frac{\partial u}{\partial x} + v \frac{\partial u}{\partial y} \right) = -\frac{\partial p}{\partial x} + \mu \left( \frac{\partial^2 u}{\partial x^2} + \frac{\partial^2 u}{\partial y^2} \right), \quad (2)$$

$$\rho \left( u \frac{\partial v}{\partial x} + v \frac{\partial v}{\partial y} \right) = -\frac{\partial p}{\partial y} + \mu \left( \frac{\partial^2 v}{\partial x^2} + \frac{\partial^2 v}{\partial y^2} \right) + g\beta (T_h - T_c). \quad (3)$$

Energy equation:

$$\rho \left( u \frac{\partial T}{\partial x} + v \frac{\partial T}{\partial y} \right) = \alpha \left( \frac{\partial^2 T}{\partial x^2} + \frac{\partial^2 T}{\partial y^2} \right). \quad (4)$$



The boundary conditions for the dimensional form of the governing equation are:

$$\begin{aligned}x = 0: u = v = 0, T = T_c, \\x = L: u = v = 0, T = T_h, \\y = h: \ddot{q} = q_{in}, \\y = 0: \ddot{q} = 0.\end{aligned}$$

Introducing Dimensionless Groups for the Governing Equations:

$$\begin{aligned}u^* = \frac{Lu}{\alpha} v^* = \frac{Lv}{\alpha} x^* = \frac{x}{L}, \\y^* = \frac{y}{L}, \\p^* = \frac{pL^2}{\rho\alpha^2}, \\\theta = \frac{T - T_c}{T_h - T_c}, \\Ra = \frac{\rho g \beta L^3 (T_h - T_c)}{\mu \alpha}, \\\Pr = \frac{\mu}{\rho \alpha}.\end{aligned}$$

The dimensional equations are non-linear, the convective terms are therefore linearized and the non-dimensionless form of the governing equations is obtained:

$$\frac{\partial u}{\partial x} + \frac{\partial v}{\partial y} = 0, \quad (5)$$

$$\left( u \frac{\partial u}{\partial x} + v \frac{\partial u}{\partial y} \right) = -\frac{\partial p}{\partial x} + \Pr \left( \frac{\partial^2 u}{\partial x^2} + \frac{\partial^2 u}{\partial y^2} \right), \quad (6)$$

$$\left( u \frac{\partial v}{\partial x} + v \frac{\partial v}{\partial y} \right) = -\frac{\partial p}{\partial y} + \Pr \left( \frac{\partial^2 v}{\partial x^2} + \frac{\partial^2 v}{\partial y^2} \right) + Ra \Pr \theta, \quad (7)$$

$$\rho \left( u \frac{\partial \theta}{\partial x} + v \frac{\partial \theta}{\partial y} \right) = \left( \frac{\partial^2 \theta}{\partial x^2} + \frac{\partial^2 \theta}{\partial y^2} \right). \quad (8)$$

The boundary conditions for the dimensionless form of the governing equation are:

$$\begin{aligned}x = 0: u = v = 0, \theta = 0, \\x = L: u = v = 0, \theta = 1, \\y = h: \ddot{q} = 1, \\y = 0: \ddot{q} = 0.\end{aligned}$$

The dimensionless governing equations subjected to the aforementioned dimensionless boundary conditions were numerically solved using the finite element method based on Galerkin weighted residual formulation. The equation was modeled in COMSOL Multiphysics software. The computational domain of the absorber tube was meshed with triangular mesh elements using finer mesh size settings to capture the temperature and velocity changes near the walls. In heat transfer problems, it is customary to use the average Nusselt number as a measure of convective heat transfer rate in cavities. The Local Nusselt number was evaluated from the dimensionless temperature gradient and was integrated over the hot wall to obtain the average Nusselt number:

$$Nu(x) = \frac{\partial \theta}{\partial X}, \quad (9)$$

$$Nu_{avg} = \int_0^1 Nu(X) dY. \quad (10)$$

The values of the average Nusselt number obtained for various Rayleigh numbers ( $Ra$ ) were compared with previous research works to test the numerical model. The results were found to show reasonable agreements with related research works (**Table 1**).

**Table 1**  
Comparison of present work with selected numerical studies

$Ra$	$10^4$	$10^5$	$10^6$
<b>Present Work</b>	<b>2.28</b>	<b>4.54</b>	<b>8.50</b>
[10]	2.240	4.51	8.82
[11]	2.246	4.521	8.984
[12]	2.302	4.646	9.012
[13]	2.247	4.532	8.893
[14]	2.234	4.517	8.948

The validated model was now extended to multiple tubes (two to six absorber tubes). The tubes were arranged to allow for uniform distribution of heat flux. The temperature distribution and average Nusselt numbers were compared for analysis.

### 3. Results and Discussion

In this study, natural convective heat transfer was investigated in an absorber tube enclosed in an air-filled cavity. The post-processed results obtained from the COMSOL Multiphysics interface are presented in **Fig. 2** via isotherms and streamlines to provide a clear picture of changes occurring in the absorber tubes due to an increase in Rayleigh number. The average surface temperature and average Nusselt number were also evaluated from the COMSOL Multiphysics interface.

**Fig. 2** shows the isotherms for Rayleigh numbers  $Ra = 10^4$ ,  $10^5$  and  $10^6$ . It should be noted that Isotherms connect points of equal temperature in such that at every point along a given isotherm, the temperature values are the same.

At Rayleigh number of  $10^4$ , the near-uniform distribution of the isotherms close to the cold wall and the assumption of an almost parallel shape by the isotherms close to the hot wall indicate the predominance of conduction over convection. An explanation to this is the stagnancy of the fluid at that Rayleigh number. With increase in  $Ra$ , fluid motion becomes significant and transition occurs from conduction to convection as indicated by the distortion of the isotherms. Apart from this, at higher values of Rayleigh number, the isotherm lines change sharply which is an indication of higher heat flux. This again implies that convection plays a dominant role in transferring heat. This corroborates and consistent with the findings of [15, 16]. This is not surprising, **Fig. 3** which is the streamlines for  $Ra = 10^4$ ,  $10^5$ , and  $10^6$  support this assertion. It should be noted that convective cells are revealed with the aid of velocity streamlines. A large convective cell is seen to occupy the whole cavity. The fluid flow follows the boundaries and it is faster at the right vertical wall where there is highest variation of temperature.

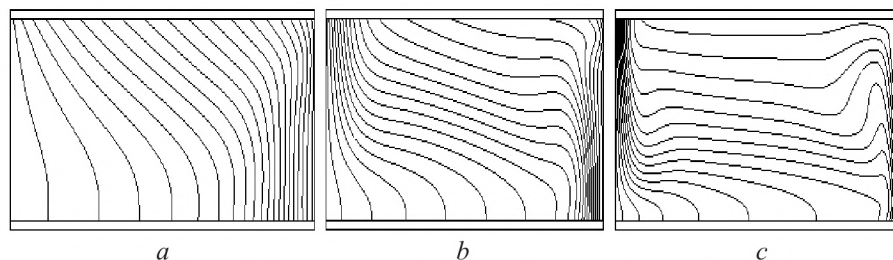


**Fig. 2.** Isotherms for  $Ra$  of:  $a = 10^4$ ;  $b = 10^5$ ;  $c = 10^6$



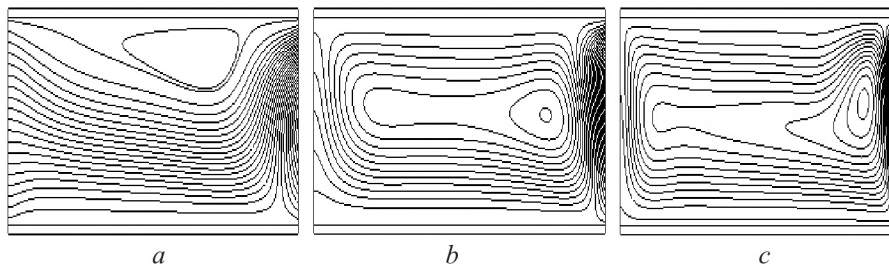


**Fig. 3.** Distribution of streamline for  $Ra$  of:  $a = 10^4$ ;  $b = 10^5$ ;  $c = 10^6$

The non-uniform distribution of streamline suggests flow flux is stronger at the outer region than in the core. At low Rayleigh number, there is less mixing of fluid due to less convection. The formation of a very weak eddy close to the top wall indicates low heat transfer activity. Meanwhile, as the Rayleigh number increases, heat transfer to the cold wall of the enclosure also increases. The buoyancy-driven flow induces recirculation zone in the absorber tube. As seen in the streamline plot of the velocity field, the elongation of the recirculation zone leads to a change in the streamline structure which is evidence of the supremacy of natural convection. The increase in  $Ra$  increases the strength of the flow and there is greater exchange of fluid between the left and right parts of the enclosure due to increased convection current.

The number of absorber tube in the enclosure which previously consisted of a single tube is increased and the value of the average surface temperature is evaluated in order to evaluate the influence of neighboring absorber tubes on the parameter. **Table 2** shows the values obtained for various numbers of absorber tubes and the variation with Rayleigh number is shown in **Fig. 4**.

**Table 2**

Variation of average surface temperature with number of tubes

Rayleigh Number	Dimensionless temperature at different number of absorber tubes					
	One Tube	Two Tubes	Three Tubes	Four Tubes	Five Tubes	Six Tubes
$10^4$	0.315	0.317	0.318	0.319	0.319	0.319
$10^5$	0.426	0.427	0.429	0.429	0.429	0.429
$10^6$	0.488	0.490	0.497	0.498	0.498	0.498

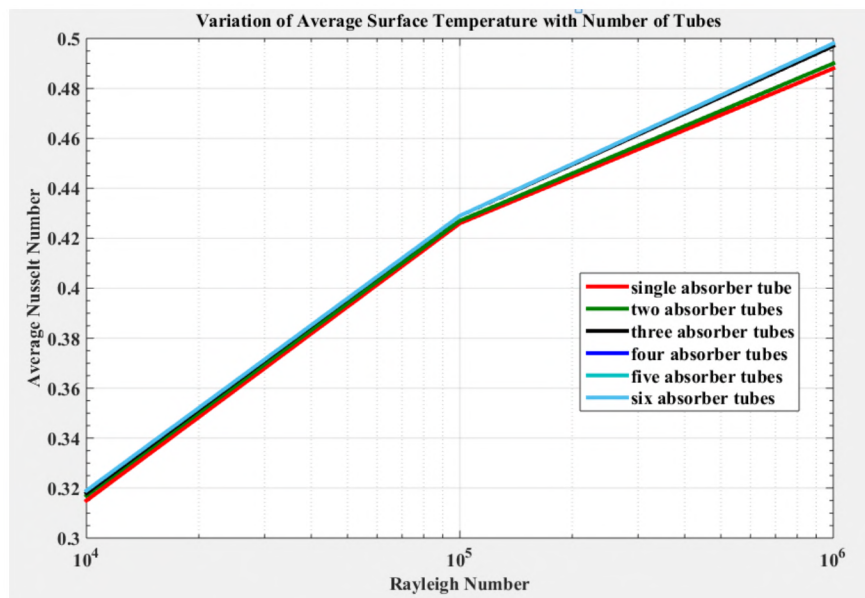


**Fig. 4.** Variation of average surface temperature with the number of tubes at different Rayleigh numbers

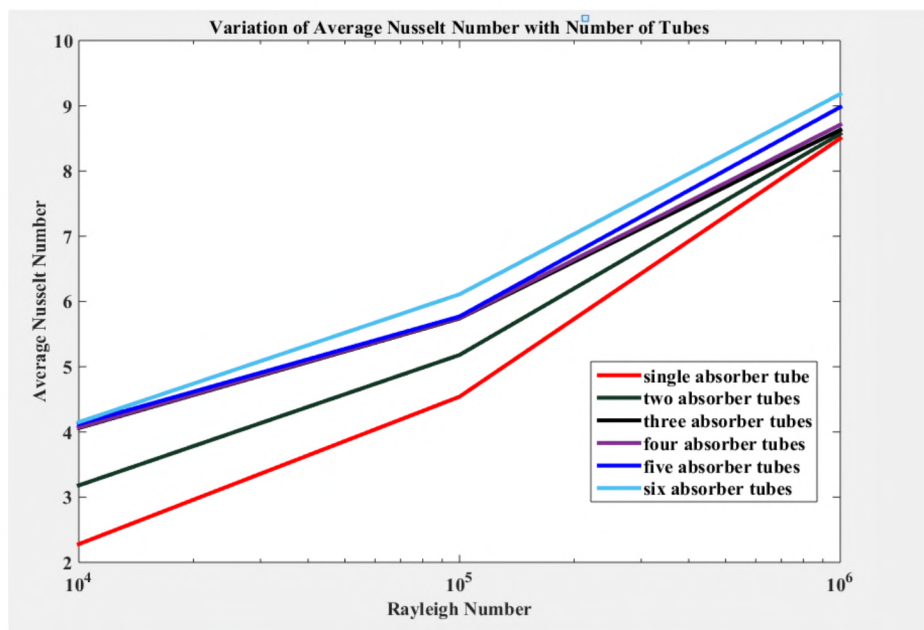
Heat transfer performances are measured in terms of temperature of the fluid in the cavity as well as average Nusselt number at the hot surface. **Fig. 4** shows the variation of the average surface temperature of the fluid with the Rayleigh number as well as the number of absorber tubes. Interestingly, as the Rayleigh number increases, average surface temperature also increases. This is not surprising, since this higher temperature difference implies higher difference in density which is a driving force for natural convection. In a similar dimension, a significant increase is experienced when the number of absorber tubes is increased. Initially, increasing the number of absorber tubes brought about a significant increase in the average surface temperature. However, the temperature increase becomes insignificant with a further increase in the number of tubes (beyond three tubes). This is shown by the overlapping of the figures. This suggests that there is limitation to increment in the value of the average surface temperature of the fluid. In this present study the threshold is three tubes beyond this the effect is insignificant.

While the previous results showed that the number of absorber tubes play significant role on the heat transfer characteristics of the system, to investigate further the influence of absorber tubes on the rate of convective heat transfer, the variation of average Nusselt number with Rayleigh number and also with the number of absorber tubes were computed as shown in **Table 3**. Similarly, **Fig. 5** depicts the variation of average Nusselt number with Rayleigh number for various number of absorber tubes. The **Fig. 5** shows an increase in the average Nusselt number with the Rayleigh number which implies that the intensity of convective heat transfer grows with Rayleigh number. This conforms to the findings of [4, 6, 15, 17]. Although the authors only considered single tube, the increase in the gradient of the lines at Rayleigh number of  $10^5$  indicates enhancement of heat transfer due to convection over conduction at higher values of  $Ra$ .

**Table 3**

Variation of Average Nusselt Number with Number of Tubes

Rayleigh Number	Nu <sub>avg</sub> at different number of absorber tubes					
	One Tube	Two Tubes	Three Tubes	Four Tubes	Five Tubes	Six Tubes
$10^4$	2.28	3.18	4.06	4.07	4.12	4.15
$10^5$	4.54	5.18	5.74	5.75	5.77	6.11
$10^6$	8.50	8.57	8.63	8.71	8.98	9.18

**Fig. 5.** Variation of average Nusselt number with number of tubes



Similarly, as the number of absorber tubes increases, the average Nusselt number is also found to increase. For instance, for the Rayleigh number of  $10^4$ ,  $10^5$  and  $10^6$ , the average Nusselt number increase with the number of absorber tubes by 13.87 %, 6.26 %, and 1.55 %, respectively. This is not surprising, since natural convection depends on macroscopic movement of fluid particles. Therefore, it can be inferred that the thermal influence of the neighboring absorber tubes facilitates an increase in the flow of the heat transfer fluid in each absorber tubes, which leads to higher heat transfer by natural convection.

It should be noted that this study is limited in scope to natural convection, laminar, and steady flow. However, future studies should explore scenarios involving forced, or mixed convection and time-dependent turbulent flow. Experiments should also be used to validate the findings of the numerical modelling.

#### 4. Conclusions

1. At low Rayleigh number ( $10^4$ ), conduction is the dominant heat transfer mechanism, the influence of convective heat transfer increased with Rayleigh number.

2. There was an increased in the average surface temperature of the absorber tube with Rayleigh number. The average Nusselt number was also found to increase with Rayleigh number indicated that intensity of convective heat transfer grows with Rayleigh number.

3. There was a significant increase in the average Nusselt number with an increase in the number of absorber tubes. For the Rayleigh number of  $10^4$ ,  $10^5$  and  $10^6$ , the average Nusselt number increased with the number of absorber tubes by 13.87 %, 6.26 %, and 1.55 %, respectively. This showed that there is increase in the intensity of convective heat transfer as the number of absorber tubes increases. This increment can be attributed to thermal interactions among the neighboring absorber tubes.

---

#### References

- [1] Taumofolau, T., Paitoonsurikarn, S., Hughes, G., Lovegrove, K. (2004). Experimental Investigation of Natural Convection Heat Loss From a Model Solar Concentrator Cavity Receiver. *Journal of Solar Energy Engineering*, 126 (2), 801–807. doi: <https://doi.org/10.1115/1.1687403>
- [2] Ngo, L. C., Bello-Ochende, T., Meyer, J. P. (2014). Numerical Modelling of Combined Natural Convection and Surface Radiation Heat Transfer in Cavity Receiver with Plate Fins. *Proceedings of the 15th International Heat Transfer Conference*. doi: <https://doi.org/10.1615/ihtc15.rne.009869>
- [3] Sojoudi, A., Saha, S. C., Gu, Y. T. (2015). Natural convection due to differential heating of inclined walls and heat source placed on bottom wall of an attic shaped space. *Energy and Buildings*, 89, 153–162. doi: <https://doi.org/10.1016/j.enbuild.2014.12.042>
- [4] Kristian, L., Bernard, F. (2002). Free convection heat losses in a flat plate solar collector. *Energy and the Environment*, 101–114.
- [5] Hinojosa, J. F., Alvarez, G., Estrada, C. A. (2006). Three-dimensional numerical simulation of the natural convection in an open tilted cubic cavity. *Revista Mexicana De Física*, 52 (2), 111–119.
- [6] Duggal, R., Jilte, R. (2017). Numerical Investigation on Trapezoidal Cavity Receiver Used In LFR with Water Flow in Absorber Tubes. *IOP Conference Series: Materials Science and Engineering*, 187, 012026. doi: <https://doi.org/10.1088/1757-899x/187/1/012026>
- [7] Sudhansu, S. S., Vargheseb, S. M., Kumarb, A., Kumarb, S., Singha, S., Banerjeea, R. (2011). An experimental and computational investigation of heat losses from the cavity receiver used in Linear Fresnel Reflector solar thermal system. *Proceedings of International Conference on Advances in Energy Research (ICAER)*.
- [8] Yaghoubi, M., Ahmadi, F., Bandehee, M. (2013). Analysis of Heat Losses of Absorber Tubes of Parabolic through Collector of Shiraz (Iran) Solar Power Plant. *Journal of Clean Energy Technologies*, 1 (1), 33–37. doi: <https://doi.org/10.7763/jocet.2013.v1.8>
- [9] Mon, M. M., Soe, M. M., Htay, M. M. (2015). 3D modeling of temperature distribution for absorber tube of parabolic trough collector. *International Journal of Engineering and Applied Sciences (IJEAS)*, 2 (6), 99–103.
- [10] Nag, A., Sarkar, A., Sastri, V. M. K. (1993). Natural convection in a differentially heated square cavity with a horizontal partition plate on the hot wall. *Computer Methods in Applied Mechanics and Engineering*, 110 (1-2), 143–156. doi: [https://doi.org/10.1016/0045-7825\(93\)90025-s](https://doi.org/10.1016/0045-7825(93)90025-s)
- [11] Ghafouri, A., Jozaei, A. F., Salari, M. (2015). Numerical evaluation of Nusselt number on the hot wall in square enclosure filled with nanofluid. *International Journal of Mechanical, Aerospace, Industrial, Mechatronic and Manufacturing Engineering*, 9 (2), 360–364.

- [12] Fusegi, T., Hyun, J. M., Kuwahara, K., Farouk, B. (1991). A numerical study of three-dimensional natural convection in a differentially heated cubical enclosure. *International Journal of Heat and Mass Transfer*, 34 (6), 1543–1557. doi: [https://doi.org/10.1016/0017-9310\(91\)90295-p](https://doi.org/10.1016/0017-9310(91)90295-p)
- [13] Shi, X., Khodadadi, J. M. (2003). Laminar Natural Convection Heat Transfer in a Differentially Heated Square Cavity Due to a Thin Fin on the Hot Wall. *Journal of Heat Transfer*, 125 (4), 624–634. doi: <https://doi.org/10.1115/1.1571847>
- [14] Elatar, A., Teamah, M. A., Hassab, M. A. (2016). Numerical study of laminar natural convection inside square enclosure with single horizontal fin. *International Journal of Thermal Sciences*, 99, 41–51. doi: <https://doi.org/10.1016/j.ijthermalsci.2015.08.003>
- [15] Omar, M. A., Ghalib, Y. K. (2015). Numerical Investigation of Natural Convection Heat Transfer from Square Cylinder in an Enclosed Enclosure Filled with Nanofluids. *International Journal of Recent Advances in Mechanical Engineering*, 4 (4), 1–17. doi: <https://doi.org/10.14810/ijmech.2015.4401>
- [16] Yao, S.-G., Duan, L.-B., Ma, Z.-S., Jia, X.-W. (2014). The Study of Natural Convection Heat Transfer in a Partially Porous Cavity Based on LBM. *The Open Fuels and Energy Science Journal*, 7 (1), 88–93. doi: <https://doi.org/10.2174/1876973x01407010088>
- [17] Moukalled, F., Acharya, S. (2000). Natural convection in trapezoidal cavities with baffles mounted on the upper inclined surfaces. *Numerical Heat Transfer, Part A: Applications*, 37 (6), 545–565. doi: <https://doi.org/10.1080/104077800274082>

Received date 08.06.2021

Accepted date 23.08.2021

Published date 13.09.2021

© The Author(s) 2021

This is an open access article  
under the Creative Commons CC BY license

**How to cite:** Oyewola, O. M., Olukayode, N. E., Ajide, O. O. (2021). Modeling of natural convection of a concentrated solar power receiver absorber tube in interaction with neighbouring absorbers. *EUREKA: Physics and Engineering*, 5, 53–61. doi: <https://doi.org/10.21303/2461-4262.2021.001871>



# ANALYSIS OF THE NUMBER AND ANGLE OF THE IMPELLER BLADE TO THE PERFORMANCE OF CENTRIFUGAL PUMP

**Sugeng Hadi Susilo**✉

*Department of Mechanical Engineering<sup>1</sup>*  
*shadis172.gh@gmail.com, sugeng.hadi@polinema.ac.id*

**Agus Setiawan**

*Department of Mechanical Engineering<sup>1</sup>*

*<sup>1</sup>State Polytechnic of Malang*

*9 Jl. Soekarno-Hatta, Malang, East-Java, Indonesia, 65141*

✉ Corresponding author

## Abstract

The paper discusses the performance of the pump in relation to the impeller. The impeller section is determined by the number and angle of the blades. Therefore, the purpose of this study was to analyze the role of the number and angle of impeller blades on the performance (discharge and discharge pressure) of centrifugal pumps based on experiments and simulations.

The method used is experiment and simulation. Using a centrifugal pump type GWP 20/4 SW, Maximum Output: 6.5 HP/3500 rpm, Inlet/Outlet: 2 Inch, Dimensions: 475×375×370 mm. Experiments and simulations by varying the number of blades 2, 4, and 6 with a blade tilt angle of 130°, 150°, and 160°. For flow simulation using solid works program.

The results show that pump performance is related to discharge pressure, impeller with 2-blades and an angle of 130° the pressure increases 0.45–2.45 bar, for 150° increases 0.14–2.96 bar, and 160° increases 0.29–3.07 bars. For a 4-blade impeller and an angle of 130°, the pressure increases by 0.48–3.12 bar, for 150° it increases by 0.39–3.39 bar, and for 160° it increases by 0.36–3.48 bar. While the impeller for 6-blades with an angle of 130° the pressure increases from 0.6 bar to 3.72 bar, for 150° increases from 1.36 to 4.34 bar, and 160° increases by 0.36–4.74 bar. While it related pump performance to flow rate, increasing the number of blades causes a decrease in flow rate. The highest flow rate is in a 2-blade impeller with a blade angle of 130° is 404.91 l/s. The lowest flow rate is on a 6-blade impeller with an angle of 160° is 279.66 l/s.

**Keywords:** pump performance, centrifugal pump, impeller, number of blades, blade angle, simulation, experiment.

DOI: 10.21303/2461-4262.2021.002001

## 1. Introduction

Water is a very vital need for survival, be it humans, animals or plants. Besides irrigation needs, but also for the supply of raw water, clean water, industrial water, electricity, plantations and other business activities that require water. With the increase in population, the need for water also increases. So that pumps are necessary to drain water from one place to another, and pumps are needed in human life in various fields [1, 2]. The pump serves to move the fluid through the pipe from one place to another [3].

The function of the pump is to change the mechanical energy of the shaft that moves the blades into kinetic energy and pressure in the form of the head in the fluid. The impeller is an important component in a centrifugal pump, and the most important part is the number and angle of the blades. This affects the performance of the pump. Pump performance is determined by the output pressure, flow capacity or flow rate, and suction strength [4].

Pump design requires a trial-and-error process, reducing the pump manufacturer's profit margins. For analytical reasons, besides experiments, simulations were also carried out at the pump design and construction stages [5]. Instability and dynamic phenomena can be studied with the help of simulation. Simulation can provide fairly accurate information about fluid behaviour, thus helping in evaluating pump performance [6].

The need for pumps in human life in various fields. For agriculture, pumps are widely used in the irrigation system so that the agricultural system continues to run even in the dry season,

in providing drinking water for the community, pumps are used to distribute drinking water from PDAM to people's homes, pumps are a tool that facilitates daily human work [7]. Therefore, research is needed that discusses the effect of the impeller exit angle ( $\beta_2$ ) on performance which includes discharge and exhaust pressure in centrifugal pumps. The role of the number of blades and the angle of the blade on the impeller affect the resulting pump pressure.

To optimize pump performance, a pump impeller is needed which plays an important role in determining the pump output pressure and flow capacity. The influence of the number of blades and the angle of the blades will cause the number of blades to change and affect the resulting pump pressure.

Research on the optimization of centrifugal pump impeller performance using design standards. Simulation is used to validate experimental test results. The experimental results were analyzed for the best combination of parameters and compared with the original pump. Research on the optimization of pressure and efficiency of centrifugal pumps to get high efficiency in using low power in operation. This study increases the head and efficiency of the centrifugal pump by changing the impeller blades and the exit angle of the centrifugal pump blades to get optimal head and efficiency [8].

This research on Centrifugal Pump Impeller Design Optimization research with the CFD approach discusses the stages of pump construction design. Based on the design results, to determine the optimal number of blade variations [9].

Research on the effect of the inlet impeller reverses 6 angles on the characteristics of the FM 50 centrifugal pump. This study discusses the effect of the inlet angle of the impeller ( $\beta_1$ ) of the pump on the centrifugal pump head for each impeller with an intake angle. The results showed that the value ( $\beta_1$ ) of the impeller did not affect the performance of the pump, but because the circulation in the impeller caused the performance of the pump to change. Based on the results of the study, it is known that the greater the head value ( $\beta_1$ ), the hydraulic power of the pump will increase. The pump flow rate also increases. On the other hand, the greater ( $\beta_1$ ), the smaller the pump efficiency produced [10].

Numerical simulation of backward impeller type centrifugal pump with variations in rotation and pump discharge. Numerical simulations were carried out on 2D and 3D steady flow with a standard turbulent k-epsilon model. Simulation by varying the speed and flow of the pump. Then the simulation results are validated with experimental results. The results obtained in the 2D numerical research are very different from the experimental results. In the 3D simulation, there is a backflow phenomenon [11].

Therefore, researchers conducted experiments and simulated the effect of the impeller exit angle on performance which includes discharge, discharge pressure on a centrifugal pump by using the influence of the number and exit angle of the impeller.

## 2. Materials and methods

### 2. 1. Centrifugal pump specifications

The type of pump used in this study is GWP 20/4 SW. Following are the specifications for the Centrifugal Pump Type GWP 20/4 SW, Maximum Output: 6.5 HP/3500 RPM, Inlet/Outlet: 2 Inch, Dimension: 475×375×370 mm. The impeller design is shown in **Fig. 1**.

**Fig. 1** shows the design of the blade position and blade angle for 2 variations of the blade angle of 160°. Manufacturing this impeller uses the welding method so that it can form a precise construction. The number of blades 2, 4, and 6 varied with blade angles of 130°, 150°, and 160°.

### 2. 2. Experimental setup

The study used a 2-inch GWP 20/4 SW centrifugal pump. The research was conducted by varying the number and angle of the blades using experimental and simulation methods. In this study, the number of blades 2, 4, and 6 varied with blade angles of 130°, 150°, and 160°. **Fig. 2** shows the experimental setup.

The experimental set-up consists of 3 main parts, namely preparing the equipment to be tested, preparing the pump, and taking data.



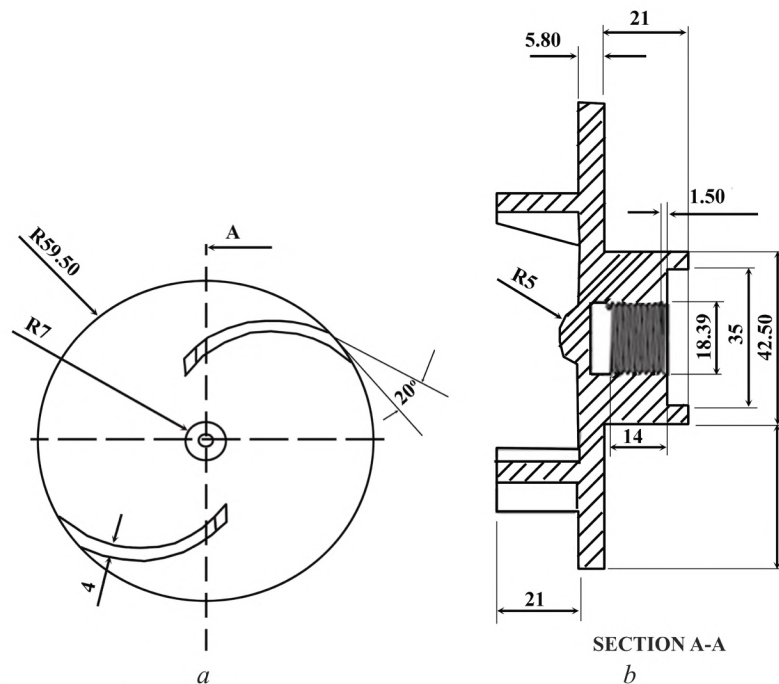


**Fig. 1.** Design of impeller for 2-blade 160°: *a* – Front view; *b* – Section A-A

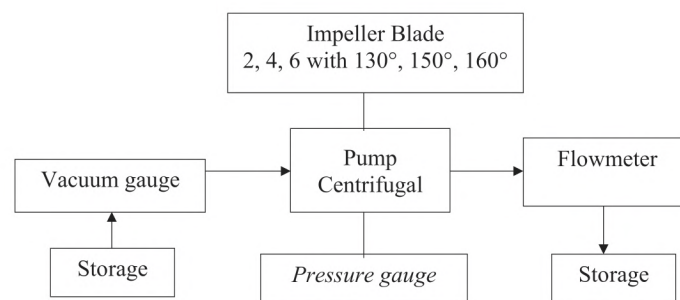


**Fig. 2.** The experimental setup

The research procedure includes:

1. Preparing the equipment according to the experimental setup.
2. Prepare the pump impeller with the number of blades and the angle to be tested.
3. Install the impeller on the volute housing and pump impeller housing.
4. Install the measuring instrument.
5. Data collection.

### 2. 3. Simulation

Flow simulation using the solidworks program. This program can analyze the integrated and can simulate the flow of liquids that are adapted to actual conditions.

#### 2. 3. 1. Boundary Conditions

1. Initial Data Collection.

At this stage, data collection on information related to pumps is carried out with the number of blades 2, 4, and 6 and the angle of inclination of the blades 130°, 150°, and 160°.

2. Parameter Setup Process.

In the simulation, the process to get results on the number and angle of the blades, setup parameters ranging from messing, boundary conditions, and goals. Referring to the internal type analysis, fluid type water, turbulent flow model, condition inlet (static pressure), outlet (total pressure) and adiabatic pump wall.

### 3. Data Retrieval.

At the data collection stage, the simulation runs the process to get the results of the discharge and the total pressure generated on the number and angle of the blade angle.

## 3. Result and Discussion

### 3.1. Result

The results of the research are pump performance data including discharge, pump pressure as shown in **Fig. 3, 4**. The visual results of the pump flow simulation are as shown in **Fig. 5**.

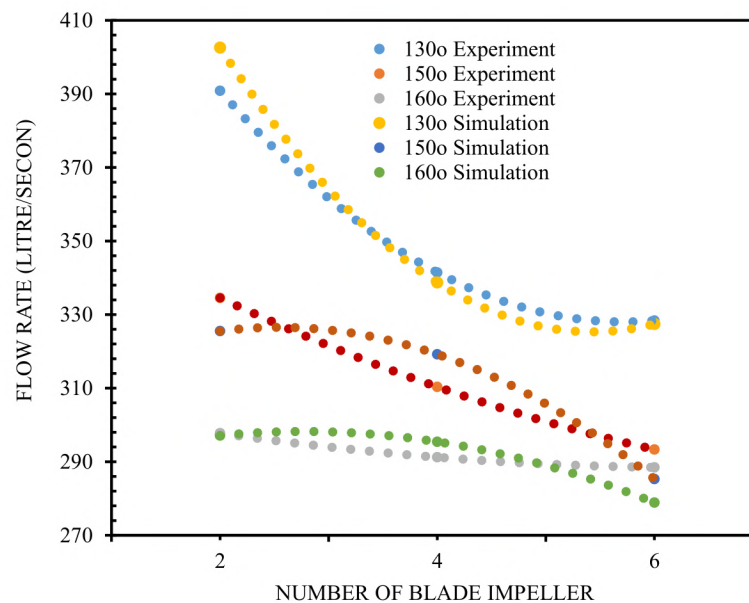


**Fig. 3.** Flow rate to the number of blades with variations in angles of 130°, 150° and 160° in experiments and simulations

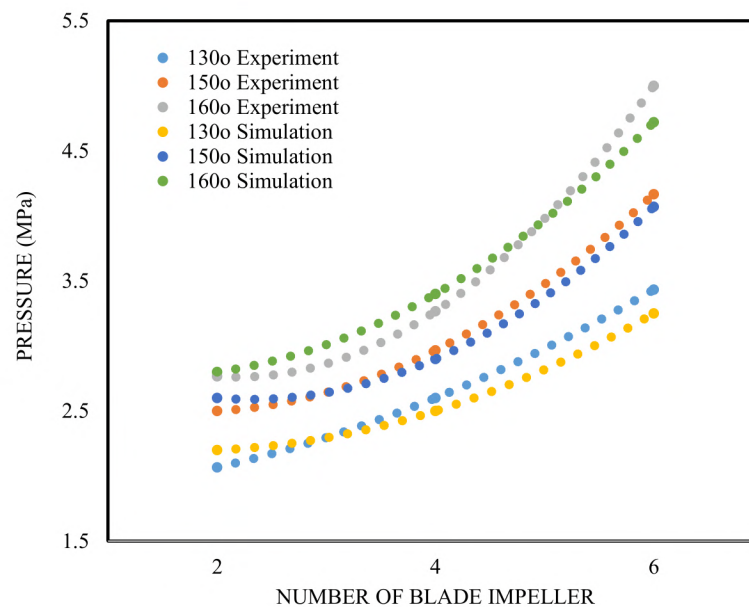


**Fig. 4.** Pump pressure on the number of blades with variations in angles of 130°, 150° and 160° in experiments and simulations

**Fig. 3** shows that there are three areas related to flow rate and discharge pressure: Area 1 is the pressure drop due to eddy currents in the opposite direction of rotation. Area 2 is a change



in pressure because of the rotation of the blades, thus affecting the pump pressure. Area 3 is an occurrence of whirlpools caused by the flow of water hitting the impeller walls, causing the fluid flow to be restrained.

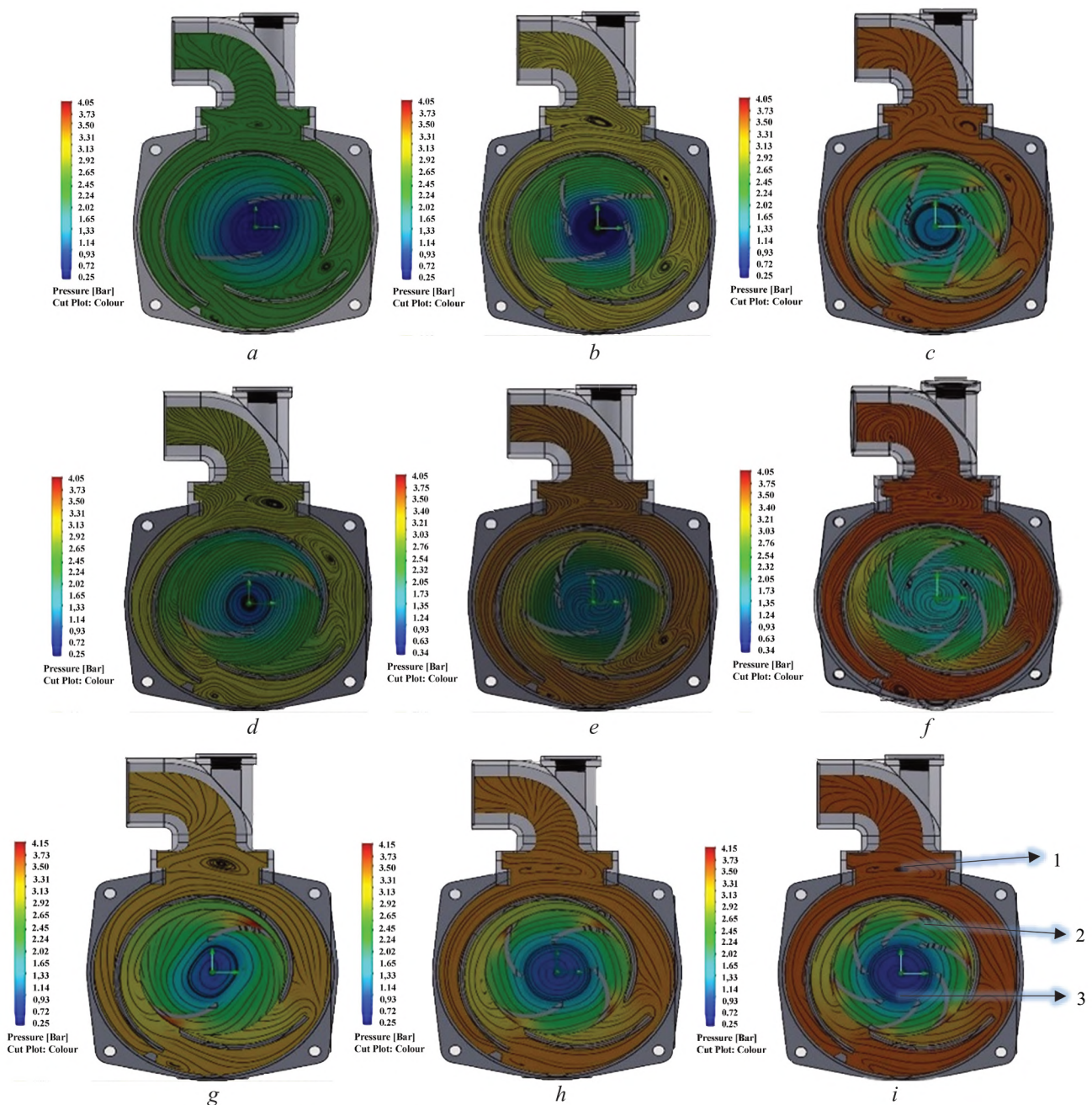


**Fig. 5.** Simulation results of variations in the number of blades and blade angles:  
*a* – 2 blades, 130°; *b* – 2 blades 150°; *c* – 2 blades 160°; *d* – 4 blades 130°; *e* – 4 blades 150°;  
*f* – 4 blades 160°; *g* – 6 blades 130°; *h* – 6 blades 150°; *i* – 6 blades 160°

### 3. 2. Discussion

Based on the results of experiments and simulations got the number of blades 2, 4, and 6 with a tilt angle of 130°, 150°, and 160°. In the volute outlet area, there is a pressure drop. This is because the whirlpool is in the opposite direction of the water flow.

In an impeller with several two blades and an angle of 130°, four vortex flows are in opposite directions of flow. This current is present at the volute outlet, volute wall and pump outlet line.



That results in a pressure drop. The distance between the eddies also affects the pressure drop. The closer the distance between the vortexes, the greater the pressure drop, causing differences in fluid flow velocity. While the increase in the number of blades 4 and 6, the pressure drop is getting smaller. An increase in the number of blades causes an increase in thrust pressure and an increase in fluid flow velocity.

In an impeller with two blades and an angle of  $150^\circ$ , there are three opposite vortices at the bottom of the volute housing line and the pump outlet line. However, the sum of the four blades caused a vortex. Its location, the housing volute outlet is next to the nearest vortex, while in the six-blade impeller, the vortex flow is at the bottom of the volute outlet. This is also almost the same as the angle of  $130^\circ$ . It's just that the location and pressure drop are different. As for the impeller with two blades and an angle of  $160^\circ$ , the pressure drops at the outlet side.

For the number of blades, four and six did not experience a decrease in pressure.

At the impeller inlet, there is a change in flow pressure. The change in colour level shows that. Where the more blades, the greater the pressure change. For two blades whose angles are  $130^\circ$ ,  $150^\circ$ , and  $160^\circ$ , there is a different pressure rise. An angle of  $130^\circ$  the pressure increases 0.45–2.45 bar, for an angle of  $150^\circ$  it increases –0.14–2.96 bar and an angle of  $160^\circ$  increases by 0.29–3.07 bar. For four blades with angles of  $130^\circ$ ,  $150^\circ$  and  $160^\circ$ , there is a different pressure rise. For an angle of  $130^\circ$ , the pressure increases 0.48–3.12 bar, for an angle of  $150^\circ$  it increases by 0.39–3.39 bar and an angle of  $160^\circ$  increases by 0.36–3.48 bar.

Even though the six-blade angles are  $130^\circ$ ,  $150^\circ$ , and  $160^\circ$ , there are differences where at the  $130^\circ$  angle the pressure increases from 0.6 bar to 3.72 bar, for the  $150^\circ$  angle it increases from 1.36–4.34 bar, and at an angle of  $160^\circ$ , increase by 0.36–4.74 bar.

In the area between the tip of the blade and the flow guide plate, there is a whirlpool caused by the flow of water hitting the impeller wall, causing a fluid flow to be obstructed. The large blade rotation produces a large resistance force so that the inflow is low. An increase in the number of blades will result in a decrease in the flow rate. The highest flow rate is found in the number of two blades with a blade angle of  $130^\circ$ . For comparison, the lowest flow rate is found in the six blades with an angle of  $160^\circ$ . There is a difference where the greater the number of blades and the greater the angle of the blade, the higher the pressure. The highest pressure is obtained in the amount of six blades with an angle of  $160^\circ$ , while the lowest pressure is obtained in the amount of two blades with an angle of  $130^\circ$ .

The research has not shown how much influence the number and angle of the blades on the pump impeller on the presence of cavitation, only discusses related to pump performance. In this study, only the impeller with the backward impeller type was used. So it is necessary to research other types.

It is necessary to develop pump studies related to the elimination of vortex flow that occurs at the outlet volute. This is very important because vortex flow increases the pressure drop. The presence of pressure drop in the outlet volute area causes the pump to cavitate. Cavitation is highly undesirable in a pumping system. Because of cavitation, the area of the fluid foam eruption experiences repeated shock pressures. So that shock pressure easily eroded the material in the area. In addition, losing pressure drop causes the flow to be smooth and without obstacles. So that the flow rate and the thrust of the fluid are getting bigger. This makes the pump performance better.

#### 4. Conclusions

1. Pump performance related to discharge pressure, for an impeller with 2-blades and an angle of  $130^\circ$ , the pressure increases 0.45–2.45 bar, for  $150^\circ$  increases 0.14–2.96 bar, and  $160^\circ$  increases 0.29–3.07 bars. For a 4-blade impeller and an angle of  $130^\circ$ , the pressure increases by 0.48–3.12 bar, for  $150^\circ$  it increases by 0.39–3.39 bar, and for  $160^\circ$  it increases by 0.36–3.48 bar. While the impeller for 6-blades with an angle of  $130^\circ$  the pressure increases from 0.6 bar to 3.72 bar, for  $150^\circ$  increases from 1.36 to 4.34 bar, and  $160^\circ$  increases by 0.36–4.74 bar.

2. While it related pump performance to flow rate, increasing the number of blades causes a decrease in flow rate. The highest flow rate is in a 2-blade impeller with a blade angle of  $130^\circ$  is 404.91 l/s. The lowest flow rate is on a 6-blade impeller with an angle of  $160^\circ$  is 279.66 l/s.



### Acknowledgments

We are very grateful to the Department of Mechanical Engineering, State Polytechnic of Malang (Indonesia), to provide equipment support and be more mature in conducting an analysis.

---

### References

- [1] Aw-Hassan, A., Rida, F., Telleria, R., Bruggeman, A. (2014). The impact of food and agricultural policies on groundwater use in Syria. *Journal of Hydrology*, 513, 204–215. doi: <https://doi.org/10.1016/j.jhydrol.2014.03.043>
- [2] Hanafizadeh, P., Ghorbani, B. (2012). Review study on airlift pumping systems. *Multiphase Science and Technology*, 24 (4), 323–362. doi: <https://doi.org/10.1615/multscientechn.v24.i4.30>
- [3] Improving Pumping System Performance (2006). Department of Energy, 117. Available at: <https://www.energy.gov/sites/default/files/2014/05/f16/pump.pdf>
- [4] Singh, V. R., Zinzuwadia, M. J., Sheth, S., Desai, R. J. (2017). “Parametric Study and Design Optimization of Centrifugal Pump Impeller. *Kalpa Publications in Engineering*, 1, 507–515. doi: <https://doi.org/10.29007/lbz2>
- [5] Asomani, S. N., Yuan, J., Wang, L., Appiah, D., Zhang, F. (2020). Geometrical effects on performance and inner flow characteristics of a pump-as-turbine: A review. *Advances in Mechanical Engineering*, 12 (4), 168781402091214. doi: <https://doi.org/10.1177/1687814020912149>
- [6] Sanda, B., Daniela, C. V. (2016). The influence of the inlet angle over the radial impeller geometry design approach with ansys. *Journal of Engineering Studies and Research*, 18 (4). doi: <https://doi.org/10.29081/jesr.v18i4.146>
- [7] Subroto, Effendy, M. (2019). Optimization of centrifugal pump performance with various blade number. *Exploring Resources, Process and Design for Sustainable Urban Development: Proceedings of the 5th International Conference on Engineering, Technology, and Industrial Application (ICETIA) 2018*. doi: <https://doi.org/10.1063/1.5112400>
- [8] Kim, J. H., Oh, K. T., Pyun, K. B., Kim, C. K., Choi, Y. S., Yoon, J. Y. (2012). Design optimization of a centrifugal pump impeller and volute using computational fluid dynamics. *IOP Conference Series: Earth and Environmental Science*, 15 (3), 032025. doi: <https://doi.org/10.1088/1755-1315/15/3/032025>
- [9] Frosina, E., Buono, D., Senatore, A. (2017). A Performance Prediction Method for Pumps as Turbines (PAT) Using a Computational Fluid Dynamics (CFD) Modeling Approach. *Energies*, 10 (1), 103. doi: <https://doi.org/10.3390/en10010103>
- [10] Li, W., Jiang, X., Pang, Q., Zhou, L., Wang, W. (2016). Numerical simulation and performance analysis of a four-stage centrifugal pump. *Advances in Mechanical Engineering*, 8 (10), 168781401667375. doi: <https://doi.org/10.1177/1687814016673756>
- [11] Si, Q., Bois, G., Liao, M., Zhang, H., Cui, Q., Yuan, S. (2019). A Comparative Study on Centrifugal Pump Designs and Two-Phase Flow Characteristic under Inlet Gas Entrainment Conditions. *Energies*, 13 (1), 65. doi: <https://doi.org/10.3390/en13010065>

Received date 14.12.2020

Accepted date 10.07.2021

Published date 13.09.2021

© The Author(s) 2021

This is an open access article  
under the Creative Commons CC BY license

**How to cite:** Susilo, S. H., Setiawan, A. (2021). Analysis of the number and angle of the impeller blade to the performance of centrifugal pump. *EUREKA: Physics and Engineering*, 5, 62–68. doi: <https://doi.org/10.21303/2461-4262.2021.002001>

# INCREASING THE EFFICIENCY OF MULTY-VARIANT CALCULATIONS OF ELECTROMAGNETIC FIELD DISTRIBUTION IN MATRIX OF A POLYGRADIENT SEPARATOR

**Jasim Mohmed Jasim Jasim**

*Department of Electrical Power Engineering Techniques  
Al-Furat Al-Awsat Technical University – Al-Musssaib Technical College  
15 Al-Hilla-Najaf main road, Al-Kufa, Iraq, 54001*

**Iryna Shvedchykova**✉

*Department of Computer Engineering and Electromechanics<sup>1</sup>  
shvedchykova.io@knu.edu.ua*

**Igor Panasiuk**

*Department of Heat Power Engineering, Resource Saving  
and Technogenic Safety<sup>1</sup>*

**Julia Romanchenko**

*Department of Electrical Engineering<sup>2</sup>*

**Inna Melkonova**

*Department of Electrical Engineering<sup>2</sup>*

<sup>1</sup>*Kyiv National University of Technologies and Design  
2 Nemyrovycha-Danchenko str., Kyiv, Ukraine, 01011*

<sup>2</sup>*Volodymyr Dahl East Ukrainian National University  
59-a Tsentralnyi ave., Severodonetsk, Ukraine, 93400*

✉ Corresponding author

## Abstract

An approach is proposed to carry out multivariate calculations of the magnetic field distribution in the working gaps of a plate polygradient matrix of an electromagnetic separator, based on a combination of the advantages of two- and three-dimensional computer modeling. Two-dimensional geometric models of computational domains are developed, which differ in the geometric dimensions of the plate matrix elements and working air gaps. To determine the vector magnetic potential at the boundaries of two-dimensional computational domains, a computational 3D experiment is carried out. For this, three variants of the electromagnetic separator are selected, which differ in the size of the working air gaps of the polygradient matrices. For them, three-dimensional computer models are built, the spatial distribution of the magnetic field in the working intervals of the electromagnetic separator matrix and the obtained numerical values of the vector magnetic potential at the boundaries of the computational domains are investigated. The determination of the values of the vector magnetic potential for all other models is carried out by interpolation. The obtained values of the vector magnetic potential are used to set the boundary conditions in a computational 2D experiment. An approach to the choice of a rational version of a lamellar matrix is substantiated, which provides a solution to the problem according to the criterion of the effective area of the working area. Using the method of simple enumeration, a variant of the structure of a polygradient matrix with rational geometric parameters is selected. The productivity of the electromagnetic separator with rational geometric parameters of the matrix increased by 3–5 % with the same efficiency of extraction of ferromagnetic inclusions in comparison with the basic version of the device.

**Keywords:** electromagnetic separator, electromagnetic field, boundary conditions, vector magnetic potential, finite element method.

DOI: 10.21303/2461-4262.2021.001713



## 1. Introduction

The most effective technology for extracting ferromagnetic particles up to 1 mm in size from various materials is polygradient magnetic separation. The working body of polygradient electromagnetic separators is a stationary matrix or a rotating rotor with a polygradient medium made of ferromagnetic bodies (balls, cylinders, rods, steel wool, pointed plates, etc.).

Most of the existing devices for polygradient magnetic separation are designed for purification of liquid media (pulp) [1]. For wet magnetic separation of weakly magnetic materials, rotary electromagnetic Jones separators of KHD Humboldt Wedag (Germany) with working ferromagnetic bodies in the form of corrugated plates are widely used; electromagnetic separators made by Sala (Sweden) and Metso minerals (Finland), which use steel mesh or cotton wool. Such devices are distinguished by a high efficiency of the working process, ensuring the removal of almost all highly magnetic particles from the pulp [2].

In connection with the growing requirements for product quality, the problem of removing finely dispersed ferromagnetic inclusions arising in the process of equipment wear is also relevant for bulk materials (flour, grain, sugar, medicinal mixtures, kaolin, etc.). The use of the above types of electromagnetic separators for solving the problems of cleaning bulk materials is economically inexpedient due to their high cost, metal and energy consumption, and the presence of small working air gaps. For cleaning bulk materials, open multi-pole magnetic systems are used, which are insufficiently effective in removing ferromagnetic impurities up to 1 mm in size. Therefore, reliable and effective cleaning of bulk materials from small metal impurities can only be provided by devices specially developed for these purposes by numerous manufacturers of magnetoseparation devices (for example, Ukrprommagnit (Ukraine), Erieze (USA), CALAMIT (Germany)). This article discusses a non-contact polygradient electromagnetic separator for cleaning bulk materials with a lamellar matrix, developed with the participation of the authors of the work. The basic version of the separator was installed at the Druzhkovka porcelain factory (Ukraine) to control the quality of kaolin purification. The device shows a fairly high efficiency of extraction of ferromagnetic inclusions, which amounted to 90.5–95.5 %.

An important stage in the design of polygradient electromagnetic separators designed to extract ferromagnetic particles up to 1 mm in size from dispersed media is the procedure for determining the rational geometric parameters of their plate matrices, which is multivariate. Usually, numerical methods for calculating magnetic fields and specialized software for two or three-dimensional modeling are used to solve it. The use of two-dimensional models is based on certain assumptions regarding the boundary conditions and the nature of the distribution of the magnetic field in the working intervals and does not require significant computing resources and calculation time. The advantages of three-dimensional models are taking into account the real geometrical dimensions of magnetic systems and the possibility of studying the influence of geometry on the flux distribution in any element of the magnetic circuit. At the same time, the determination of the spatial distribution of the field in complex three-dimensional models of electromagnetic separators is a rather laborious and time-consuming process. This determines the urgency of developing new approaches to multivariate calculations of magnetic fields in polygradient matrices of electromagnetic separators capable of providing the necessary computational efficiency and accuracy.

Numerous publications are devoted to the study of the distribution of the magnetic field in the working body (matrix) of polygradient magnetic separators. In work [3] it is shown that the method of polygradient magnetic separation is effective for removing or filtering small and weakly magnetic particles and is widely used for processing minerals, water purification, purification of cells and proteins. It is noted that the magnetic matrix is the most important structural element of the magnetic separator. The material, geometry, dimensions and arrangement of matrix elements can significantly affect the gradient and distribution of the magnetic field. But questions about the influence of the structural elements of the matrix on the performance of the separator remained unresolved. In [4], a new design of the rod matrix is described, which provides higher values of the magnetic field gradient. To study the influence of the structural parameters of the matrix on the efficiency of extraction of fine particles, a numerical-field analysis of the spatial distribution of the magnetic field by the finite element method (FEM) is carried out using the software Ansoft



Maxwell 3D (USA). The tetrahedron is adopted as the main mesh element in the modeling. For each model, about 100,000 tetrahedrons are used. The average time spent on simulation is about 6–8 hours in a personal computer with a Pentium 4 processor. Due to the high complexity of calculations, a limited number of standard sizes of matrix rods with a diameter of 3.0 and 3.5 mm are investigated. Taking this into account, in [5], an approach is proposed for calculating the magneto-static field in a doubly periodic heterogeneous medium (separator matrix) by the method of integral equations. The integral equation is formulated for the magnetization vector of the elements of the medium. The calculation of the field characteristics is carried out by solving the field problem in the area of the main parallelogram of periods without setting boundary conditions on its sides. Calculated expressions for the field strength and magnetic permeability tensor are obtained. The results of the study of the magnetic force field of the matrix of high-gradient magnetic separator are presented. At the same time, the method proposed in [5], although it is universal, is developed for calculating the characteristics of the magnetic field in local zones.

As the analysis of publications [6–11] shows, a more flexible FEM is mainly used for calculating the magnetic fields of electromagnetic devices. Thus, in [6], to study the effect of the configuration of the elements of the separator matrix on the efficiency of particle capture in high-gradient magnetic fields, three-dimensional finite element models were analyzed using the COMSOL Multiphysics software product (Sweden). The research results presented in [7], obtained only for a certain configuration of the polygradient matrix medium based on a single and multielement magnetic wire. It remains unclear whether these results can be extended to other types of polygradient media.

In [8], the principles of automated formation of two-dimensional geometric models of electrical machines for calculating their magnetic fields using the FEMM program (USA) are shown. The article [9] presents the principles and results of the numerical-field determination of the electromagnetic and energy parameters of three-phase asynchronous motors for the purpose of their verification analysis also using the FEMM program (USA). The calculation results obtained in a two-dimensional formulation require further experimental verification.

The article [10] reflects the results of numerous studies of two types of permanent magnet electric generators. The calculation of the characteristics of the generators under study was carried out in a three-dimensional setting using the Simcenter MagNet and Simcenter MotorSolve software packages. The article [11] presents the results of research on the performance characteristics of a permanent magnet disk generator. The calculation of the magnetic field and device characteristics was carried out using the Infolytica Magnet software package. The expediency of carrying out calculations using three-dimensional computer models has been substantiated, but their high labor intensity has been noted.

Thus, the analysis of publications allows to assert that in the study of magnetic fields of electromagnetic devices, in particular magnetic separators, numerical methods have found wide application, first of all, FEM in a two- or three-dimensional formulation. The experience of using numerical methods in calculating magnetic fields has shown that three-dimensional modeling requires significant computational and time resources, and the use of two-dimensional models is associated with certain assumptions. Therefore, it is expedient to conduct a study devoted to the development of a more efficient and universal combined approach to the analysis of magnetic fields, taking into account the advantages of finite element analysis in both two-dimensional and three-dimensional formulations.

The aim of research is the development and practical implementation of an approach that allows for multivariate calculations of the magnetic field distribution in the working gaps of the plate matrix of the electromagnetic separator with increased computational efficiency.

To achieve the aim, the following objectives are set:

- to substantiate an approach to carrying out multivariate calculations of the magnetic field distribution;
- to determine the boundary conditions for the working areas of the matrix using the selected three-dimensional models of the electromagnetic separator;
- to carry out variant calculations and determine the rational geometric parameters of the plate elements of the magnetic matrix using two-dimensional models of working zones.



## 2. Substantiation of the approach to carrying out multivariate calculations of the magnetic field distribution

The previous author's works [12–14] reflect the results of studies of a polygradient electromagnetic separator designed for cleaning bulk materials from fine ferromagnetic impurities up to 1 mm in size, namely:

– using the methodological tools of genetic synthesis and symmetry transformations, six structural variants of the lamellar polygradient matrix of an electromagnetic separator based on triangular elements are obtained [12];

– a preliminary comparative analysis of the synthesized structures is carried out to assess the degree of inhomogeneity of the magnetic field in their working intervals using a numerical MSE in a two-dimensional formulation [13];

– a rational structural version of the plate matrix of the separator is substantiated, the geometric model of which, indicating the main geometric dimensions, is shown in **Fig. 1** [14].

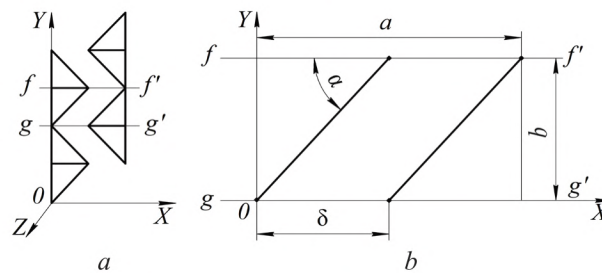


**Fig. 1.** Rational structural version of the lamellar matrix:  
 $a$  – geometric model;  $b$  – the main geometric dimensions of the working area

The main geometrical dimensions of the working area (**Fig. 1**):  $\delta$  – pole-to-pole working gap;  $\alpha$  – angle at the top of the pole protrusion;  $a$  – working width of the matrix;  $b$  is the base of the pole performance. The following geometric similarity criteria were set for the regions under study:  $X_1 = b/a$  and  $X_2 = \alpha$ . The ranges of variation of the geometric similarity criteria  $X_1$  and  $X_2$ , which are of practical interest, were:  $X_1 = b/a = 0.18 \dots 0.4$ ,  $X_2 = \alpha = 0.11\pi \dots 0.18\pi$ . The thickness  $t$  of the matrix plates (not shown in **Fig. 1**) in the direction of the  $Oz$  axis was taken  $t = 6$  mm. Taking into account the accepted ranges of variation of the geometric similarity criteria, 55 variants of the polygradient matrix were obtained and 2D models of their working clearances were constructed (**Fig. 2**), for which the boundary conditions were required to be specified. In particular, it was necessary to determine the values of the vector magnetic potential along the boundaries  $ch$  and  $de$  in **Fig. 2**, which coincide with the lines of force of the computational domain. In this case, if for the vector magnetic potential along one of the boundaries (for example, for the boundary  $ch$ ), the zero value  $A_{ch} = 0$  can be taken, then the vector magnetic potential  $A_{de}$  along the second boundary must be determined.

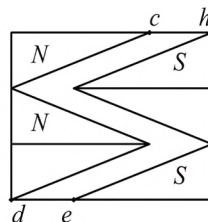


**Fig. 2.** 2D-model of the working area

The difference in the values of the vector magnetic potential  $|\overline{A_{de}} - \overline{A_{ch}}| = |\overline{A_{de}}|$  is equal to the average flux of the magnetic induction vector  $\Phi$  in the working air gap, which is per unit of pole thickness  $t$  in the direction of the  $Oz$  axis (**Fig. 1, a**;  $t = 6$  mm). That is, it is determined by the ratio  $|\overline{A_{de}}| = \Phi/t$ . Therefore, to determine the value of the potential  $A_{de}$ , it is necessary to calculate the magnetic flux  $\Phi$ . This problem can be solved only with the use of three-dimensional computer models.

To increase the computational efficiency of calculations of the magnetic flux and vector magnetic potential, it was decided to limit the construction and study of only three three-dimensional models of the electromagnetic system of the separator, which differ in the size of the working air gap  $\delta$ . For further analysis, the following three options of the electromagnetic separator were selected:

- option 1 (with the maximum  $\delta_{\max}$  value of the working gap): the distance between adjacent projections of the plates  $b=32.4$  mm ( $X_1=b/a=0.18$ ), the angle at the apex of the pole protrusion  $2\alpha=54^\circ$  ( $X_2=\alpha=0.15\pi$ ), working pole gap  $\delta=53$  mm;
- option 2 (with an average value  $\delta_{av}$  of the working gap, which satisfies the condition  $\delta_{\min}\leq\delta_{av}\leq\delta_{\max}$ ): the distance between adjacent protrusions of the  $b=72$  mm ( $X_1=b/a=0.4$ ), the angle at the apex of the pole protrusion  $2\alpha=66^\circ$  ( $X_2=\alpha=0.18\pi$ ), working pole gap  $\delta=37$  mm;
- option 3 (with a minimum  $\delta_{\min}$  value of the working gap): the distance between adjacent projections of the plates  $b=50$  mm ( $X_1=b/a=0.28$ ), the angle at the apex of the pole protrusion  $2\alpha=40^\circ$  ( $X_2=\alpha=0.11\pi$ ), the working pole gap  $\delta=13.6$  mm. These parameters correspond to the basic design of the electromagnetic separator.

It should be noted that the air gap  $\delta$  is determined through the geometric similarity criteria  $X_1=b/a$  vs  $X_2=\alpha$ . For the selected models, the air gap  $\delta$  varies in a fairly wide range: from  $\delta=13.6$  mm (option 3) to  $\delta=53$  mm (option 1). The determination of the values of the vector magnetic potential for all other models was carried out by interpolation.

To determine the magnetic flux  $\Phi$  in the working air gaps, the Magnet module of the Infolytica software package (Canada) was used [15]. The construction of the geometry of the 3D model (Fig. 3) of the electromagnetic separator for the purpose of importing it into the Magnet module was carried out in the KOMPAS program (Russia). Fig. 3 shows on the example of option 1 ( $\delta=53$  mm) a three-dimensional geometric model of an electromagnetic separator (Fig. 3, a) and a picture of the magnetic field distribution (Fig. 3, b).

When modeling, the following initial data were taken: current strength in the windings – 3.2 A; material of the magnetic circuit, matrix plates, matrix walls, which are parallel to the poles of the magnetic circuit – steel grade St. 3, the other two walls are aluminum.

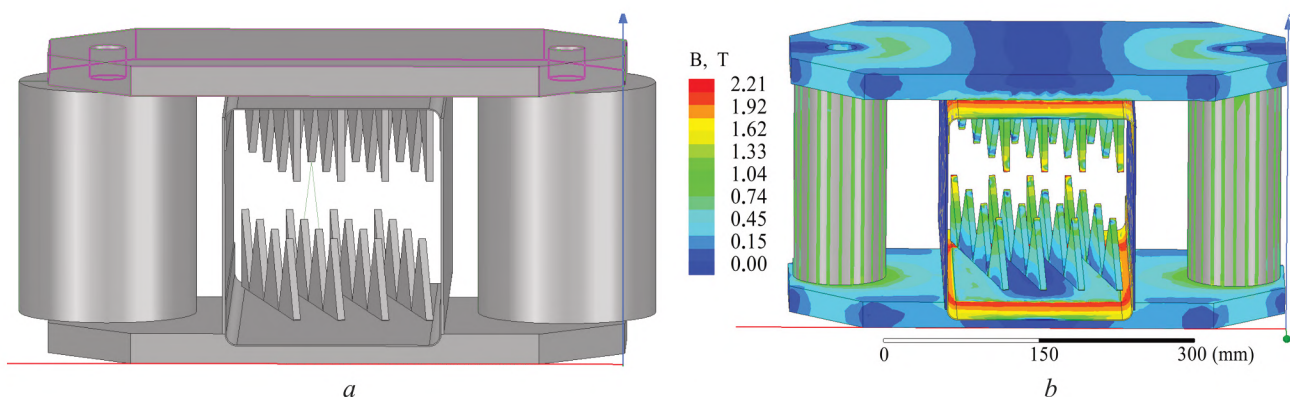


**Fig. 3.** Three-dimensional modeling of an electromagnetic separator:  
a – geometric model of the separator; b – distribution pattern of the magnetic field

To substantiate the possibility of using the Infolytica software package, a test task was solved and a 3D computer model of the electromagnetic separator was verified. The verification results showed that the use of the Infolytica program for computer modeling allows obtaining quantitative and qualitative data on the distribution of the magnetic field. These data can serve as a basis for further studies of the magnetic flux in the working interpole zone of the electromagnetic separator [16].

### 3. The results of research to determine the boundary conditions for the working areas of the matrix

Calculations of the magnetic flux  $\Phi$  through the area  $S$  (Fig. 4) with a width of  $t=6$  mm, limiting the working air gap of the separator matrix, have been carried out. According to these



calculations, the magnetic flux  $\Phi$  through the site  $S$  was: for option 1 – 0.0000126111 Wb, for option 2 – 0.0000558067 Wb, for option 3 – 0.0000640057 Wb. Accordingly, the value of the vector magnetic potential  $A_{de}$  in the section  $de$  (**Fig. 2**) was: for option 1 – 0.00630554 Wb/m, for option 2 – 0.027903332 Wb/m, for option 3 – 0.032002859 Wb/m.

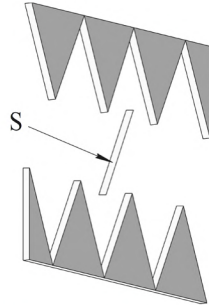


**Fig. 4.** To the calculation of the vector magnetic potential

To carry out variant calculations, it is necessary to determine the numerical values of the vector magnetic potential  $A_{de}$  at the boundary  $de$  (**Fig. 2**) for all 55 two-dimensional regions of the synthesized structures.

According to the results of 3D analysis, it was found that the value of the vector magnetic potential  $A_{de}$  depends on the filling of the working gap of the matrix with metal elements. So, the so-called filling factor  $k_m$  was introduced for consideration, which connects the basic geometric relations ( $X_1 = b/a$ ,  $X_2 = \alpha$ ) of the elements of the separator matrix,

$$k_m = \frac{b}{a} \operatorname{ctg} \alpha. \quad (1)$$

For structural variants of the matrix of the electromagnetic separator, which were investigated, the fill factor  $k_m$  was, respectively: for variant 1 –  $k_m = 0.3532$ ; for option 2 –  $k_m = 0.616$ ; for option 3 –  $k_m = 0.769$ .

**Table 1** shows the calculated values of the fill factor  $k_m$  with varying the geometric relationships  $X_1 = b/a$  and  $X_2 = \alpha$  in the ranges:  $X_1 = b/a = 0.18 \dots 0.4$ ,  $X_2 = \alpha = 0.1\pi \dots 0.18\pi$ .

Based on the data obtained, a graph was constructed (**Fig. 5**), which describes the dependence of the vector magnetic potential  $A_{de}$  on the fill factor  $k_m$ . Using this graph, the  $A_{de}$  values are determined by interpolation for any intermediate points belonging to the range  $0.3532 \leq k_m \leq 0.769$ .

**Table 1**  
Fill factor  $k_m$

$\alpha \backslash b/a$	0.18	0.20	0.25	0.28	0.30	0.35	0.40
0.11 $\pi$	0.495	0.549	0.687	0.769	0.824	0.962	–
0.12 $\pi$	0.455	0.505	0.631	0.707	0.758	0.884	–
0.13 $\pi$	0.416	0.462	0.578	0.647	0.693	0.809	0.924
0.14 $\pi$	0.386	0.429	0.536	0.600	0.643	0.751	0.858
0.15 $\pi$	0.3532	0.393	0.491	0.55	0.589	0.687	0.785
0.16 $\pi$	0.325	0.361	0.451	0.505	0.541	0.631	0.722
0.17 $\pi$	0.312	0.346	0.433	0.485	0.520	0.606	0.693
0.18 $\pi$	0.277	0.308	0.385	0.431	0.462	0.539	0.616

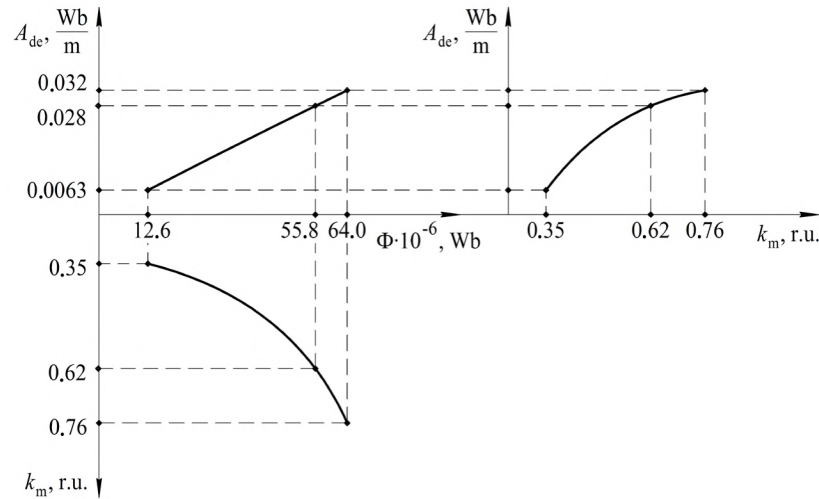


**Fig. 5.** Dependence of the vector magnetic potential  $A_{de}$  on the fill factor  $k_m$

To calculate the  $A_{de}$  values at intermediate points of the considered interval  $0.3532 \leq k_m \leq 0.769$ , an approximating function (regression) was constructed using the least squares method [17]:

$$A_{de} = -0.1349k_m^2 + 0.2132k_m - 0.0522. \quad (2)$$

Based on the results of polynomial approximation (2), the vector magnetic potential  $A_{de}$  was determined for various combinations of  $X_1$  and  $X_2$ . For clarity, the results of calculating  $A_{de}$  are shown in the form of a volumetric graph (Fig. 6).

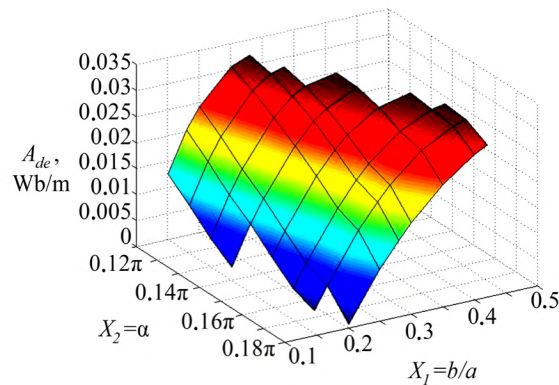


**Fig. 6.** Distribution of vector magnetic potential  $A_{de}$

Thus, the values of the vector magnetic potential  $A_{de}$  have been determined for various combinations of geometric similarity criteria  $X_1$  and  $X_2$  of the selected structure of the separator matrix.

These data were used to set the boundary conditions in a computational 2D experiment when choosing an electromagnetic separator matrix with rational geometric dimensions.

#### 4. Optional calculations of the magnetic matrix of an electromagnetic separator using two-dimensional models of working zones

For the basic model of the separator (option 3), during the computational experiment, the fraction  $P_b$  of the area of the working zone (pole-to-pole gap) of the matrix was determined, in which the value of the force parameter  $f_{np}$  satisfies the requirement:

$$f_{\min} \leq f_{np} \leq f_{\max}, \quad (3)$$



where  $f_{\min}$  – the minimum threshold value of the power  $f_{\min} = (H \text{grad}(H))_{\min}$ , at which, based on the experience of separator design, a sufficiently high efficiency of extraction of ferromagnetic inclusions is ensured (in the calculations, the value  $f_{\min} = 3 \cdot 10^8 \text{ A}^2/\text{m}^3$  was taken);  $f_{\max}$  – the maximum value of the specific reduced force, which for the base model was  $f_{\max} = (H \text{grad}(H))_{\max} = 8.6 \cdot 10^9 \text{ A}^2/\text{m}^3$ .

This part of the area of the working area  $P_b$  was expressed as a percentage in relation to the value  $P$  of the entire area of the working area:  $\gamma = P_b/P$ . In this case, the parameter  $\gamma$  depends significantly on the geometric relationships  $X_1$  and  $X_2$  and can be defined as the effective area of the working area of the matrix [14]. For the basic version of the separator, the parameter  $\gamma$  was  $\gamma = 5.3 \%$ . Some of the calculation results obtained during the computational experiment are shown in Fig. 7.

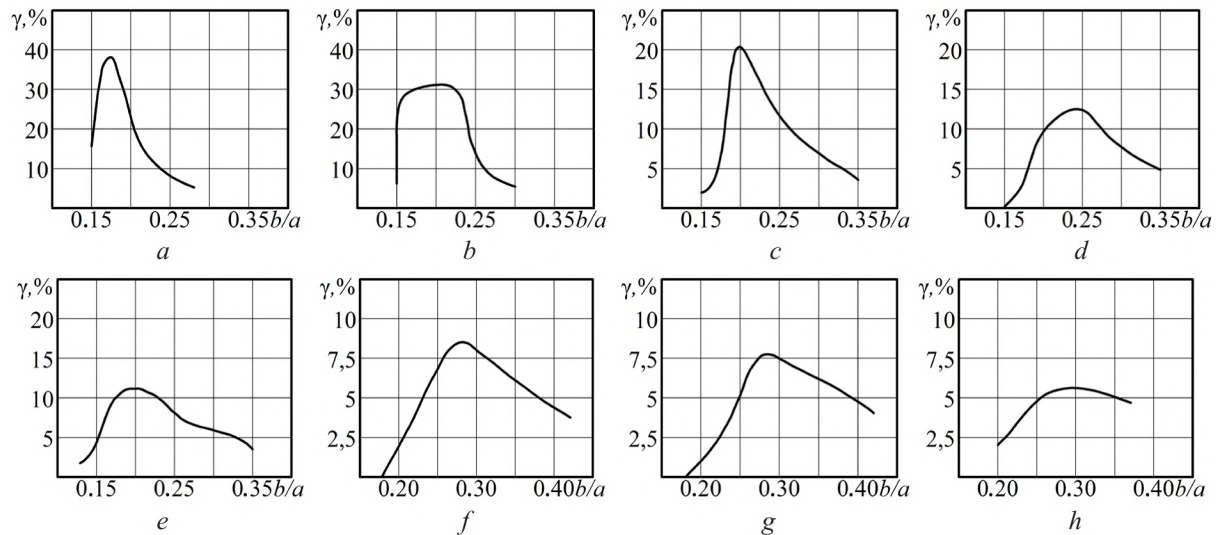


**Fig. 7.** Results of optional calculations of the parameter  $\gamma$ :

$a - X_2 = \alpha = 0.11\pi$ ;  $b - X_2 = \alpha = 0.12\pi$ ;  $c - X_2 = \alpha = 0.13\pi$ ;  $d - X_2 = \alpha = 0.14\pi$ ;  $e - X_2 = \alpha = 0.15\pi$ ;  
 $f - X_2 = \alpha = 0.16\pi$ ;  $g - X_2 = \alpha = 0.17\pi$ ;  $h - X_2 = \alpha = 0.18\pi$

Options of the investigated systems that satisfy the condition:

$$\gamma(X_1, X_2) \rightarrow \max. \quad (4)$$

The calculation results obtained during the computational experiment showed that condition (4) is satisfied by the structure of the matrix with geometric similarity criteria  $X_1 = b/a = 0.18$ ;  $X_2 = \alpha = 0.11\pi$ , for which the parameter  $\gamma$  takes the maximum value  $\gamma = 36.5 \%$ . For comparison, the  $\gamma$  parameter for the basic structure was  $5.3 \%$ . Thus, the following parameters should be considered rational:  $X_1 = b/a = 0.18$  i  $X_2 = \alpha = 0.11\pi$ .

The reliability of the results obtained during the computational experiment was confirmed by comparison with the results obtained by other researchers [2, 18–20]. According to estimated calculations, the productivity of an electromagnetic separator with rational geometric parameters of a plate matrix will increase by 3–5 % with a constant extraction efficiency of ferromagnetic inclusions in comparison with the basic version of the device.

## 5. Discussion of the results of studying the distribution of the magnetic field in the matrix of the polygradient separator

The paper substantiates an approach to multivariate calculations of the magnetic field distribution, based on the use of the advantages of two- and three-dimensional computer modeling. This made it possible to reduce the time costs associated with three-dimensional modeling, and thus increase the computational efficiency of calculations in general.

The practical implementation of the proposed approach provided for the use of a limited number of three-dimensional models of the electromagnetic system of the separator, as auxiliary

ones, for finding the boundary conditions of the computational domains. Three versions of the electromagnetic separator were chosen with different values of the working air gap  $\delta$ : minimum  $\delta_{\min}$ , maximum  $\delta_{\max}$  and average  $\delta_{av}$  ( $\delta_{\min} \leq \delta_{av} \leq \delta_{\max}$ ). **Fig. 3** shows, for example, a three-dimensional geometric model of an electromagnetic separator (**Fig. 3, a**) and a picture of the magnetic field distribution (**Fig. 3, b**) for a variant of the device with the maximum value of the working gap ( $\delta_{\max} = 53$  mm).

To solve the second problem of the study, the boundary conditions were determined, in particular the vector magnetic potential  $A_{de}$  in the section  $de$  (**Fig. 2**) for the working areas of the matrix using the selected three-dimensional models of the electromagnetic separator. An approximating regression model is built – formula (2), with the help of which the vector magnetic potential  $A_{de}$  is determined for various combinations of geometric similarity criteria  $X_1$  and  $X_2$ .

The boundary conditions for the vector magnetic potential  $A_{de}$ , obtained from the results of three-dimensional computer modeling, were further used to carry out variant calculations and determine the rational geometric parameters of the plate elements of the magnetic matrix according to the criterion  $\gamma$  of the effective area of the working area of the matrix using two-dimensional models. It is shown that the variants of the systems under study that satisfy condition (4) will be considered rational. The analysis of the results obtained, presented in **Fig. 7**, made it possible to determine the numerical values of the geometric similarity criteria ( $X_1 = b/a = 0.18$ ;  $X_2 = \alpha = 0.11\pi$ ) for which the parameter  $\gamma$  takes the maximum value ( $\gamma = 36.5$  %).

At the initial stage of the study of the spatial distribution of the magnetic field in the working gaps of the matrix of the polygradient separator, it was assumed to use the numerical finite element method in a three-dimensional formulation. The undoubted advantage of 3D modeling is the ability to calculate the magnetic field in any structural element of the electromagnetic separator and to approximate the calculation results to real processes. At the same time, the analysis of the field distribution for 55 computer 3D models of the electromagnetic separator, which differ in the geometric dimensions of the matrix elements, required a significant computation time. Taking this into account, a reasonable approach to carrying out multivariate calculations of the magnetic field distribution, based on the use of the advantages of two- and three-dimensional computer modeling. This made it possible to reduce the time costs associated with three-dimensional modeling, and thus increase the computational efficiency of calculations in general.

The distribution of the magnetic field in the working areas of the matrix is also influenced by other factors, for example, the shape of the matrix elements. The work investigated plate matrices, the elements of which have the shape of an equilateral triangle. Determination of the influence on the distribution of the magnetic field of plate elements with a different geometric shape, for example, trapezoidal, was not included in the research tasks. The study of this influence can be the subject of further research work.

## 6. Conclusions

1. A combined approach to the analysis of magnetic fields is substantiated, taking into account the advantages of finite element analysis in both two-dimensional and three-dimensional formulations. This approach is capable of providing the required computational efficiency and accuracy.

2. An approach is proposed to determine the boundary condition (vector magnetic potential) at the boundary  $de$  of two-dimensional computational domains, based on the study of the spatial distribution of the magnetic field in the working gap of the electromagnetic separator. The numerical values of the vector magnetic potential at the boundary of the region are obtained for three three-dimensional models of the electromagnetic system of the separator using the Magnet module of the Infolytica software package. The calculation of the boundary conditions for all other models was carried out by interpolation.

3. The choice of a rational version of the polygradient matrix of the electromagnetic separator is carried out according to the criterion  $\gamma$  of the effective area of the working area. The analysis carried out using the method of simple enumeration of options showed that the structure with the parameters  $X_1 = b/a = 0.18$  and  $X_2 = \alpha = 0.11\pi$  in terms of a high value of the effective area  $\gamma$  of the



working area ( $\gamma=36.5\%$ ) can be considered rational. A variant of the structure of the polygradient matrix with rational parameters  $X_1=b/a=0.18$  and  $X_2=\alpha=0.11\pi$  is adopted in comparison with the basic design of a separator with parameters  $X_1=b/a=0.28$ ,  $X_2=\alpha=0.11\pi$ , chosen empirically, is characterized by the following:

- the maximum intensity  $H_{\max}$  and the maximum intensity gradient  $\text{grad}(H)_{\max}$  of the magnetic field of the structure with rational parameters exceed almost 3 times the corresponding indicators of the basic structure;
- for a structure with rational parameters, the value of the effective area of the working zone  $\gamma$  is almost 7 times larger than that of the base one.

### Acknowledgments

The authors express their sincere gratitude to the staff of the Electromechanical Systems Department of the Institute of Electrodynamics of the National Academy of Sciences of Ukraine for their help in carrying out numerical calculations using the Infolytica software package.

---

### References

- [1] Soloshych, I., Shvedchykova, I. (2016). Development of systematics ranked structure of environmental protecting equipment for cleaning of gas emissions, wastewater and solid waste. *Eastern-European Journal of Enterprise Technologies*, 6 (10 (84)), 17–23. doi: <https://doi.org/10.15587/1729-4061.2016.86462>
- [2] Svoboda, J. (2004). *Magnetic techniques for the treatment of materials*. Springer, 642. doi: <https://doi.org/10.1007/1-4020-2107-0>
- [3] Ge, W., Encinas, A., Araujo, E., Song, S. (2017). Magnetic matrices used in high gradient magnetic separation (HGMS): A review. *Results in Physics*, 7, 4278–4286. doi: <https://doi.org/10.1016/j.rinp.2017.10.055>
- [4] Li, W., Han, Y., Xu, R., Gong, E. (2018). A Preliminary Investigation into Separating Performance and Magnetic Field Characteristic Analysis Based on a Novel Matrix. *Minerals*, 8 (3), 94. doi: <https://doi.org/10.3390/min8030094>
- [5] Tolmachev, S. T., Bondarevskiy, S. L., Il'chenko, A. V. (2020). Magnetic properties of multicomponent heterogeneous media with a doubly periodic structure. *Electrical Engineering & Electromechanics*, 1, 29–38. doi: <https://doi.org/10.20998/2074-272x.2020.1.05>
- [6] Zeng, J., Tong, X., Yi, F., Chen, L. (2019). Selective Capture of Magnetic Wires to Particles in High Gradient Magnetic Separation. *Minerals*, 9 (9), 509. doi: <https://doi.org/10.3390/min9090509>
- [7] Chen, H., Bockenfeld, D., Rempfer, D., Kaminski, M. D., Liu, X., Rosengart, A. J. (2008). Preliminary 3-D analysis of a high gradient magnetic separator for biomedical applications. *Journal of Magnetism and Magnetic Materials*, 320 (3-4), 279–284. doi: <https://doi.org/10.1016/j.jmmm.2007.06.001>
- [8] Milykh, V. I. (2018). The system of automated formation of electrical machines computational models for the femm software environment. *Tekhnichna Elektrodynamika*, 2018 (4), 74–78. doi: <https://doi.org/10.15407/technd2018.04.074>
- [9] Milykh, V. I. (2018). Numerically-field analysis of the adequacy of the design data of three-phase induction motors and the method of their refinement on this basis. *Tekhnichna Elektrodynamika*, 2018 (1), 47–55. doi: <https://doi.org/10.15407/technd2018.01.047>
- [10] Grebenikov, V. V., Gamaliia, R. V. (2019). Comparative Analysis of Two Types of Generators with Permanent Magnets for Wind Turbine. 2019 IEEE International Conference on Modern Electrical and Energy Systems (MEES). doi: <https://doi.org/10.1109/mees.2019.8896375>
- [11] Dobzhanskyi, O., Hossain, E., Amiri, E., Gouws, R., Grebenikov, V., Mazurenko, L. et. al. (2019). Axial-Flux PM Disk Generator With Magnetic Gear for Oceanic Wave Energy Harvesting. *IEEE Access*, 7, 44813–44822. doi: <https://doi.org/10.1109/access.2019.2908348>
- [12] Shvedchykova, I., Lutsenko, I., Romanchenko, J. (2015). A study of polygradient media structure regularities. *Eastern-European Journal of Enterprise Technologies*, 4 (7 (76)), 62–67. doi: <https://doi.org/10.15587/1729-4061.2015.47785>
- [13] Shvedchykova, I., Romanchenko, J., Nikitchenko, I. (2017). Comparative analysis of inhomogeneity degree of magnetic field of polygradient magnetic separators for purification of bulk materials. 2017 International Conference on Modern Electrical and Energy Systems (MEES). doi: <https://doi.org/10.1109/mees.2017.8248873>
- [14] Gerlici, J., Shvedchykova, I. A., Romanchenko, J. A., Nikitchenko, I. V. (2018). Determination of the rational geometrical parameters of plate type elements of magnetic matrix of the polygradient separator. *Electrical Engineering & Electromechanics*, 4, 58–62. doi: <https://doi.org/10.20998/2074-272x.2018.4.10>
- [15] Maliar, V. S. (2018). *Teoretychni osnovy elektrotekhniki*. Lviv: Vydavnytstvo Lvivskoi politekhniki, 416.

- [16] Simcenter MAGNET. Available at: <https://www.plm.automation.siemens.com/global/en/products/simcenter/magnet.html>
- [17] Chekotovskyi, E. (2018). Statystychni metody na osnovi Microsoft Excel 2016. Kyiv: Znannia, 408.
- [18] Ren, L., Zeng, S., Zhang, Y. (2015). Magnetic field characteristics analysis of a single assembled magnetic medium using ANSYS software. International Journal of Mining Science and Technology, 25 (3), 479–487. doi: <https://doi.org/10.1016/j.ijmst.2015.03.024>
- [19] Song, C., Ning, G., Yuan, Z., Jing, L., Hui, C., Yao, M. (2014). Investigation of the influence of different matrix rotation angles on the surrounding magnetic field in a uniform magnetic field. Ming Metall Eng, 34, 290–294.
- [20] Shun, Z., Liang, S., Juan, W., Yue, W. (2012). Experimental study on magnetic separation by conical flux gathering media and optimization of its cone angle. Min Process Equip, 74–79.

Received date 15.12.2020

Accepted date 12.03.2021

Published date 13.09.2021

© The Author(s) 2021

This is an open access article under the CC BY license

(<http://creativecommons.org/licenses/by/4.0>).

**How to cite:** Jasim, J. M. J., Shvedchykova, I., Panasiuk, I., Romanchenko, J., Melkonova, I. (2021). Increasing the efficiency of multy-variant calculations of electromagnetic field distribution in matrix of a polygradient separator. EUREKA: Physics and Engineering, 5, 69–79. doi: <https://doi.org/10.21303/2461-4262.2021.001713>



## ANALYSIS OF RELIABILITY OF THE DRILL PIPE IN THE CLAMPING MECHANISM

**Emin Musa Afandiyev**

*Department of Engineering and Applied Science<sup>1</sup>*

**Mahammadali Nuraddin Nuriyev**✉

*Department of Engineering and Applied Science<sup>1</sup>*

*mehman62@mail.ru*

<sup>1</sup>*Azerbaijan State Economic University (UNEC)*

*6 Istiglaliyyat str., Baku, Azerbaijan, AZ 1001*

✉ **Corresponding author**

### Abstract

In oilfield equipment, a significant place is occupied by clamping mechanisms used to grip pipes during tripping operations. They are mainly divided into 2 groups. The first includes mechanisms with a forced clamping of the part. The second group includes self-clamping devices with a wedge mechanism. Here, the clamping force increases in proportion to the axial shear force. In these clamping devices, clamping jaws serve as a common element. In addition to smooth jaws, there may be jaws with notches on the inner cylindrical surface. Such notches contribute to an increase in the coefficient of adhesion when clamping cylindrical parts, in particular pipes. During the operation of clamping devices with corrugated jaws, the teeth of the notch are introduced into the pipe walls under the action of the clamping force. The shearing force can then displace the pipe relative to the jaws. The adhesion coefficient  $\mu$  is the ratio of the shear force  $P$  to the clamping force  $Q$ , i. e.  $P/Q$ . Exceeding the shear force  $P$  of the limit value causes the pipe to be clamped to move. The correct choice of the place of load application is also of great importance.

Optimum clamping performance can be achieved by clamping workpieces without slipping from shear forces. At the same time, it is necessary to ensure reliability, efficiency, productivity. Therefore, all factors that determine the holding capacity of clamping mechanisms should be considered. These factors include the coefficient of adhesion, the design of the working surfaces of the clamping elements, the type of notch of the corrugated jaws and the place of application of the clamping force.

**Keywords:** holding capacity, drill pipe, clamping mechanism, string weight, clamping area.

**DOI: 10.21303/2461-4262.2021.001765**

### 1. Introduction

The factors influencing the quality of drill pipes in the clamping mechanism during operation are considered. Pipes are subject to elastic and plastic deformation. They are subjected to high loads from clamping forces, as well as axial tensile forces from the weight of the column. Therefore, increased requirements are imposed on the reliability of pipes. Experiments were carried out to establish the effect of the load application on the stresses and deformations of cylindrical thin-walled parts.

Practice shows that wedge grips used in round-trip operations are widely used in the oil-field business. Significant loads acting both on the wedge grips and on the pipes being clamped place high demands on their holding capacity. The elimination of accidents associated with the breakage of a string at the rig requires significant resources. This explains the relevance of the presented work.

The holding capacity of the wedge grip is related to the magnitude and nature of the stresses and deformations arising in the section of the pipe at the point of its grip. The correct choice of the area for fixing cylindrical parts will reduce deformation during operation. An important role is played by the methodology for calculating the maximum permissible weight of the pipe string. To achieve this aim, the following objectives were set:

- determine the effect of the place of application of the clamping force on the stress state of the cylindrical part in the clamping mechanism,
- improve the methodology for calculating the maximum permissible weight of a pipe string during tripping operations while drilling oil and gas wells.

## 2. Literature review and problem statement

The high labor intensity and energy intensity of the oil production process make increased demands on the quality of drilling equipment, in particular, clamping mechanisms and drill pipes. Extending the service life of drill pipes minimizes the occurrence of emergencies. Therefore, work in this direction is of great practical importance.

In work [1], the design features of clamping devices used in round-trip operations when drilling wells are considered. However, not enough attention has been paid to damage to the outer surface of the pipe by clamping jaws.

In work [2] it is shown that the state of the pipe in the clamping device is influenced by various factors, such as radial and axial loads, clamping force, column mass, place of load application. It is noted that the most optimal operation of the clamping jaws is characterized by an oblique intersecting notch, which provides a high holding capacity of the clamping mechanisms.

Scientific research on the operation of clamping mechanisms with oilfield pipes has also been carried out at the American Petroleum Institute (API). In these works, it was noted that deformations of drill pipes occur due to cuts, which are left by the teeth of the clamping jaws of the drill tongs or wedge grips [3].

Work [4] is devoted to the study of the influence of external factors on the stress state of the pipe. The analysis of adhesion coefficients in clamping devices is given. Methods for improving their elements in order to increase the adhesion coefficients are described. Methods for improving the design of their elements are proposed in order to increase the adhesion coefficients.

Other works have also investigated the effect of clamping device design elements on the stress state and deformation of the pipe, and recommendations are given for improving their design in order to increase the holding capacity. A method of surface hardening is proposed to increase the service life of drill pipes [5–7].

In works [8, 9] it is noted what deformations the pipe is subject to during operation. The reasons for material creep are considered, which can be a consequence of stress relaxation under prolonged action of significant stresses. The process of stress relaxation and models for their determination and accounting are considered in [9]. These processes show that in order to increase the holding capacity of clamping devices, it is necessary to comprehensively study all the factors that affect the deformation of the drill pipe during tripping operations.

In studies [10, 11], attention is paid to the issues of safe operation of the pipe string during tripping operations.

Despite the extensive literature on this topic, many problems related to the behavior of drill pipes during tripping operations still await their solution. Insufficient attention is paid to recommendations for reducing stresses and deformations when fastening thin-walled cylindrical and other similar parts in clamping devices. There are practically no dependencies for calculations and analysis of loading schemes.

Reliability and durability of clamping devices when working with thin-walled cylindrical parts is of great importance, both in mechanical engineering and in the oil and gas industry. Therefore, studying the issues of increasing the holding capacity of clamping mechanisms and reducing pipe deformations is an urgent task.

## 3. The aim and objectives of research

The aim of this research is to determine the possibility of increasing the holding capacity of wedge grips and other clamping mechanisms in different conditions of work with cylindrical parts.

To achieve this aim, it is necessary to solve the following objectives:

- to determine the influence of the place of application of the clamping force on the stress state of the cylindrical part in the clamping mechanism;
- to improve the methodology for calculating the maximum permissible weight of a pipe string during tripping operations while drilling oil and gas wells.



#### 4. Materials and methods of research

##### 4. 1. Analysis of the place of load application

An analysis of the influence of the place of action of clamping forces on the value of the maximum radial deformation of thin-walled cylindrical parts was carried out using an experimental research method.

The hypothesis was the idea that the place of application of the clamping load plays a significant role in the magnitude of the radial deformation of the cylindrical part. An experiment was carried out using a specially designed pipe-clamping chuck for clamping the part (Inventor's Certificate No. 910370) **Fig. 1**. When clamping the parts, the chuck pads are closed and the pipe is pre-clamped. When the pipe is screwed in, it rotates under the action of a torque, and an additional clamping of the pipe occurs.

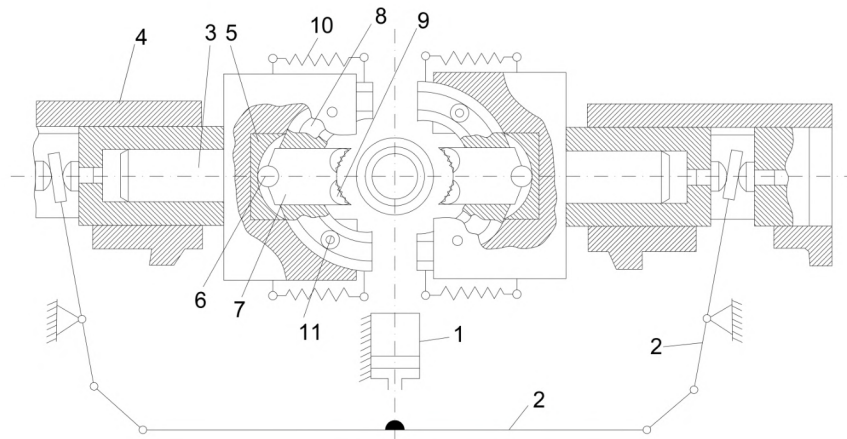


**Fig. 1.** Pipe-clamping chuck

The maximum radial deformation of the pipe as a result of the action of a uniformly distributed annular load  $Q$  applied at the end of the pipe is determined by the formula:

$$W_{\max} = \frac{Q}{2\beta^3 D}, \quad (1)$$

where  $\beta$  – angle of coverage with one jaw (**Fig. 2**).

With a load applied in the middle part of the pipe at a distance  $C \geq 3/4 \cdot \pi/\beta = L/2\beta$  from the end, the deformation is equal to:

$$W_{\max cp} = \frac{Q}{8\beta^3 D}, \quad (2)$$

where  $L$  – the limiting deformation zone.

Comparison of the values of the maximum deformations, which are determined by expressions (1), (2), indicates that with distance from the end face of the place of application of the load  $Q$ , the maximum deformation decreases, which reaches a minimum at  $C \geq \pi/2\beta \approx 1.6/\beta \approx L_1$  and remains equal  $Q/8\beta^3 D$ . In this case, a decrease in deformation is possible by 4 times.

The maximum radial deformation of a cylindrical part of small length (rings, bushings, sleeves) under the action of an annular force  $Q$  applied in the end section is equal to:

$$W_{\max av} = \frac{Q}{8\beta^3 D} k_1, \quad (3)$$

applied in the middle of the cylinder is equal to:

$$W_{\max av} = \frac{Q}{8\beta^3 D} k_2, \quad (4)$$

where  $k_1$  and  $k_2$  are coefficients depending on the length of the short cylinder, given in **Table 1**.

**Table 1**

Auxiliary data for the transition from long cylindrical parts to short

$\beta l_1$	0.4	0.6	0.8	1.0	1.2	1.4	1.7	2.0	3.0	6.0
$K_1$	4.990	3.310	2.507	2.019	1.699	1.479	1.265	1.137	1.007	1.000
$K_2$	1.601	1.406	1.228	1.079	0.975	0.921	0.915	0.946	1.000	1.000

Here  $\beta l_1$  – the reduced length of the short cylindrical part.

According to the above formulas (3), (4) and the data in Table 1, the ratios  $W_{\max \text{ end}}/W_{\max \text{ av}}$  are determined depending on the reduced length of the short part  $\beta l_1$  (**Table 2**).

**Table 2**Reduction of deformations of a short cylindrical part of length  $\beta l_1$  when it is fixed in the middle

$\beta l_1$	0.4	0.6	0.8	1.0	1.2	1.4	1.7	2.0	3.0	6.0
$W_{\text{end}}/W_{\text{av}}$	12.5	9.45	8.2	7.5	7.0	6.43	5.55	4.8	4.028	4.0

When clamping short cylinders (rings, sleeves), clamping forces should be applied not at the end, but in the middle of the workpiece being clamped. In this case, the maximum deformations are reduced up to 10 times. With a decrease in the length of the part  $\beta l_1$ , the reliability of fixing in the middle part increases.

In existing clamping mechanisms, the clamping force is distributed over the area. To check the optimal choice of the place for fixing the pipe in the mechanism that provides a uniformly distributed load on the section  $l_i$ , 2 options are possible:

1. Uniformly distributed load acts at the end on the length  $l_i$ , and the maximum value of the radial deformation is obtained in the section at the end  $W_{\max \text{ end } l_i}$ .
2. Uniformly distributed load acts on the same length  $l_i$  in the middle part of the part. And the maximum radial deformation  $W_{\max \text{ av } l_i}$  is observed in the middle of the section where the force is applied.

The results of comparison of the maximum deformations  $W_{\max \text{ end } l_i}$  and  $W_{\max \text{ av } l_i}$  arising at different lengths of the loading section  $\beta l_1$  are given in **Table 3**.

**Table 3**

Reducing pipe deformations when fixing it in the middle part

$\beta l_1$	0.2	0.4	1	1.4	2	2.6	3	4	7
$W_{\text{end } l_i}/W_{\text{av } l_i}$	3.61	3.26	2.37	1.94	1.47	1.24	1.10	0.95	0.97

It follows from the above table that when fixing a cylindrical part with a uniformly distributed load of  $Q$  value over a length  $\beta l_1$ , it is advisable to use the clamping force in the middle part at a distance  $l_2 \geq 3/4 \cdot \pi/4\beta$  from the end.

#### 4. 2. Calculation of the permissible load on the drill pipe

With increasing drilling depths, special attention should be paid to calculating the maximum permissible pipe load. This is due to the fact that with a large weight, the risk of column breakage increases. To ensure reliable operation of the clamping device, it is necessary to determine the maximum load on the pipe. Such a load should not exceed the moving load. A method for calculating the permissible load on the drill pipe is proposed.

When selecting drill pipe strings, only axial load is taken into account, that is, weight. The obtained results of experimental studies made it possible to develop a methodology for calculating



the maximum permissible weight of drill strings, taking into account the influence of some factors. The determination of the ultimate axial load on a pipe clamped in a wedge grip (**Fig. 2**) is carried out according to the formula [11]:

$$P = \frac{\sigma F}{1 + \frac{d_{av}}{4l \operatorname{tg}(\alpha + \varphi)}}, \quad (5)$$

where  $F$  – cross-sectional area of the pipe;  $\alpha$  – slope angle of the wedge;  $\varphi$  – angle of friction between the outer surface of the wedges and the body;  $l$  – wedge length;  $d_{av}$  – average diameter of the pipe section.

The safety factor is taken to  $k = 1.15\text{--}1.2$ .

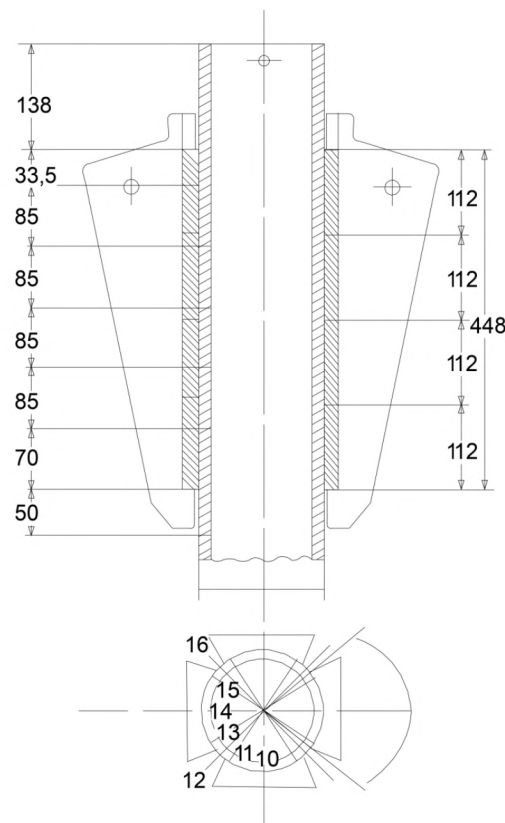


**Fig. 2.** Drill pipe in wedge grip

**Fig. 2** shows the zone of action of the wedge grip on the pipe during the round trip operations.

**Fig. 1** shows a chuck used to investigate the effect on deformation of a load location on short cylindrical parts.

Comparison of the results of ultimate loads, calculated using this formula, with experimental data obtained when determining stresses and strains in a drill pipe clamped in a wedge grip, showed that the above formula gives overestimated values of the permissible load.

When calculating the load, one should also take into account the error in the shape of the pipe, inaccuracy in the manufacture of parts of the clamping mechanism, incomplete coverage of the pipe with clamping jaws, etc. Taking into account the experimental data obtained, coefficients reflecting the actual conditions of clamping should be introduced into the above formula.

The maximum permissible load on a drill pipe clamped in a wedge grip with a uniformly distributed load should be determined by the formula, taking into account the coefficient  $k$ , taking into account the actual contact area of the jaws with the pipe:

$$P = \frac{\sigma F}{1 + \frac{d_{av}}{4l \operatorname{tg}(\alpha + \varphi)}} \frac{1}{k_1}, \quad (6)$$

where  $k$  – coefficient taking into account the actual contact area of the jaws with the pipe, 0.4–0.7;  $k_1$  – safety factor 1.2–1.6.

The ultimate load  $P$  on the drill pipe clamped in a wedge grip with gaps between the jaws  $>5^\circ$  should be calculated by the formula:

$$P = \frac{\sigma F}{1 + \frac{d_{av} k_3}{4l k_2 \operatorname{tg}(\alpha + \varphi)}} \frac{1}{k_1}, \quad (7)$$

where  $k_2$  – coefficient that takes into account the actual angle of coverage of the pipe with jaws:

$$k_2 = \frac{n\beta}{360}, \quad (8)$$

where  $\beta$  – angle of coverage with one jaw;  $n$  – number of jaws along the perimeter;  $k_3$  – coefficient characterizing the value of the bending moment in the section between the jaws in connection with a decrease in  $\beta$ ;

$$k_3 = \frac{\eta_1}{\eta}, \quad (9)$$

where  $\eta$  – coefficient characterizing the value of the bending moment in the section between the jaws ( $\alpha = 45^\circ$ );  $\eta_1$  – coefficient characterizing the value of the bending moment in the section  $\alpha = 45^\circ$  when clamping a part with a load evenly distributed along the perimeter.

$\eta$  is determined by the formula:

$$\eta_i = \frac{1}{\pi} \left[ \theta(1 + 2\sin^2 \theta) + 3\sin \theta \cos \theta \right] - \sin \theta (\sin \alpha + \cos \alpha), \quad (10)$$

where

$$\theta = \frac{\beta}{2}.$$

Using the above formulas, it is possible to determine the permissible weights of drill strings for various sizes and strength groups of the pipe material. The values of the coefficients are determined according to the given method.

## 5. Results and discussion of the study of the state of the cylindrical part in the clamping mechanism, as well as the factors affecting the permissible weight of the drill string

In the process of clamping short cylindrical parts such as pipes, rings, sleeves, a radial load is exerted on them, causing deformations of the shape, which depend on the place of application of the load. The experiments carried out made it possible to compile tables of deformations of cylindrical parts in different places of action of clamping forces. Analysis of these tables shows that the smallest deformations occur when clamping parts in the middle part of a cylindrical part under the same radial loads. The results of the analysis show that thin-walled cylindrical parts (pipes, sleeves, rings) should be fixed not at the end, but in the middle part, so as in this case, the maximum deformation is less with the same clamping forces.

When clamping short cylinders (rings, sleeves), clamping forces should be applied not at the end, but in the middle of the workpiece being clamped. In this case, the maximum deformations are reduced up to 10 times. With a decrease in the length of the part, the reliability of fastening in the middle part increases.



During tripping operations, at individual peak points, the compressive stresses exceed the pipe's yield point. These points are formed by repeatedly clamping the pipe in the same area, which can lead to an emergency. The existing calculation of the maximum permissible weight of a pipe string does not take into account factors that arise in real conditions, and gives overestimated values of permissible loads. Coefficients are entered into the calculation formula taking into account the actual clamping conditions.

The influence of the place of application of clamping forces on the value of the maximum radial deformation of thin-walled cylindrical parts is considered.

Based on the results of the experiments, tables of radial deformations of cylindrical parts are compiled for different variants of places of load application. The results of maximum deformations at different lengths of loading sections are compared. From the analysis carried out, it follows that the cylindrical parts must be fixed not at the end, but in the middle part, due to the fact that the maximum deformation in this case decreases with the same clamping forces.

The sources on deformations of thin-walled parts did not consider the question of the optimal place for applying a load to a short cylindrical part. Materials of cylindrical parts, grades of alloys and their physical and mechanical properties can be taken into account in further work. The complexity of this study is the need for extensive industrial testing. During tripping operations in a wedge grip, the drill or casing is subjected to multiple clamping in the same range. If, at individual peak points, the compressive stresses exceed the yield strength of the pipe, plastic deformation occurs at these points on the pipe surface. With a large number of clampings, plastic deformation manifests itself at different points of the pipe along the length and circumference, forming a decrease in the outer diameter of the pipe in this area. In this case, timely rejection of damaged pipes is necessary in order to avoid creating an emergency.

The existing method for calculating the maximum allowable weight of a pipe string does not take into account the factors that arise in practical conditions and gives overestimated values of the allowable loads. This can lead to pipe failure. Factors have been entered into the formula to take into account the actual clamping conditions.

In the future, industrial tests of new designs of elements of clamping devices should be carried out. These studies were conducted with drill pipes only, although the main findings can be applied to other types of pipes. The development of this study may consist in the application of the results for drill and casing pipes from different types of materials, alloy grades and physical and mechanical properties, and with the use of other types of loads.

## 6. Conclusions

On the stand simulating the operation of the wedge clamping device, experiments were carried out to determine the influence of the operating conditions of the clamping devices on the stress state of the clamped pipe during operation.

The results of the comparison of deformations show that short thin-walled cylindrical parts (pipes, sleeves, rings) should be fixed not at the end, but in the middle part. In this case, the maximum deformation is less with the same clamping forces. When clamping short cylinders (rings, sleeves), clamping forces should be applied not at the end, but in the middle part of the clamped part. In this case, the maximum deformations are reduced up to 10 times. With a decrease in the length of the part, the reliability of fastening in the middle part increases.

The method for calculating the maximum permissible weight of a pipe string has been improved. In practical terms, it is necessary to take into account such factors as the out-of-roundness of the pipe, inaccuracy in the manufacture of the elements of the clamping device and the associated incomplete coverage of the pipe with jaws. The calculation formula includes coefficients that take into account the actual clamping conditions.

---

## References

- [1] Markov, O., Gerasimenko, O., Khvashchynskyi, A., Zhytnikov, R., Puzyr, R. (2019). Modeling the technological process of pipe forging without a mandrel. *Eastern-European Journal of Enterprise Technologies*, 3 (1 (99)), 42–48. doi: <https://doi.org/10.15587/1729-4061.2019.167077>

- [2] Afandiyev, E. M., Nuriyev, M. N. (2019). Studying the quality of drill pipes clamped in a wedge clamp. Eastern-European Journal of Enterprise Technologies, 4 (7 (100)), 16–21. doi: <https://doi.org/10.15587/1729-4061.2019.174494>
- [3] Rukovodstvo po trubam neftyanogo sortamenta i ih soedineniyam, primenyaemym za rubezhom (1969). Moscow: Nedra, 296.
- [4] Afandiyev, E. M., Nuriyev, M. N. (2020). Improving the retention capacity of clamping elements. Eastern-European Journal of Enterprise Technologies, 1 (1 (103)), 47–51. doi: <https://doi.org/10.15587/1729-4061.2020.195193>
- [5] Wang, L., Guo, S., Gong, H., Shang, X. (2016). Research and development of a self-centering clamping device for deep-water multifunctional pipeline repair machinery. Natural Gas Industry B, 3 (1), 82–89. doi: <https://doi.org/10.1016/j.ngib.2015.12.012>
- [6] Yakhin, A. R., Ismakov, R. A., Garifullin, R. R., Yangirov, F. N. (2014). Surface hardening for drill pipe life improvement. Oil and Gas Business, 4, 381–399. doi: <https://doi.org/10.17122/ogbus-2014-4-381-399>
- [7] Djukic, L. P., Sum, W. S., Leong, K. H., Hillier, W. D., Eccleshall, T. W., Leong, A. Y. L. (2015). Development of a fibre reinforced polymer composite clamp for metallic pipeline repairs. Materials & Design, 70, 68–80. doi: <https://doi.org/10.1016/j.matdes.2014.12.059>
- [8] Afandiyev, E. M., Nuriyev, M. N. (2021). Analysis of the condition of a pipe fixed in a clamping device. EUREKA: Physics and Engineering, 1, 78–85. doi: <https://doi.org/10.21303/2461-4262.2021.001587>
- [9] Markov, O., Gerasimenko, O., Aliieva, L., Shapoval, A. (2019). Development of the metal rheology model of high-temperature deformation for modeling by finite element method. EUREKA: Physics and Engineering, 2, 52–60. doi: <https://doi.org/10.21303/2461-4262.2019.00877>
- [10] Bulatov, A. I., Proselkov, Yu. M., Shamanov, S. A. (2003). Tehnika i tehnologiya bureniya neftyanyh i gazovyh skvazhin. Moscow, 1007.
- [11] Lopatuhin, I. M. (1989). Razrabotka zazhimnyh ustroystv neftepromyslovogo oborudovaniya s povyshennoy uderzhivayushey sposobnost'yu. Moscow.

Received date 25.02.2021

Accepted date 01.04.2021

Published date 13.09.2021

© The Author(s) 2021

This is an open access article under the CC BY license

(<http://creativecommons.org/licenses/by/4.0>).

**How to cite:** Afandiyev, E. M., Nuriyev, M. N. (2021). Analysis of reliability of the drill pipe in the clamping mechanism. EUREKA: Physics and Engineering, 5, 80–87. doi: <https://doi.org/10.21303/2461-4262.2021.001765>



# ABOUT THE POSSIBILITY OF APPLICATION OF LASER VACUUM WELDING FOR THE INTEGRATION OF ELEMENTS OF HEAT-PROTECTIVE STRUCTURES FROM POWDER MATERIALS

**Walid Alnusirat**

*Department of Industrial Engineering  
Al-Balqa Applied University  
1911 Al-Salt, Amman, Jordan, P.O.box 206*

**Alexandr Salenko**

*Department of Machine Tools and Machinery Systems  
National Technical University of Ukraine «Igor Sikorsky Kyiv Polytechnic Institute»  
37 Peremohy ave., Kyiv, Ukraine, 03056*

**Olga Chenchewa**✉

*Department of Industrial Engineering<sup>1</sup>  
chenchevaolga@gmail.com*

**Sergii Shlyk**

*Department of Manufacturing Engineering<sup>1</sup>*

**Irina Gusarova**<sup>2</sup>

**Alexandr Potapov**<sup>2</sup>

*<sup>1</sup>Kremenchuk Mykhailo Ostrohradskyi National University  
20 Pershotravneva str., Kremenchuk, Ukraine, 39600*

*<sup>2</sup>Yuzhnoye Design Office  
3 Kryvorizka str., Dnipro, Ukraine, 49008*

✉ Corresponding author

## Abstract

The results of studying the process of laser vacuum welding of elements of heat-shielding panels made of heat-resistant dispersion-strengthened powder materials Ni-20Cr-6Al-Ti-Y<sub>2</sub>O<sub>3</sub> of increased strength are presented. Such materials can be used to create ultralight heat-shielding panels, which are systems integrated on the surface of aircraft from typical modules of a cellular structure.

Technical solutions of heat-insulating modules are considered, which are a cellular (honeycomb) structure consisting of two plates with a thickness of 0.1 to 0.14 mm, inside which there is a thin honeycomb filler. It is shown that the small thickness of the plates and the complexity of integrating the elements into a single system significantly impair the formation of a strong connection of such elements and do not allow the direct use of the known methods of diffusion welding or vacuum brazing.

It has been established that laser welding of elements of heat-shielding structures in vacuum provides satisfactory strength of the structure of the heat-shielding element as a whole. Local heating at certain points prevents deformation of the parts to be joined during the welding process. The use of a pulsed Nd:Yag laser with a power of 400–500 W, operating in the frequency range of 50–200 Hz, allows welding with or without a filler powder. It was found that the use of filler additives practically does not affect the mechanical properties of the welded joint, however, it reduces the melt zone, while increasing the density of the welded joint.

Based on the results obtained, it was concluded that it is possible to use laser vacuum welding for the integration of thin elements of heat-shielding modules. It is shown that a satisfactory joint strength is achieved by ensuring high cleanliness of the surfaces of elements before welding, maintaining a high vacuum (less than 10<sup>-2</sup> Pa) and rational thermal loading of the surfaces of the elements to be integrated.

The use of the proposed process makes it possible to obtain a stronger and denser seam in comparison with the known methods of soldering multicomponent powder dispersion-strengthened materials.

**Keywords:** laser vacuum welding, strength of welded joint, dispersion-strengthened alloys, heat-shielding structures.

DOI: 10.21303/2461-4262.2021.001998

## 1. Introduction

Designs of heat-shielding panels for reusable spacecraft with an outer metal plate are being actively developed by leading experts from many countries [1, 2]. Today it is becoming evident that the most effective thermal protection consists of individual tile-modules attached to the hull of the spacecraft. Such protective tiles typically consist of a top and bottom plate with a honeycomb core in between. The tiles are mechanically attached to the hull of the spacecraft. At the same time, tiles can also be integrated into a single system and separately from the body, with subsequent placement on surfaces requiring thermal protection.

Such integration requires welding or soldering of the plates simultaneously with the installation of a U-shaped elastic heat-compensating element, as well as additional fasteners (legs) that ensure fastening of the thermal protection to the surface of the spacecraft (**Fig. 1**).

Promising materials used to create heat-shielding systems are multicomponent powder materials based on (Ni-Cr), in particular, a five-component powder composite material consisting of metallic (Ni-Cr), intermetallic (Al-Ni<sub>3</sub>) and oxide (Y<sub>2</sub>O<sub>3</sub>) phases. However, its application, despite numerous advantages, is difficult due to the exceptional complexity of welding or brazing [3, 4] of non-rigid thin structural elements.

So, according to [4], when brazing structures in a vacuum furnace, prolonged exposure to high temperatures leads to the appearance of residual thermal deformations of the processed parts (**Fig. 2**), causing their warpage. The stability of the strength and density indicators of the weld is significantly reduced. The recommendation to solder in one setup is applicable only for attaching the upper and lower plates, as well as the U-shaped insert between them.

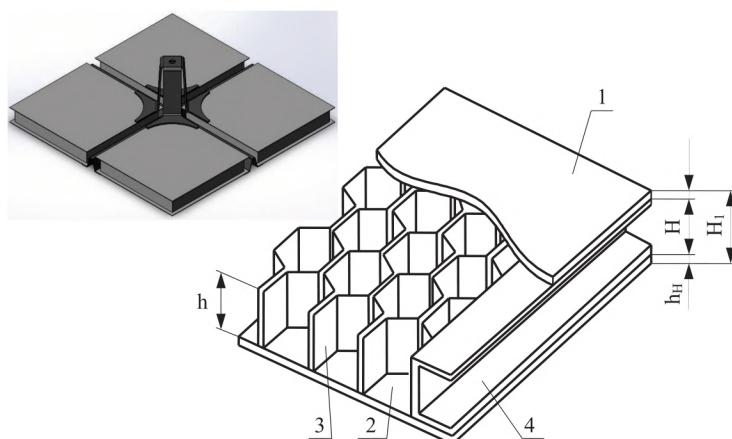


**Fig. 1.** Typical heat-insulating systems of spacecraft and their design:  
1 – top plate; 2 – bottom plate; 3 – honeycomb filler; 4 – side plate



**Fig. 2.** Residual thermal deformations of workpieces

The efficiency of the use of lasers in welding and related processes (in the processing of the surface layer) is considered in a number of works [5–8]. In [5], the features of using gas lasers for welding non-ferrous metals are analyzed, in [6] – for welding alloyed, heat-resistant and diffi-



cult-to-machine materials. Work [7] shows the prospects for using pulsed lasers for welding special steels. At the same time, some researchers believe that a higher quality of the formation of permanent joints is provided under conditions of high or low vacuum [8]. This is especially true for cases of integration of elements prone to embrittlement and warping.

Porosity and low bond strength for Ni-based alloys is one of the important problems due to the high sensitivity of Ni to the content of impurities in the material (P, S) and an increase in the concentration of dissolved gases in the weld or spot. «Hydrogen disease» occurs due to a sharp decrease in the solubility of O<sub>2</sub>, H<sub>2</sub>, H<sup>+</sup> and CO with a decrease in the temperature of the molten liquid metal and with a limitation of the possibility of removing gases during the crystallization of the weld pool.

However, the greatest degree of pore formation is associated with the saturation of the molten bath with N, especially in the presence of oxygen. For heat-resistant alloys, the weld material is prone to embrittlement and the formation of a network of microcracks, which is due to the appearance of the Ni-NiO eutectic ( $T_{pl} = 1438$  °C), distributed outside the crystallites during the cooling of the weld pool. This reduces the strength of the grain boundaries, makes the seam not only porous, but also brittle.

From this point of view, the prospect of using a vacuum chamber to ensure reliable protection of the welding zone from the atmosphere, as well as the use of high-purity filler materials for brazing or laser welding, is reasonable and reasonable.

For the manufacture of thermal protection models, it is of interest to overlap and butt welding of thin sheet elements of heat-resistant dispersion-strengthened material Ni-20Cr-6Al-Ti-Y<sub>2</sub>O<sub>3</sub> by methods of local (high intensity) heating of the contact zone using a laser.

The aim of the work is to study the possibility of creating reliable permanent joints from thin-leaf (0.1...0.14 mm) billets Ni-20Cr-6Al-Ti-Y<sub>2</sub>O<sub>3</sub> in contact with each other.

## 2. Materials and methods

To integrate the elements into a single design of the heat protection module, it is necessary to perform laser overlap and butt welding. The process diagram is shown in **Table 1**.

Heating of the surface by the laser, provided that the radiation intensity is distributed at the laser output window in accordance with the Gaussian law:

$$I(w) = I_0 \exp(-w^2 / w_G^2),$$

$I_0$  – the radiation intensity on the beam axis;  $w$  – current radius;  $w_G$  – radius at which the radiation intensity decreases by a factor of  $e$ , and, taking into account:

$$\frac{\partial T}{\partial t} = \alpha \left( \frac{\partial^2 T}{\partial x^2} + \frac{\partial^2 T}{\partial y^2} + \frac{\partial^2 T}{\partial z^2} \right),$$

will be described by the equation:

$$T(x, z, t) = \frac{q(x)r^2}{\lambda} \left( \frac{a}{\pi} \right)^{1/2} \int_0^t \frac{P(t-\tau) \exp \left[ \frac{z^2}{4a\tau} - \frac{x^2}{4a\tau} \right]}{\sqrt{\tau(4a\tau + r^2)}} d\tau, \quad (1)$$

where  $\lambda$  – coefficient of thermal conductivity;  $a$  – coefficient of thermal conductivity;  $t$  – current time;  $P$  – power of laser radiation.

Boundary conditions on the heated surface:

$$-k \frac{\partial T}{\partial z} \Big|_{z=0} = q(x, y, t),$$

where

$$q = q_0(1-R),$$

$q_0$  – the radiation power density;  $R$  – surface reflection coefficient;  $k$  – coefficient of thermal conductivity of the material.

To determine the average temperature on the surface of a semi-infinite body at a point with coordinates  $(x, y, z)$  heated by a laser beam moving at a speed  $v$ , one can use the relation coefficient of thermal conductivity;  $a$  – coefficient of thermal conductivity;  $t$  – current time;  $P$  – power of laser radiation.

$$\bar{T} = \frac{16}{\sqrt{\pi}} \int_0^{\infty} \frac{1}{\sqrt{(c'^2 + \tau^2)(b'^2 + \tau^2)}} \exp \left[ -\frac{(2\bar{x}'^2 + \bar{v}'\tau)^2}{4(\bar{c}'^2 + \tau^2)} - \frac{\bar{y}^2}{\bar{b}^2 + \tau^2} - \frac{\bar{z}^2}{\bar{t}^2} \right] d\tau, \quad (2)$$

moreover,

$$\bar{v} = \frac{v_r}{2a}; \quad \bar{x}' = \frac{x}{r}; \quad \bar{y}' = \frac{y}{r}; \quad \bar{z}' = \frac{z}{r}; \quad \bar{c}' = \frac{c}{r}; \quad \bar{b}' = \frac{b}{r}; \quad r^2 = cb;$$

$A_0$  – reflective (absorption) ability of the material of the workpiece;  $P$  – power of laser radiation;  $b, c$  – parameters of the density (power) distribution of laser radiation.

For continuous heating, the temperature change on the irradiation plane is determined by the ratio:

$$T(x, y, z, t) = \frac{P}{\pi \frac{1}{2} \rho c} \int_0^t \frac{e^{\frac{(x-v(t-z))^2}{4\alpha\tau + A^2} - \frac{y^2}{4\alpha\tau + B^2}}}{\left[ (4\alpha\tau + A^2)(4\alpha\tau + B^2)\alpha\tau \right]^{1/2}} \times \left[ e^{-\frac{z^2}{4\alpha\tau}} - \eta(\pi\alpha\tau)^{1/2} \operatorname{erfc} \left( \frac{z}{2(\alpha\tau)^{1/2}} + \eta(\alpha\tau)^{1/2} \right) \times e^{\eta z + \eta^2 \alpha\tau} \right] d\tau, \quad (3)$$

where  $x, y, z$  – coordinates;  $t$  – time;  $\eta$  – coefficient of heat transfer from the surface of the workpiece;  $\alpha$  – thermal conductivity coefficient;  $A$  and  $B$  – major and minor axes of the heating spot;  $P = \pi qAB$  – power of the emitter, and the distribution of heat will occur in the plane of the plates of limited thickness.

The use of a pulsed laser requires taking into account the redistribution of temperature in the period between pulses,

$$T(t) = T_{\max} - \frac{q_1 \delta}{\lambda} \left[ \frac{2}{\sqrt{\pi}} \frac{\sqrt{a(t-\tau)}}{\delta} + \exp \left( \frac{a(t-\tau)}{\delta^2} \right) \operatorname{erfc} \left( \frac{\sqrt{a(t-\tau)}}{\delta} \right) \right], \quad (4)$$

where  $\delta$  – depth of heating;  $q_1 = f(c, p, t)$ .

The process of thermal conductivity in the volume of the material bounded by the region  $\Omega$ , with the surface  $\partial\Omega$ , is described by: a scalar temperature field  $T = T(P, t)$ ; vector field of the heat flux  $q = q(P, t)$ ,  $P = \{(x, y, z)\} \in \Omega$ , scalar field with specific thermal  $e = e(T)$ .

The boundary conditions on the outer surfaces for  $\tau > 0$  will be as follows:

$$\left\{ \begin{array}{l} \Gamma_1: -\lambda \frac{\partial t}{\partial n} = q_r; \quad \Gamma_2: \frac{\partial t}{\partial n} = 0; \quad \Gamma_3: -\lambda \frac{\partial t}{\partial n} = \alpha (t - t_{\text{medium}}); \end{array} \right.$$

Conditions at the contact boundary  $\Gamma_4$  at  $\tau_0$ :

$$\left\{ \begin{array}{l} t|_{\Gamma_4^-} = t|_{\Gamma_4^+}, \\ -\lambda_- \frac{\partial t}{\partial n} \Big|_{\Gamma_4^-} = \lambda_+ \frac{\partial T}{\partial t} \Big|_{\Gamma_4^+}, \end{array} \right. \left\{ \begin{array}{l} t < t_m - \frac{\Delta t}{2}, \lambda_1(t) = \lambda_s; [c_p(t)\rho(t)]_1 = c_{ps}\rho_s; \\ t_m - \frac{\Delta t}{2} \leq t \leq t_m + \frac{\Delta t}{2}, \lambda_1(t) = \lambda_s + \frac{\lambda_m - \lambda_s}{\Delta t} \left( t - t_m + \frac{\Delta t}{2} \right); \\ [c_p(t)\rho(t)]_1 = c_{ps}\rho_s + \frac{c_{pm}\rho_m - c_{ps}\rho_s}{\Delta t} \left( t - t_m + \frac{\Delta t}{2} \right) + \frac{L_f}{\Delta t}; \\ t > t_m + \frac{\Delta t}{2}, \lambda_1(t) = \lambda_m; [c_p(t)\rho(t)]_1 = c_{pm}\rho_m; \end{array} \right.$$



where  $n$  – normal to the surface;  $q_r$  – power density;  $\alpha$  – heat transfer coefficient;  $\Gamma_1$  – irradiated surface;  $\Gamma_2$  – axial symmetry surface;  $\Gamma_3$  – contact surface with the external environment;  $\Gamma_4$  – contact boundary of two welded elements.

The motion of the phase boundaries can be set based on the one-dimensional non-stationary heat conduction equation  $\frac{\partial^2 T}{\partial z^2} = \frac{1}{D} \frac{\partial T}{\partial t}$ , where  $D = K/(\rho c)$  – thermal diffusivity.

The dimensionless velocity of the phase boundary movement depending on the dimensionless time for the temperature  $T(z, t)$  with the boundary conditions on the moving boundary  $z = \lambda(t)$  takes the form:

$$\frac{d\xi}{dt} = \left[ 1 + \varepsilon \left\{ \frac{1}{2} \operatorname{erfc} \left( \frac{\tau^{1/2}}{2} \right) - \frac{1}{(\pi\tau)^{1/2}} e^{-\frac{\tau}{4}} \right\} \right] \frac{2}{\pi} \left\{ 1 + \frac{\varepsilon}{\pi\tau^{1/2}} \right\} \arcsin \left\{ \left( 1 - \frac{\pi\varepsilon^2}{4\tau} \right)^{1/2} \right\}.$$

The static formulation of the problem allows one to estimate the expected size of the melt spot, taking into account the thermophysical properties of the elements being welded.

In practice, the obtained equations are rather difficult to use, since a significant number of thermal engineering coefficients for a powder material is rather difficult to determine, as are the contact conditions for a butt-welding scheme of plates. For the case of overlapping welding, equation (3) is difficult to use due to the limited area of contact.

To determine the rational conditions for the thermal effect of the laser on the integrated plates, the process of thermal loading of the surface under high vacuum conditions was simulated. In the simulation, it was assumed that the heating of the plate surface alternated with the propagation of heat into the material at the moment of the absence of a pulse.

Welding modes are given under the corresponding schemes in **Table 1**, and the obtained temperature fields are in the second column of the **Table 1**.

The obtained pictures of the temperature distribution on the surface and over the cross-section of the workpieces in the contact zone made it possible to establish the time (and, consequently, the number of pulses), during which the temperature in the center of irradiation above 1175 °C (the temperature of phase transformations), as well as the temperature of formation of the melt bath, will be reached. over 1460 °C.

It was found that for a Nd:YAG laser operating at a frequency of 125 Hz with a power of 0.4 kW, the heating time of the welding point of a 0.8 mm diameter part should not exceed 120–150 ms. Such calculations are approximate for a welding station built on the basis of a VUP-5 universal vacuum station, the laser radiation into the working chamber of which was fed using a system of mirrors from a universal laser complex LSK-400-5 [9] (**Fig. 3**). During welding, the beam was focused in the plane of the upper integrated part. Positioning was carried out using an automated cross table of working movements, which provides welding at several points with different duration of the process. The latter ranged from 0.1 s to 0.15 s; the exposure time of the weld point was provided by a mechanical interrupter. The movement between the welding points was carried out according to the program.

Mechanical tests of the finished samples were performed on a R-20 tensile testing machine equipped with an m-Daq ADC automated data collection system and means for displaying the diagram and loading conditions. The samples were tested at room temperature and at the expected operating temperature ( $T = 500 \dots 600$  °C).

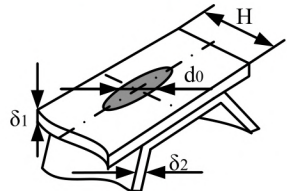
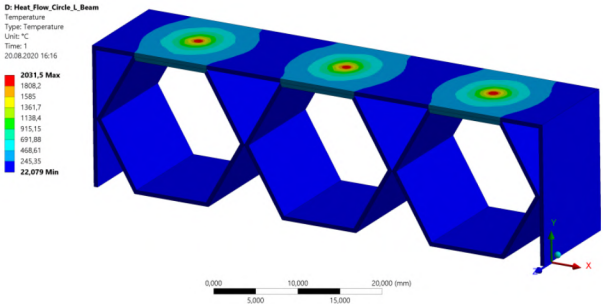
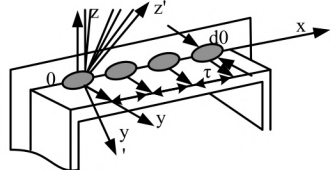
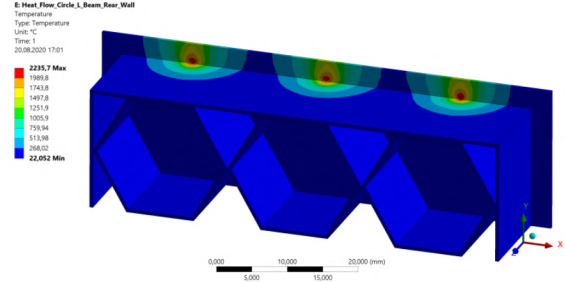
Placement of samples in a vacuum chamber is performed so that the weld pool is formed in a horizontal plane. Welding was carried out both without filler metal, and with those:

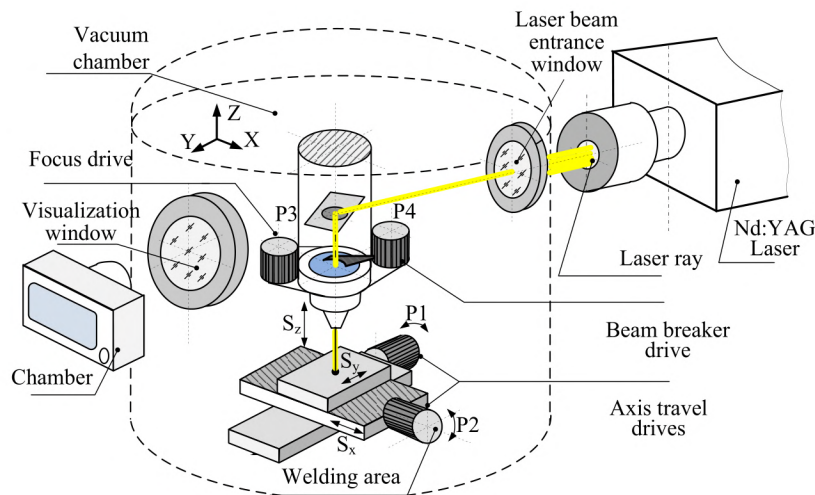
- 1) VPr36 [10] (composition 0.2 % C; 8–10 % Cr; 2.5–6.0 % Al; 1.4–2.0 % Mo; 2–5 % Nb; 2–6 % W; 2.5–3.0 % B; the rest is Ni);
- 2) finely dispersed Ni powder (Ni; 5 % W; 1.0–1.5 % B).

The tests were carried out both for the material Ni-20Cr-6Al-Ti-Y<sub>2</sub>O<sub>3</sub> and for other high-temperature alloys: YIPM-1200, YIPM-Ni-20Cr-3Al. The mechanical properties of materials are given in **Table 2**. Control over the weld condition and study of the material structure were carried out using a scanning electron microscope REM-106-I (Ukraine).

**Table 1**

Simulation results of the vacuum welding process

No.	Welding scheme and modes	Temperature fields
1	 <p>Contact: thickness: <math>\delta_1 = 0.14</math> mm; <math>\delta_2 = 0.14</math> mm; <math>d_0 = 0.5</math> mm; <math>H = 14.0</math> mm; clamping force – 5 N; beam power – 400 W; pulse repetition rate – 125 Hz; pulse energy – 8 J</p>	 <p>D: Heat_Flow_Circle_L_Beam Temperature Type: Temperature Unit: °C Time: 1 20.08.2020 16:16</p>
2	 <p>End: thickness: <math>\delta_1 = 0.14</math> mm; <math>\delta_2 = 0.14</math> mm; <math>d_0 = 2.5</math> mm; <math>H = 14.0</math> mm; clamping force – 20 N; beam axis angle – <math>\pi/4</math> (coordinate system <math>XOZ_1Y_1</math>); beam power – 400 W; pulse repetition rate – 125 Hz; pulse energy – 8 J</p>	 <p>E: Heat_Flow_Circle_L_Beam_Rear_Wall Temperature Type: Temperature Unit: °C Time: 1 20.08.2020 17:01</p>

**Fig. 3.** The equipment used and the scheme of exposure of the beam to the surface

Thermal etching was used to identify the composition and structure of multicomponent alloys by scanning electron microscopy. The essence of the method was to obtain thin sections with a surface roughness of  $Ra\ 0.16\ \mu\text{m}$ , followed by their heating to a temperature of  $550\ ^\circ\text{C}$  and holding for 12 min.

The sections were made according to the standard technique, the material removal was less than  $0.08\ \text{mm}$ , and there were no surface defects. The size of the irradiation zone, and, consequently,



the welding zone was changed with the help of electromechanical focus adjustment, which made it possible to ensure the local heating of the surface from 0.27 mm to 1.8 mm in diameter.

**Table 2**

Mechanical properties of the used nichrome – based alloys

Characteristic	$T, ^\circ\text{C}$	YIPM-1200	YIPM-Ni <sub>20</sub> Cr <sub>3</sub> Al	YIPM-Ni <sub>20</sub> Cr <sub>6</sub> Al Y <sub>2</sub> O <sub>3</sub>
Aluminum content, %	–	–	3.0	5.0–6.0
Density, m <sup>3</sup> /kg	–	8300	7950	7500
Tensile strength, $\sigma_b$ , MPa/MPa/kg	20	738/0.09	1020/0.136	1005/0.134
	800	237/0.03	542/0.07	999
	1100	45	–	–
	1200	–	40	56
Yield strength, $\sigma_{0.2}$ , MPa	20	364	624	760
	800	228	457	687
	1100	40	–	–
	1200	–	35	51
Elongation, $\delta$ %	20	36.5	21	12.9
	800	36.7	18.1	2.0
	1100	32.8	18	–
	1200	–	18	22.3

The composition of the elements of the connection zone, as well as adjacent areas, was studied. The study was carried out by the method of energy dispersive X-ray microanalysis.

### 3. Results and discussion

When preparing samples for welding (the formation of U-shaped elements, strips of honey-comb fillers), preliminary heat treatment was carried out – annealing in vacuum for 20 to 30 minutes at a temperature of 780 to 800 °C. Such annealing modes are recommended for work hardening of integrated elements made of Ni-Cr alloy and subjected to plastic deformation. This made it possible to improve the structure of the processed elements and reduce the tendency of the material to interlayer cracking with the release of particles of coagulated material, which is characteristic of the powder components used in sintering (**Fig. 4, a, b**).

Without heat treatment, the workpieces were destroyed even with relatively small deformations.

The welding mode was selected based on the results of modeling temperature fields (**Table 2**) according to (4).

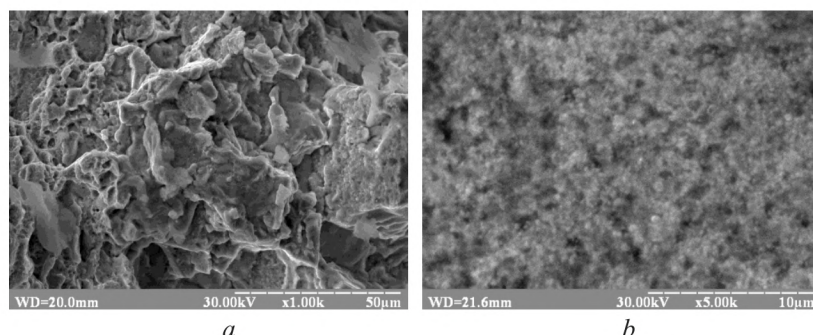


**Fig. 4.** Fracture of the workpiece (0.4 mm) during bending: *a* – before heat treatment; *b* – after heat treatment

Microelectronic analysis of the weld points showed that the weld pool was formed unevenly, the material splashed out of the weld pool and formed a rather large (up to 200 µm) droplet influx (**Fig. 5**). Almost all points had through penetration (which is due to the small thickness of the workpieces,  $h = 0.14\text{--}0.4$  mm), while the shape of the holes obtained differed from the correct

geometric circle and amounted to 0.2–1.3 mm. This is due to the fact that the used laser with a wavelength of 1062 nm with the specified pulse generation parameters is powerful enough to perform welding operations. In addition, the laser beam was introduced into the chamber through special windows equipped with silicate glass, since special phosphate glasses were not available. An attempt to form a seam with a linear feed motion somewhat improved the result, however, it was not possible to fully obtain stable seam parameters. The reason may also be the shutter used, the response time of which ( $\tau = 0.07$  s) is comparable to the duration of the laser action on the surface. There were no significant differences in the formed welding points for different alloys (YIPM-1200, YIPM-Ni<sub>20</sub>Cr<sub>3</sub>Al, Ni-20Cr-6Al-Ti-Y<sub>2</sub>O<sub>3</sub>), however, for YIPM-1200, YIPM-Ni<sub>20</sub>Cr<sub>3</sub>Al, burn-throughs and holes were less (no more than 0.3 mm) diameter.

It was found that the low thermal conductivity of Ni and nickel alloys during welding leads to an increase in grain size and, as a consequence, to a decrease in the toughness and strength of the weld as a whole.

Attempts to carry out heat treatment aimed at preventing structural changes in the welding zone and in the near-welding zone are less effective than the introduction of melt modifier additives (Ti, Mo, Al) and limiting the welding energy per unit length. Prevention of the formation of Ni-Al was carried out by sharp cooling (lasting from 3 to 5 min) Of the samples after welding by blowing the vacuum chamber with argon cooled to a temperature of  $-30...-20$  °C.

Of interest is the result of studying the trace element composition of the welding zone with and without filler powder (**Fig. 6, a**). The analysis was carried out at three points – directly in the melt zone, in the near region of the weld, which was heated above 950 °C, and on the bearing surface (**Fig. 6, b**).

**Table 3** shows a comparison of the results obtained – laser welding and brazing in vacuum (both in a clean zone and using a filler powder of the APC type). The presence of a significant proportion of C is caused by carbon «poisoning» of the surface from the graphite tile of the table, which was used as a thermal insulation element together with ceramic plates of Al<sub>2</sub>O<sub>3</sub>. This is obvious if to neglect the insignificant proportion of Na, S, Cl, K, Ca detected during the analysis and present in parts of the vacuum chamber.

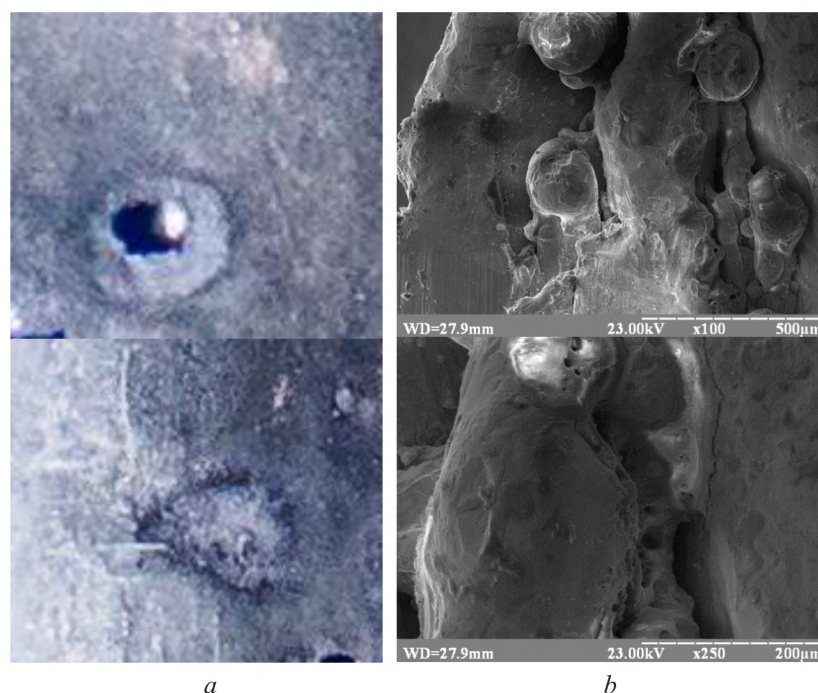


**Fig. 5.** Welding points: *a* – heat-shielding module made of Ni-20Cr-6Al-1Ti-1Y<sub>2</sub>O<sub>3</sub> material; *b* – microelectronic photo of the melt pool surface: upper example – welding with burn-through,  $\varnothing 0.85$  mm; bottom example – satisfactory welding



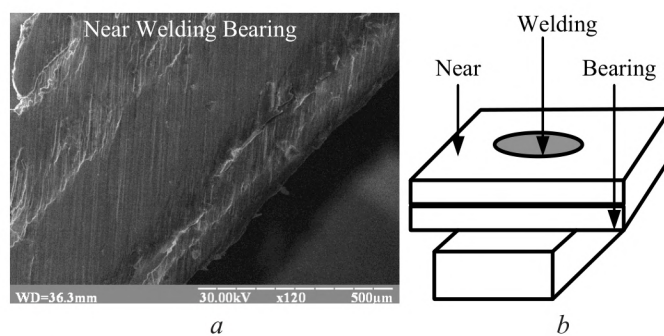


**Fig. 6.** Study of an element of the weld zone on a thin plate: *a* – microelectronic photograph of the welding zones; *b* – diagram of welding zones

**Table 3**

Mass fraction of elements for various types of welding

	Laser welding			Laser welding with APC			Soldering process		
	Near	Welding	Bearing	Near	Welding	Bearing	Near	Welding	Bearing
C	24.3	15.81	4.79	33.8	12.1	4.79	57.25	52.16	7.75
O	4.6	3.05	6.67	4.6	17.4	16.7	34.96	34.96	2.51
Na	2.38	0.07	0.23	2.4	–	–	–	–	–
Al	2.76	5.72	6.63	1.7	22.1	16.6	–	–	6.16
S	0.28	0.05	0.0	–	–	–	–	–	–
Cl	2.25	0.0	0.04	–	–	–	–	–	–
K	0.47	0.08	0.01	–	0.2	–	1.15	2.93	–
Ca	0.39	0.1	0.1	–	–	–	0.48	0.47	–
Ti	0.56	0.1	0.0	–	1.18	–	1.1	1.31	–
Cr	17.6	15.8	21.6	10.7	6.15	20.7	1.15	9.95	17.55
Ni	44.2	58.1	59.04	43.8	37.2	39.2	0.45	–	64.33
Y	0.21	1.12	0.89	0.4	0.8	1.9	1.1	0.2	1.9

The presence of oxygen at the points under study can be explained by the oxidation of a rather loose layer on the surfaces (**Fig. 4**), and this oxygen remains in the melt bath after the end of the process. Obviously, the use of laser welding provides better structural and elemental characteristics, since the absence of an atmosphere and local heating do not lead to significant changes in the base material in the area around the weld.

The use of brazing alloys as filler materials has a certain effect on the structure and quality of the formed weld, but requires further optimization of the process. In this case, only partial melting of one of the plates is possible, and with the use of additional ballasts, the process can be reduced to the process.

Subsequent mechanical tests of the resulting joint showed that the welded joint was destroyed by a static load perpendicular to the plane of formation of the weld point. It was found that the fault occurs mainly in the heat-affected zone, in the place of cracking.

It was noted that a significant decrease in the number of pulses (up to 5–10 per cycle) leads to the formation of a low strength joint, for which прочности 120 МПа at  $T = 20\text{ }^{\circ}\text{C}$ , although burn-through of the weld was not observed.

Local heating of the workpiece prevents significant structural changes in the integrated elements, as well as their thermal deformation. At the same time, the resulting joint is susceptible to cracking with destruction of the contact zone upon application of a load of 30–40 %  $[\sigma]$  (critical value) for the material,  $\sigma_b = 1005\text{ МПа}$ ,  $T = 20\text{ }^{\circ}\text{C}$ .

Comparison of the results of welding without filler metals and solder for BPr showed that the spread of adhesion strength at five points on ten samples is higher in welding with additives and amounts to 10–18 %. Relative elongation changes quite significantly, and decreases for welds

with filler material to  $\delta = 1.3...2.2\%$  at operating temperature ( $T = 500\text{ }^{\circ}\text{C}$ ) (**Fig. 7, a–c**). At the same time, overlapping welding of plates without additives made it possible to obtain (30–35 %)  $\delta$  of the starting material. At a temperature of  $T = 20\text{ }^{\circ}\text{C}$ , the relative elongations were large and amounted to  $\delta = 4.3...9.1\%$ . Other mechanical characteristics remain practically unchanged and correspond to **Table 2**.

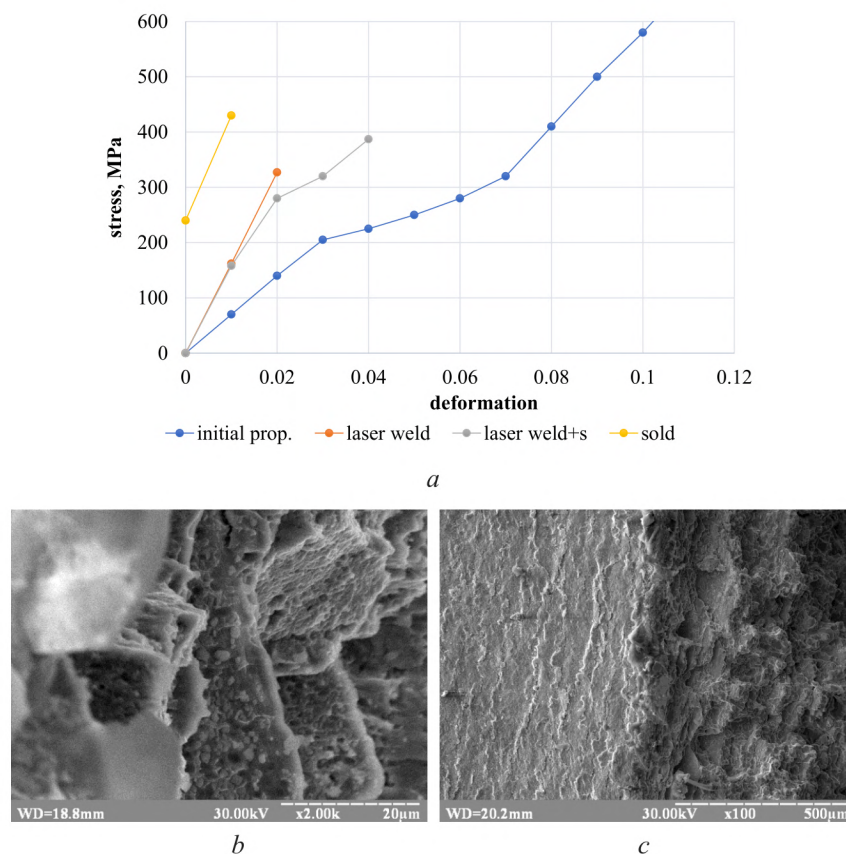


**Fig. 7.** Mechanical tests of the welding joint ( $T = 20\text{ }^{\circ}\text{C}$ ): *a* – the results of mechanical tests; *b, c* – fracture of a destroyed specimen obtained under static loading

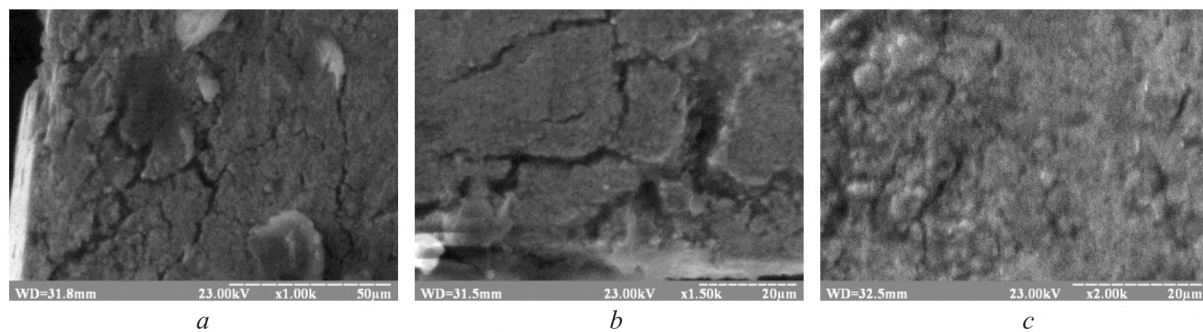
Improving the process can improve these indicators, most likely by preventing the formation of a porous structure at the boundary of the melt pool and zones with microcracks.

It should be borne in mind that the initial billet from Ni-20Cr-6Al-Ti-Y<sub>2</sub>O, obtained by powder metallurgy [11], is subsequently rolled into sheets of the required thickness (0.4–0.14 mm). In this case, changes in its structure and phases occur, the initial porosity decreases, and at the same time the amount of intermetallic compounds and oxides on the surface increases. This phenomenon worsens, and in some cases almost completely excludes weldability.

Electron microscopic studies have shown that there is a clearly defined dispersed structure in the Ni-20Cr-6Al-Ti-Y<sub>2</sub>O plates, and the surfaces of the two mating samples are practically identical. In **Fig. 8**, and the particles are on the order of 1–2 μm; microvoids and cavities are observed in the surface layer. The entire investigated surface (**Fig. 8, b, c**) is covered with a network of microcracks. It can be assumed that the alloy contains a large amount of Ni-Al, intermetallic compounds with an ordered cubic body-centered crystal lattice. As a result, it was possible to consider such intermetallic compounds in some micrographs of the end parts of the plates. This explains a number of failures in obtaining a reliable welded joint in the traditional way.

Since the sintered dispersion-strengthened composite is prone to the formation of intermetallic inclusions that affect the mechanical properties of the material, further search for special methods of ensuring the welding process is required.



**Fig. 8.** Test samples:

*a* – surface layer; *b*, *c* – end side of the workpiece with a thickness of 0.14 mm

Another factor affecting the low weldability of elements into a single structure is the unevenness of the structural composition and oxide inclusions observed on the surface of the workpiece, apparently representing conglomerates of  $Y_2O_3$ . Rather large areas can be explained by incomplete mixing of nanoparticles and their tendency to form separate surface clusters. In such zones, thermodynamic instability can appear, and when exposed to heat, such foci cause an exothermic oxidation reaction of Al, as a result of which burn-throughs and fistulas occur (for thin-sheet blanks).

It becomes obvious that improving the quality of welding is possible both due to a more thorough preparation of the initial workpieces (alignment, heat treatment with the above modes, removal of surface contaminants and oxides), and due to optimization of the modes of welding in a vacuum chamber.

At the same time, the multicomponent composition of the composite, the presence of  $Y_2O_3$  in its structure significantly limits the application of the proposed welding method, requires adaptation of the process for other heat-resistant materials.

It should be noted that in order to prevent cracking of the weld, further research should be aimed at ensuring a tight fit and high-quality contact connection of elements before welding. Another way to improve the quality of the joint is to increase the vacuum level to  $10^{-3}$  Pa, as well as to ensure the required cooling cycle of the workpiece. A promising method is high-frequency laser welding using screens and heat-removing elements (ballasts).

Thus, further research should be aimed at finding rational welding conditions, ensuring the required composition of the filler metal in the molten pool, as well as the formation of a continuous weld.

Improvements are also required in the vacuum chamber: using a drive system to move the work piece in a controlled manner will allow for a more stable welding process.

#### 4. Conclusions

Mechanical tests of welded joints made by spot welding of powder dispersion-hardened alloy Ni-20Cr-6Al-Ti- $Y_2O_3$  are carried out. The possibility of using laser vacuum welding for the integration of thin-sheet elements in the design of heat-shielding systems is shown.

Welding points made in a vacuum chamber with a pressure of  $10^{-2}$  Pa have through damage (due to the thickness of the plates – 0.1...0.14 mm and restrictions imposed on the use of a laser of this type) caused by exposure to a laser beam, and the diameter of the resulting holes is directly determined by the number of radiation pulses. A decrease in the number of pulses (up to 5–10 per cycle) leads to the formation of low-strength joints, for which Ni-20Cr-6Al-Ti- $Y_2O_3$  120 MPa at  $T = 20$  °C. The maximum strength of the weld section for the contact area is achieved when the surface is irradiated with a defocused laser beam  $\varnothing 0.7$ –0.8 mm with a pulse energy of 8 J and is 0.4–0.5 [ $\sigma_b$ ] strength of the base metal, or about 130–145 MPa (at temperatures  $T = 500$ ...600 °C). The destruction of the contact zone during mechanical tensile tests occurs according to the scheme of active cracking.

The presence of powdered solders in the melt pool (in the experiments, VPR-36 solder was used) reduces the change in the parameters of the formed welded joint and increases its crack



resistance. Relative elongation of specimens welded with filler material is  $\delta = 1.3...2.2\%$ , without additives –  $\delta = 0.5...1.1\%$  ( $T = 500...600\text{ }^{\circ}\text{C}$ ).

### Acknowledgement

The work was carried out within the framework of project No. 607182 of the 7th European Framework Program for the creation of ultralight thermal protection structures.

The authors are grateful for the opportunity provided to carry out these studies in conjunction with the «Yuzhnoye» State Design Office (topic No. 384/17 «Manufacturing and welding of elements of the TPG model»). «Yuzhnoye» is a high-tech research and production center of Ukraine in the field of creation and production of spacecraft and launch vehicles, and for which these studies are relevant and significant. Special thanks to the Frantsevich Institute for Problems of Materials Science named of the National Academy of Sciences of Ukraine, which provided blanks, materials and powders for experimental research. We would also like to express our gratitude to the V. Bakul Institute for Superhard Materials for assistance in carrying out certain laboratory studies and tests.

---

### References

- [1] Husarova, I. O., Potapov, O. M., Manko, T. A., Falchenko, Y. V., Petrushintsev, L. V., Frolov, G. A., Soltsev, V. P. (2017). Problems of creations of reusable spacecraft heat protection. *Technological Systems*, 4 (81), 47–55. doi: <https://doi.org/10.29010/081.6>
- [2] Uyanna, O., Najafi, H. (2020). Thermal protection systems for space vehicles: A review on technology development, current challenges and future prospects. *Acta Astronautica*, 176, 341–356. doi: <https://doi.org/10.1016/j.actaastro.2020.06.047>
- [3] Lukin, V. I., Ryl'nikov, V. S., Afanasyev-Khodykin, A. N., Timofeyeva, O. B. (2013). Special features of diffusion welding of EP975 creep-resisting alloy and VKNA-4U cast single-crystal intermetallic alloy for blisk structures. *Welding International*, 28 (7), 562–567. doi: <https://doi.org/10.1080/09507116.2013.840043>
- [4] Rai, R., Elmer, J. W., Palmer, T. A., DebRoy, T. (2007). Heat transfer and fluid flow during keyhole mode laser welding of tantalum, Ti-6Al-4V, 304L stainless steel and vanadium. *Journal of Physics D: Applied Physics*, 40 (18), 5753–5766. doi: <https://doi.org/10.1088/0022-3727/40/18/037>
- [5] Cai, C., Chen, H., Zhang, W. (2017). Research status and development prospects of laser welding under vacuum. *Opto-Electronic Engineering*, 44 (10), 945–952. Available at: <http://www.oejournal.org/oej-data/oej/2017/10/PDF/gdgc-44-10-945.pdf>
- [6] Nawi, I. N., Saktioto, Fadhal, M., Hussain, M. S., Ali, J., Yupapin, P. P. (2011). Nd:YAG Laser Welding of Stainless Steel 304 for Photonics Device Packaging. *Procedia Engineering*, 8, 374–379. doi: <https://doi.org/10.1016/j.proeng.2011.03.069>
- [7] Geng, Y., Akbari, M., Karimipour, A., Karimi, A., Soleimani, A., Afrand, M. (2019). Effects of the laser parameters on the mechanical properties and microstructure of weld joint in dissimilar pulsed laser welding of AISI 304 and AISI 420. *Infrared Physics & Technology*, 103, 103081. doi: <https://doi.org/10.1016/j.infrared.2019.103081>
- [8] Reisgen, U., Olschok, S., Jakobs, S., Turner, C. (2016). Laser beam welding under vacuum of high grade materials. *Welding in the World*, 60 (3), 403–413. doi: <https://doi.org/10.1007/s40194-016-0302-3>
- [9] Salenko, A., Chenchova, O., Glukhova, V., Shchetynin, V., Budar, M. R. F., Klimenko, S., Lashko, E. (2020). Effect of slime and dust emission on micro-cutting when processing carbon-carbon composites. *Eastern-European Journal of Enterprise Technologies*, 3 (1 (105)), 38–51. doi: <https://doi.org/10.15587/1729-4061.2020.203279>
- [10] Alnusirat, W. (2019). Application of Laser Radiation for Intensification of Chemical Heat Treatment. *Lasers in Manufacturing and Materials Processing*, 6 (3), 263–279. doi: <https://doi.org/10.1007/s40516-019-0093-z>
- [11] Salenko, O. F., Shchetynin, V. T., Lashko, E. E., Husarova, I. O., Solntsev, V. P., Sytnyk, O. O. (2018). Guaranteeing of the Mechanical Characteristics of Soldered Thin-Walled Structures of Ni-20Cr-6Al-1Ti-1Y<sub>2</sub>O<sub>3</sub> Refractory Alloy. *Materials Science*, 54 (2), 260–265. doi: <https://doi.org/10.1007/s11003-018-011-4>

Received date 10.07.2020

Accepted date 07.07.2021

Published date 13.09.2021

© The Author(s) 2021

This is an open access article  
under the Creative Commons CC BY license

**How to cite:** Alnusirat, W., Salenko, A., Chenchova, O., Shlyk, S., Gusarova, I., Potapov, A. (2021). About the possibility of application of laser vacuum welding for the integration of elements of heat-protective structures from powder materials. *EUREKA: Physics and Engineering*, 5, 88–99. doi: <https://doi.org/10.21303/2461-4262.2021.001998>



# A NUMERICAL STUDY TO IMPROVE THE POSITION AND ANGLE OF THE PRODUCER GAS INJECTOR INSIDE THE INTAKE MANIFOLD TO MINIMIZE EMISSIONS AND EFFICIENCY ENHANCEMENT OF A BI ENGINE

**Hussein A. Mahmood**✉

*Department of Reconstruction and Projects<sup>1</sup>*  
*husseinadel@uobaghdad.edu.iq*

**Ali O. Al-Sulttani**

*Department of Water Resources Engineering*  
*College of Engineering<sup>1</sup>*

**Osam H. Attia**

*Department of Reconstruction and Projects<sup>1</sup>*

**Nor Mariah. Adam**

*Department of Science and Technology*  
*Universiti Putra Malaysia Bintulu Sarawak Campus*  
*Nyabau Road, Bintulu, Sarawak, Malaysia, 97008*

<sup>1</sup>*University of Baghdad*

*Karrada, Al-Jadriya – Baghdad, Iraq*

✉ Corresponding author

## Abstract

To develop a petrol engine so that it works under the bi-engine pattern (producer gas-petrol) without any additional engine modifications, a single-point injection method inside the intake manifold is a simple and inexpensive method. Still, it leads to poor mixing performance between the air and producer gas. This deficiency can cause unsatisfactory engine performance and high exhaust emissions. In order to improve the mixing inside the intake manifold, nine separate cases were modelled to evaluate the impact of the position and angle orientation inside the intake manifold on the uniformity and spread of the mixture under AFR = 2.07. A petrol engine (1.6 L), the maximum engine speed (8000 rpm), and bi-engine mode (petrol-producer gas engine). The employ of the numerical simulation software (ANSYS workbench 19), the propagation, flow characteristics, and uniformity of the blend within the nine different cases were evaluated. According to the outcomes of the numerical simulation, it was found that creating vortices and turbulent flow for the producer gas and air inside the intake manifold is the perfect method to obtain a uniformity mixture of air and producer gas inside the intake manifold. In addition, extending the blending duration allows air and producer gas fuel to be mixed efficiently. Furthermore, the greatest uniformity and the maximum spread rate at the outlet of manifold are obtained in cases 1, 4, and 7, when the producer gas injector location is constant (P1, P2 or P3). In addition, the weakest spread of producer gas at the outlet of the manifold is observed in case 9 in comparison with the other cases. Moreover, it is observed that case (1) generated the maximum uniformity index (UI) level.

**Keywords:** mixture homogeneity, gas injector orientation, producer gas, computational fluid dynamics, environment.

DOI: 10.21303/2461-4262.2021.002045

## 1. Introduction

The energy crisis deeply impacted negatively on the environment by increasing its contamination [1]. Many methods are used to reduce this effect by figuring out a new power source such as renewable energy [2, 3]. Significant contributions of renewable energy are appeared by the reduction of environment contamination depends on many developed techniques such as electric cars, fuel cells, biomass, hydrogen, LPG, methane, and solar-powered vehicles, these techniques have been used to reduce the emission levels from the transportation sector [2, 4]. Of all the renewable

resources of power for rural regions, the producer gas (PG) from biomass seems to have the highest opportunity [5, 6]. Farming countries have a vast amount of biomass sources. It is reported that between 40 and 60 percent of farming crop residues are either wasted or put to inefficient usage. The producer gas was created by biomass gasification from solid carbonaceous fuels such as coal, wood, charcoal, agricultural and forest wastes, and also animal residues [7, 8]. With combustible components; being methane ( $\text{CH}_4$ ), carbon monoxide ( $\text{CO}$ ), carbon dioxide ( $\text{CO}_2$ ), nitrogen ( $\text{N}_2$ ), hydrogen ( $\text{H}_2$ ), and other trace hydrocarbons at low temperatures between 700 °C to 1000 °C, where the producer gas be used directly as a fuel gas [9, 10].

Using producer gas in bi-engine petrol mode not only permits the cultivation of alternative fuels for cleaner combustion but also enhances the economy of the fuel. A single-point injection is a simpler and cheaper method for changing a petrol engine so that it works in bi-engine phase without any additional alterations to the engine [4, 11–13]. But using a single-point injection leads to poor mixing performance between the air and producer gas. This deficiency can cause unsatisfactory engine performance and high exhaust emissions. The producer gas is stimulated in the bi-engine together with the intake air and compressed as in a traditional petrol engine. The mixture of air and producer gas is ignited by the spark plug. Moreover, the most crucial aspects impacting the engine output, combustion efficiency, and emission decline in gases are AFR and mixture homogeneity which connect directly with the angle and position of the gas injector inside the intake manifold. Homogeneous mixing increased when combustion efficiency increases [14].

The main characteristics of gaseous fuel, which are regarded as a critical challenge facing gaseous fuel during mixture formation, are lower density and poorer fuel permeation. Although gaseous fuel can be rapidly blended with air due to its high diffusivity properties, it could be an inadequate period for blending, especially at a higher rotational speed of the engine. If the injector of gas is positioned at a wide area from the engine cylinder to permit more blending period, the inductive fuel may not enter inside the engine during the required duration. Furthermore, placing the injector near the combustion chamber affected the fluid to not blend correctly because of the short blending period. Hence, Enhancing the burning process and reducing environmental emissions is also closely linked to enhancing the uniformity of the blend (air-fuel) within the engine [15–18].

The orientation of the gas injector also impacts fluid blending properties, such as spread and turbulence. If the injector of gas is positioned in the opposite orientation to the flow of the air, the propagation and turbulence can be enhanced. But it relies on the momentum of the injection of gas fuel. If the gaseous fuel is pumped in the opposite path of the airflow with low pressure, it will not achieve the desired outcomes [19, 20]. Although many reports on the blending properties of air with gaseous fuel have been published, the knowledge is limited for bi-engine worked with producer gas as fuel. Thus, in the presented research, a study has been created to investigate the effect of the gas injector position and direction on the uniformity and spread of the blend inside the intake manifold (air and producer gas) under a bi-engine using CFD software. This research will contribute to enhancing the economy of fuel, improving engine performance, and reducing emissions by determining the optimal location and angle orientation of the producer gas injector inside the intake manifold, which results in homogenous mixing for the producer gas and air mixture based on engine speed.

## 2. Materials and methods

### 2. 1. Improvement of the producer gas Injector position and angle within the Inlet Manifold

To obtain uniformity blend for the air with producer gas within the intake manifold under single-point injection, nine separate cases were generated to determine the effects of the injector positions and angles on the uniformity and propagation of the blend inside the intake manifold (**Tables 1, 2** and **Fig. 1**). In this research, a manifold in the shape of an inverted «L», was utilized to enhance the orientation of the gas injector (position and angle). At three test points (P1, P2, and P3) with three different injection angles for each test point. A real test engine was used to model the dimensions of the intake manifold.



**Table 1**  
Air and producer gas properties [8, 17]

Properties	Air	Producer Gas
Density (Kg/m <sup>3</sup> )	1.225	0.9071756
Viscosity (Pa s)	1.179 E-05	1.49E-05
Specific Heat (J/kg K)	1005.148	3630.11
Thermal Conductivity (W/m K)	0.0240	0.051785

**Table 2**  
Supplied Producer Gas composition [1]

Component	Concentration
Hydrogen	19.16 %
Carbon monoxide	29.60 %
Methane	5.27 %
Carbon dioxide	5.41 %
Nitrogen	40.56 %

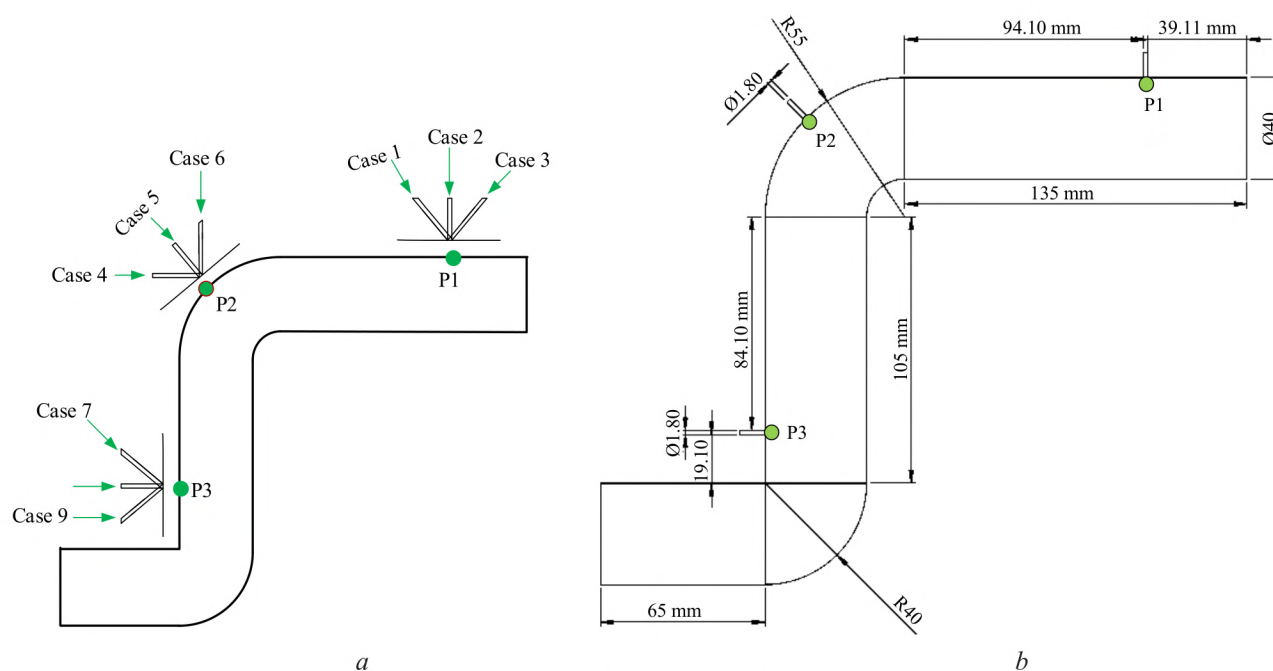


**Fig. 1.** Main parameters of inlet manifold with Producer Gas injector under different cases:  
*a* – schematic view under different cases of injectors; *b* – the main dimensions for manifold

**Fig. 1** demonstrates the dimension of the intake manifold. The ANSYS workbench 19 program was employed to draw nine separate cases of single-point injection within the intake manifold. The specification of producer gas and air that used in this study, as shown in **Table 1**.

## 2. 2. CFD Analysis

Intake manifold under single-point injection was modelled with ANSYS workbench CFD utilization, as shown in **Fig. 2**. Numerical simulation software (ANSYS fluent), was employed to simulate single-phase multi-species flow.

The equations of Reynolds Averaged Navier Stokes (RANS) govern the ANSYS fluent software. The RANS equations are solved by utilizing the algorithm of fully implicit, a finite-volume and pressure-based [13, 18–22].

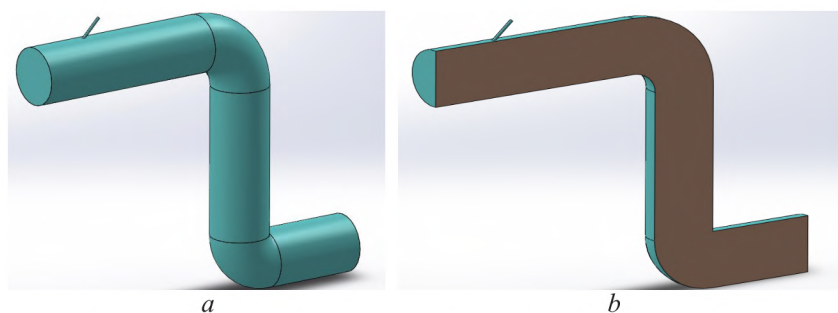


**Fig. 2.** Inlet manifold geometry after drawing with ANSYS workbench software:  
*a* – Isometric display of the inlet manifold; *b* – Inlet manifold section display

### 2. 2. 1. Grid Independent Test (GIT)

ANSYS workbench 19 was used to mesh the nine separate cases of single-point injection within the inlet manifold. An Independent test (IT) was done on the intake manifold with the single producer gas injector (case 1) at engine speed (8000 rpm) and AFR = 2.07. In order to conduct an independent test, six different models of meshing were selected (**Table 3**). ANSYS workbench program was employed to evaluate the grid-independent test on the geometry of the inlet manifold (model 1). The tetrahedron approach was used to mesh the six models, as seen in **Fig. 3**. Tetrahedral forms are applied in this approach to divide the inlet manifold geometry. For the six models, an independent test was carried out by comparing the findings of the producer gas mass fraction, and the UI at the inlet manifold outlet (model 1) as shown in **Fig. 4, 5**.

**Table 3**

Values of elements and nodes employed in IT under case 1

Models	Elements	Nodes
Model 1	211700	40570
Model 2	350200	499065
Model 3	495700	701200
Model 4	668302	938789
Model 5	795701	1114237
Model 6	967719	1349342

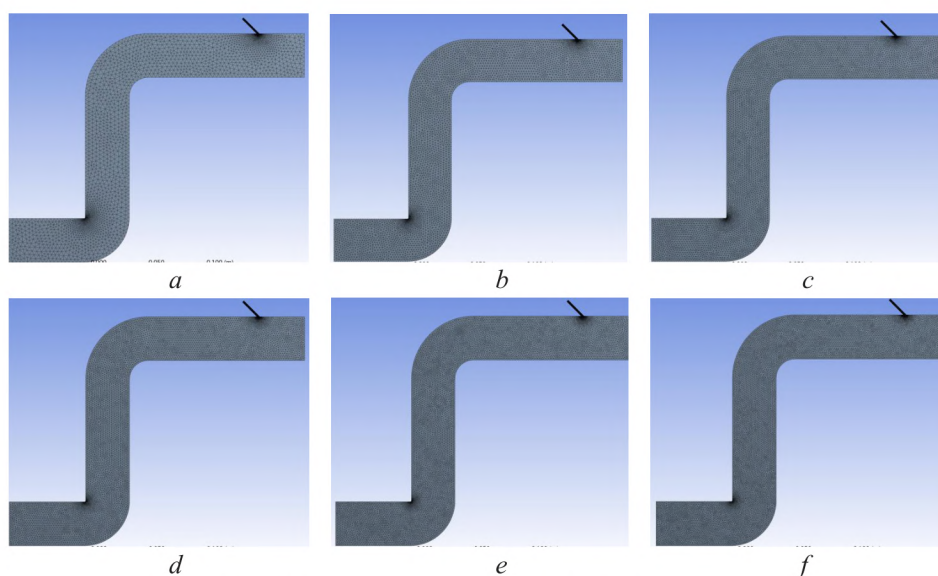


**Fig. 3.** Meshing models that are used in the IT under case 1:  
*a* – model 1; *b* – model 2; *c* – model 3; *d* – model 4; *e* – model 5; *f* – model 6



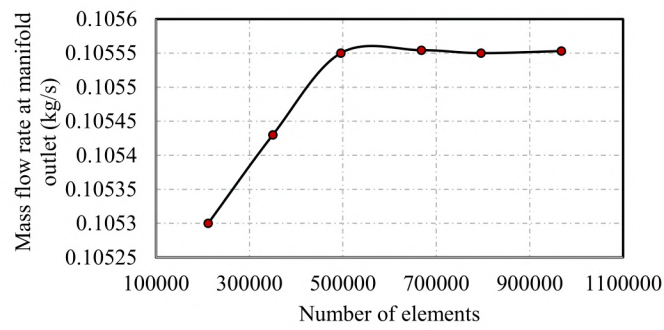


**Fig. 4.** The mass flow rate of the mixture at manifold outlet (case 1), IT results

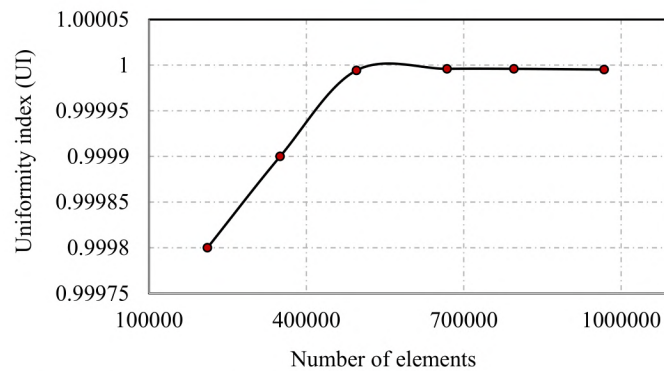


**Fig. 5.** Uniformity index of the mixture at manifold outlet (case 1), IT results

Model 3 has been selected to apply to all cases based on IT, as it provides more precise outcomes and Saves the period of simulation.

### 2. 2. 2. Boundary Condition for the Inlet Manifold with producer gas Injector

The mass flow rate was defined as initial conditions at the inlets and the outlet of the intake manifold under the nine different cases of single-point injection for producer gas inside manifold, as shown in **Fig. 6**.

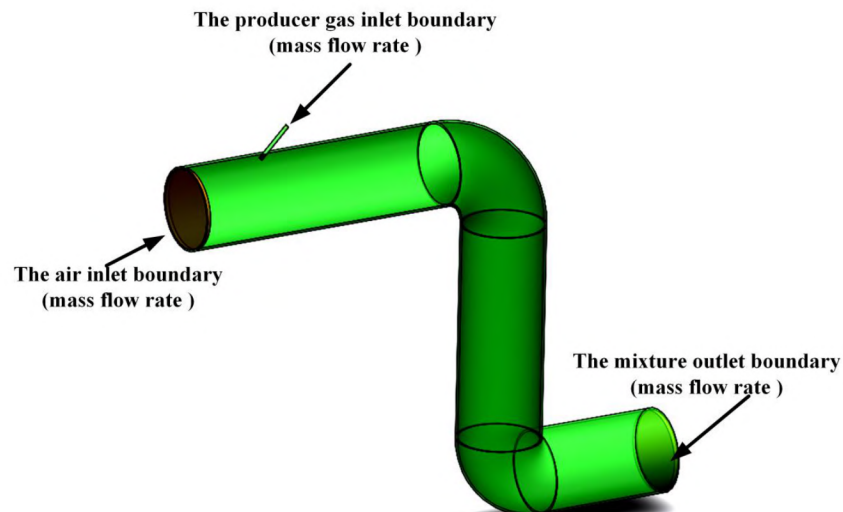


**Fig. 6.** The boundary conditions for the inlet manifold with producer gas injector

The air mass fraction through the air inlet is 1 while the producer gas mass fraction through producer gas inlet is 1 [11, 23].

### 3. Results and Discussion

The calculation of producer gas mass fraction at the inlet of manifold and UI at the outlet of it are achieved by ANSYS software and mixture homogeneity is evaluated under  $AFR = 2.07$ . UI indicator of mixture homogeneity is with ranges between 0 and 1, when the UI value is equal to 1; the air is totally homogeneous with producer gas. Moreover, the producer gas is completely unmixed with air when the UI approaches zero. In addition, to achieve a uniform mixture of air and producer gas at the manifold outlet, producer gas concentration must be uniform and convergent. Fewer colour contours in the mixing area are denoted better blending for air and producing gas.

Single-point injection inside the manifold inlet was tested with nine different cases to figure out the UI values for producer gas at the manifold outlet, as indicated in **Fig. 7**. By the disparity, the highest UI values of 0.9999952 for producer gas are obtained using case 1, and the lowest value is 0.8636226 obtained from case 9. **Fig. 8, 9** demonstrate the contour and volume rendering of producer gas inside the nine different cases of single-point injection within the inlet manifold. **Fig. 10** shows the mass fraction contour of producer gas at the manifold outlet of the nine different cases of single-point injection at the outlet of the inlet manifold under air-producer gas ratio 2.07. The analysis findings show that the highest concentration of producer gas is at the producer gas inlet. There is a significant variation in the spread of producer gas for the zones between the inlet of producer gas and the outlet of the manifold as shown in **Fig. 8–10**.

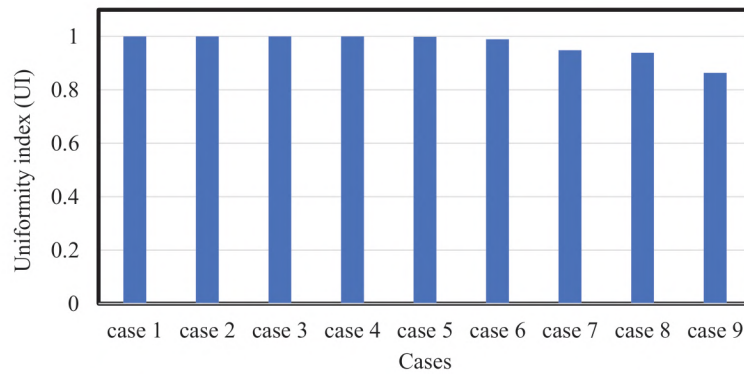


**Fig. 7.** Uniformity index values for producer gas according to the simulation findings for the nine different cases of single-point injection inside the inlet manifold

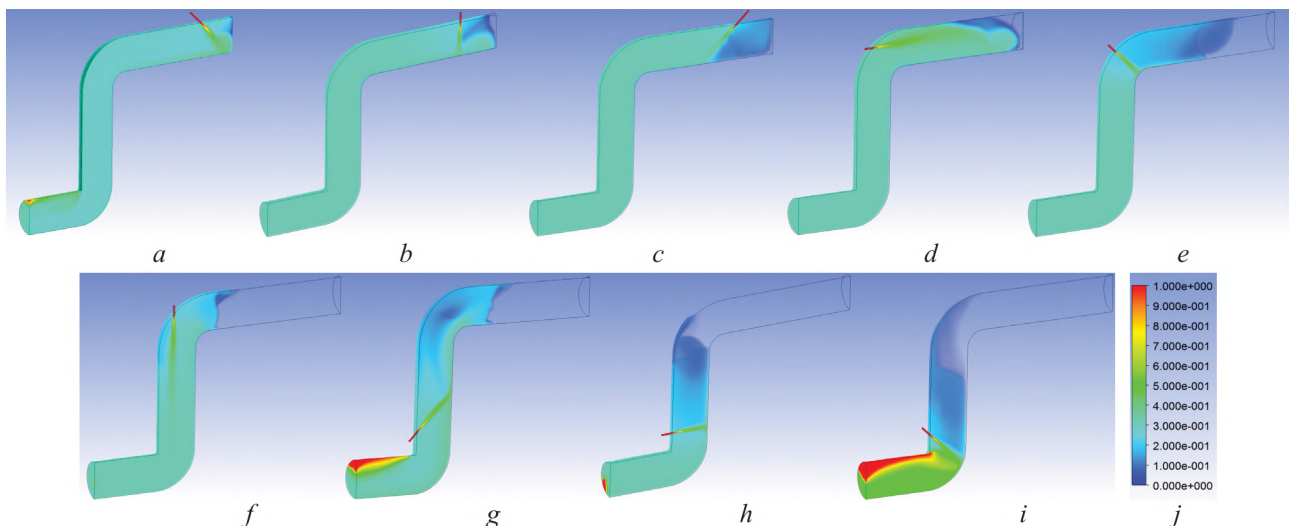


**Fig. 8.** Producer gas mass fraction volume rendering inside the nine different cases of single-point injection inside the inlet manifold under air-producer gas ratio 2.07:  
*a* – case 1; *b* – case 2; *c* – case 3; *d* – case 4; *e* – case 5; *f* – case 6; *g* – case 7;  
*h* – case 8; *i* – case 9; *j* – scale



As achieved from **Fig. 8–10**, the weakest spread of producer gas at the outlet of the manifold is observed in case 9 in comparison with the other cases. This outcome is due to the fact that the declining in the range between the producer gas injector and the manifold outlet decreases the blending period between the producer gas and air, consequently low mixture homogeneity.

**Fig. 8–10** illustrate that all the cases that have producer gas injectors in the same path as the flow of air do not reach the sufficient blending (UI) for producer gas and air when the injector location is constant (P1 or P2 or P3). This outcome is attributable to the reality that the flow within the cases which include injector in the same path as the flow of air is similar to streamline flow inside the manifold with the low swirl. This status prevents the full mixing of producer gas with air.

Furthermore, the greatest uniformity and the maximum spread rate at the outlet of manifold when the producer gas injector location is constant (P1, P2, or P3) as shown in **Fig. 1**, are obtained in cases 1, 4, and 7.

This finding is achieved because the orientation of the gas producer injector is opposite to the flow of air, that way permitting the production of intensely turbulence inflow and extreme swirls within the manifold and the blending of producer gas with air for as long as possible. Besides, case 1 indicates a better distribution of producer gas relative to the other cases (**Fig. 7–10**).

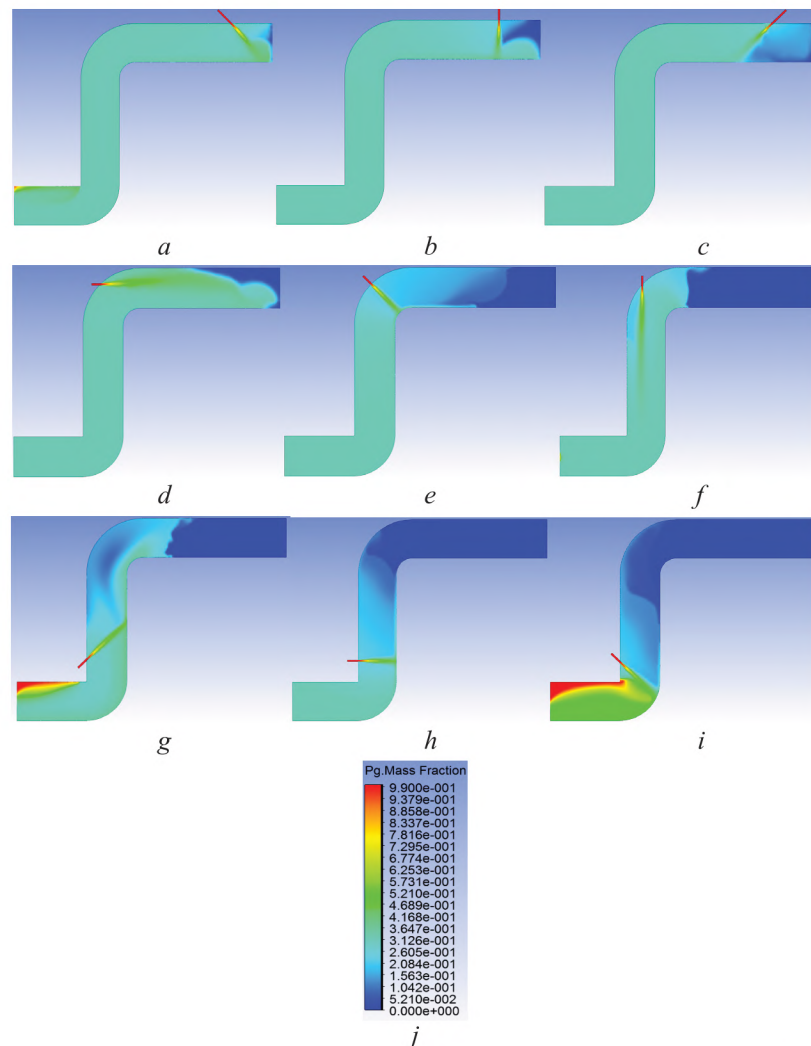


**Fig. 9.** Producer gas mass fraction contour at the plane inside the nine different cases of single-point injection inside inlet manifold under air- producer gas ratio 2.07:

*a* – case 1; *b* – case 2; *c* – case 3; *d* – case 4; *e* – case 5; *f* – case 6; *g* – case 7;  
*h* – case 8; *i* – case 9; *j* – scale

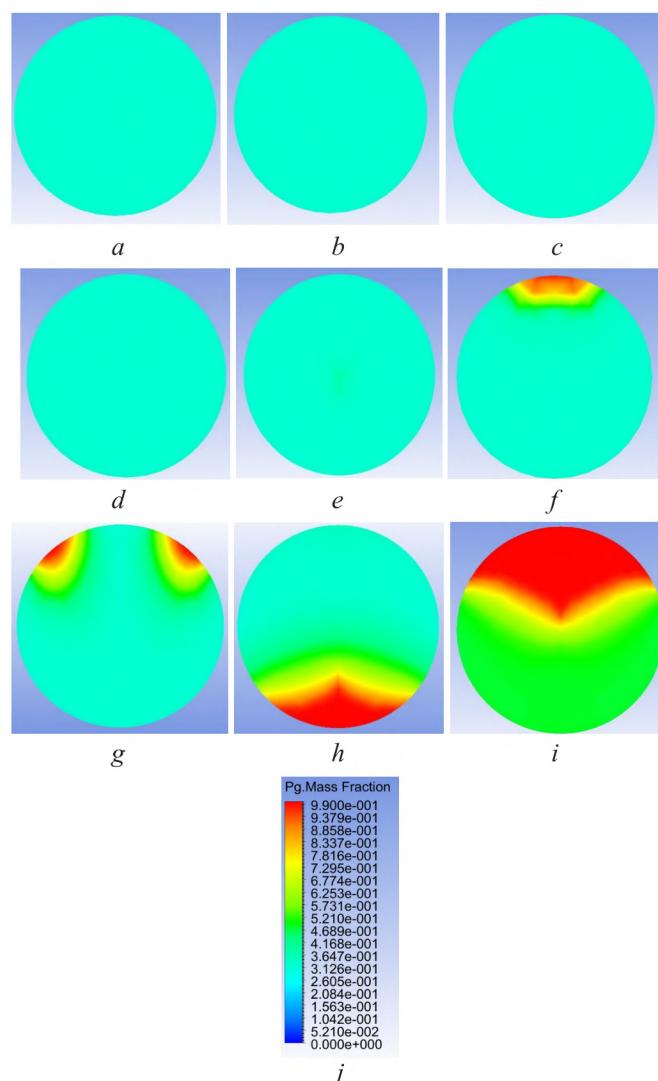


**Fig. 10.** Mass fraction contour of producer gas at the manifold outlet of the nine different cases of single-point injection at the outlet of the inlet manifold under air- producer gas ratio 2.07:  
*a* – case 1; *b* – case 2; *c* – case 3; *d* – case 4; *e* – case 5; *f* – case 6; *g* – case 7;  
*h* – case 8; *i* – case 9; *j* – scale

#### 4. Discussion of numerical results

This research contributes to improving the economy of fuel, improving the performance of the engine, and minimizing emissions by finding the best position and angle orientation of producer gas injector inside the intake manifold that leads to homogeneous mixing for producer gas and air mixture according to engine speed. In addition, the scope of this research is as follows:

1. ANSYS WORKBENCH 19 software was utilized to create nine separate models of the intake manifold with a single-point injector to investigate the effects of the injector positions and angles on the uniformity and propagation of the blend inside the intake manifold under AFR = 2.07.
2. The nine separate models of the intake manifold with single-point injector were tested and checked with bi-engine mode (petrol-producer gas engine), (1.6 L) and the maximum engine speed (8000 rpm).

While the limitation of this study can be summarized as follows.

This research did not deal with investigating and testing the performance of bi-engine experimentally (petrol-producer gas) (power, emission, brake-specific fuel consumption (BSFC) and volumetric efficiency) with the new position and angle orientation of producer gas injector inside the intake manifold in state with and without supercharge.



## 5. Conclusion

The nine different cases of single-point injection inside the inlet manifold were developed to evaluate the uniformity and propagation of the air-producing gas blend utilizing ANSYS Workbench 19. The outcomes of the simulation illustrate that several parameters, such as location and the injector orientation within the intake manifold influence the uniformity and homogeneity of the mixture for producer gas and air within the intake manifold. In addition, creating vortices and turbulent flow for the producer gas and air inside the intake manifold is the perfect method to obtain a uniformity mixture of air and producer gas inside the intake manifold. Furthermore, the producer gas must be in close contact with the air in order to be allowed to blend correctly. In addition, extending the blending duration allows air and producer gas fuel to be mixed efficiently. However, the length of the mixing period is essentially connected to the form of the flow. The outcomes of the analysis show that the highest UI values of 0.9999952 for producer gas are obtained using case 1, and the lowest value is 0.8636226 obtained from case 9.

## Acknowledgments

We would like to extend our sincere gratitude to the support provided who given knowledge and insight that significantly helped the research.

---

## References

- [1] Alhamdany, A. A., Hameed, A. Q., Salman, Q. M. (2018). Experimental Investigation for the Removal of Toxic Gases from Vehicle Exhaust using Non-Thermal Plasma. *Journal of Engineering*, 24 (8), 55. doi: <https://doi.org/10.31026/j.eng.2018.08.05>
- [2] Ali, A. A. M. M., Ali, K., Kim, C., Lee, Y., Oh, S., Kim, K. (2019). Numerical Study of the Combustion Characteristics in a Syngas-diesel Dual-fuel Engine under Lean Condition. *International Journal of Automotive Technology*, 20 (5), 933–942. doi: <https://doi.org/10.1007/s12239-019-0087-7>
- [3] Pichayapat, K., Sukchai, S., Thongsan, S., Pongtornkulpanich, A. (2014). Emission characteristics of using HCNG in the internal combustion engine with minimum pilot diesel injection for greater fuel economy. *International Journal of Hydrogen Energy*, 39 (23), 12182–12186. doi: <https://doi.org/10.1016/j.ijhydene.2014.06.004>
- [4] Karagöz, Y., Güler, İ., Sandalcı, T., Yüksek, L., Dalkılıç, A. S., Wongwises, S. (2016). Effects of hydrogen and methane addition on combustion characteristics, emissions, and performance of a CI engine. *International Journal of Hydrogen Energy*, 41 (2), 1313–1325. doi: <https://doi.org/10.1016/j.ijhydene.2015.11.112>
- [5] Vinay, S., Ravi, S., Prema Kumar, G., Rajan, N. (2008). Numerical and experimental modeling of producer gas carburetor. *Proc. of the International Conference on Advances in Mechanical Engineering*.
- [6] Suryawanshi, S., Yarasu, R. (2014). Design and Simulation of a Producer Gas Carburetor – A Review. *International Journal of Current Engineering and Technology*, 3, 10–13. Available at: <http://inpressco.com/wp-content/uploads/2014/04/Paper310-13.pdf>
- [7] Feng, S. (2017). Numerical Study of the Performance and Emission of a Diesel-Syngas Dual Fuel Engine. *Mathematical Problems in Engineering*, 2017, 1–12. doi: <https://doi.org/10.1155/2017/6825079>
- [8] Dzombo, D., Kiplimo, R., Kiplagat, J. (2014). Use of Biomass Gas in Running Internal Combustion Engine to Generate Electricity-A Review. *Proceedings of 2013 Mechanical Engineering Conference on Sustainable Research and Innovation*, 5, 89–95. Available at: <https://ir-library.ku.ac.ke/bitstream/handle/123456789/15469/Use%20of%20Biomass%20Gas%20in%20Running%20Internal.pdf?isAllowed=y&sequence=1>
- [9] Biradar, S., Ebinezar, R. R. (2013). Validation of Producer Gas Carburetor Using CFD. *International Journal of Latest Research in Science and Technology*, 2 (6), 90–94. Available at: [https://www.mnkjournals.com/journal/ijlrst/pdf/Volume\\_2\\_6\\_2013/10236.pdf](https://www.mnkjournals.com/journal/ijlrst/pdf/Volume_2_6_2013/10236.pdf)
- [10] Azimov, U., Okuno, M., Tsuboi, K., Kawahara, N., Tomita, E. (2011). Multidimensional CFD simulation of syngas combustion in a micro-pilot-ignited dual-fuel engine using a constructed chemical kinetics mechanism. *International Journal of Hydrogen Energy*, 36 (21), 13793–13807. doi: <https://doi.org/10.1016/j.ijhydene.2011.07.140>
- [11] Mahmood, H. A., Adam, N. M., Sahari, B. B., Masuri, S. U. (2016). Investigation on the Air-Gas Characteristics of Air-Gas Mixer Designed for Bi-Engines. *International Journal of Applied Engineering Research*, 11 (12), 7786–7794. Available at: [https://www.researchgate.net/profile/Hussein-Mahmood-4/publication/309072869\\_Investigation\\_on\\_the\\_air-gas\\_characteristics\\_of\\_air-gas\\_mixer\\_designed\\_for\\_bi-engines/links/5e7f8506299b1a91b86624b/Investigation-on-the-air-gas-characteristics-of-air-gas-mixer-designed-for-bi-engines.pdf](https://www.researchgate.net/profile/Hussein-Mahmood-4/publication/309072869_Investigation_on_the_air-gas_characteristics_of_air-gas_mixer_designed_for_bi-engines/links/5e7f8506299b1a91b86624b/Investigation-on-the-air-gas-characteristics-of-air-gas-mixer-designed-for-bi-engines.pdf)

- [12] Gorjibandpy, M., Sangsereki, M. K. (2010). Computational investigation of air-gas venturi mixer for powered bi-fuel diesel engine. *World Academy of Science, Engineering and Technology*, 4 (11), 1197–1201. Available at: <https://publications.waset.org/1578/computational-investigation-of-air-gas-venturi-mixer-for-powered-bi-fuel-diesel-engine>
- [13] Danardono, D., Kim, K.-S., Lee, S.-Y., Lee, J.-H. (2011). Optimization the design of venturi gas mixer for syngas engine using three-dimensional CFD modeling. *Journal of Mechanical Science and Technology*, 25 (9), 2285–2296. doi: <https://doi.org/10.1007/s12206-011-0612-8>
- [14] Mahmood, H. A., Mariah Adam, N., Sahari, B. B., Masuri, S. U., Ahmed, H. E. (2019). An Investigation of Air-Gas Mixer Types Designed for Dual Fuel Engines: Review. *Journal of Engineering and Applied Sciences*, 14 (4), 1014–1033. doi: <https://doi.org/10.36478/jeasci.2019.1014.1033>
- [15] Mahmood, H. A., Mariah. Adam, N., Sahari, B. B., Masuri, S. U. (2018). Development of a particle swarm optimisation model for estimating the homogeneity of a mixture inside a newly designed CNG-H<sub>2</sub>-AIR mixer for a dual fuel engine: An experimental and theoretic study. *Fuel*, 217, 131–150. doi: <https://doi.org/10.1016/j.fuel.2017.12.066>
- [16] Chintala, V., Subramanian, K. A. (2013). A CFD (computational fluid dynamics) study for optimization of gas injector orientation for performance improvement of a dual-fuel diesel engine. *Energy*, 57, 709–721. doi: <https://doi.org/10.1016/j.energy.2013.06.009>
- [17] Hagos, F. Y., Aziz, A. R. A., Sulaiman, S. A. (2014). Trends of Syngas as a Fuel in Internal Combustion Engines. *Advances in Mechanical Engineering*, 6, 401587. doi: <https://doi.org/10.1155/2014/401587>
- [18] Yusaf, T., Yusoff, M. Z. (2000). Development of a 3D CFD model to investigate the effect of the mixing quality on the CNG-diesel engine performance. in *Proceedings of the International Conference and Exhibition and Natural Gas Vehicles*. Yokohama.
- [19] Yusaf, T., Baker, P., Hamawand, I., Noor, M. M. (2013). Effect of Compressed Natural Gas Mixing on the Engine Performance and Emissions. *International Journal of Automotive and Mechanical Engineering*, 8, 1416–1429. doi: <https://doi.org/10.15282/ijame.8.2013.29.0117>
- [20] ANSYS FLUENT 12.0 Theory Guide. Available at: [https://www.afs.enea.it/project/neptunius/docs/fluent/html/th/main\\_pre.htm](https://www.afs.enea.it/project/neptunius/docs/fluent/html/th/main_pre.htm)
- [21] Abo-Serie, E., Özgür, M., Altinsik, K. (2015). Computational analysis of methane-air venturi mixer for optimum design. *Proceedings of the 13th International Combustion Symposium*. Bursa, 9–11.
- [22] Sharma, H., Singh, S., Goel, R. (2014). CFD analysis of the natural gas based Carburetor for a two stroke spark Ignition engine. *National Conference on “Recent Advances in Mechanical Engineering” RAME – 2014*. Available at: [http://www.ijmerr.com/SpecialIssue/12\\_\(p.82-88\).pdf](http://www.ijmerr.com/SpecialIssue/12_(p.82-88).pdf)
- [23] Mahmood, H. A., Adam, N. M., Sahari, B. B., Masuri, S. U. (2016). Investigation On The Air-Gas Characteristics Of Air-Gas Mixer Designed For Dual Fuel-Engines. *International Journal of Control Theory and Applications*, 9 (30), 195–216.

Received date 18.03.2021

Accepted date 02.09.2021

Published date 13.09.2021

© The Author(s) 2021

This is an open access article  
under the Creative Commons CC BY license

**How to cite:** Mahmood, H. A., Al-Sulttani, A. O., Attia, O. H., Adam, N. M. (2021). A numerical study to improve the position and angle of the producer gas injector inside the intake manifold to minimize emissions and efficiency enhancement of a bi engine. *EUREKA: Physics and Engineering*, 5, 100–109. doi: <https://doi.org/10.21303/2461-4262.2021.002045>



# ANALYSIS OF PHYSICAL PROPERTIES AND COMPRESSIBILITY OF AVIAN EGGSHELL NANOPOWDERS IN SOLID STATE REACTION

**Poppy Puspitasari**✉

*Departement of Mechanical Engineering  
Center of Advanced Materials and Renewable Energy<sup>1</sup>  
poppy@um.ac.id*

**Muhammad Asrorul Iftiharsa**

*Departement of Mechanical Engineering<sup>1</sup>*

**Herin Fikri Naufal Zhorifah**

*Departement of Mechanical Engineering<sup>1</sup>*

**Rara Warih Gayatri**

*Public Health Department<sup>1</sup>*

*<sup>1</sup>State University of Malang  
5 Semarang str., Malang, East Java, Indonesia, 65145*

✉ Corresponding author

## Abstract

Eggshell is bioceramic material that produces by avian that commonly contains of 94 % calcium carbonate, 1 % magnesium carbonate, 1 % calcium phosphate, and 4 % other organic element. This study proposed to investigate the synthesis and characterization of avian eggshell powders. The avian eggshell that used in this study involved chicken, duck, and quail eggshells. The characterization of avian eggshell nanopowder for reducing their grain size from micro to nano involved ball milling process (solid state reaction) with the variation of milling times (3, 5, and 7 hours) and sintering temperature at 1000 °C for 2 hours. X-Ray Diffraction (XRD) test presented the phase characterization of quail eggshell nanopowder which ball-milled for 7 hours, obtained the smallest crystallite size at 19.2 nm. Scanning Electron Microscopy (SEM) test presented the morphological analysis that showed changes in grain size and shape of each variety of the avian eggshell such as spherical, oval, wormlike, cubical, triangular, and some irregular grains. Energy Dispersive X-Ray (EDX) test presented the compound in avian eggshell powders that showed Ca and O level were the highest, while C was the lowest level. Fourier Transform Infrared (FTIR) test presented the possibility of the functional group of the avian eggshell powders that showed Ca-O, Ca=O groups, CaCO<sub>3</sub>, asymmetric C-O, -CO<sub>3</sub>, amide, C=O, -OH, alkyl CH, and C-H. While compressibility shown the increase along with the decrease of crystallite and particles size in cubical grain. The highest compression ratio is 67.75 % for chicken eggshell nano powder with 5 hours milling time at 2000 kgf of compression loading.

**Keywords:** Phase identification, compressibility, avian eggshell, solid state reaction, ball milling, milling time, morphology, molecular bonding, bioceramic, grain shape.

DOI: 10.21303/2461-4262.2021.001670

## 1. Introduction

Avian eggshells are bioceramic materials that produced by avian, functioning to protect the egg from mechanical damage [1]. The eggshells are complex permeable bioceramic materials and very structured with large mixing both organic and non-organic phases that showed simple overlap between non-calcified and calcified eggshell membrane [2]. Eggshell contains about 8.5–11 % total mass of the egg, with thickness about 355 µm [3, 4]. Generally, eggshell arranged by 94 % calcium carbonate (CaCO<sub>3</sub>), 1 % magnesium carbonate (MgCO<sub>3</sub>), 1 % calcium phosphate (Ca<sub>3</sub>(PO<sub>4</sub>)<sub>2</sub>), and 4 % organic matter, usually protein, collagen, and sulfated polysaccharides [3–6].

Utilizations of eggshell biological wastes are highly recommended in our society because of environmental and economic reasons. It is known that eggshell wastes contain valuable organic and inorganic component which can be used in commercial product with new value in this waste materials [5]. Especially in Indonesia, that has abundant eggshell wastes. This is because the amount of egg consumption by the Indonesian people is quite high, besides that the shell waste is also

produced from the remnants of the hatchery in the chicken nursery industry [7]. Another reason is because the egg production in Indonesia increases each year, for example, the production of quail egg in 2013 was 18,936 tons then increases to 25,272 tons in 2017 [8].

Eggshells itself have been used in various research such as catalyst for biodiesel and used as a binder [9]. The eggshell also used as filler and precursor for cement mortar in making of gypsum, even used as drug delivery in medical sector [10, 11]. For other applications, eggshells also used as reinforcement at cast metal alloy, even used as basic material to make hydroxyapatite which can be used as an implant material for bone and used as tooth filler [7, 12, 13]. In the form of  $\text{CaCO}_3$ , many application has been discussed. One of them is the application for alkali-activated aluminosilicate binders [14]. It was revealed that the addition of  $\text{CaCO}_3$  intensified the nano-structured formation processes in the direction of formation of Na-Ca zeolite-like phases and shortening the required time for cement stone to gain water resistance in normal conditions [15].

Based on these data, the objective of this research is to utilize eggshell waste into  $\text{CaCO}_3$  powder in an easy and inexpensive way that can later be used in various applications. The synthesis that was carried out to obtain  $\text{CaCO}_3$  from eggshells was by ball-milling process, therefore to get the best results, this study used variations in milling time and carried out characterization in the form of phase identification, morphology, functional groups, and compressibility values. The results of this characterization will be useful for the application of  $\text{CaCO}_3$  as a tooth filler in dental implants.

## 2. Materials and methods

In this research the specimen that used are variation of dried avian eggshells which includes chicken, duck, and quail eggshell. The synthesis of avian eggshells done with ball mill method using planetary ball mill (MTI QM-3SP2), which intend to produce particles in nano-sized by mixing 300 g micro-sized of eggshell with 100 ml of acetone, to obtain the optimum result of final particle size [16]. The mixing was carried out with the variation of milling time, i. e. 3, 5, and 7 hours for each variety of the eggshell. After ball mill process, drying was done at temperature  $110^\circ\text{C}$  for 1 hour [15]. The next process is crushing for 1 hour [8]. After crushing, sintering process has been done at temperature  $1000^\circ\text{C}$  for 2 hours [7]. After sintering, do crushing for 1 hour [8]. The characterization process aims to identify phase, morphology, elemental composition, and functional groups using XRD (PanAnalytical E'xpert Pro), SEM-EDX (FEI Inspect-S50), and FTIR (Shimadzu IRPrestige21). For compressibility test, it used cold pressing by using universal testing machine (ILE IL-904) with load of 1000 kgf and 2000 kgf for 90 seconds [17].

**Fig. 1** shows the samples after ball milling process for 7 hours that consist of sintering and non-sintering powder.

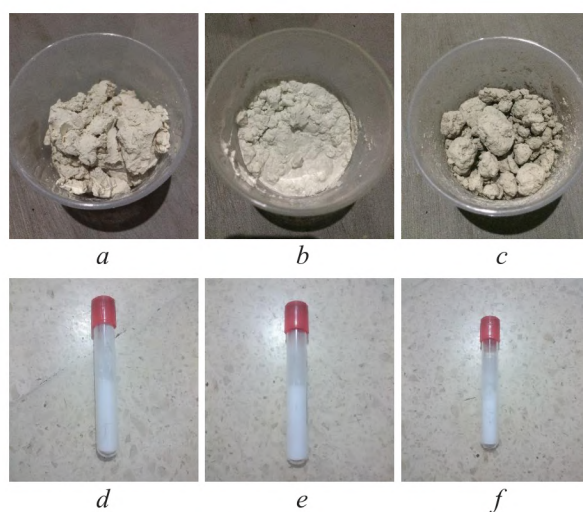


**Fig. 1.** Avian eggshells after ball mill process: *a* – chicken eggshell non-sintering; *b* – duck eggshell non-sintering; *c* – quail eggshell non-sintering; *d* – chicken eggshell after sintering; *e* – duck eggshell after sintering; *f* – quail eggshell after sintering



**Fig. 1, a, b, and c** are the chicken, duck, and quail eggshell without sintering process and crushed for 1 hours, respectively. **Fig. 1, d, e, f** are the chicken, duck, and quail eggshell with sintering process at 1000 °C for 2 hours in environmental condition and crushed for 1 hours.

### 3. Results

Naming of samples in this discussion using (CES) for chicken eggshell, (DES) for duck eggshell, and (QES) for quail eggshell with (M3H) for 3 hours of milling time, (M5H) for 5 hours of milling time, and (M7H) for 7 hours of milling time.

#### 3.1. Phase Identification

The results of XRD test were shown in **Fig. 2**. Intensity, FWHM, d-spacing, and crystallite size are shown in **Table 1**. The crystallite size was calculated using Scherrer (1) as [8, 15]:

$$d = \frac{k \cdot \lambda}{\beta \cos \theta} \quad (1)$$

Where  $d$  is the diameter of crystallite,  $K$  is the constant (0.89–0.9),  $\lambda$  is the wavelength (1.5406 Å), and  $\beta$  is Full-Width Half Maximum (FWHM).

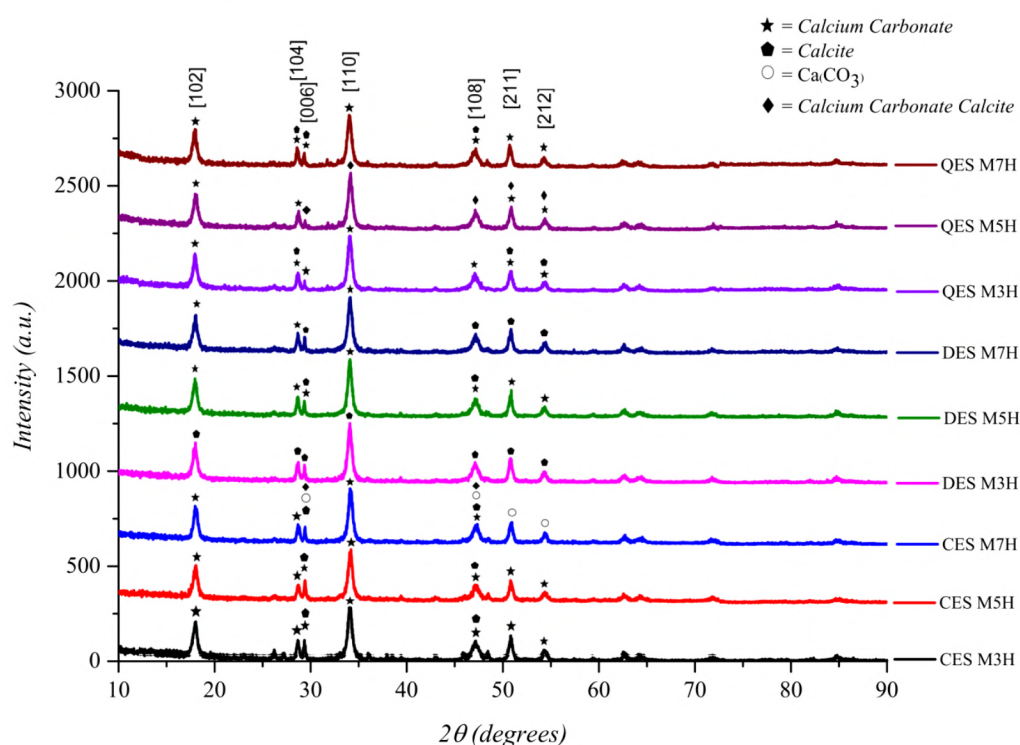


**Fig. 2.** Diffractogram graph of avian eggshell nanopowders

XRD test results were analyzed using Match! software (v3.8.0.137) with crystallography reference database used (COD-Inorg REV218120 2019.09.10). The results of XRD test shown that all samples have several peaks, namely [102], [104], [006], [110], [108], [211], and [212] which appropriate with trigonal phase. The highest peak is positioned at 34,1 °2Th. The existence of peak indicated the presence of  $\text{CaCO}_3$ , with the form of  $\text{Ca}(\text{CO}_3)$  which has crystal system of monoclinic, calcium carbonate calcite which has crystal system of rhombohedral, and calcium carbonate and calcite which has crystal system of trigonal (hexagonal axes).

Based on **Fig. 2**, it can be seen visually that the XRD results have similar pattern. However, **Table 1** shows that there is a difference in intensity and FWHM. Also, based on **Table 1**, it can be seen that the intensity has a correlation with the crystallite size. The higher the intensity, the larger crystallite size originating from the increase of FWHM [2]. The smallest crystallite

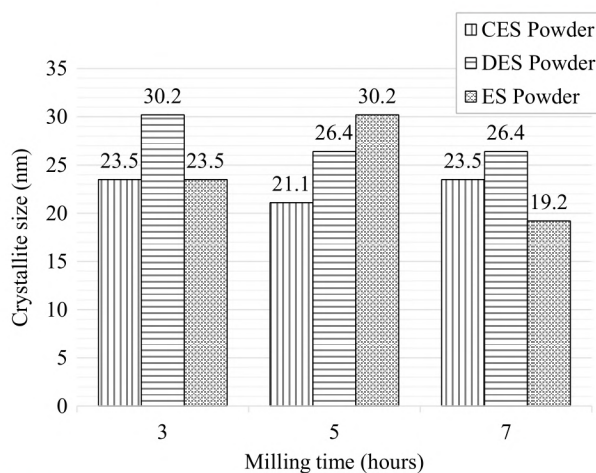
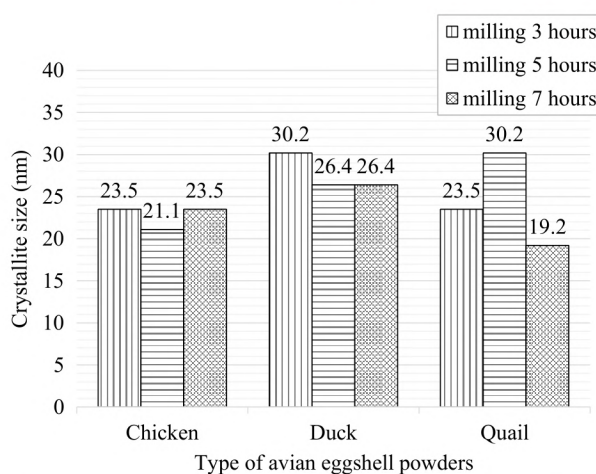
size which counted is 19.2 nm at quail eggshell nanopowder with 7 hours of milling time, and the largest crystallite size which counted is 30.2 nm at duck eggshell nanopowder with 3 hours of milling time and quail eggshell nanopowder with 5 hours of milling time.

**Table 1**

Intensity, FWHM, d-spacing, and crystallite size of avian eggshell nanopowders

Samples	X-Ray Diffraction (correspond to peak [110])			
	Intensity (cts)	FWHM (rad)	d-spacing (Å)	Crystallite size (nm)
CES M3H	260.02	0.006181956	2.62657	23.5
CES M5H	238.64	0.006869616	2.62356	21.1
CES M7H	255.92	0.006181956	2.62236	23.5
DES M3H	285.00	0.004808382	2.62849	30.2
DES M5H	274.76	0.005496042	2.62877	26.4
DES M7H	260.26	0.005496042	2.62810	26.4
QES M3H	275.07	0.006181956	2.62807	23.5
QES M5H	277.43	0.004808382	2.62466	30.2
QES M7H	262.90	0.007557276	2.63164	19.2

The correlation between milling time and crystallite size was shown in **Fig. 3**, while the correlation between type of avian eggshell powder and crystallite size was shown in **Fig. 4**.

**Fig. 3.** Correlation between milling time and crystallite size**Fig. 4.** Correlation between type of avian eggshell powder and crystallite size



### 3. 2. Morphological Characterization

The morphology of avian eggshell was observed by using SEM [2–4]. The SEM results of avian eggshell powders with variation of milling times, shown in **Fig. 5**.

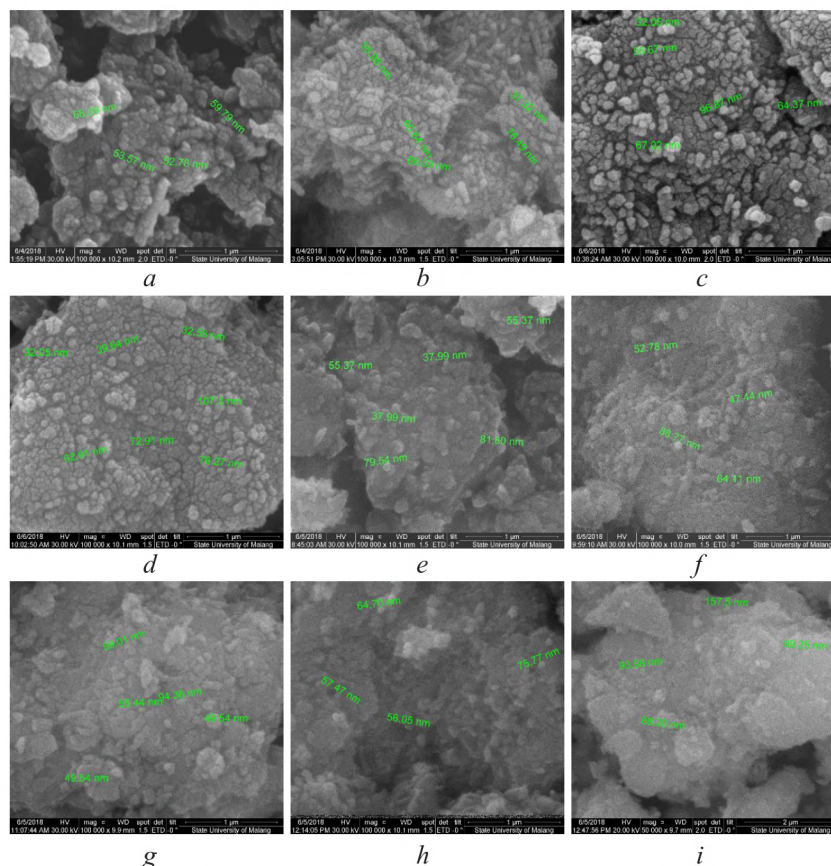


**Fig. 5.** Morphology of avian eggshell nanopowders:

*a* – CES M3H; *b* – CES M5H; *c* – CES M7H; *d* – DES M3H; *e* – DES M5H; *f* – DES M7H;  
*g* – QES M3H; *h* – QES M5H; *i* – QES M7H

**Fig. 5** shows the morphology of avian eggshell nanopowders with magnification of 100000 times. **Fig. 5, a** shows the morphology of chicken eggshell nanopowder with 3 hours of milling time was spherical with few of oval with the smallest size was 52.78 nm and the largest size was 68.59 nm. **Fig. 5, b** shows the morphology of chicken eggshell nanopowder with 5 hours of milling time was have the form of wormlike with the smallest size was 37.32 nm and the largest size was 76.49 nm. **Fig. 5, c** shows the morphology of chicken eggshell nanopowder with 7 hours of milling time was roundness and few of oval with the smallest size was 32.05 nm and the largest size was 96.87 nm.

**Fig. 5, d** shows the morphology of duck eggshell nanopowder with 3 hours of milling time was spherical with few of oval with the smallest size was 32.05 nm and the largest size was 107.8 nm. **Fig. 5, e** shows the morphology of duck eggshell nanopowder with 5 hours of milling time was cubical with the smallest size was 37.99 nm and the largest size was 81.80 nm. **Fig. 5, f** shows the morphology of duck eggshell nanopowder with 7 hours of milling time was spherical and few of irregular with the smallest size was 47.44 nm and the largest size was 88.77 nm.

**Fig. 5, g** shows the morphology of quail eggshell nanopowder with 3 hours of milling time was spherical, with few of cubical and triangular with the smallest size was 49.54 nm and the largest size was 94.38 nm. **Fig. 5, h** shows the morphology of quail eggshell nanopowder with 5 hours of milling time was spherical and few of oval with the smallest size was 56.05 nm and the largest size was 75.77 nm. **Fig. 5, i** shows the morphology of quail eggshell nanopowder with

7 hours of milling time was cubical, spherical, and few of triangular with the smallest size was 88.20 nm and the largest size was 157.5 nm.

In Fig. 5, *a–d*, the uniformity in the structure of grains on the surface showed that agglomeration was the sediment particles on the membrane of eggshell nanopowders grains [2]. While in Figure Fig. 5, *e–i*, the uniformity in the structure of grains on the surface showed that agglomeration was occurred as particles deposited on the membrane of eggshell nanopowders grains [2]. There is no significant change in the particles size which cause by kinetic energy used in milling process that causing the reduction of particle size can be achieved by longer milling time [5].

### 3. 3. Functional Groups Characterization

The functional group of avian eggshell nanopowders has been observed by using FTIR test. The results of FTIR test were showed in Fig. 6.

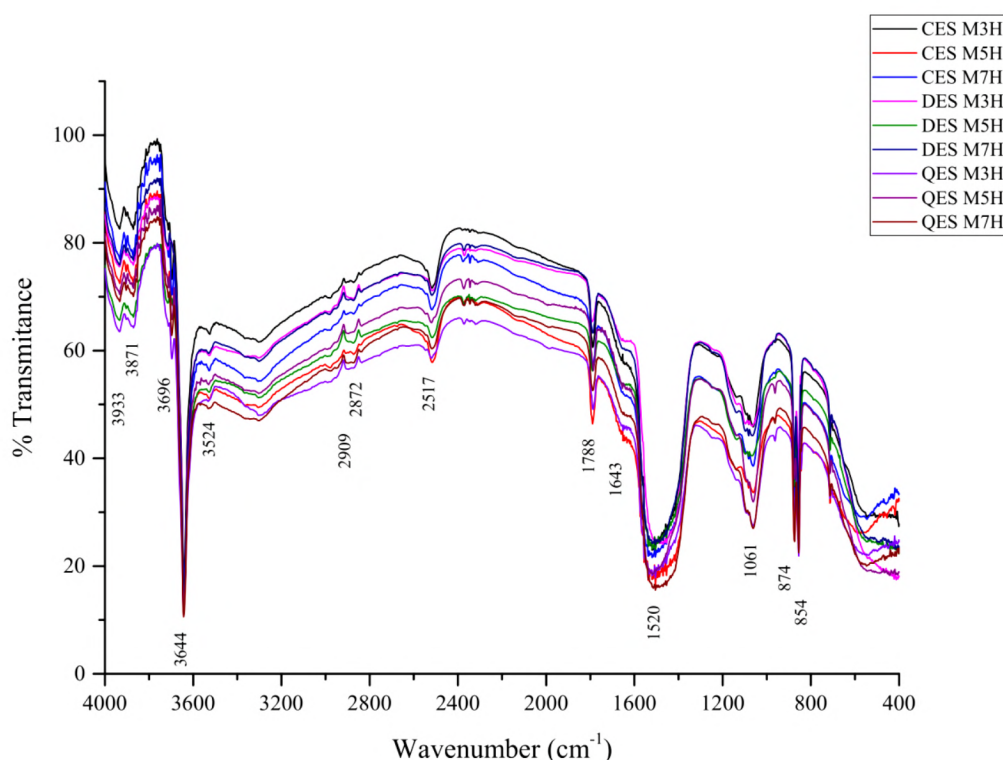


Fig. 6. FTIR spectra of avian eggshell nanopowders

Fig. 6 shows that the strong peaks were observed at the bands 3644 and 1520  $\text{cm}^{-1}$ . Bands at 3644 and 2517  $\text{cm}^{-1}$  possibly indicate to the presence of hydroxyl alcohol group (-OH) stretching during adsorption of water by CaO and acidic hydrogen group (-OH) stretching, respectively [8, 18]. Band at 1520  $\text{cm}^{-1}$  can be related to the presence of carbonate mineral ( $\text{CO}_3$ ) in the matrix of eggshell powders [18, 19]. Bands at 854 and 874  $\text{cm}^{-1}$  possibly related to in-plane and out-plane deformations, which indicate to the presence of calcium carbonate ( $\text{CaCO}_3$ ) [8, 18, 20]. Bands at 874 and 1520  $\text{cm}^{-1}$  also related with asymmetric C-O with carbonate group vibration [8]. Bands at 2909 and 2872  $\text{cm}^{-1}$  represent C-H vibration and assign to alkyl CH, which indicating the existence of organic layers, built from amino acids, in the eggshells [8, 18]. Bands at 1788 and 1643  $\text{cm}^{-1}$  correspond with C=O and carbonyl group stretching (amide), respectively [18]. Bands at 500–580  $\text{cm}^{-1}$  and 586  $\text{cm}^{-1}$  shows the presence of Ca-O bond and Ca=O group, respectively [8, 20]. The differences of FTIR spectra of avian eggshell powders can be occur because of chemical treatment like oxidation, addition, and substitution that would effect the chemical nature of membrane top layer [21]. It also known that the final stoichiometry depends on the control and monitoring of the milling conditions [6].



### 3. 4. Analysis of compressibility

Compressibility and compression ratio has been calculated using (2), (3) [22, 23], respectively. The results have been sorted by the grain shapes that found on each sample and has been shown in Table 3. Fig. 7–10 has showed the correlations between physical properties and compressibility of the samples.

$$\rho_p = \frac{m}{V}, \quad (2)$$

$$CR = \frac{h_0 - h_p}{h_0} \cdot 100 \%, \quad (3)$$

where  $\rho_p$  is the compressibility ( $\text{g/cm}^3$ );  $m$  is compact mass (g);  $V$  is compact volume ( $\text{cm}^3$ );  $CR$  is compression ratio (%);  $h_0$  is height at zero pressure (cm),  $h_p$  is compact height (cm).

**Table 3**

Crystallite sizes, particle sizes, compression ratio, and compressibility of eggshell nanopowders

Grain shapes	Samples	Crystallite size (nm)	Particle sizes (nm)	Compression ratio ( %)		Compressibility ( $\text{g/cm}^3$ )	
				1000 kgf	2000 kgf	1000 kgf	2000 kgf
Spherical	QES M5H	30.2	56.05	59.50	61.00	1.56	1.60
Oval	DES M3H	30.2	32.05	63.25	63.00	1.64	1.67
	DES M7H	26.4	47.44	61.25	67.00	1.64	1.76
	CES M3H	23.5	52.78	64.00	67.50	1.56	1.70
Cubical	DES M5H	26.4	37.99	58.00	64.00	1.63	1.76
Triangular	QES M3H	23.5	49.54	60.00	61.50	1.57	1.65
Spherical	CES M7H	23.5	32.05	60.75	61.25	1.56	1.66
Oval	QES M7H	19.2	88.2	53.75	60.75	1.56	1.61
Wormlike	CES M5H	21.1	37.32	63.50	67.75	1.63	1.71
Irregular							

Fig. 7, 8 show that the compressibility and compression ratio of samples with spherical and oval grain shapes have increase on both 1000 and 2000 kgf of load. It is because of the increasing of compressibility and compression ratio along with the decreasing of crystallite and particle sizes [23, 24]. While Fig. 9, 10 show that the compressibility and compression ratio in samples with cubical, triangular, spherical and oval grain shapes slightly decrease on both 1000 and 2000 kgf of load, due to morphology such as particle sizes and grain shapes take effect on compressibility [25]. It is because the irregular grain shapes of grain are more difficult to compact than spherical grain shapes, due to it can make it easier to shear deformations to happen [26]. In this reasearch, the milling times does not have significant effect to the compressibility.

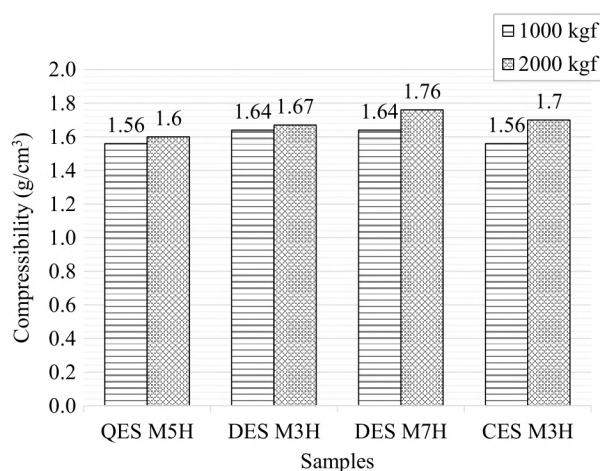


**Fig. 7.** Compressibility in spherical and oval grain shapes

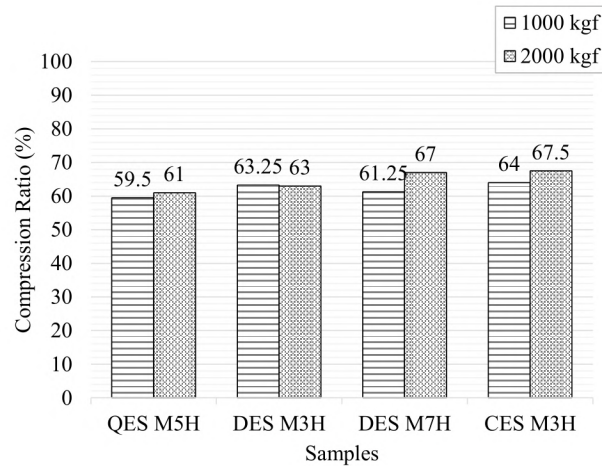


**Fig. 8.** Compression ratio in spherical and oval grain shapes

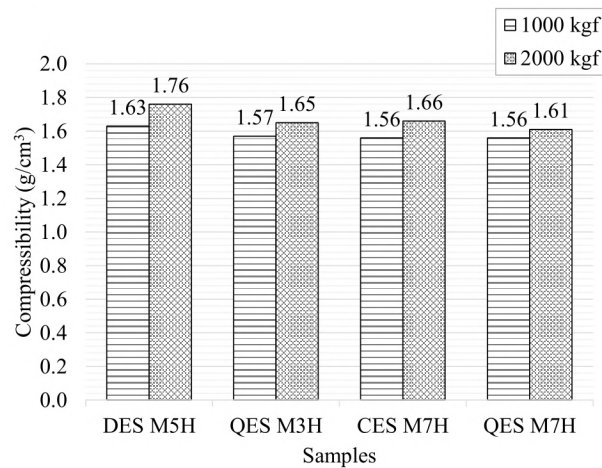


**Fig. 9.** Compressibility in cubical, triangular, spherical, and oval grain shapes

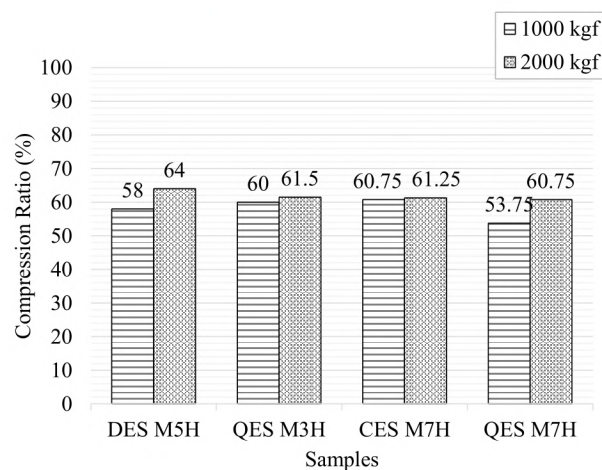


**Fig. 10.** Compression ratio in cubical, triangular, spherical, and oval grain shapes

#### 4. Discussion of experimental results

The results of data analysis showed that the crystallite size with a longer milling time had a smaller size. Meanwhile, larger crystallite sizes can be due to agglomeration and also the sintering process which can cause larger grain sizes [7]. This is because at the same time, the grain



size increases as the temperature increases, it approaching  $1\text{ }\mu\text{m}$  at  $1000\text{ }^{\circ}\text{C}$  ( $1273\text{ K}$ ) [27]. The phases found in this study are calcium carbonate and calcite which have a trigonal crystal system (hexagonal axes),  $\text{Ca}(\text{CO}_3)$  which has a monoclinic crystal system, and calcium carbonate calcite which has a rhombohedral crystal system. The crystalline phase in this study did not change significantly, it was indicated by all the phases found that were still included in the carbonate mineral. This means that the milling process cannot change the structure of the test specimen. Theoretically, the energy supplied from this process cannot overcome the breakdown of the structure [15].

Based on SEM result, it is also known that the dominant grain diameter size of the powdered poultry egg shell with the variation of the milling time is on average below  $100\text{ nm}$  which makes it classified as a nanopowder. In the test specimens of eggshell powder, it can be seen that the particle size is not much different, it could be due to the milling time which is not too different. This is because the kinetic energy used in the milling process which causes a reduction in particle size can be obtained with a longer milling time [28].

Differences in the FTIR spectra of eggshell powder can occur due to chemical treatments such as oxidation, addition, and substitution which can result in chemical properties of the top layer of the membrane [21]. It is also known that the final stoichiometry depends on controlling and monitoring the milling conditions [28].

This research offers a synthetic method for processing large amounts of eggshell waste using a solid state reaction. When compared to other synthesis methods, such as sol-gel and coprecipitation, the solid state reaction method is a method that can produce a large number of products. The drawback of this method is that the results obtained have a morphology that is not uniform and tends to agglomerate, therefore, to achieve the uniform size of nanoparticles it is necessary to carry out further synthesis or by using high energy ball milling process. The correlation between physical properties and compressibility is influenced by the grain shape and the size of the crystal or particle. Meanwhile, in this research, it was shown that the milling time did not have a significant effect on grain shape, crystal size, and particle size. This indicates that the milling time used in this study has small effect on the correlation between physical properties and compressibility of poultry eggshell nano powder (chicken, duck, and quail). From this results,  $\text{CaCO}_3$  derived from eggshell is a good candidate for tooth filler because it has good compressibility for almost all the type of eggshells. From all characterization results, the three types of eggshells have similarities with each other. But if we look more closely, duck eggshells have a more stable character in terms of crystallite size, compressibility, and uniform morphology not to mention about the availability compare to the quail eggshell. This study focused on the use of eggshells as implant material and from this study, the best eggshells were duck eggshells with a milling time variation of 5 hours. From the simulation results in the previous research,  $\text{CaCO}_3$  from eggshell powder was increase the strength of mastication 40 times and the most important parameter is the crystallite size of  $\text{CaCO}_3$  [7, 8]. Other application that related to the implant material is hydroxyapatite (HA) that can be obtain from  $\text{CaCO}_3$  and natrium phosphate. The biocompatibility and bioactivity properties of HA from eggshell powder has similarities with inorganic components of hard tissue in natural tissue of bones and teeth [29, 30].

## 5. Conclusion

Nanopowders of the avian eggshell wastes had been successfully produced by the ball mill process. The smallest crystallite size which counted is  $19.2\text{ nm}$  at quail eggshell nanopowder with 7 hours of milling time, and the largest crystallite size which counted is  $30.2\text{ nm}$  at duck eggshell nanopowder with 3 hours of milling time and quail eggshell nanopowder with 5 hours of milling time. The morphology shows that the major shape of the grains is spherical, but there is no significant change to the grains of avian eggshell nanopowders. The elemental composition represents the dominant element that can be found in avian eggshell nanopowders are calcium (Ca), oxygen (O), and carbon (C). The functional group shows the existence of  $\text{CaCO}_3$ ,  $\text{CaO}$ , and carbonate mineral contained in avian eggshell nanopowders. While compressibility of avian eggshell nanopowders will increase along with decreasing of crystallite and particle sizes. The grain shapes will take effect of the compressibility because it can effect



deformations. Based on the results, by knowing the physical properties of the avian eggshell nanopowders, it can be used for multipurpose applications such as material to make hydroxyapatite, tooth filler, catalyst, reinforce, and also become proper material for mass production of  $\text{CaCO}_3$  and  $\text{CaO}$ .

### Acknowledgement

The authors would like to thank to Kemenristek/BRIN for Hibah PDUPT lanjutan 2020 for Poppy Puspitasari.

---

### References

- [1] Sun, C., Duan, Z., Qu, L., Zheng, J., Yang, N., Xu, G. (2016). Expression analysis for candidate genes associated with eggshell mechanical property. *Journal of Integrative Agriculture*, 15 (2), 397–402. doi: [https://doi.org/10.1016/s2095-3119\(14\)60969-2](https://doi.org/10.1016/s2095-3119(14)60969-2)
- [2] Hincke, M., Gautron, J., Rodriguez-Navarro, A. B., McKee, M. D. (2011). The eggshell: structure and protective function. *Improving the Safety and Quality of Eggs and Egg Products*, 151–182. doi: <https://doi.org/10.1533/9780857093912.2.151>
- [3] Aygun, A. (2017). The Eggshell Microbial Activity. *Egg Innovations and Strategies for Improvements*, 135–144. doi: <https://doi.org/10.1016/b978-0-12-800879-9.00013-5>
- [4] Fernandes, E. de A., Litz, F. H. (2017). The Eggshell and Its Commercial and Production Importance. *Egg Innovations and Strategies for Improvements*, 261–270. doi: <https://doi.org/10.1016/b978-0-12-800879-9.00025-1>
- [5] Yew, M. C., Ramli Sulong, N. H., Yew, M. K., Amalina, M. A., Johan, M. R. (2013). The formulation and study of the thermal stability and mechanical properties of an acrylic coating using chicken eggshell as a novel bio-filler. *Progress in Organic Coatings*, 76 (11), 1549–1555. doi: <https://doi.org/10.1016/j.porgcoat.2013.06.011>
- [6] Saeb, M. R., Rastin, H., Nonahal, M., Paran, S. M. R., Khonakdar, H. A., Puglia, D. (2018). Cure kinetics of epoxy/chicken eggshell biowaste composites: Isothermal calorimetric and chemorheological analyses. *Progress in Organic Coatings*, 114, 208–215. doi: <https://doi.org/10.1016/j.porgcoat.2017.10.018>
- [7] Zhorifah, H. F. N., Puspitasari, P., Andoko, Tsamroh, D. I., Permanasari, A. A. (2019). Optimization of the mastication strength of hydroxyapatite as an eggshell-based tooth filler. *International Conference on Biology and Applied Science (ICOBAS)*. doi: <https://doi.org/10.1063/1.5115686>
- [8] Supriyanto, N. S. W., Sukarni, Puspitasari, P., Permanasari, A. A. (2019). Synthesis and characterization of  $\text{CaO}/\text{CaCO}_3$  from quail eggshell waste by solid state reaction process. *International Conference on Biology and Applied Science (ICOBAS)*. doi: <https://doi.org/10.1063/1.5115670>
- [9] Ayodeji, A. A., Modupe, O. E., Rasheed, B., Ayodele, J. M. (2018). Data on  $\text{CaO}$  and eggshell catalysts used for biodiesel production. *Data in Brief*, 19, 1466–1473. doi: <https://doi.org/10.1016/j.dib.2018.06.028>
- [10] Pliya, P., Cree, D. (2015). Limestone derived eggshell powder as a replacement in Portland cement mortar. *Construction and Building Materials*, 95, 1–9. doi: <https://doi.org/10.1016/j.conbuildmat.2015.07.103>
- [11] Jayasree, R., Madhumathi, K., Rana, D., Ramalingam, M., Nankar, R. P., Doble, M., Kumar, T. S. S. (2018). Development of Egg Shell Derived Carbonated Apatite Nanocarrier System for Drug Delivery. *Journal of Nanoscience and Nanotechnology*, 18 (4), 2318–2324. doi: <https://doi.org/10.1166/jnn.2018.14377>
- [12] Zhu, H., Guo, D., Sun, L., Li, H., Hanaor, D. A. H., Schmidt, F., Xu, K. (2018). Nanostructural insights into the dissolution behavior of Sr-doped hydroxyapatite. *Journal of the European Ceramic Society*, 38 (16), 5554–5562. doi: <https://doi.org/10.1016/j.jeurceramsoc.2018.07.056>
- [13] Puspitasari, P., Safarudin, R. A., Sasongko, M. I. N., Achyarsyah, M., Andoko. (2019). Analysis of Mechanical and Physical Properties of Al-Si (Al-Si) Casting Alloys Reinforced with Various Eggshell Nanopowders. *IOP Conference Series: Materials Science and Engineering*, 515, 012028. doi: <https://doi.org/10.1088/1757-899x/515/1/012028>
- [14] Bodnarova, L., Guzii, S., Hela, R., Krivenko, P., Vozniuk, G. (2018). Nano-Structured Alkaline Aluminosilicate Binder by Carbonate Mineral Addition. *Solid State Phenomena*, 276, 192–197. doi: <https://doi.org/10.4028/www.scientific.net/ssp.276.192>
- [15] Puspitasari, P., Yuwanda, V., Sukarni, Dika, J. W. (2019). The Properties of Eggshell Powders with the Variation of Sintering Duration. *IOP Conference Series: Materials Science and Engineering*, 515, 012104. doi: <https://doi.org/10.1088/1757-899x/515/1/012104>
- [16] Nandiyanto, A. B. D., Andika, R., Aziz, M., Riza, L. S. (2018). Working Volume and Milling Time on the Product Size/Morphology, Product Yield, and Electricity Consumption in the Ball-Milling Process of Organic Material. *Indonesian Journal of Science and Technology*, 3 (2), 82. doi: <https://doi.org/10.17509/ijost.v3i2.12752>
- [17] Qosim, N., Murdanto, P., Puspitasari, P. (2018). Analisis Sifat Fisik dan Kompresibilitas Nanopowder Zinc Oxide ( $\text{ZnO}$ ) sebagai Alternatif Material Amalgam. *Jurnal Rekayasa Mesin*, 9 (1), 9–14. doi: <https://doi.org/10.21776/ub.jrm.2018.009.01.2>



- [18] Tizo, M. S., Blanco, L. A. V., Cagas, A. C. Q., Dela Cruz, B. R. B., Encoy, J. C., Gunting, J. V. et. al. (2018). Efficiency of calcium carbonate from eggshells as an adsorbent for cadmium removal in aqueous solution. *Sustainable Environment Research*, 28 (6), 326–332. doi: <https://doi.org/10.1016/j.serj.2018.09.002>
- [19] Carvalho, J., Araujo, J., Castro, F. (2011). Alternative Low-cost Adsorbent for Water and Wastewater Decontamination Derived from Eggshell Waste: An Overview. *Waste and Biomass Valorization*, 2 (2), 157–167. doi: <https://doi.org/10.1007/s12649-010-9058-y>
- [20] Choudhary, R., Koppala, S., Swamiappan, S. (2015). Bioactivity studies of calcium magnesium silicate prepared from eggshell waste by sol-gel combustion synthesis. *Journal of Asian Ceramic Societies*, 3 (2), 173–177. doi: <https://doi.org/10.1016/j.jascer.2015.01.002>
- [21] Mohamed, M. A., Jaafar, J., Ismail, A. F., Othman, M. H. D., Rahman, M. A. (2017). Fourier Transform Infrared (FTIR) Spectroscopy. *Membrane Characterization*, 3–29. doi: <https://doi.org/10.1016/b978-0-444-63776-5.00001-2>
- [22] Neikov, O. D., Yefimov, N. A. (2019). Powder Characterization and Testing. *Handbook of Non-Ferrous Metal Powders*, 3–62. doi: <https://doi.org/10.1016/b978-0-08-100543-9.00001-4>
- [23] Yu, Y., Zhao, L., Lin, X., Wang, Y., Feng, Y. (2020). A model to simultaneously evaluate the compressibility and compactibility of a powder based on the compression ratio. *International Journal of Pharmaceutics*, 577, 119023. doi: <https://doi.org/10.1016/j.ijpharm.2020.119023>
- [24] Espin, M. J., Ebri, J. M. P., Valverde, J. M. (2019). Tensile strength and compressibility of fine CaCO<sub>3</sub> powders. Effect of nano-silica addition. *Chemical Engineering Journal*, 378, 122166. doi: <https://doi.org/10.1016/j.cej.2019.122166>
- [25] Llusà, M., Faulhammer, E., Biserni, S., Calzolari, V., Lawrence, S., Bresciani, M., Khinast, J. (2014). The effects of powder compressibility, speed of capsule filling and pre-compression on plug densification. *International Journal of Pharmaceutics*, 471 (1-2), 182–188. doi: <https://doi.org/10.1016/j.ijpharm.2014.04.073>
- [26] Schatt, W., Wieters, K.-P. (1997). *Powder Metallurgy - Processing and Materials*. EPMA, 492.
- [27] German, R. M. (2014). *Sintering: From Empirical Observations to Scientific Principles*. Butterworth-Heinemann. doi: <https://doi.org/10.1016/c2012-0-00717-x>
- [28] El-Eskandarany, M. S. (2015). Controlling the powder milling process. *Mechanical Alloying*, 48–83. doi: <https://doi.org/10.1016/b978-1-4557-7752-5.00003-6>
- [29] El-Eskandarany, M. S. (2015). Controlling the powder milling process. *Mechanical Alloying*, 48–83. doi: <https://doi.org/10.1016/b978-1-4557-7752-5.00003-6>
- [30] Farzadi, A., Solati-Hashjin, M., Bakhshi, F., Aminian, A. (2011). Synthesis and characterization of hydroxyapatite/β-tricalcium phosphate nanocomposites using microwave irradiation. *Ceramics International*, 37 (1), 65–71. doi: <https://doi.org/10.1016/j.ceramint.2010.08.021>

Received date 25.02.2021

Accepted date 26.08.2021

Published date 13.09.2021

© The Author(s) 2021

This is an open access article  
under the Creative Commons CC BY license

**How to cite:** Puspitasari, P., Iftiharsa, M. A., Zhorifah, H. F. N., Gayatri, R. W. (2021). Analysis of physical properties and compressibility of avian eggshell nanopowders in solid state reaction. *EUREKA: Physics and Engineering*, 5, 110–120. doi: <https://doi.org/10.21303/2461-4262.2021.001670>

## DEVELOPMENT OF ORGANIZATIONAL AND TECHNICAL METHODS FOR PREDICTING EMERGENCY SITUATIONS AND POSSIBLE LOSSES AS THEIR RESULTS

**Hryhorii Ivanets**

*Department of Fire Tactics and Rescue Operations  
National University of Civil Defence of Ukraine  
94 Chernyshevska str., Kharkiv, Ukraine, 61023*

**Stanislav Horielyshev**

*Scientific and Research Center of Service and Military Activities  
of the National Guard of Ukraine<sup>1</sup>*

**Martin Sagradian**

*Department of Mathematics and Statistics  
Macquarie University  
16 University ave., Sydney, NSW Australia, 2109*

**Mykhailo Ivanets**

*Scientific and Research Center of the Air Force<sup>2</sup>*

**Igor Boikov**✉

*Department of Armoured Vehicles<sup>1</sup>  
biv543@ukr.net*

**Dmitro Baulin**

*Scientific and Research Center of Service and Military Activities  
of the National Guard of Ukraine<sup>1</sup>*

**Yurij Kozlov**

*Department of Metrology and Technical Expertise  
Kharkiv National University of Radio Electronics  
14 Nauki ave., Kharkiv, Ukraine, 61166*

**Aleksandr Nakonechnyi**

*Department of Armament of Air Defense of Ground Forces<sup>2</sup>*

**Lyudmila Safoshkina**

*Scientific and Research Center of Service and Military Activities  
of the National Guard of Ukraine<sup>1</sup>*

<sup>1</sup>*National Academy of the National Guard of Ukraine  
3 Zakhysnykiv Ukrainy sq., Kharkiv, Ukraine, 61001*

<sup>2</sup>*Ivan Kozhedub Kharkiv National Air Force University  
77/79 Symyska str., Kharkiv, Ukraine, 61023*

✉ Corresponding author

---

### Abstract

Emergency prevention is based on analysis, forecasting and early response to emergencies. A systematic approach to solving the problem of preventing emergencies envisages forecasting emergencies by type, level and possible losses caused as a their results both in the state as a whole and in its regions. To implement a systematic approach based on a formalized mathematical model, an organizational and technical method has been developed for predicting emergencies and possible losses caused as their results.



The method is a combination of a variable order polynomial regression method, a weighted least squares method, and a probabilistic statistical method. This allows to compensate for the shortcomings of some at the expense of others, which will lead to an increase in forecasting accuracy.

A control algorithm has been developed for the implementation of an organizational and technical method for predicting emergency situations and possible losses caused as their results. Its use involves the implementation of a number of interrelated procedures. At the first stage, the collection, processing and analysis of information on emergency situations in the country for a certain period of monitoring is carried out. This is the basis for predicting the processes of emergencies in general, in nature, level and types, as well as losses due to them both in the state and its regions. The information received is taken into account when forming a decision on the actions of civil protection units in order to adequately respond to emergency situations and eliminate their consequences. Based on the analysis of the effectiveness of the actions of the response units, the decisions on the elimination of emergency situations are adjusted.

The developed method makes it possible to reasonably approach the planning and implementation of organizational and technical measures to prevent emergency situations, taking into account the potential threats to the territories and population of the country's regions.

**Keywords:** formalized model, organizational and technical method, control algorithm, emergency, losses.

DOI: 10.21303/2461-4262.2021.002007

## 1. Introduction

In the last decade, a stable trend of climate change has been observed all over the world, an increase in the level of seismic activity of the earth's crust, an increase in the size and power of technical systems, and a progressive human intervention in nature [1]. All this significantly increases the risks of man-made accidents and natural disasters, which leads to an increase in the number and scale of emergency situations of various natures.

The consequences of emergencies negatively affect the environment [2], the economies of countries [3], are accompanied not only by material, but also human losses, the spread of epidemics and pandemics.

The experience of the developed countries of the world shows that the costs of measures related to the prevention of emergency situations are much less than the costs of restoring the losses caused by them and the damage to the environment.

Emergency prevention is a set of measures aimed at regulating natural and man-made safety, assessing risk levels and responding in advance to them in order to prevent emergencies or mitigate possible consequences [4].

An important aspect of this activity is the early forecasting of the possibility of occurrence and economic consequences of emergencies of a technogenic, natural and social nature.

Therefore, the development of an organizational and technical method for predicting emergencies and possible losses caused as their results both in the state and its regions is an urgent scientific and practical problem in the field of civil protection. Solving this problem will increase the efficiency of planning and carrying out a set of measures to prevent emergencies or minimize possible consequences.

The effectiveness of planning and implementing measures to prevent emergencies is determined by the quality of forecasting emergencies threats and possible consequences as their results. Disaster prevention is based on analysis, early detection, forecasting and early response to emergencies. A systematic approach to solving the problem of forecasting emergency situations and possible losses caused as their results provides for forecasting emergency situations in the whole country and its regions; forecasting natural emergencies in general, by type and level; forecasting emergency situations of a technogenic nature; forecasting emergency situations of a social nature by types, levels; forecasting possible losses as a result of emergency situations.

Information containing information on the predicted number of emergencies, possible damage and consequences as their results is important for the development of measures to prevent and respond to emergencies. Emergency forecasting methods depend on the available statistical information about emergency situations and the dynamics of their development after



some previous monitoring period, as well as the causes and factors that cause emergencies of a different nature.

Forecasting emergencies of various nature and consequences as their results is carried out on the basis of the analysis of statistical information about emergencies in the state after some previous monitoring period.

When predicting emergency situations [5, 6], consider:

- statistical information on man-made and natural sources of emergency situations;
- possible options for the emergence and development of emergencies;
- results of extrapolation of the identified trends;
- expert assessments.

Forecasting emergencies of various natures has its own levels of complexity, for example, natural emergencies carry a large component of uncertainty, in contrast to man-made emergencies, which mainly depend on the state of technology and the human factor and are subject to formalized calculations.

The authors of works [7, 8] considered and analyzed the probabilistic-statistical, probabilistic-deterministic, deterministic-probabilistic methods of forecasting emergency situations of a technogenic and natural character.

The main disadvantage of the probabilistic approach is the complexity of developing models of emergency processes, which significantly complicates the analysis of the development of these processes in dynamics. To overcome these inconveniences, linear, nonlinear, stepwise, ordinal regressions are used [9]. The advantages of these models include simplicity, flexibility, and unambiguity of their analysis and design.

The disadvantages of linear regression models are low adaptability and the lack of the ability to model nonlinear processes. To estimate the parameters of linear regression models, the ordinary least squares method (OLS) is used. One of the conditions for using OLS to obtain unbiased independent effective estimates of the parameters of the regression model is the constancy of the variance of the residuals for each observation or groups of observations (homoscedasticity of the residuals). Since the models of the processes of emergence of natural and man-made emergencies, as a rule, have a non-linear character, this condition is not met. This means that the estimates of the regression parameters obtained using OLS will not have a minimum variance, which worsens the forecast accuracy. One way to solve this problem is to use weighted OLS to estimate the parameters of the regression model.

The main disadvantage of nonlinear regression models is the complexity of determining the type of functional dependence, as well as the difficulty of determining the parameters of the model [10].

To estimate the parameters of linear regression models [5], the ordinary least squares method (OLS) is used. One of the conditions for using OLS to obtain unbiased independent effective estimates of the parameters of the regression model is the constancy of the variance of the residuals for each observation or groups of observations (homoscedasticity of the residuals). Since the models of the processes of emergence of technogenic emergencies, as a rule, are nonlinear, this condition is not met. This means that the estimates of the regression parameters obtained using OLS will not have a minimum variance, which worsens the forecast accuracy. One way to solve this problem is to use weighted OLS to estimate the parameters of the regression model.

A large number of technogenic emergencies are caused by violations associated with equipment failure (due to its lack of reliability, suitability, functional qualities during operation, physical wear and tear). The root causes of equipment malfunctions are lack or inadequate monitoring of equipment performance or lack of procedures. One of the main ways to prevent technogenic emergencies [5] is to ensure reliable control over the condition and operation of equipment at industrial and other enterprises, and effective preventive measures.

For modeling nonlinear processes, such as the processes of occurrence of technogenic and natural emergencies, the authors of [11] propose to use neural network models. The main advantage of neural network models is nonlinearity, that is, the ability to establish nonlinear relationships between the future and actual values of processes. The disadvantages of such models are the lack of



transparency in modeling, the complexity of the choice of architecture and the learning algorithm of the neural network.

The authors of [12] have developed methods for predicting the risks associated with emergencies as a result of forest fires, and losses from emergencies. A significant drawback of this work is the lack of a mathematical apparatus that would describe the relationship of physical processes at different stages of the emergence and course of emergencies of this type. An effective method of preventing emergencies [13] is to determine the source of the fire from artificial earth satellites. The availability of satellite data of high spatial resolution based on a geographic information system (GIS) allows solving the problems of early detection of forest fires and determining their spatial coordinates in real time, predicting their consequences and developing a set of measures to prevent their development. The main disadvantages of such systems are the low accuracy of detecting fire foci and the need to develop a general mathematical model for preventing such emergencies.

In [6], a combined method for predicting the process of emergence of natural emergencies is proposed, which allows taking into account the tendencies of periodic changes in this process. However, the frequency of changes in the processes of emergencies is characteristic only for natural emergencies and is not typical for emergencies of a technogenic or social nature.

Methods of expert assessments and sociological research are used to predict emergencies of a social nature; statistical and probabilistic methods that use data after a certain previous monitoring period have been studied to a lesser extent [5]. The methods of expert assessments are based on: obtaining the necessary information from qualified specialists of various profiles; scientific generalization of individual opinions of experts to develop an objective judgment on this issue.

Prediction of possible incurred losses as a result of an accident is possible only on the basis of an analysis of factual information about emergencies in the state for a certain period of monitoring. Factographic forecasting methods [10] are based on emergency monitoring data. Factual forecasting methods include extrapolation and interpolation methods, methods of extrapolation by envelope curves, regression and correlation, factor models, expert models of logical modeling, construction of development scenarios [5, 14]. In most cases, regression analysis methods are used to solve this problem; statistically – probabilistic methods that use factual information for a certain monitoring period have been studied to a lesser extent.

Thus, the analysis of literary sources shows that the known methods are mainly aimed at predicting certain types of emergencies of a technogenic and natural nature. They are not of a systemic nature and do not allow the forecast of emergencies as a whole, by type and level, of possible losses incurred both in the state and its regions.

This indicates the need to develop an organizational and technical method (OTM) for forecasting emergencies and possible losses caused as their results both in the state and its regions on the basis of a systematic approach to solving this problem.

The aim of research is to develop OTM for forecasting emergencies and the damage caused as their results.

To achieve this aim, it is necessary to solve the following objectives:

1. Develop, on the basis of a formalized mathematical model, OTM for forecasting emergency situations and possible losses caused as their results.
2. Develop a control algorithm for the implementation of OTM for forecasting emergency situations and possible losses caused as their results.
3. Check the effectiveness of the use of OTM for forecasting emergencies and possible losses caused as their results.

## **2. Materials and methods**

### **2. 1. Development of an organizational and technical method for predicting emergency situations and damage caused as their results**

The method is based on a formalized mathematical model for predicting emergency situations and possible losses caused as their results, which has the form:

$$\begin{aligned}
n_E(t) &= U_1 \{r_0, r_1, r_2, \dots, t\}; \\
n_E^i(t) &= U_2 \{n_E(t), P_E^i\}; \\
n_{TC}(t) &= F_1 \{n_E(t), P_{TC}\}; \\
n_{NC}(t) &= F_2 \{n_E(t), P_{NC}\}; \\
n_{SC}(t) &= F_3 \{n_E(t), P_{SC}\}; \\
l_i(t) &= \Psi_1 \{n_{TC}(t), P_{TCi}\}; \\
v_i(t) &= \Psi_2 \{n_{NC}(t), P_{NCi}\}; \\
r_i(t) &= \Psi_3 \{n_{SC}(t), P_{SCi}\}; \\
n_{TC}^i(t) &= S_1 \{n_{TC}(t), P_{TC}^i\}; \\
n_{NC}^i(t) &= S_2 \{n_{NC}(t), P_{NC}^i\}; \\
n_{SC}^i(t) &= S_3 \{n_{SC}(t), P_{SC}^i\}; \\
n_{DP}(t) &= Q_1 \{n_E(t), P_{DP}\}; \\
n_{PP}(t) &= Q_2 \{n_E(t), P_{PP}\}; \\
n_{MP}(t) &= Q_3 \{n_E(t), P_{MP}\}; \\
n_{OP}(t) &= Q_4 \{n_E(t), P_{OP}\}; \\
n_{DP}^i(t) &= \Phi_1 \{n_{DP}(t), P_{DP}^i\}; \\
n_{PP}^i(t) &= \Phi_2 \{n_{PP}(t), P_{PP}^i\}; \\
n_{MP}^i(t) &= \Phi_3 \{n_{MP}(t), P_{MP}^i\}; \\
n_{OP}^i(t) &= \Phi_4 \{n_{OP}(t), P_{OP}^i\}; \\
L(t) &= \Theta \{n_{DP}(t), n_{PP}(t), n_{MP}(t), n_{OP}(t)\};
\end{aligned} \tag{1}$$

where  $n_E(t)$  – the number of emergency situations in the state;  $(r_0, r_1, r_2, \dots, r_k)$  – function parameters;  $n_E^i(t)$  – the number of emergency situations in the  $i$ -th region;  $P_E^i$  – likelihood of an emergency in the  $i$ -th region in the event of an emergency in the state;  $n_{TC}(t)$ ,  $n_{NC}(t)$ ,  $n_{SC}(t)$  – the number of emergency situations in accordance with a technogenic, natural and social nature;  $P_{TC}$ ,  $P_{NC}$ ,  $P_{SC}$  – probability of emergencies in accordance with the technogenic, natural and social character in the state;  $l_i(t)$ ,  $v_i(t)$ ,  $r_i(t)$  – the number of emergency situations by type in accordance with the technogenic, natural and social character in the state;  $P_{TCi}$ ,  $P_{NCi}$ ,  $P_{SCi}$  – the likelihood of emergencies of a technogenic, natural and social nature of the  $i$ -th type in the state;  $n_{TC}^i(t)$ ,  $n_{NC}^i(t)$ ,  $n_{SC}^i(t)$  – the number of emergency situations in accordance with the technogenic, natural and social character in the  $i$ -th region;  $P_{TC}^i$ ,  $P_{NC}^i$ ,  $P_{SC}^i$  – likelihood of an emergency in accordance with a technogenic, natural and social nature in the  $i$ -th region in the event of an emergency in the state;  $n_{DP}(t)$ ,  $n_{PP}(t)$ ,  $n_{MP}(t)$ ,  $n_{OP}(t)$  – the number of emergency situations, respectively, at the state, regional, local and facility levels;  $P_{DP}$ ,  $P_{PP}$ ,  $P_{MP}$ ,  $P_{OP}$  – probability of emergencies, respectively, at the state, regional, local and facility levels in the state;  $n_{DP}^i(t)$ ,  $n_{PP}^i(t)$ ,  $n_{MP}^i(t)$ ,  $n_{OP}^i(t)$  – the number of emergency situations, respectively, of the state, regional, local and facility levels in the  $i$ -th region in the event of an emergency in the state;  $P_{DP}^i$ ,  $P_{PP}^i$ ,  $P_{MP}^i$ ,  $P_{OP}^i$  – probability of emergencies, respectively, of the state, regional, local and facility levels in the  $i$ -th region in the event of an emergency in the state;  $L(t)$  – losses due to the emergencies in the state.

Thus, the formalized mathematical model for forecasting emergency situations and possible losses as their results is a system of formalized analytical dependencies that describe the processes of emergencies both in the state and in its regions.

In accordance with the model (1), OTM is proposed for forecasting emergency situations and losses due to them. For this, models have been developed for forecasting emergency situations in general, by type, by levels and losses due to them both in the state and its regions. The model for forecasting the total number of emergencies in the state is a power polynomial of the form:



$$n_E^{pr} = a_0 + a_1 t_{pr} + a_2 t_{pr}^2 + a_3 t_{pr}^3 + \dots + a_k t_{pr}^k, \quad (2)$$

where  $n_E^{pr} = n_E(t_{pr})$  – predicted value of the number of emergency situations in the state at the time of the forecast  $t = t_{pr}$ ;  $(a_0, a_1, a_2, \dots, a_k)$  – the coefficients of the polynomial.

The polynomial coefficients are calculated based on the weighted least squares method [15].

The predicted number of emergencies in the  $i$ -th region of the state in accordance with the model (1) is calculated based on the predicted number of emergencies in the country  $n_E^{pr}$  as a whole and the probability of emergencies in the region of the state  $P_E^i$  as follows:

$$n_{prE}^i = n_E^{pr} \cdot P_E^i, \quad (3)$$

where  $n_{prE}^i = n_{E_i}(t_{pr})$  – predicted number of emergencies in the  $i$ -th region of the state at the time of the forecast  $t = t_{pr}$ .

In this case, the following condition must be met:

$$\sum P_E^i = 1.$$

The predicted number of emergencies in the state by the nature of origin and levels (1) is calculated on the basis of the predicted total number of emergency situations in the state  $n_E^{pr}$  and the probabilities of emergencies  $P_{TC}, P_{NC}, P_{SC}, P_{DP}, P_{PP}, P_{MP}, P_{OP}$  of the corresponding nature and level [6]:

$$n_{prTC} = n_E^{pr} \cdot P_{TC}; \quad n_{prNC} = n_E^{pr} \cdot P_{NC}; \quad n_{prSC} = n_E^{pr} \cdot P_{SC}, \quad (4)$$

$$n_{prDP} = n_E^{pr} \cdot P_{DP}; \quad n_{prPP} = n_E^{pr} \cdot P_{PP}; \quad n_{prMP} = n_E^{pr} \cdot P_{MP}; \quad n_{prOP} = n_E^{pr} \cdot P_{OP}, \quad (5)$$

where  $n_{prTC} = n_{TC}(t_{pr})$ ,  $n_{prNC} = n_{NC}(t_{pr})$ ,  $n_{prSC} = n_{SC}(t_{pr})$  – predicted number of emergency situations in accordance with a technogenic, natural and social nature in the state for the forecast period  $n_{EDP} = n_{DP}(t_{pr})$ ,  $n_{prPP} = n_{PP}(t_{pr})$ ,  $n_{prMP} = n_{MP}(t_{pr})$ ,  $n_{prOP} = n_{OP}(t_{pr})$  – predicted number of emergency situations, respectively, at the state, regional, local and facility levels in the state at the time of forecast  $t = t_{pr}$ .

In this case, the following conditions must be met:

$$P_{TC} + P_{NC} + P_{SC} = 1; \quad P_{DP} + P_{PP} + P_{MP} + P_{OP} = 1.$$

In accordance with the model (1), the predicted number of emergencies of the corresponding nature and level in the regions of the state is equal to:

$$n_{prTC}^i = P_{TC}^i \cdot n_{prTC}; \quad n_{prNC}^i = P_{NC}^i \cdot n_{prNC}; \quad n_{prSC}^i = P_{SC}^i \cdot n_{prSC}, \quad (6)$$

$$n_{prDP}^i = P_{DP}^i \cdot n_{prDP}; \quad n_{prPP}^i = P_{PP}^i \cdot n_{prPP}; \quad n_{prMP}^i = P_{MP}^i \cdot n_{prMP}; \quad n_{prOP}^i = P_{OP}^i \cdot n_{prOP}, \quad (7)$$

where  $n_{prTC}^i = n_{TC_i}(t_{pr})$ ,  $n_{prNC}^i = n_{NC_i}(t_{pr})$ ,  $n_{prSC}^i = n_{SC_i}(t_{pr})$  – predicted number of emergencies in accordance with the technogenic, natural and social nature in the  $i$ -th region of the state for the forecast period;  $n_{prDP}^i = n_{DP_i}(t_{pr})$ ,  $n_{prPP}^i = n_{PP_i}(t_{pr})$ ,  $n_{prMP}^i = n_{MP_i}(t_{pr})$ ,  $n_{prOP}^i = n_{OP_i}(t_{pr})$  – predicted number of emergency situations, respectively, at the state, regional, local and facility levels in the regions of Ukraine for the forecast period.

In this case, the following condition must be met:

$$\sum P_{TC}^i = 1; \quad \sum P_{NC}^i = 1; \quad \sum P_{SC}^i = 1.$$

The predicted number of emergencies by type in accordance with the technogenic, natural and social nature in the state is calculated based on the forecast of the total number of technogenic, natural and social emergencies in the country:

$$l_i(t_{pr}) = n_{prTC} \cdot P_{TC_i}; \quad v_i(t_{pr}) = n_{prNC} \cdot P_{NC_i}; \quad r_i(t_{pr}) = n_{prSC} \cdot P_{SC_i}, \quad (8)$$

the necessary conditions:

$$\sum P_{TC_i} = 1; \quad \sum P_{NC_i} = 1; \quad \sum P_{SC_i} = 1.$$

Forecast data on the number of natural, technogenic and social emergencies in accordance with the types and levels are the basis for assessing possible losses as their results. The total forecasted losses as result of an emergency in the state is the amount of damage caused as a result of an emergency of a man-made, natural and social nature:

$$L(t_{pr}) = L_{TC}(t_{pr}) + L_{NC}(t_{pr}) + L_{SC}(t_{pr}), \quad (9)$$

where  $L(t_{pr})$  – total predicted losses as a result of emergency situations;  $L_{TC}(t_{pr})$  – losses due to emergencies of a technogenic nature;  $L_{NC}(t_{pr})$  – losses due to emergencies of a natural nature;  $L_{SC}(t_{pr})$  – losses due to emergencies of a social nature.

Forecasting of losses due to emergencies of a technogenic nature of  $L_{TC}(t_{pr})$  is carried out in accordance with the regression-probabilistic forecasting method. It takes into account the average losses and their standard deviations from real values based on the statistical data on emergencies for a certain monitoring period.

Estimates of the predicted values of losses will be in the range:

$$L_{prTC}^{av} - \sigma < L_{TC}(t_{pr}) < L_{prTC}^{av} + \sigma, \quad (10)$$

where  $L_{prTC}^{av}$  – estimate of the predicted average damage caused as a result of a technogenic emergency;  $L_{TC}(t_{pr})$  – estimate of the predicted damage caused by emergencies of a technogenic nature;  $\sigma$  – average deviation of the estimated estimates of the damage caused as a result of a technogenic emergency.

Prediction of possible losses as a result of natural emergencies is based on the fact that the total amount of damage from them is calculated as the sum of losses due to emergencies of various types:

$$L_{NC}(t_{pr}) = \sum_{j=1}^n L_j(t_{pr}), \quad (11)$$

where  $L_{NC}(t_{pr})$  – total amount of forecasted losses due to emergencies of a natural nature;  $L_j(t_{pr})$  – losses due to natural emergencies of the  $j$ -th type.

Forecasted losses as a result of natural emergencies of the  $j$ -th type can be estimated taking into account their number by levels and the share in incurred losses per one emergency. So, for example, the predicted losses as a result of the emergencies of a hydrometeorological nature can be estimated in accordance with the following expression:

$$L_j(t_{pr}) = v_{jDP}(t_{pr}) \cdot \Pi_{jDP} + v_{jPP}(t_{pr}) \cdot \Pi_{jPP} + v_{jMP}(t_{pr}) \cdot \Pi_{jMP} + v_{jOP}(t_{pr}) \cdot \Pi_{jOP}, \quad (12)$$

where  $\Pi_{jDP}$ ,  $\Pi_{jPP}$ ,  $\Pi_{jOP}$ ,  $\Pi_{jMP}$  – the share in the inflicted losses of the  $j$ -th type of the national system, respectively, of the state, regional, local and facility levels;  $v_{jDP}(t_{pr})$ ,  $v_{jPP}(t_{pr})$ ,  $v_{jMP}(t_{pr})$ ,  $v_{jOP}(t_{pr})$  – predicted number of emergency situations of the  $j$ -th type, respectively, of the state, regional, local and facility levels.

Forecasting of losses due to a social accident of the  $L_{SC}(t_{pr})$  is carried out on the basis of the average losses per one accident and the forecasted number of emergency situations.

Thus, the proposed OTM for forecasting emergencies and possible losses caused as their results.

The method is based on a formalized mathematical model, which includes:

- wmergency forecasting models for the whole country and its regions;
- forecasting models of natural emergencies in general, by types and levels in the state and its regions;



- forecasting models of technogenic emergencies in general, by types and levels in the state and its regions;
- forecasting models for emergencies of a social nature in general, by type and level in the state and its regions;
- models of forecasting losses due to the emergencies in the state.

## 2. 2. Development of a control algorithm for an organizational and technical method for predicting emergencies and damage caused as their results

The control algorithm that implements OTM for predicting emergency situations and damage caused as their results, shown in **Fig. 1**. The algorithm consists of 9 blocks located at 7 hierarchical levels.

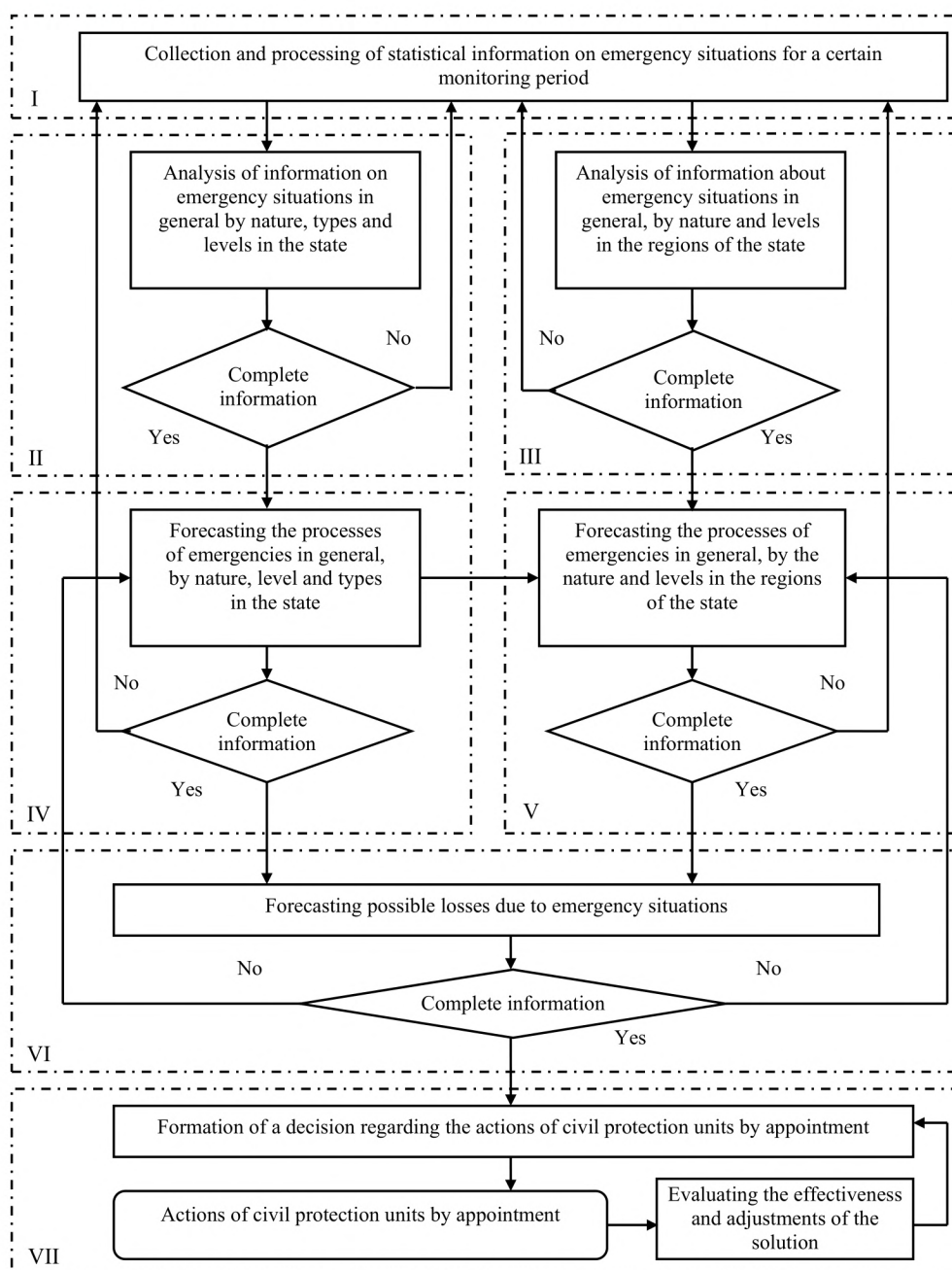


**Fig. 1.** The control algorithm of the organizational and technical method for predicting emergencies and damage caused as their results

The first level is a block for collecting and processing statistical information about emergencies for a certain monitoring period. Collection of information about sources, risks and consequences of emergencies is aimed at obtaining statistical information about emergencies both in the state as a whole and in its regions. Systematization of information provides for such processing and reduction of information to a form that allows for its analysis and development of management decisions. The second level includes a block for analyzing information about emergencies as a whole, by nature, types and levels in the state. At the third level, there is a block for analyzing information about emergency situations in general, by nature and levels in the regions of the state. At the fourth level, there is a block for forecasting the processes of emergencies in general, by nature, level and types in the state. At the fifth level there is a block for forecasting processes.

At the sixth level, there is a block for predicting possible losses caused as a result of emergency situations. The seventh level is a block for forming a decision regarding the actions of civil protection units (CP) for the intended purpose and a block for evaluating the effectiveness and correcting decisions based on an analysis of the actions of CP units.

Thus, the OTM control algorithm for forecasting emergency situations and losses due to them implements the developed mathematical model and consists of 9 blocks, which are located at 7 hierarchical levels and are connected by direct and feedback links.

### 3. Results and discussion

Let's check the effectiveness of the developed method on the basis of emergency monitoring statistics for a certain period of observation. It should be noted, however, that statistical data must be complete, objective and correct. Otherwise, the results obtained may have significant errors, or may not correspond to reality at all.

The features of the use of OTM for forecasting emergencies and the damage caused as their results in different countries will be determined by the following factors:

- availability and reliability of emergency statistics;
- regional structure of the state;
- specifics of the classification of emergency situations by type and level.

Based on the statistical data on emergencies [16, 17], studies of the effectiveness of the use of OTM were carried out on the example of Ukraine, based on the following reasons:

- unlike other countries, for Ukraine, correct statistical data on emergencies in general, by type, level and nature of origin, are fully generalized;
- for emergencies, there are known signs of their classification by types and levels.

However, only statistical data for 2013–2018 were taken into account, since the data for 2019 and 2020 are not entirely correct and do not correspond to reality throughout Ukraine. This is due to the lack of data on emergencies in some territories of the state temporarily controlled by Ukraine. Therefore, forecasting emergency situations for 2019–2020 due to the lack of data on emergency situations in such parts of Ukraine as Autonomous Republic of Crimea, Donetsk, Luhansk regions will have significant errors.

As an efficiency criterion, let's choose the module of the relative forecast error, which is calculated on the basis of previous statistical data as follows:

$$|\Delta| = \frac{\sum_{i=1}^n |\Delta_i|}{n}, \quad (13)$$

where  $|\Delta|$  – module of the average relative forecast error;  $|\Delta_i|$  – module of the relative error of the  $i$ -th step of the forecast;  $n$  – amount of statistical data.

The forecast of the number of emergencies in general, by type and level both in the state and its regions, in this study is assessed as an optimistic option  $n_E^{pr_o} = n_E^{pr} (1 - |\Delta|)$ , and a pessimistic one  $n_E^{pr_n} = n_E^{pr} (1 + |\Delta|)$ .

The results of studies using OTM for predicting emergencies and damage caused as their results are given in **Table 1**.



**Table 1**

Comparison of forecast and actual values for the period 2013–2018

Parameter		Year					
		2013	2014	2015	2016	2017	2018
Number of technogenic emergencies	Actual quantity	75	74	63	56	50	48
	Optimistic forecast	74	67	59	54	49	46
	Pessimistic forecast	86	79	67	62	54	50
Number of natural emergencies	Actual quantity	56	59	77	89	107	77
	Optimistic forecast	51	48	62	88	97	76
	Pessimistic forecast	58	59	78	97	108	81
Number of social emergencies	Actual quantity	12	10	8	4	9	3
	Optimistic forecast	11	9	7	4	8	3
	Pessimistic forecast	15	13	9	6	11	5
Number of emergency situations at the state level	Actual quantity	1	5	2	1	2	2
	Optimistic forecast	1	4	1	1	1	1
	Pessimistic forecast	2	5	2	2	2	2
Number of emergency situations at the regional level	Actual quantity	11	9	9	9	8	6
	Optimistic forecast	10	8	8	8	7	5
	Pessimistic forecast	12	10	9	9	9	7
Number of emergency situations at the local level	Actual quantity	58	59	62	64	70	64
	Optimistic forecast	55	52	54	56	63	63
	Pessimistic forecast	64	62	64	67	72	65
Number of emergency situations at the facility level	Actual quantity	73	70	75	75	86	56
	Optimistic forecast	70	62	65	66	79	55
	Pessimistic forecast	81	74	77	78	89	58
Losses due to emergencies (million EUR)	Actual quantity	12.01	6.02	16.14	8.04	27.18	15.45
	Optimistic forecast	11.82	4.55	13.64	6.67	24.25	13.7
	Pessimistic forecast	13.64	6.36	16.24	8.18	27.27	15.69

Using expressions (9)–(12), predictive (optimistic, pessimistic) values of losses due to emergency situations are calculated. Analyzing the statistical data [16, 17] and expression (12), it is possible to conclude that the main contribution to the amount of losses from emergencies is made by the emergencies of the state level, and then the regional one.

From the data obtained (**Table 1**), it can be seen that when predicting, for example, the number of technogenic emergencies for 2018, let's obtain a range of possible values from 46 to 50. Moreover, the actual value of the number of emergencies is 48. Based on the forecast of the number of emergencies, an assessment of losses due to these emergency situations was carried out. The calculation of losses due to the emergencies was carried out in the national currency of Ukraine (UAH), however, for clarity, in **Table 1** the received data are recalculated at the current exchange rate and reflected in EUR (1 EUR – 33 UAH). Thus, the value of the range of losses as a result of emergency situations for 2018 is 13.7...15.69 million EUR, and the actual value is 15.45 million EUR. It should be noted that the larger the sample of statistical data for previous years, the more accurate forecasting can be made. In addition, it is possible to use OTM to make a forecast for a longer period (two, three years). However, this will lead to a significant increase in the relative error.

The main disadvantage of the existing methods and models for forecasting emergencies and damage caused is the focus on forecasting certain types of emergencies, does not allow for a comprehensive forecast of emergencies as a whole.

The advantage of the developed OTM is that it has a combined character. OTM allows to forecast the processes of emergencies in a complex manner, by nature, types, levels, and to assess

possible losses as their results, both in the state and in its regions. The model for forecasting the number of emergency situations for a certain warning period makes a forecast taking into account the systematic (trend), periodic and random components of this process. Evaluation of these components of the forecasting process allows for a deeper analysis of the causes of their occurrence.

In the results of experimental studies, it was found that OTM makes it possible to forecast emergency situations as a whole, by type and level for a year ahead with an average relative forecast error of no more than 8 %. The error in estimating possible losses caused as a result of an accident is no more than 6.2 % (**Table 1**). This is due to the combination of various methods, in particular the polynomial-regression method with variable order, the weighted least squares method and the probabilistic-statistical method, allowing to compensate for the shortcomings of some at the expense of others.

The developed OTM allows reasonably, taking into account predictive information about the processes of emergencies in the state, regions, to approach the planning and implementation of organizational and technical measures aimed at preventing emergencies and minimizing possible consequences.

Restrictions on the use of OTM may be caused by the insufficient volume or incorrectness of reliable statistical data on emergencies in the state and its regions.

Further development of research in this direction should be focused on studying the influence of various destabilizing factors, both separately and in their totality. As such factors, it is possible to consider the frequency and cyclicity of the processes of emergencies (in particular, their seasonal fluctuations) in the state and its various regions of the country.

Thus, the aforementioned confirms the prospects of applying OTM to solving the problem of forecasting emergencies and the damage caused as their results.

#### 4. Conclusions

1. OTP for forecasting emergencies and possible losses caused as their results has been developed. The method is based on a formalized mathematical model, which includes models for forecasting emergencies as a whole, by type, level and possible losses as their results both on a national scale and in each region. OTM combines a variable-order polynomial-regression method, a weighted least squares method, and a probabilistic-statistical method. The use of the method makes it possible to improve the accuracy of forecasting emergency situations and assessing possible losses both in the state as a whole and in its regions. The method implements the principle of a systematic approach to solving the problem of comprehensive forecasting of emergency processes both in the state and its regions. This makes it possible to reasonably approach the planning and implementation of organizational and technical measures to prevent emergencies, taking into account the potential threats to the territories and population of the country's regions.

2. A control algorithm has been developed that implements OTM for forecasting emergency situations and possible losses caused as their results. Its use involves the implementation of a number of interrelated procedures. At the first stage, the collection, processing and analysis of information about emergencies in the state for a certain period of monitoring is carried out. This is the basis for predicting the processes of emergencies in general, in terms of nature, level and types, as well as losses due to them both in the state and its regions. The information obtained is taken into account when forming a decision on the actions of the central control units in order to adequately respond to emergencies and eliminate their consequences. Based on the analysis of the effectiveness of the actions of the response units, the decisions on the elimination of emergencies are adjusted. The algorithm consists of 9 blocks located at 7 hierarchical levels and connected by direct and reverse logical connections.

3. The results of experimental studies have shown that the use of OTM makes it possible to forecast emergencies in general, by type and level, both in the state and in its regions. Moreover, the average relative forecast error does not exceed 8 %. The average relative error in forecasting possible incurred losses as a result of an accident is 6.2 %. The effectiveness of the use of OTM will depend on the reliability of statistical data on the nature, type, level of emergencies and their regional distribution in the state for a certain period of monitoring.



## References

- [1] Chen, W.-K. (2012). Managing Emergency Response of Air Pollution by the Expert System. *Air Pollution – A Comprehensive Perspective*. doi: <https://doi.org/10.5772/50080>
- [2] Guskova, N. D., Neretina, E. A. (2013). Threats of natural character, factors affecting sustainable development of territories and their prevention. *Zbornik Radova Geografskog Instituta Jovan Cvijic, SANU*, 63 (3), 227–237. doi: <https://doi.org/10.2298/ijgi1303227g>
- [3] Rybalova, O., Artemiev, S., Sarapina, M., Tsymbal, B., Bakhareva, A., Shestopalov, O., Filenko, O. (2018). Development of methods for estimating the environmental risk of degradation of the surface water state. *Eastern-European Journal of Enterprise Technologies*, 2 (10 (92)), 4–17. doi: <https://doi.org/10.15587/1729-4061.2018.127829>
- [4] Tiutiunyk, V. V., Ivanets, H. V., Tolkunov, I. A., Stetsyuk, E. I. (2018). System approach for readiness assessment units of civil defense to actions at emergency situations. *Scientific Bulletin of National Mining University*, 1, 99–105. doi: <https://doi.org/10.29202/nvngu/2018-1/7>
- [5] Novoselov, S. V., Panikhidnikov, S. A. (2017). Problems in prediction of number of emergencies by statistical methods. *Mining Informational and Analytical Bulletin*, 10, 60–71. doi: <https://doi.org/10.25018/0236-1493-2017-10-0-60-71>
- [6] Ivanets, H., Horielyshev, S., Ivanets, M., Baulin, D., Tolkunov, I., Gleizer, N., Nakonechnyi, A. (2018). Development of combined method for predicting the process of the occurrence of emergencies of natural character. *Eastern-European Journal of Enterprise Technologies*, 5 (10 (95)), 48–55. doi: <https://doi.org/10.15587/1729-4061.2018.143045>
- [7] Deng, S. C., Wu, Q., Shi, B., Chen, X. Q., Chu, X. M. (2014). Prediction of Resource for Responding Waterway Transportation Emergency Based on Case-Based Reasoning. *China Safety Science Journal*, 24 (3), 79–84.
- [8] Vasiliev, M. I., Movchan, I. O., Koval, O. M. (2014). Diminishing of ecological risk via optimization of fire-extinguishing system projects in timber-yards. *Scientific Bulletin of National mining university*, 5, 106–113. <http://www.nvngu.in.ua/index.php/en/component/jdownloads/finish/49-05/1443-2014-5-vasiliev/0>
- [9] Sun, B., Ma, W., Zhao, H. (2013). A fuzzy rough set approach to emergency material demand prediction over two universes. *Applied Mathematical Modelling*, 37 (10-11), 7062–7070. doi: <https://doi.org/10.1016/j.apm.2013.02.008>
- [10] Kryanev, A., Ivanov, V., Romanova, A., Sevastianov, L., Udumyan, D. (2018). Extrapolation of Functions of Many Variables by Means of Metric Analysis. *EPJ Web of Conferences*, 173, 03014. doi: <https://doi.org/10.1051/epjconf/201817303014>
- [11] Al-Jumeily, D., Ghazali, R., Hussain, A. (2014). Predicting Physical Time Series Using Dynamic Ridge Polynomial Neural Networks. *PLoS ONE*, 9 (8), e105766. doi: <https://doi.org/10.1371/journal.pone.0105766>
- [12] Evangelidou, N., Balkanski, Y., Cozic, A., Hao, W. M., Mouillot, F., Thonicke, K. et. al. (2015). Fire evolution in the radioactive forests of Ukraine and Belarus: future risks for the population and the environment. *Ecological Monographs*, 85 (1), 49–72. doi: <https://doi.org/10.1890/14-1227.1>
- [13] Goldammer, J. G., Kashparov, V., Zibtsev, S., Robinson, S. (2014). Best practices and recommendations for wildfire suppression in contaminated areas, with focus on radioactive terrain. OSCE. Available at: <http://gfmcc.online/globalnetworks/seeurope/OSCE-GFMC-Report-Fire-Management-Contaminated-Terrain-2014-ENG.pdf>
- [14] Migalenko, K., Nuianzin, V., Zemlianskyi, A., Dominik, A., Pozdieiev, S. (2018). Development of the technique for restricting the propagation of fire in natural peat ecosystems. *Eastern-European Journal of Enterprise Technologies*, 1 (10 (91)), 31–37. doi: <https://doi.org/10.15587/1729-4061.2018.121727>
- [15] Ivanets, H., Ivanets, M. (2019). Algorithm increase exactness of prognostication process origin extraordinary situations on basis regressive models. *Nauka i tekhnika Povitrianykh Syl Zbroinykh Syl Ukrainy*, 1 (34), 117–122. doi: <https://doi.org/10.30748/nitps.2019.34.16>
- [16] Zvit pro osnovni rezultaty diyalnosti Derzhavnoi sluzhby Ukrainy z nadzvychainykh sytuatsiy u 2018 rotsi. Available at: <https://www.dsns.gov.ua/files/2019/1/18/321/%D0%9F%D1%83%D0%B1%D0%BB%D1%96%D1%87%D0%BD%D0%B8%D0%B9%20%D0%B7%D0%B2%D0%B8%D1%82%20%D0%B7%D0%B0%202018%20%D1%80%D1%96%D0%BA.pdf>
- [17] Zvit pro osnovni rezultaty diyalnosti Derzhavnoi sluzhby Ukrainy z nadzvychainykh sytuatsiy u 2017 rotsi. Available at: [http://www.dsns.gov.ua/files/2018/1/26/Zvit%202017\(KMY\).pdf](http://www.dsns.gov.ua/files/2018/1/26/Zvit%202017(KMY).pdf)

Received date 17.02.2021

Accepted date 05.08.2021

Published date 13.09.2021

© The Author(s) 2021

This is an open access article  
under the Creative Commons CC BY license

**How to cite:** Ivanets, H., Horielyshev, S., Sagradian, M., Ivanets, M., Boikov, I., Baulin, D., Kozlov, Y., Nakonechnyi, A., Safoshkina, L. (2021). Development of organizational and technical methods for predicting emergency situations and possible losses as their results. *EUREKA: Physics and Engineering*, 5, 121–132. doi: <https://doi.org/10.21303/2461-4262.2021.002007>

# USE OF THE PASS-THROUGH METHOD TO SOLVE SOUND RADIATION PROBLEMS OF A SPHERICAL ELECTRO-ELASTIC SOURCE OF ZERO ORDER

**Oleksii Korzhyk**

*Department of Acoustic and Multimedia Electronic Systems<sup>1</sup>*

**Sergey Naida**

*Department of Acoustic and Multimedia Electronic Systems<sup>1</sup>*

**Sergii Kurdiuk**

*Department of Marine Corps Institute  
National University «Odessa Maritime Academy»  
8 Didrikhson str., Odessa, Ukraine, 65029*

**Valeriia Nizhynska** ✉

*Department of Acoustic and Multimedia Electronic Systems<sup>1</sup>  
nvv0807190-ames21@ill.kpi.ua*

**Maxim Korzhyk**

*Department of Acoustic and Multimedia Electronic Systems<sup>1</sup>*

**Anton Naida**

*Department of Acoustic and Multimedia Electronic Systems<sup>1</sup>*

<sup>1</sup>*National Technical University of Ukraine «Igor Sikorsky Kyiv Polytechnic Institute»  
37 Peremohy ave., Kyiv, Ukraine, 03056*

✉ Corresponding author

---

## Abstract

In the article was solved the problem of radiation of a sound by the electroacoustic transducer which is executed in the form of a thin spherical cover, using a pass-through method. The outer and inner surfaces of the shell are completely electroded.

The application of this method provides an opportunity to avoid inaccuracies that arise during the traditional formulation of boundary conditions for acoustic mechanical fields, the use of equivalent substitution schemes and the absence of boundary conditions for the electric field in general. Given methodology eliminates these shortcomings by applying conjugation conditions, taking into account the types of electroding of the surfaces of piezoceramic transducers, the introduction of boundary conditions for current and voltage. The results of the solution demonstrate the high capabilities of this pass-through method, in terms of taking into account the peculiarities of determining the characteristics of these fields, values and dependences of the main complex characteristics of the electroelastic transducer, and auxiliary material constants of the piezoelectric material.

The proposed approach is relevant, because it allows to increase the reliability of modeling the operating conditions of acoustic transducers in the context of wave problems of acoustics. Aim is to enhance the range of performances and build algorithms solving problems of stationary mode hydroelectroelasticity sound radiation. The expected results are presented in terms of improving approaches to studying the features of the oscillatory process of the active elements of sound-emitting systems and the accompanying effects of the transformation of interconnected fields involved in the formation of the acoustic signal in the liquid.

**Keywords:** acoustics, field interaction, connectivity electroelastic radiation mode, electroacoustic transducer, hydroelectric.

DOI: 10.21303/2461-4262.2021.001292

---

## 1. Introduction

Pass-through formulations in the problems of mechanics and acoustics were initiated as a separate class of piezoelectric problems based on the provisions of Maison's physical acoustics [1] and the scientific schools of NASU academicians [2]. The important achievements of the founders include, first of all, the monograph [2], which substantiates the use of such productions in theoretical



and applied issues of electroacoustic transducers of sound and ultrasound ranges. The convenience of such formulations in relation to the possibilities provided by them for in-depth study of the spatial and energy characteristics of electroacoustic piezoceramic transducers even leads to the popularization of the initiated approaches of the end-to-end problem (for example, source materials [3]).

Further development of theoretical and practical aspects of construction and use of electroelastic systems operating in conditions of static and dynamic deformation, was aimed at the problems of wave acoustics, theory and practice of development of sonar transducers and antennas. In this case, as examples of works on this topic include articles [4–10]. The work of followers, in accordance with the tasks of applied acoustics, expanded the physical aspects of pass-through stationary and non-stationary productions, supplementing them with Kirchhoff-Lev hypotheses, enriched the models with technological elements such as screens [10], elastic sealing layers, [11] orientations, liquid and solid fillers [12] and others. Special mention should be made of the work [2], which initiates the process of solving, systematizing and ordering the electroelastic models of transducers of certain canonical forms.

An attractive feature of the pass-through approach methodology is to take into account and visually predict the spatial properties of transducers by using individual modes, or combinations thereof. This is due to the peculiarities of the stress-strain state of the transducers design, types of electroding, kinematic and force conditions of conjugation.

It so happened that until recently more attention was paid to cylindrical multimode transducers and their systems, [9–11, 13]. Spherical, rod and bending transducers are somewhat less covered. At the same time, the frequency characteristics of the eigenforms of cylindrical and spherical shells, the features of electroding and electrical boundary conditions are of special interest. These issues are partially considered in [2, 4, 6, 14–16].

Expanding the range of pass-through statements [15–20] should lead to a more correct consideration of the operating conditions of electroelastic transducers, but requires a more thorough understanding of the interaction of acoustic, mechanical and electrical factors. Therefore, due to this, the physical aspects of end-to-end productions can be successfully used in the creation of models of receiving and radiating sonar systems.

All the above areas and work require further development, improvement and systematization.

Thus, the proposed «pass-through» approach is relevant and modern, because it allows to increase the reliability of modeling the operating conditions of acoustic transducers in the context of wave problems of acoustics with the replacement of boundary conditions by acoustic-mechanical fields – conjugation conditions and electrical boundary conditions. Aim is to enhance the range of performances and build algorithms solving problems of stationary mode hydroelectroelasticity sound radiation. The expected results are presented in terms of improving approaches to studying the features of the oscillatory process of the active elements of sound-emitting systems and the accompanying effects of the transformation of interconnected fields involved in the formation of the acoustic signal in the liquid.

## 2. Materials and methods

The problem under consideration is based on theoretical materials of the basic provisions of electric elasticity [2, 6] in terms of involvement in the solution: equations of motion of points on the surface of a thin sphere (Newton's second law), equations of state for piezoceramics, generalized Hooke's law, Cauchy relations and the Helmholtz equation for the acoustic field.

The solution is performed using generalized boundary conditions for acoustic, mechanical and electric fields using traditional methods of mathematical physics (Fourier method), vector analysis and orthogonal properties of spherical functions.

The work is structured in accordance with the order of solving traditional problems of sound scattering, reception and radiation [10–12, 15].

### 2. 1. The formulation of problem

Suppose that a spherical electroacoustic transducer-emitter, supplied by a closed thin electrostress shell with radial polarization, is placed in the working medium, which is represented

by an ideal liquid (**Fig. 1**). A spherical  $O, r, \varphi, \theta$  and rectangular  $O, X, Y, Z$  coordinate system is introduced into the medium, the centers of which coincide with the phase and geometric centers of the sphere (point  $O$ ); the radius of the inner surface of the shell –  $R$ , external –  $R_1$ ; shell wall thickness –  $h_s = R_1 - R$ . In the volume of the shell is a vacuum. From the outside – a liquid with the density  $\rho_0$  and speed of sound  $c_0$ . The inner ( $r = R$ ) and outer ( $r = R + h_s$ ) surfaces of the shell are completely electroded.

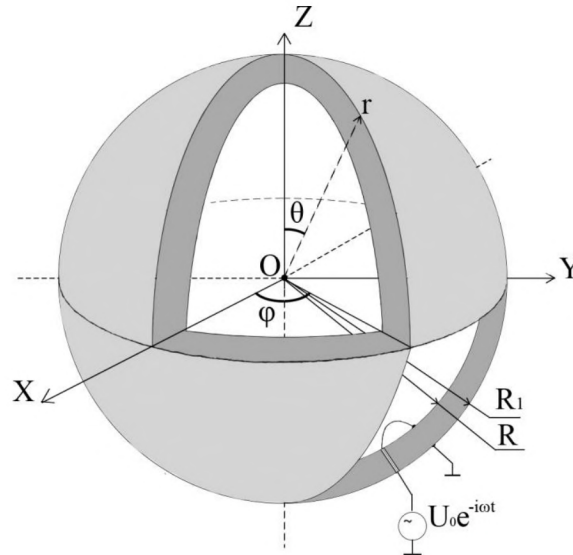


**Fig. 1.** Design scheme of a hollow sphere polarized by thickness

In the mode of radiation of the monochromatic signal, when performing the inequality  $h_s \ll R$ , the specified conditions of the transducer and the type of surface electroding [2, 14] allow to assume that:

- mechanical tensions  $\sigma_{ij}$  and deformations  $\varepsilon_{ij}$  (where  $i, j$  single orts) – constant in the thickness of the shell wall (i.e. in the coordinate  $r$ );
- the radial component of the electric field vector  $E_r$  in the direction of polarization of the shell in the gap  $h_s$  is also constant;
- disturbance and formation of mechano-acoustic fields – corresponds to the zero mode of oscillations of the sphere.

The inner and outer surfaces of the spherical transducer are connected [6] to a fixed frequency generator and together with it and the elements of the electrical installation form an external electrical excitation circuit. The elements of the electrical mounting of the inner electrode are brought out through a special infinitesimal technological hole. The inner electrode is potential, the outer electrode is grounded. Let's believe that the electrodes, shells and elements of electrical installation in their technological properties in no way affect the operation of the transducer – the shell.

After turning on the generator and applying to the electrodes the potential difference  $U = U_0 e^{-i\omega t}$  under the influence of the generated electric field, the stress-strain state of the shell changes. The resulting electric field arising in the volume of the shell consists of both external (which is perturbed by the generator) and internal field, which is caused by displacements from the equilibrium of the ions of the piezoelectric material of the shell (direct piezoelectric effect).

The connection of the main (electric, mechanical and acoustic) physical fields involved in the process of converting electric energy into acoustic, and the circumstances of the problem in terms of technological features and type of electrode necessitate the joint solution of the following equations and the use of the following relations and conditions [2, 6, 14]:

- state equations for piezoceramics;
- equations of motion of material points of a spherical thin shell (or Newton's second law):



$$\frac{1}{R_1}(\sigma_{\varphi\varphi} + \sigma_{\theta\theta}) + \rho_m \omega^2 u_r = 0, \quad (1)$$

where,  $\sigma_{\varphi\varphi}$ ,  $\sigma_{\theta\theta}$  – amplitude values of mechanical compressive-tensile tensions along the axes of azimuthal (latitudinal) and polar (meridional) angles of a spherical coordinate system;  $\rho_m$  – density of piezoceramics;  $u_r$  – amplitude value of a harmonically variable radial component of the centrally symmetric vector of displacement of material particles of piezoceramics;

– generalized Hooke's law, written for environments with complex properties:

$$\sigma_{rr} = c_{11}^E \varepsilon_{rr} + c_{12}^E \varepsilon_{\varphi\varphi} + c_{12}^E \varepsilon_{\theta\theta} - e_{11} E_r, \quad (2)$$

$$\sigma_{\varphi\varphi} = c_{12}^E \varepsilon_{rr} + c_{22}^E \varepsilon_{\varphi\varphi} + c_{12}^E \varepsilon_{\theta\theta} - e_{12} E_r, \quad (3)$$

$$\sigma_{\theta\theta} = c_{12}^E \varepsilon_{rr} + c_{12}^E \varepsilon_{\varphi\varphi} + c_{22}^E \varepsilon_{\theta\theta} - e_{12} E_r, \quad (4)$$

where  $\varepsilon_{rr}$ ,  $\varepsilon_{\varphi\varphi}$ ,  $\varepsilon_{\theta\theta}$  – amplitudes of compression-tension deformations along the corresponding axes of the spherical coordinate system;  $c_{11}^E$ ,  $c_{12}^E$  – components of the matrix of the modulus of elasticity;  $e_{11}$ ,  $e_{12}$  – components of a matrix of piezomodules;

– Cauchy relations for deformations of the form:

$$\varepsilon_{rr} = u_r / r$$

and

$$\varepsilon_{\varphi\varphi} = \varepsilon_{\theta\theta} = u_r / r; \quad (5)$$

– Helmholtz equation for an acoustic field written in spherical coordinates:

$$\Delta p_a(r, \varphi, \theta) + k^2 p_a(r, \varphi, \theta) = 0, \quad (6)$$

where  $k = \omega/c_0$  – wave number;  $\omega = 2\pi f$  – stake frequency(rad);  $f$  – frequency(Hz).

Due to the selected type of electrode, the radiation is undirected. Therefore, the solution of equation (6) will depend only on the radial coordinate  $r$ :

$$p(r, \varphi, \theta, i) = p_a(r, i) = \frac{p_a}{r} e^{-i(\omega i - kr)} \quad (7)$$

and the radial component of the displacement vector is related to the pressure and the normal component of the vector of the oscillatory velocity of the points on the surface of the sphere  $v_r(r, t)$  by the following condition:

$$v_r(r, i) \Big|_{r=R_1} = -\frac{1}{i\omega\rho_0} \frac{\partial p_a(r)}{\partial r} \Big|_{r=R_1} = -i\omega u_r \Big|_{r=R_1}. \quad (8)$$

Thus the compatible solution of equations (1)–(6) should occur with involvement of acoustic mechanical boundary conditions which are formulated and applied as conditions of conjugation of force type:

$$\sigma_{ii} \Big|_{r=R_1} = p = \Delta p = p_{out} \Big|_{r=R_1} - p_{in} \Big|_{r=R},$$

when

$$(r = R + h_s). \quad (9)$$

The list ends with the condition of orthogonality of trigonometric and spherical wave functions and the Sommerfeld condition.

Regarding the boundary conditions for the electric field, let's note that in accordance with [2, 6, 14] they determine the following situations:

- the first concerns the imposition of the condition of the absence of free electrons in the shell material  $\text{div}D = 0$  ( $D$  – vector of electrical induction);
- the second – the conditions of connection of the electric field strength in the volume of the transducer with the electric voltage  $E = -\text{grad}\Psi$ , ( $\Psi$  – electric potential,  $\Delta\Psi$  – potential difference);
- the third – the condition illustrating communication of an electric current  $I$  and surface density of charges on the electroded surfaces of a cover  $Q$ :  $I = -i\omega Q$ .

Note that all the above characteristics of the main physical fields – electric, mechanical and acoustic are functions of frequency and distance. This dependence (to simplify the presentation) is not shown in the intermediate results and is given only on the final relations, where the search for values gives the amplitude-frequency dependence of some factors. The distance can be fixed.

Thus, using the results of the statement, let's note that the frequency dependencies of the transmittance of the transducer (electric voltage – acoustic pressure)  $K_t(\omega)$ , as well as the frequency dependencies of pressure  $p_a(\omega)$  and electrical impedance  $Z_{el}(\omega)$  are to be determined.

## 2. 2. The solving of radiation problem

Thus, the external load of the spherical shell is a liquid. In the middle of the shell is a vacuum. Consequently, the sound field in the middle of the sphere cannot exist and is not taken into account. The load on the sphere is reduced to the pressure difference  $\Delta p_a$  on its outer and inner surfaces  $\Delta p = p_{out}|_{r=R_1} - p_{in}|_{r=R_1}$ , one of which is zero  $p_{in}|_{r=R_1}$ , due to the vacuum condition.

Let's apply condition (8). For the amplitude, of the normal component of mechanical tensions, the force conjugation force is valid:

$$\sigma_{rr}|_{r=R_1} = p|_{r=R_1} = \frac{p_a}{r} e^{-i(\omega t - ikr)} \Big|_{r=R_1}, \quad (10)$$

where  $p_a$  – pressure amplitude; and the kinetic condition of the conjugation:

$$v_r|_{r=R_1} = \frac{1}{i\omega\rho} \frac{\partial p_a}{\partial r} \Big|_{r=R_1} = v_n|_{r=R_1}, \quad (11)$$

$v_r, v_n$  – the velocity of displacement in the radial direction of the material points of the shell surface and the velocity of the normal particles of the medium at the boundary  $r = R_1$  respectively.

## 2. 3. Determination of the frequency response of the transmission factor $K_t(\omega)$ and electrical impedance $Z_{el}(\omega)$

Applying condition (10), after substitution in equation (2) let's find the amplitude value of the deformation  $\varepsilon_{rr}$ :

$$\varepsilon_{rr} = \frac{p_a}{c_{11}^E} - \frac{c_{12}^E}{c_{11}^E} (\varepsilon_{\varphi\varphi} + \varepsilon_{\theta\theta}) - \frac{e_{11}}{c_{11}^E} E_r. \quad (12)$$

After a series of transformations associated with the exclusion of deformations  $\varepsilon_{rr}$  from equations (3), (4), for the normal components of mechanical tensions  $\varepsilon_{\varphi\varphi}$  and  $\varepsilon_{\theta\theta}$  let's obtain:

$$\varepsilon_{\varphi\varphi} = c_{11} p_a + c_{22} \varepsilon_{\varphi\varphi} + c_{12} \varepsilon_{\theta\theta} - e_{11}^* E_r, \quad (13)$$

$$\varepsilon_{\theta\theta} = c_{11} p_a + c_{12} \varepsilon_{\varphi\varphi} + c_{22} \varepsilon_{\theta\theta} - e_{12}^* E_r, \quad (14)$$

where  $c_{11} = \frac{c_{12}^E}{c_{11}^E}$ ,  $c_{12} = c_{11}^E \left( 1 - \frac{c_{12}^E}{c_{11}^E} \right)$ ,  $c_{22} = \left( c_{22}^E - \frac{(c_{12}^E)^2}{c_{11}^E} \right)$ ,  $e_{12}^* = \left( -e_{11} \frac{c_{12}^E}{c_{11}^E} + e_{12}^* \right)$  – material (15) constants.



Further, taking into account the relationship between displacements and deformations, which is determined by the Cauchy ratios [2]:

$$\varepsilon_{\varphi\varphi} = \varepsilon_{\theta\theta} = u_r/R. \quad (16)$$

Expressions (13), (14) can be represented as:

$$\varepsilon_{\varphi\varphi} = \varepsilon_{\theta\theta} = c_{11}p_a + Y \frac{u_r}{R} - e_{12}^* E_r, \quad (17)$$

where  $Y = (c_{12} + c_{22})$  – effective modulus of elasticity.

The symmetrical deformation of the spherical shell, which occurs when it is excited by an external generator, leads to the fact that the electric induction vector  $D$  is completely determined by its radial component  $D_r$  and in accordance with [6] for the sphere is written as:

$$D_r = e_{11}\varepsilon_{rr} + e_{12}(\varepsilon_{\varphi\varphi} + \varepsilon_{\theta\theta}) + \chi_{11}^\sigma E_r, \quad (18)$$

where  $\chi_{11}^\sigma = \chi_{11}^\varepsilon + e_{11}^2/c_{11}^E$  – components of the dielectric constant, set at zero (constant) normal mechanical tensions  $\sigma_{rr}$  and deformations  $\varepsilon_{rr}$ .

After substituting expression (10) for deformations  $\varepsilon_{rr}$  in expression (16), and using expression (17), let's change the record for the vector component  $D_r$ :

$$D_r = 2 \frac{u_r}{R} e_{12}^* + e_{11}p_a + \chi_{11}^\sigma E_r, \quad (19)$$

where

$$e_{12}^* = \left( e_{12} - e_{11} \frac{c_{12}^E}{c_{11}^E} \right), \quad \chi_{11}^\sigma = \left( \chi_{11}^\varepsilon + \frac{(e_{11})^2}{c_{11}^E} \right), \quad e_{11} = \frac{e_{11}}{c_{11}^E}. \quad (20)$$

Let's apply boundary conditions on an electric field concerning induction  $\text{div} D = 0$  [2, 6, 9, 14] which defines absence of free carriers of electricity in piezomaterial and in spherical coordinates makes equality:

$$\text{div} \vec{D}_r = \frac{1}{r^2} \frac{\partial}{\partial r} (r^2 \vec{D}_r) = 0. \quad (21)$$

For the electric field strength in the volume of ceramics and the potential difference at the electrodes of the shell, let's use the second condition [2]:

$$U = \int_R^{R_1} E_r dr = \Delta \Psi, \quad \Psi(r)|_{r=R} = U_0, \quad \Psi(r)|_{r=R_1} = 0. \quad (22)$$

Regarding the determination of current, let's write the relationship of electrical characteristics – as follows:

$$Q = \int_S D_r dS, \quad I = i\omega Q, \quad (23)$$

where  $Q$  surface density of electric charges on the electrode with area  $S$ .

The solution of the differential equation (21) in the standard form will be:

$$\vec{D}_r = \frac{C_{02}}{R_1^2} \Big|_{r=R_1}, \quad (24)$$

where  $C_{02}$  – unknown constant to be found.

Expression (19), substitute in (24), then let's obtain the equality:

$$D_r = 2 \frac{u_r}{R} e_{12}^* + e_1 p_a + \chi_{11}^\sigma E_r = \frac{C_{02}}{R^2}, \quad (25)$$

whence let's find tension  $E_r$ :

$$E_r = \frac{1}{\chi_{11}^\sigma} \left( \frac{C_{02}}{R^2} - 2e_{12}^* \frac{u_r}{R} - e_1 p_a \right). \quad (26)$$

Substitute (26) in equations (16), (17) and for the mechanical field let's obtain:

$$\sigma_{\varphi\varphi} = \sigma_{\theta\theta} = Y^D \frac{u_r}{R} + Y_1^D p_a - \frac{e_{12}^* C_{02}}{\chi_{11}^\sigma R^2}, \quad (27)$$

where  $Y^D = Y + 2 \frac{e_{12}^*}{\chi_{11}^\sigma}$ ,  $Y_1^D = c_{11} + e_1 \frac{e_{12}^*}{\chi_{11}^\sigma}$  – effective modulus of elasticity, which is determined taking

into account the interconnectedness of electric and elastic (mechano-acoustic) fields.

Now, in turn, let's use expression (1), which corresponds to Newton's law. Substitution of expression (27) and carrying out a number of transformations gives for the radial component of the movement of material particles of the shell  $u_r$ :

$$u_r = u_r(\omega) = \frac{\frac{2 e_{12}^*}{Y^D \chi_{11}^\sigma} \frac{C_{02}}{R} - 2 \frac{Y_1^D}{Y^D} p_a R}{\left[ 2 - (\gamma R)^2 \right]}, \quad (28)$$

where  $\gamma^2 = \rho_m \omega^2 / Y^D$  – the square of the wave number of centrally symmetric oscillations of a closed spherical electroelastic shell.

Let's use a group of boundary conditions for the electric field (22):

$$E_r = -\frac{\partial \Psi(r)}{\partial r} = -\frac{\Delta \Psi(r)}{\Delta r} = -\frac{\Psi_{out} - \Psi_{in}}{h_s} = -\frac{\Psi_{R_i} - \Psi_{R_o}}{h_s}. \quad (29)$$

That is, in the left part of equation (26) let's put condition (29) and let's obtain:

$$E_r = -\frac{\partial \Psi(r)}{\partial r} = \frac{1}{\chi_{11}^\sigma} \left( \frac{C_{02}}{R^2} - 2e_{12}^* \frac{u_r}{R} - e_1 p_a \right) \Rightarrow \frac{\partial \Psi(r)}{\partial r} = -\frac{1}{\chi_{11}^\sigma} \frac{C_{02}}{R^2} + 2e_{12}^* \frac{u_r}{\chi_{11}^\sigma R} + \frac{e_1}{\chi_{11}^\sigma} p_a \quad (30)$$

Next, in equation (30) let's substitute the expression for the radial component of the displacement  $u_r$  (expression (28)) and after the introduction of the coefficient of electro-mechanical coupling  $k_{emc} = e_{12}^* \sqrt{2/Y^D \chi_{11}^\sigma}$  and a number of algebraic transformations:

$$\frac{\partial \Psi(r)}{\partial r} = -\frac{1}{\chi_{11}^\sigma} \frac{C_{02}}{R^2} \left\{ \frac{\left[ (1 + k_{emc}^2) \left[ 2 - (\gamma R)^2 \right] - 2k_{emc}^2 \right]}{(1 + k_{emc}^2) \left[ 2 - (\gamma R)^2 \right]} \right\} + \frac{p_a}{\chi_{11}^\sigma} \left\{ \frac{\left[ (1 + k_{emc}^2) \left[ 2 - (\gamma R)^2 \right] e_1 - e_2 2k_{emc}^2 \right]}{(1 + k_{emc}^2) \left[ 2 - (\gamma R)^2 \right]} \right\}. \quad (31)$$

Using an integrated representation:

$$U = \int_R^{R+h_s} E_r dr, \quad (32)$$

integrate the left and right parts (31) on  $r$  for the situation  $r = R$ ,  $r = R_1$  and get for the electric potential:



$$\begin{aligned} \Psi(r)|_{r=R_1} &= -\frac{r}{\chi_{11}^\sigma} \frac{C_{02}}{R^2} \left\{ \frac{\left\{ \left(1+k_{emc}^2\right) \times \right. \right.}{\left. \left. \times \left[ 2 - \left(\gamma R\right)^2 \right] - 2k_{emc}^2 \right\}}{\left(1+k_{emc}^2\right)\left[ 2 - \left(\gamma R\right)^2 \right]} \right\} + \frac{p_a r}{\chi_{11}^\sigma} \left\{ \frac{\left\{ \left(1+k_{emc}^2\right) \times \right. \right.}{\left. \left. \times \left[ 2 - \left(\gamma R\right)^2 \right] e_1 - e_2 2k_{emc}^2 \right\}}{\left(1+k_{emc}^2\right)\left[ 2 - \left(\gamma R\right)^2 \right]} \right\} \Bigg|_R^{R_1} + C_{01} = \\ &= -\frac{h_s}{\chi_{11}^\sigma} \frac{C_{02}}{R^2} \left\{ \frac{\left\{ \left(1+k_{emc}^2\right)\left[ 2 - \left(\gamma R\right)^2 \right] - 2k_{emc}^2 \right\}}{\left(1+k_{emc}^2\right)\left[ 2 - \left(\gamma R\right)^2 \right]} \right\} + \frac{p_a h_s}{\chi_{11}^\sigma} \left\{ \frac{\left\{ \left(1+k_{emc}^2\right)\left[ 2 - \left(\gamma R\right)^2 \right] e_1 - e_2 2k_{emc}^2 \right\}}{\left(1+k_{emc}^2\right)\left[ 2 - \left(\gamma R\right)^2 \right]} \right\}, \end{aligned} \quad (33)$$

where  $C_{01} = 0$ .

The obtained results of determining the electric voltage correspond to the boundary conditions of the form (22) selected during the statement of the problem.

The unknown coefficient  $C_{02}$  after transformations can be written as:

$$C_{02} = U_0 \frac{\chi_{11}^{\sigma}}{h_s} R^2 \left\{ \frac{(1 + k_{emc}^2) [2 - (\gamma R)^2]}{\{(1 + k_{emc}^2) [2 - (\gamma R)^2] - 2k_{emc}^2\}} \right\} - p_a R^2 \left\{ \frac{\{(1 + k_{emc}^2) [2 - (\gamma R)^2] e_1 - e_2 2k_{emc}^2\}}{\{(1 + k_{emc}^2) [2 - (\gamma R)^2] - 2k_{emc}^2\}} \right\}. \quad (34)$$

Therefore, applying the conditions (28) and the found coefficient C02 (34), it is possible to calculate the amplitudes of the displacements of the material points of the surface of the spherical shell. In addition, the use of (34), (23) and Ohm's law for the circuit section can find the value of the electrical impedance of the transducer-shell  $Z_{el}$ :

$$Z_{el} = -\frac{U_0}{I} = -\frac{U_0}{i\omega 4\pi R^2} \frac{1}{D_z} =$$

$$= \frac{U_0}{i\omega 4\pi} \frac{\left\{ (1 + k_{emc}^2) [2 - (\gamma R)^2] - 2k_{emc}^2 \right\}}{\frac{U_0 \chi_{11}^\sigma}{h_s} R^2 (1 + k_{emc}^2) [2 - (\gamma R)^2] - p_a R^2 \left\{ (1 + k_{emc}^2) [2 - (\gamma R)^2] e_1 - 2e_2 k_{emc}^2 \right\}}, \quad (35)$$

or after the introduction of electrical static capacity of the spherical shell:

$$C_0 = \frac{i\omega 4\pi R^2 \chi_{11}^\sigma}{h_s},$$

$$Z_{el} = -\frac{U_0}{i\omega C_0} \frac{\{(1+k_{emc}^2)[2-(\gamma R)^2]-2k_{emc}^2\}}{U_0(1+k_{emc}^2)[2-(\gamma R)^2]-i\omega 4\pi p_a R^2\{(1+k_{emc}^2)[2-(\gamma R)^2]e_1-2e_2k_{emc}^2\}}. \quad (36)$$

In the case where the external environment is a vacuum, the situation is greatly simplified. In this case  $\sigma_{rr}=0$ ,  $p_a=0$  and the expression for the impedance (36) takes the form:

$$Z_{el} = -\frac{1}{i\omega C_0} \frac{\{(1+k_{emc}^2)[2-(\gamma R)^2]-2k_{emc}^2\}}{(1+k_{emc}^2)[2-(\gamma R)^2]} = -\frac{1}{i\omega C_0} L_0(\omega), \quad (37)$$

where

$$L_0(\omega) = \frac{\{(1+k_{emc}^2)[2-(\gamma R)^2]-2k_{emc}^2\}}{(1+k_{emc}^2)[2-(\gamma R)^2]}, \quad (38)$$

and has the content of the frequency-dependent transfer coefficient of the transducer  $K_I(\omega)$  in a circle «generator – working medium» (vacuum).

#### 2. 4. Determination of acoustic pressure frequency response $p_a(\omega)$

Thus, the above obtained a number of useful relationships. These include equation (28) for the radial component of the displacements of the material particles of the shell  $u_r$ , expression for the coefficient  $C_{02}$  (34), kinematic conjugation condition (11), properties of orthogonality of spherical and trigonometric wave functions and solution of the Helmholtz equation (6) for the case of realization of zero mode of shell oscillations of known type:

$$p_a(r) = \frac{p_0}{r} e^{ikr}. \quad (39)$$

Let's apply the relationship of oscillating speed with displacement and acoustic pressure of the species:

$$v(r) = -i\omega u_r = v_r(r) = \frac{1}{i\omega\rho} \frac{\partial p_0(r)}{\partial r}, \quad (40)$$

and after substituting in (28) expressions (34), (39), fulfilling the kinematic conditions of conjugation (11) and equality (40), after the transformations let's obtain the amplitude of the acoustic pressure  $p_a(r)$  at  $r = R_1$  recorded for the frequency range  $\omega$  as:

$$p_0(\omega) = \frac{\omega^2 \rho U_0 L_1(\omega) R_1^2}{(1 + \omega^2 \rho (L_2(\omega) + L_3(\omega)))}, \quad (41)$$

where

$$\left. \begin{aligned} L_1(\omega) &= \left( \frac{\chi_{11}^\sigma R_1^2}{h_s} \right) \left( \frac{2e_{12}^*}{\chi_{11}^\sigma Y^D R_1} \right) \left( \frac{F_1(\omega)}{F_3(\omega)} \right), \\ L_2(\omega) &= (R_1^2) \left( \frac{2e_{12}^*}{\chi_{11}^\sigma Y^D R_1} \right) \left( \frac{F_2(\omega)}{F_3(\omega)} \right), \\ L_3(\omega) &= (R_1^2) \left( \frac{2Y_1^D R_1}{Y^D} \right) \left( \frac{1}{F_3(\omega)} \right), \end{aligned} \right\} \quad (42)$$

$$\left. \begin{aligned} F_1(\omega) &= \frac{\{(1 + k_{emc}^2)[2 - (\gamma R_1)^2] - 2k_{emc}^2\}}{(1 + k_{emc}^2)[2 - (\gamma R_1)^2]}, \\ F_2(\omega) &= \frac{\{(1 + k_{emc}^2)[2 - (\gamma R_1)^2]e_1 - 2e_2 k_{emc}^2\}}{(1 + k_{emc}^2)[2 - (\gamma R_1)^2]}, \\ F_3(\omega) &= [2 - (\gamma R_1)^2]. \end{aligned} \right\} \quad (43)$$

The actual acoustic pressure  $p_a(\omega)$  is determined by using the expression for the pressure amplitude (41), (42) in equation  $p_0(\omega)$  (39).

#### 2. 5. Experiment

The obtained theoretical results are confirmed experimentally in terms of measuring the acoustic pressure created by the transducer in the free field  $p_a(\omega)$ .

The measurement results  $p_a(\omega)$  are represented by frequency characteristics in the frequency range of the calculated part. Evolutions were carried out in the measuring basin of the State Enterprise Research Institute «Hydropylad» in Kyiv, according to the scheme (**Fig. 2**).

The working space during the measurements corresponded to the conditions of the far field, and in the receiving path the method of gating the useful signal by time and distance was implemented. At the same time the relation was carried out:  $U_S/U_D \geq 15$  dB, where  $U_S$  – electric voltage on the recorder of the useful signal,  $U_D$  – electric voltage of damage.



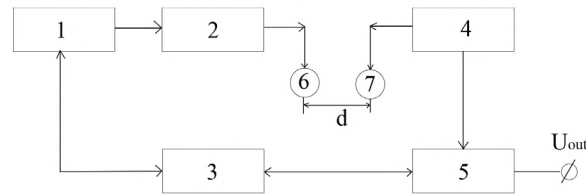


**Fig. 2.** Measurement scheme: 1 – master generator; 2 – power amplifier; 3 – selector; 4 – amplifier; 5 – bandpass filter; 6 – transformer; 7 – control hydrophone

The results of acoustic pressure measurements at the frequencies of the working range of numerical studies show (**Fig. 3**) that the frequency dependences of pressures measured in the resonance region of the zero mode of oscillations of the sphere, provided doubling the distance from the emitter to the control hydrophone, decreases by 6 dB. That is, the law of inverse radii is fulfilled, which corresponds to the nature of the calculated curves (**Fig. 6**).

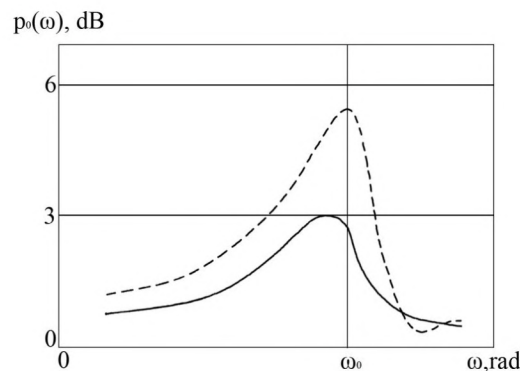


**Fig. 3.** Amplitude-frequency characteristic of pressure  $p(\omega)$ , dB  $\left( \text{---}d \geq \frac{2D^2}{\lambda}, \text{---}2d \right)$

Based on the obtained graphs, let's believe that the theoretical studies correspond to the practical results of the work.

### 3. Results and discussion

Calculations of frequency dependences of coefficients  $K_t(\omega)$ ,  $Z_{el}(\omega)$ ,  $p_a(\omega)$  were carried out for a spherical cover with radius  $R_1 = 0.5$  m which is made of CTS-19 piezoelectric material having coefficient  $k_{emc} = 0.5$ . Estimated distances for acoustic pressures were 1 m and 10 m.

The results of calculations are shown in **Fig. 4–6**.

In **Fig. 4, a** the calculated graph of  $K_t(\omega)$  is shown, which has two local extremes – local minimum and local maximum. The local minimum of  $K_t(\omega)$  determines the situation of the largest amplitudes of displacements of the radial components of the shell movements and is a resonance of the electromechanical nature of the corresponding frequency  $\omega_r$ , for which equality must be satisfied:

$$2 - (\gamma R_1)^2 - 2k_{emc}^2 = 2 - \left( \frac{\omega_r}{\omega_a} \right)^2 = 0, \quad (44)$$

where  $\gamma^2 = \rho_0 \omega_r^2 / Y^D$ ,  $k_{emc}^2 = \left[ 2 - \left( \frac{\omega_r}{\omega_a} \right)^2 \right] \frac{1}{2}$  accordingly, the square of the wave number of oscillations of the shell and the square of the coefficient of electromechanical coupling.

The second local extremum determines the situation of the smallest radial displacements of the points of the shell surface and is an electromechanical antiresonance with frequency  $\omega_a$ . The equality  $F_3(\omega) = \left[ 2 - (\gamma R_1)^2 \right]$  holds for it.

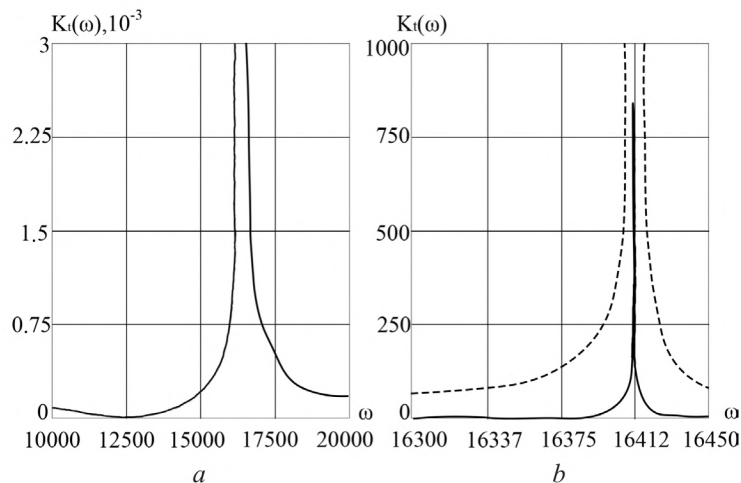


**Fig. 4.** Frequency response of transmission coefficients  $K_t(\omega)$ : *a* – working medium – vacuum; *b* – working medium – water

The modulus of elasticity is calculated by the formulas:

$$Y^D = \frac{\omega_a^2 \rho_0}{2} R_1, \quad Y = Y^D \frac{1}{(1 + k_{emc}^2)}.$$

In our computational situation, the frequency of electromechanical resonance is 2600 Hz and the introduction of the load from the working medium (**Fig. 4, b**) affects the frequency response for the selected computational situations only in part of the active load.

The given situation with change of amplitudes of radial components taking into account connectivity should correspond to change of electric impedance  $Z_{el}(\omega)$  of hydroelectric-elastic system. Indeed (**Fig. 5**), at the resonance frequency the impedance  $Z_{el}(\omega)$  is small and in the circuit – «generator-working medium», there will be a maximum of the current mode, which includes the bias current and the current in the external circuit. The opposite situation is observed at the antiresonance frequency.

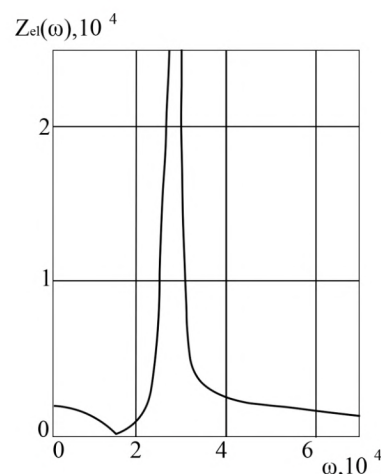


**Fig. 5.** Frequency response of electrical impedance  $Z_{el}(\omega)$

Regarding the frequency response of the acoustic pressure, it is obvious that the frequency dependence of the pressure is expected. The graphs themselves contain a local maximum, which is at the resonant frequency  $\omega_r$  of the zero mode of oscillations.

The calculations were performed for two situations: the first – standard, for which the pressure is determined at a traditional distance of 1 m, and the second – at a distance of 10 m.



In this case, (**Fig. 6**) the levels of local maxima decrease by 20 dB with an increase in the calculated distance by 10 times, which is fully consistent with the law of inverse radii and confirmed experimentally (**Fig. 3**).

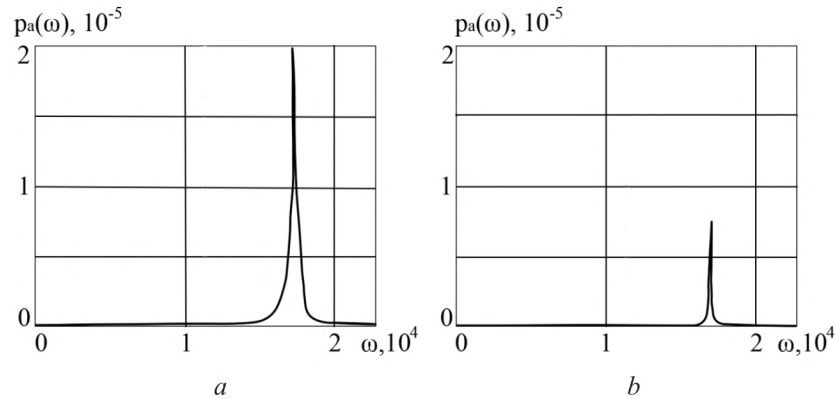


**Fig. 6.** Frequency response of acoustic pressure  $p_a(\omega)$ :  $a - R_1 = 1$  m;  $b - R_1 = 10$  m

The obtained results of using the «pass-through» method in the problem of sound radiation show a new generalizing approach that allows one to obtain its exact solutions in the representation of a transducer – a thin-walled piezoceramic shell. Thus, the result of the formation of a field of zero-order acoustic waves can be described by jointly solving the equations of oscillations of the source, the equation for the acoustic field, the equation of state for piezoelectric ceramics, and the Cauchy relations for displacements and deformations. The key point of the work is the solution within the framework of the theory of thin shells of revolution and the conditions of conjugation in the acoustic, mechanical, and also in the electric field. Let's also note the fact that the traditional method of equivalent circuits [21], which is successfully used in the resonance region of the frequency response of a sound source, worsens the reliability of the numerical results, the more the further from the resonance the frequency region under consideration is.

Features of the proposed solution consist in taking into account, for the considered oscillatory system, the connection of acoustic mechanical elastic forces with forces of electrical nature. In this case, the electric boundary conditions determine the absence of free electric charges in the piezoceramics and the presence of only a dynamic component of current values – in the form of the surface density of electric charges in the region of the electroded surfaces of the shell.

Of course, the proposed formulation and solution have a number of limitations. These include the following:

- restrictions associated with the thickness of the shell wall (it should be no more than 10 % of the radius);
- restrictions associated with the method and type of electroplating of the surfaces of the sphere (full or partial);
- technological limitations associated with the uniformity of electrode deposition and the provision of reliable electrical contact on the inner and outer electrodes (in the work these technological features are idealized and are not taken into account);
- taking into account the possible presence of the throat of the sphere and the associated possible changes in the frequency characteristics of the acoustic field;
- idealization of the setting device cable line.

Some of these restrictions can be removed. First of all, this concerns the features of a constructive and technological nature in terms of electroplating the surfaces of the converter, which play an important role in the formation of its spatial properties and in the future can be considered taking into account the presented material and the worked out tasks [11, 13–16].

Further development of the proposed scientific instrument of the «pass-through» method implies its use in various areas of research into the spatial and energy characteristics of acoustic antennas and transducers as applied not only to the problems of radiation, but also reception.

This requires the complication of the mathematical apparatus in terms of the special functions used (from cylindrical functions to spheroidal or ellipsoidal – for converters of basic canonical forms and systems based on them), solution methods (from standard methods for solving differential equations to methods for solving infinite systems with complex terms), issues of convergence of complex series and conditions of electrical and acoustic loading of transducers, as well as the presence of acoustic screens, methods of location and connection of transducers, etc.

In the development of the proposed topic, after modification of the formulations of the corresponding equations and boundary conditions, it is assumed that the «pass-through» method will provide a broader physical interpretation of the effects of the interaction of acoustic, mechanical and electric fields of the transducer and their influence on the spatial and energy properties of transducers and systems based on them. This concerns the replacement of the boundary conditions by the conjugation conditions and the description of methods for forming the spatial characteristics of single transducers and their systems for various types of electroding of transducers, as well as the type and nature of electrical and acoustic loads.

#### 4. Conclusions

The application of the method of the end-to-end problem of the direction «hydroelectric elasticity» in the situation of sound radiation shown on the example of operation of a spherical electroacoustic source of zero order in an ideal liquid. The electroacoustic emitter source is supplied by a spherical piezoceramic thin-walled shell with complete electroding of its surfaces.

In terms of the load of the transducer from the working environment shows, the possibility, in fact, the solution of the radiation problem taking into account the effects of connectivity of the main physical fields, which are characterized by elastic forces of mechano-acoustic nature and Coulomb forces (electric forces).

The analysis of the main frequency dependences of complex characteristics of the emitter is calculated and made:  $K_t(\omega)$ ,  $Z_{et}(\omega)$ ,  $p_a(\omega)$ . Possibilities of a decision in part of definition of material constants of piezomaterial of a cover of the fixed geometrical sizes and frequency dependences of the basic electroacoustic characteristics of a source are shown.

It is determined that this approach is promising and should be extended to the problem of radiation-reception of sound, within the wave acoustics of infinite and bounded spaces.

#### Acknowledgments

The work was performed within the initiative scientific topic: «Problems of underwater sound communication», registration number in KPI named after Igor Sikorsky FEL – 1/3, state registration number № 0113U008183.

---

#### References

- [1] Mason, W. P. (1950). Piezoelectric crystals and their application to ultrasonics. Van Nostrand, 508.
- [2] Grinchenko, V. T., Ulitko, A. F., Shul'ga, N. A. (1989). Mekhanika svyazannykh pol'y v elementakh konstruksiy. Vol. 5. Elektropругost'. Kuiv: Nauk. dumka, 280.
- [3] Ustinov, Yu. A. (1996). Electroelasticity. Fundamentals of the theory and some applications. Sorosovskiy obrazovatel'niy zhurnal, 3, 122–127. Available at: [https://web.archive.org/web/20060828163531/http://journal.issep.rssi.ru/articles/pdf/9603\\_122.pdf](https://web.archive.org/web/20060828163531/http://journal.issep.rssi.ru/articles/pdf/9603_122.pdf)
- [4] Aronov, B. (2009). Coupled vibration analysis of the thin-walled cylindrical piezoelectric ceramic transducers. The Journal of the Acoustical Society of America, 125 (2), 803–818. doi: <https://doi.org/10.1121/1.3056560>
- [5] Shul'ga, N. A., Grigorenko, A. Y., Loza, I. A. (1984). Axisymmetric electroelastic waves in a hollow piezoelectric ceramic cylinder. Soviet Applied Mechanics, 20 (1), 23–28. doi: <https://doi.org/10.1007/bf00883567>
- [6] Petrishchev, O. N. (2012). Harmonic oscillations of piezoceramic elements. Part 1. Harmonic oscillations of piezoceramic elements in vacuum and the resonance-antiresonance method. AVERS.
- [7] Babaev, A. E., Leyko, A. A., Savin, V. G. (1989). Akusticheskie i mekhanicheskie polya radial'no polarizovannogo tsilindricheskogo vibratora pri impul'snom elektricheskom vzbuzhdenii. Akusticheskiy zhurnal, 35 (2), 211–217.
- [8] Morgun, I. O., Savin, V. G. (2007). Acoustic-to-electric pulse transforming by a spherical piezoceramic shell baffled with an external elastic shell. Akustichnyi visnyk, 10 (3), 60–69. Available at: <http://dspace.nbuv.gov.ua/handle/123456789/1047>



- [9] Derepa, A., Dzhanazian, V., Leiko, O., Drozdenko, O. (2019). Modern approaches to the design of hydroacoustic antennas of ship hydroacoustic stations. *Weapons and military equipment*, 22 (2), 93–98. doi: [https://doi.org/10.34169/2414-0651.2019.2\(22\).93-98](https://doi.org/10.34169/2414-0651.2019.2(22).93-98)
- [10] Korzhyk, O. V. (2010). Application of the «through» problem to the study of the amplitude-frequency characteristics of the acoustic field of a receiving cylindrical piezoceramic transducer with cut-off electrodes. *Elektronika ta zv'yazok*, 15(3), 160–166.
- [11] Korzhyk, A. V., Kuroiedova, T. S., Philippova, N. Y. (2013). The analysis of electromechanical characteristics of radiating cylindrical piezoceramic transducer with surface coated by solid electrodes located in the closed ring layer. *Electronics and Communications*, 18 (1), 102–109. doi: <https://doi.org/10.20535/2312-1807.2013.18.1.189189>
- [12] Novak, D. D., Korzhyk, O. V., Petryshchev, O. M., Hubinets, Yu. V. (2014). The output voltage determination on the load of piezoelastic spherical transducer with acoustic medium inside (the theoretical basis and solution). *Information Processing Systems*, 7 (123), 49–56.
- [13] Leiko, O. H., Sviatnenko, A. O. (2017). Physical fields aimed sonar antennas based on cylindrical emitters with internal screens. *Electronics and Communications*, 22 (2), 66–72. doi: <https://doi.org/10.20535/2312-1807.2017.22.1.86484>
- [14] Korzhyk, O. V. (2013). To the boundary conditions for problem of sound receiving by spherical electroelastic transducer with disconnecting electrodes. *Electronics and Communications*, 18 (2), 97–103. doi: <https://doi.org/10.20535/2312-1807.2013.18.2.186872>
- [15] Aronov, B., Brown, D. A., Yan, X., Bachand, C. L. (2011). Modal analysis of the electromechanical conversion in piezoelectric ceramic spherical shells. *The Journal of the Acoustical Society of America*, 130 (2), 753–763. doi: <https://doi.org/10.1121/1.3593364>
- [16] Leiko, O., Derepa, A., Pozdniakova, O., Starovoit, Y. (2018). Acoustic fields of circular cylindrical hydroacoustic systems with a screen formed from cylindrical piezoceramic radiators. *Romanian Journal of Acoustics and Vibration*, 15 (1), 41–46. Available at: <http://rjav.sra.ro/index.php/rjav/article/view/49>
- [17] Derepa, A. V., Leiko, O. H., Drozdenko, O. I., Svyatnenko, A. O. (2019). Properties of electric fields of hydroacoustic radiators with internal screens. *Ozbroynnya ta viys'kova tekhnika*, 4 (24), 41–48. Available at: [http://nbuv.gov.ua/UJRN/ovt\\_2019\\_4\\_6](http://nbuv.gov.ua/UJRN/ovt_2019_4_6)
- [18] Starovoit, Y. I., Kurdiuk, S. V., Leiko, O. H. (2018). Physical fields of hydroacoustic sonar arrays with baffle and cylindrical piezoceramic radiators with radial polarization. *Microsystems, Electronics and Acoustics*, 23 (1), 30–36. doi: <https://doi.org/10.20535/2523-4455.2018.23.1.99725>
- [19] Shyshkova, K. A., Leiko, O. H. (2019). Radiation of Sound by a Cylindrical Piezoceramic Converter with Radial Polarization and a Rigid Screen. *Microsystems, Electronics and Acoustics*, 24 (4), 68–73. doi: <https://doi.org/10.20535/2523-4455.2019.24.4.184027>
- [20] Philippova, N. (2014). Setting and solution problem of sound emission of multimode piezoceramic transducer, placed in a closed loop layer. *Vestnik Zabaykal'skogo gosudarstvennogo universiteta*, 01 (104), 74–82.
- [21] Aronov, B. S. (1990). *Elektromekhanicheskie preobrazovateli iz p'ezoelektricheskoy keramiki*. Leningrad: Energoatomizdat.

Received date 03.08.2020

Accepted date 06.07.2021

Published date 13.09.2021

© The Author(s) 2021

This is an open access article  
under the Creative Commons CC BY license

**How to cite:** Korzhyk, O., Naida, S., Kurdiuk, S., Nizhynska, V., Korzhyk, M., Naida, A. (2021). Use of the pass-through method to solve sound radiation problems of a spherical electro-elastic source of zero order. *EUREKA: Physics and Engineering*, 5, 133–146. doi: <https://doi.org/10.21303/2461-4262.2021.001292>